Coarse-grid simulation of reacting and non-reacting gas-particle flows

Final Technical Report

September 14, 2000 – September 13, 2004

Author: Sankaran Sundaresan

Department of Chemical Engineering

Princeton University

Princeton, NJ 08544

(609) 258-4583 (tel)

(609) 258-0211 (fax)

sundar@princeton.edu

October 2004

Award # DE-FC26-00NT40971

DOE Vision 21 Virtual Demonstration Initiative

Name of the submitting organization: Princeton University, Princeton, NJ 08544

Disclaimer

Project Summary

Many processes involved in coal utilization involve handling of fine particles, their pneumatic transport, and their reactions in fluidized beds, spouted beds and circulating fluidized beds. One of the factors limiting our ability to simulate these processes is the hydrodynamics encountered in them. Two major issues that contribute to this limitation are lack of good and computationally expedient models for frictional interaction between particles, and models to capture the consequences of mesoscale structures that are ubiquitous in gas-solid flows. This project has focused on the development of these models through a combination of computer simulations and experiments.

The principal goal of this project, funded under the *DOE Vision 21 Virtual Demonstration Initiative* is better simulation of circulating fluidized bed performance. The principal challenge funded through this cooperative agreement is to devise sound physical models for the rheological characteristics of the gas-particle mixtures and implement them in the open-domain CFD code MFIX. During the course of this project, we have made the following specific advances.

(a) We have demonstrated unequivocally that sub-grid models are essential to capture, even qualitatively correctly, the macroscale flow structures in gas-particle flows in vertical risers. To this end, we developed sub-grid models of different levels of detail and exposed the sensitivity of the results obtained in coarse-grid simulations of gas-particle flow in a riser to the level of sophistication of the sub-grid models.

(b) We have demonstrated that sub-grid model for the fluid-particle drag force is the most important additional feature and that the corrections for the granular phase viscosity and pressure are of secondary importance. We have also established that sub-grid models for dispersion of heat and mass are of secondary importance only.

(c) We have brought forth the general character of the sub-grid model for the drag force.

(d) We have performed for the first time in the literature a detailed analysis of the impact of unipolar electrostatic charges on gas-particle flow characteristics in a riser.

(e) We have examined in detail the effect of wall friction and particle-particle contact (frictional) stresses on fluidization and defluidization behavior of particle assemblies, and brought forth their importance for stable operation of standpipes in a circulating fluidized bed circuit.

(f) We have demonstrated that the general characteristics of contact stresses in particle assemblies and wall friction are similar for many different particles, establishing that a simple model framework can be widely applicable.

(g) We have developed constitutive models for frictional regime, implemented them in MFIX and demonstrated the capability of simulating dense gas-solid flows in the frictional regime.

(h) We have also performed detailed experiments to expose the nature of the stick-slip flows in silos, as a simple model system for under-aerated standpipes.

All theoretical advances made in the study are implemented in MFIX and are available for public use.

Table of Contents

1. Introduction

The principal goal of our project, funded under the *DOE Vision 21 Virtual Demonstration Initiative* is better simulation of circulating fluidized bed (CFB) performance. Virtual demonstration of CFB performance requires modeling and simulation of the entire spectrum of gas-particle flow conditions ranging from dense phase flows in standpipes to dilute phase flow conditions of risers.

We had proposed enabling a *virtual demonstration tool*, which is based on the open-domain CFD code MFIX, originally developed at NETL. MFIX is based on a model framework in which the gas and particle phases are treated as interpenetrating continua. The general structure of Eulerian equations of motion for each of the phases is well understood, although specific constitutive equations describing the rheological behavior of gas-particle suspensions are still being developed. MFIX includes the capability to carry out reactive flow simulations, so the tool that we have set out to develop will permit both cold flow and reactive flow simulations. The principal challenge funded through this cooperative agreement is to devise and implement in MFIX sound physical models for the rheological characteristics of the gas-particle mixtures. These models address issues related to performance of standpipes, fluidized beds and risers, which are the main components of a circulating fluidized bed.

2. Specific Objectives of Proposed Research

One of the objectives of our research is to develop methodologies for practical simulation of gas-particle flows in fast-fluidized beds and risers, where the particle concentration is typically in the range of 1-30 volume %. We have shown that meso-scale structures that take the form of clusters and streamers, which have been observed in risers, can be captured qualitatively through transient integration of continuum equations for the gas and particle phases. These structures arise as a result of two instability mechanisms, both of which are accounted for in a rheological model deduced in the literature by adapting the kinetic theory of gases to gas-particle mixtures. These meso-scale structures are too small in size to be resolved in simulations of flow in large process vessels, and are invariably invisible in the coarse-grid simulations. Yet, they affect the flow characteristics profoundly; in particular, they alter the effective interaction force that

couples the gas and particle phases, and dramatically increase the effective viscosities of the two phases. We set out to develop a more practical approach, where we simulate the dynamics of only the large clusters using coarse grids and account for the effects of smaller, unresolved clusters through suitable sub-grid approximations. Specifically, we had proposed to develop such sub-grid models and implement them into MFIX.

The second objective of our study is concerned with dense flows. The volume fraction of particles in dense fluidized beds, standpipes and valves is usually sufficiently large that the particles make enduring contact with multiple neighbors. In such instances, stress transmission between particles, and between particles and bounding solid surfaces occurs predominantly through frictional interactions. In this regime of flow, when the strength of frictional interaction between particles becomes sufficiently weak, flow of gas-solid suspension becomes unstable and a bubbly suspension results. Once formed, these bubbles dictate the macroscale flow characteristics, and therefore detailed CFD simulation of suspensions in this regime should account for the dynamics associated with the gas bubbles. This is possible only if frictional stresses are modeled properly. With this in mind, we set out to develop and implement a model for frictional rheology into MFIX, thus creating a framework for realistic representation of frictional stresses. We also proposed to devise procedures for evaluating frictional model parameters experimentally.

3. Accomplishments

In order to achieve these objectives, we had proposed a three year long research program involving computational experiments on statistical characteristics of mesoscale structures and a combination of simple laboratory experiments on frictional stress in dense gas-particle systems. We now summarize briefly the major accomplishments.

3.1 Mesoscale Structures in Gas-Particle Flows through Risers

Studies performed in our group and elsewhere have established concretely that continuum models for gas-particle flows, such as those based on the kinetic theory of granular materials, can capture at least qualitatively correctly the occurrence of meso-scale structures in fluidized gas-

particle suspensions. Details of these can be found in Agrawal et al. (2001), included here as appendix A. A more general discussion of instabilities in fluidized suspensions is presented by Sundaresan (2003), included here as appendix B.

Detailed simulation of flow over small domains reveal that spatiotemporal fine structures, whose length scale is of the order of ten or so particle diameter, are present in these flows. Therefore, to fully resolve these structures, grid sizes of the order of few particle diameters are needed. However, such fine grids are impractical in any industrial scale problem (e.g., see Sundaresan, 2000), where simulations can only be performed using coarse grids. These simulations would resolve the larger flow structures, but not those smaller than the grid size. We have demonstrated that these unresolved flow structures contribute appreciably to the momentum exchange between the gas and particle phases, and that stress transmission from one grid to another in the coarse-grid analysis (Agrawal et al., 2001). The challenge is then to develop sub-grid models to capture the essential consequences of the unresolved sub-grid structures.

We have carried out a number of highly resolved simulations of the continuum equations for gas-particle flows in spatially periodic domains (both two-dimensional and three-dimensional), whose size is commensurate with grid sizes typically used in coarse-grid simulations of gas-particle flows. Through such calculations we ascertained that meso-scale structures arise spontaneously through a local instability and can be sustained even in the absence of macro-scale shear. We examined the extent to which the macro-scale shear modifies the consequences of the meso-scale structures (i.e. those which will be unresolved in coarse-grid simulations) and found that the shear had a modest effect in 2-D simulations and a much weaker influence in 3-D simulations. Quite importantly, the results obtained in 2-D and 3-D simulations were very similar, suggesting that much of the concept development could be done via 2-D computational experiments. Furthermore, as macro-scale shear had only a weak effect on the meso-scale structures, the effect of this shear was deemed to be of secondary importance in the sub-grid models. With this in mind, much of the work on sub-grid model development was performed through highly resolved computational experiments in unsheared fluidized suspensions in small 2-D periodic domains. Through these simulations, we examined how the effective drag coefficient, normal stresses and particle phase viscosity varied with size of the domain, particle volume fraction and other particle properties. (A detailed discussion of these results can be found in appendix A.)

We constructed *ad hoc* sub-grid models of different levels of sophistication through detailed simulations in small periodic domains. Specifically, we considered a set of sub-grid corrections referred to as the time-averaged sub-grid model and a more detailed stochastic sub-grid model. To examine the consequences of these sub-grid models on the predicted behavior of gas-particle flows in a riser, a number of coarse-grid simulations were carried out. A detailed account of these results has been reported by Andrews et al. (2004), included here as Appendix C. The main findings of this work are summarized below.

We have performed many 2-D coarse-grid simulations of gas-particle flow in a vertical channel to assess the impact of the sub-grid models and the sensitivity of the results to various components of the sub-grid models. Our study clearly showed that the results obtained in coarse-grid integration of the microscopic equations for gas-particle flows in large process vessels change appreciably if sub-grid corrections to account for the effects of unresolved structures are included. The most dramatic difference occurred in our simulations when a simple *time-averaged* sub-grid model was added to the *no sub-grid* model case. Although the level of sophistication of the sub-grid model did make a difference in the quantitative results in our simulations, even a simple time-averaged sub-grid model was able to capture the main qualitative effects.

The simple time-averaged sub-grid model is, in a strict sense, flawed, as there is no separation of time scales between the unresolved (sub-grid) structures and those resolved in the coarse-grid simulations. To account for this lack of separation of time scale, an enhancement of the time-averaged sub-grid model that took the form of a stochastic correction to the drag coefficient was implemented. It was found that such a stochastic sub-grid model yielded qualitatively the same results as the time-averaged sub-grid model. Thus the lack of separation of time scales does not appear to be a severe deficiency.

We have also examined the effect of stochastic fluctuations at the riser inlet on the flow structure produced in the riser, and demonstrated that the inlet fluctuations aid the development of time-dependent flow structures in the riser, and eliminates spurious solutions which can be predicted by simulations under some conditions.

Through these studies, we have not only shown that sub-grid models are essential, but also devised a method to evaluate the sub-grid models for a given problem through simple

computational experiments. We have also demonstrated how to incorporate these sub-grid models in MFIX.

3.2 Sub-grid models for mass and heat dispersion induced by meso-scale structures

We have also studied the role of meso-scale structures on gas dispersion in gas-particle flows. Tracer gas dispersion is an important and commonly used tool for experimental characterization of flows in risers and other fluidized suspensions. The influence of fluctuations at different scales (more specifically, those resolved in a coarse-grid simulation and those unresolved in these calculations) on the dispersion process was probed in our studies. Unresolved flow structures contribute to the dispersion of mass and heat, in addition to the momentum considered above – we performed highly resolved simulations in small periodic domains to assess the magnitude of sub-grid correction for the dispersion resulting from the structures which would have been invisible in coarse-grid simulations. Details of this study have been reported by Loezos & Sundaresan (2002), included here as Appendix D. Our coarse-grid simulations revealed that macro-scale dispersion arose primarily due to the hydrodynamic fluctuations which were resolved in the flow calculations and that the sub-grid corrections played only a negligible role. Therefore, we concluded that sub-grid models are important for hydrodynamic analysis, but less so for heat and mass transport calculations.

3.3 *Effect of electrostatics on riser flow characteristics*

A significant effort that we undertook in this cooperative agreement concerns the effect of electrical charges carried by the particles on the flow behavior. In the past few years, this issue has emerged as a possibly very important, but completely overlooked phenomenon in riser performance. We began with a thorough literature search of typical level of charges carried by particles in riser flows and in pneumatic conveying applications. We then formulated a simple model for fully-developed flow of gas-particle mixtures in vertical pipes where we postulated that the particles carried specified levels of charge. Much to our surprise, we found that even at very small charge levels, a significant electric field can develop inside the riser and that it can

lead to appreciable segregation of particles towards the riser walls (Al-Adel et al., 2003). Appendix E describes this study in detail.

3.4 Dense Gas-particle Flows in fluidized beds and standpipes

A few years ago, we performed experiments where we examined the CFB performance characteristics at different levels of standpipe aeration, probing specifically the flow behavior in the standpipe and the conditions at which the loop instability sets in (Srivastava et al., 1998). It was clear from that study that contact stresses in the particle phase and wall friction played important roles in imparting stability to CFB hydrodynamics. Yet, a robust modeling framework to handle frictional stresses in CFD codes such as MFIX was unavailable prior to the present study.

We undertook as a part of this cooperative agreement a study to understand contact stresses and wall friction in a quantitative sense. We performed simple fluidization and defluidization experiments in tubes of various diameters to extract information on the compressive yield strength of particle assemblies at various volume fractions and wall friction parameters. We then used information on wall friction and contact stresses extracted from fluidization and defluidization experiments to show that the standpipe performance data could be explained quantitatively on the basis of wall friction and granular stresses (Srivastava & Sundaresan, 2002, included here as Appendix F).

Having ascertained that granular stresses and wall friction played important roles in standpipe flows, we set out to understand the general characteristics of these quantities for a variety of particles. This study (Loezos et al., 2002, included here as Appendix G), demonstrated the robustness of the dependence of granular stress on particle volume fraction (for seven different types of particles) and the consistent role of wall friction. This led us to focus our efforts on the development of a general model framework to incorporate the contact (frictional) stresses between the particles and particle-wall friction into the two-fluid models for gas-particle flows.

We have developed a multi-dimensional frictional-kinetic model for gas-particle flow which combines the flow characteristics in the dense regime with those at the dilute rapid granular flow regime. This model and friction boundary conditions at bounding surfaces have been

implemented into MFIX and used to study model discharge problems, thus demonstrating the robustness of the model and the CFD implementation. Further details can be found in Srivastava & Sundaresan (2003), included here as Appendix H.

We felt that it is very important to understand the manner in which stick-slip flow occurs in dense granular flow through pipes, in order to develop a better physical understanding of the flow patterns in such a flow regime. Such stick-slip flow, for example, occurs in under-aerated standpipes of circulating fluidized beds. To this end, we devised a simple experiment, where we studied the manner in which particles discharged from a tube equipped with a central orifice at the bottom. The details of this study by Muite et al. (2004) is included here as Appendix I. This study provides new insight on vibration of the structure associated with stick-slip flow, and an accompanying phenomenon known as silo music.

4. Deliverables

The deliverables in this project consist of advanced process models for a virtual demonstration tool. We believe that the work performed through this cooperative agreement has significantly advanced the knowledge base in the field of gas-solid flow, which is critical element in DOE's Vision 21. The specific deliverables that we have made from our research are as follows:

a) A fundamentally based sub-grid model for effective drag force, stresses and dispersion, which is deduced through scores of computational experiments and theoretical analysis, and can be used in coarse-grid simulation of gas-solid flows.
b) A version of MFIX code to NETL with the above sub-grid model implemented and tested.
c) A mathematical model for frictional stresses in dense suspensions, which is supported by experimental data on a variety of powders.
d) A simple experimental protocol to determine the parameters appearing in this frictional model, and methodology to determine these parameters from experimental data.
e) A version of MFIX code to NETL, with this frictional model implemented and tested.

5. Bibliography

K. Agrawal, P. N. Loezos, M. Syamlal and S. Sundaresan, "The Role of Meso-scale Structures in Rapid Gas-solid Flows", *J. Fluid Mech.*, **445**, 151 – 185 (2001).

A. T. Andrews, P. N. Loezos and S. Sundaresan, "Coarse-grid Simulation of Gas-Particle Flows in Vertical Risers", paper presented at 2003 AIChE Annual Meeting and submitted to Industrial & Engineering Chemistry Research (2004).

P. N. Loezos & S. Sundaresan, "Simulation of dispersion in gas-particle flows through a riser", *Circulating Fluidized Beds* VII, eds. J. R. Grace, J. Zhu and H. I. de Lasa, Can. Society of Chemical Engineering, Ottawa, pp 427-434, (2002).

P. N. Loezos, P. Costamagna & S. Sundaresan, "The role of contact stresses and wall friction on fluidization", *Chem. Eng. Sci.*, **57**, 5123 – 5141 (2002).

P. N. Loezos, P. Costamagna & S. Sundaresan, "The role of contact stresses and wall friction on fluidization", *Chem. Eng. Sci.*, **57**, 5123 – 5141 (2002).

B. Muite, S. F. Quinn, S. Sundaresan and K. K. Rao, "Silo Music and Silo Quake: Granular Flow Induced Vibration", *Powder Technology*, **145**, 190 – 202 (2004).

A. Srivastava, K. Agrawal, S. Sundaresan, S. B. Reddy Karri and T. M. Knowlton, "Dynamics of gas-particle flow in circulating fluidized beds", *Powder Technology*, **100**, 173 – 182 (1998).

A. Srivastava & S. Sundaresan, "Role of wall friction in fluidization and standpipe flow", *Powder Technology*, **124**, 45 – 54 (2002).

A. Srivastava & S. Sundaresan, "Analysis of a Frictional-kinetic model for Gas-Particle Flows", *Powder Technology*, **129**, 72 – 85 (2003).

S. Sundaresan, "Perspective: Modeling the Hydrodynamics of Multiphase Flow Reactors: Current Status and Challenges", *AIChE J.*, **46**, 1102-1105 (2000).

S. Sundaresan, "Instabilities in Fluidized Suspensions", *Annu. Rev. Fluid Mech.*, 35, 63 - 88 (2003)

6. Publications Resulting from This Study

K. Agrawal, P. N. Loezos, M. Syamlal and S. Sundaresan, "The Role of Meso-scale Structures in Rapid Gas-solid Flows", *J. Fluid Mech.*, **445**, 151 – 185 (2001). [Appendix A]

S. Sundaresan, "Instabilities in Fluidized Suspensions", *Annu. Rev. Fluid Mech.*, **35**, 63 - 88 (2003) [Appendix B]

A. T. Andrews, P. N. Loezos and S. Sundaresan, "Coarse-grid Simulation of Gas-Particle Flows in Vertical Risers", paper presented at 2003 AIChE Annual Meeting and submitted to I& EC Research (2004). [Appendix C]

P. N. Loezos & S. Sundaresan, "Simulation of dispersion in gas-particle flows through a riser", *Circulating Fluidized Beds* VII, eds. J. R. Grace, J. Zhu and H. I. de Lasa, Can. Society of Chemical Engineering, Ottawa, pp 427-434, (2002). [Appendix D]

M. Al-Adel, D. A. Saville & S. Sundaresan, "The effect of static electrification on gas-solid flows in vertical risers", *Ind. Eng. Chem. Res.*, **41**, 6224 – 6234 (2002). [Appendix E]

A. Srivastava & S. Sundaresan, "Role of wall friction in fluidization and standpipe flow", *Powder Technology*, **124**, 45 – 54 (2002). [Appendix F]

P. N. Loezos, P. Costamagna & S. Sundaresan, "The role of contact stresses and wall friction on fluidization", *Chem. Eng. Sci.*, **57**, 5123 – 5141 (2002). [Appendix G]

A. Srivastava & S. Sundaresan, "Analysis of a Frictional-kinetic model for Gas-Particle Flows", *Powder Technology*, **129**, 72 – 85 (2003). [Appendix H]

B. Muite, S. F. Quinn, S. Sundaresan and K. K. Rao, "Silo Music and Silo Quake: Granular Flow Induced Vibration", *Powder Technology*, **145**, 190 – 202 (2004). [Appendix I]

7. Abbreviations Used in This Report

CFB	–	**C**irculating **F**luidized **B**ed
CFD	–	**C**omputational **F**luid **D**ynamics
DOE	–	**D**epartment **O**f **E**nergy
MFIX	–	**M**ultiphase **F**low with **I**nterphase exchange
NETL	–	**N**ational **E**nergy **T**echnology **L**aboratory
2 – D		two-dimensional
3 – D		three-dimensional

Coarse-grid simulation of reacting and non-reacting gas-particle flows

Final Technical Report

Award # DE-FC26-00NT409071
DOE Vision 21 Virtual Demonstration Initiative

Appendix A

J. Fluid Mech. (2001), *vol.* 445, *pp.* 151–185.
DOI: 10.1017/S0022112001005663 Printed in the United Kingdom

The role of meso-scale structures in rapid gas–solid flows

By KAPIL AGRAWAL[1], PETER N. LOEZOS[1], MADHAVA SYAMLAL[2] AND SANKARAN SUNDARESAN[1]†

[1]Department of Chemical Engineering, Princeton University, Princeton, NJ 08544, USA
[2]Fluent Inc., P.O. Box 880, Morgantown, WV 26507-0880, USA

(Received 6 January 2000 and in revised form 2 May 2001)

Meso-scale structures that take the form of clusters and streamers are commonly observed in dilute gas–particle flows, such as those encountered in risers. Continuum equations for gas–particle flows, coupled with constitutive equations for particle-phase stress deduced from kinetic theory of granular materials, can capture the formation of such meso-scale structures. These structures arise as a result of an inertial instability associated with the relative motion between the gas and particle phases, and an instability due to damping of the fluctuating motion of particles by the interstitial fluid and inelastic collisions between particles. It is demonstrated that the meso-scale structures are too small, and hence too expensive, to be resolved completely in simulation of gas–particle flows in large process vessels. At the same time, failure to resolve completely the meso-scale structures in a simulation leads to grossly inaccurate estimates of inter-phase drag, production/dissipation of pseudo-thermal energy associated with particle fluctuations, the effective particle-phase pressure and the effective viscosities. It is established that coarse-grid simulation of gas–particle flows must include sub-grid models, to account for the effects of the unresolved meso-scale structures. An approach to developing a plausible sub-grid model is proposed.

1. Introduction

Experimental studies on high-velocity gas–particle flows in vertical pipes have revealed that particles are usually distributed over the cross-section of the pipe in a non-uniform fashion (e.g. see Weinstein, Shao & Schnitzlein 1986; Bader, Findlay & Knowlton 1988). This non-uniformity may introduce downflow of particles and gas in some regions, usually near the pipe wall, even though the cross-sectional average flows of particles and gas are upward. Riser flows are inherently unsteady with large fluctuations in suspension density (Schnitzlein & Weinstein 1988). It is now well established that meso-scale structures, namely clusters and streamers of particles, whose characteristic size is on the order of 10–100 particle diameters, are present in such flows (Grace & Tuot 1979; Gidaspow 1994; Horio 1995; Tsukada 1995). These structures affect the overall flow behaviour significantly and should therefore be accounted for in computational fluid dynamic (CFD) simulations of riser flows.

† Author to whom correspondence should be addressed: sundar@princeton.edu

Unfortunately, the meso-scale structures cannot be adequately resolved in CFD simulations of typically sized risers. It will be demonstrated in this paper that a sub-grid model to account for the effect of the unresolved meso-scale structures must be developed and incorporated into the coarse-grid simulations. Small-scale structures in gas–particle flows arise because of local instabilities and macro-scale shear is not necessary to induce them. Macro-scale shear modifies the small-scale structures and produces anisotropic normal stresses and a shear-thinning behaviour.

A brief review of the evolution of continuum models for riser flows is presented in § 2. The origin of meso-scale structures is discussed in § 3, where we show that continuum models based on the kinetic theory of granular materials (for example, see Gidaspow 1994) do contain the essential physics needed to capture the clusters and streamers in a qualitatively correct manner. The various routes to cluster formation are discussed in § 4, where we argue that these structures arise as a result of two mechanisms operating in parallel: an instability due to damping of the fluctuating motion of particles by the interstitial fluid and inelastic collisions between particles and an inertial instability associated with gas–particle slip.

In § 5, we demonstrate that coarse-grid simulations which fail to recognize the sub-grid microstructure (i.e. small clusters and streamers) overestimate the drag force and underestimate the rate of production and dissipation of pseudo-thermal energy, effective viscosities of the gas and particle phases and the effective normal stress in the particle phase. An approach to developing a sub-grid model for coarse-grid simulation of gas–particle flow in risers is also described.

2. Continuum modelling of gas–solid flows

Model equations

The total number of particles typically present in most gas–particle flows of practical interest is extremely large, making it impractical to solve for the motion of each particle. Consequently, gas–particle flows in large process units are usually modelled via averaged equations of motion (Anderson & Jackson 1967). The model equations we work with in this paper are given in table 1. Equations (1)–(4) are the continuity and momentum balance equations for the particle and gas phases. Here, ϕ is the volume fraction of particles; $\boldsymbol{v}$ and $\boldsymbol{u}$ are the local average velocities of the particle and gas phases, respectively; ρ_s and ρ_g are the densities; $\boldsymbol{\sigma}_s$ and $\boldsymbol{\sigma}_g$ are the stress tensors associated with the two phases expressed in a compressive sense; $\boldsymbol{f}$ is the interaction force between the phases per unit volume of the bed; and $\boldsymbol{g}$ is the specific gravity force.

The concentration of particles in riser flows is sufficiently large that direct interaction of particles through collisions occurs easily and rapidly. In such situations, it is now common to invoke the kinetic theory of granular materials to close the solids-phase stress (Sinclair & Jackson 1989). This closure requires that we augment the above equations with a balance of pseudo-thermal energy (PTE) of particle velocity fluctuations as the solids phase stress depends directly on this quantity (e.g. see Lun *et al.* 1984; Gidaspow 1994). Equation (5) represents the PTE balance, where T denotes the granular temperature. The first term on the right-hand side of this equation represents the diffusive transport of PTE, with $\boldsymbol{q}$ denoting the diffusive flux of PTE. The second and third terms represent rates of production of PTE by shear and gas–particle slip, respectively. The fourth and the fifth terms denote rates of dissipation of PTE through inelastic collisions and viscous damping, respectively.

$$\frac{\partial \phi}{\partial t} + \nabla \cdot (\phi \boldsymbol{v}) = 0, \tag{1}$$

$$\frac{\partial (1-\phi)}{\partial t} + \nabla \cdot [(1-\phi)\boldsymbol{u}] = 0, \tag{2}$$

$$\left[\frac{\partial (\rho_s \phi \boldsymbol{v})}{\partial t} + \nabla \cdot (\rho_s \phi \boldsymbol{v}\boldsymbol{v})\right] = -\nabla \cdot \boldsymbol{\sigma}_s - \phi \nabla \cdot \boldsymbol{\sigma}_g + \boldsymbol{f} + \rho_s \phi \boldsymbol{g}, \tag{3}$$

$$\left[\frac{\partial (\rho_g (1-\phi)\boldsymbol{u})}{\partial t} + \nabla \cdot (\rho_g (1-\phi)\boldsymbol{u}\boldsymbol{u})\right] = -(1-\phi)\nabla \cdot \boldsymbol{\sigma}_g - \boldsymbol{f} + \rho_g (1-\phi)\boldsymbol{g}, \tag{4}$$

$$\left[\frac{\partial \left(\frac{3}{2}\rho_s \phi T\right)}{\partial t} + \nabla \cdot \left(\frac{3}{2}\rho_s \phi T \boldsymbol{v}\right)\right] = -\nabla \cdot \boldsymbol{q} - \boldsymbol{\sigma}_s : \nabla \boldsymbol{v} + \Gamma_{slip} - J_{coll} - J_{vis}. \tag{5}$$

Gas-phase stress tensor

$$\boldsymbol{\sigma}_g = p_g \boldsymbol{I} - \hat{\mu}_g \left[\nabla \boldsymbol{u} + (\nabla \boldsymbol{u})^T - \tfrac{2}{3}(\nabla \cdot \boldsymbol{u})\boldsymbol{I}\right]. \tag{6}$$

Gas-particle drag (Gidaspow 1994)

$$\boldsymbol{f} = \beta(\boldsymbol{u} - \boldsymbol{v}), \quad \beta = \frac{3}{4} C_D \frac{\rho_g (1-\phi)\phi |\boldsymbol{u} - \boldsymbol{v}|}{d} F(\phi), \quad F(\phi) = (1-\phi)^{-2.65}, \tag{7}$$

$$C_D = \begin{cases} (24/Re_g)(1 + 0.15 Re_g^{0.687}), & Re_g < 1000 \\ 0.44, & Re_g \geqslant 1000, \end{cases} \quad Re_g = \frac{(1-\phi)\rho_g d |\boldsymbol{u} - \boldsymbol{v}|}{\mu_g}. \tag{8}$$

Solids stress

$$\begin{aligned} \boldsymbol{\sigma}_s = {} & [\rho_s \phi (1 + 4\eta \phi g_o) T - \eta \mu_b (\nabla \cdot \boldsymbol{v})]\boldsymbol{I} \\ & - \left(\frac{2+\alpha}{3}\right)\left\{\frac{2\mu^*}{g_o \eta (2-\eta)}(1 + \tfrac{8}{5}\phi \eta g_o)(1 + \tfrac{8}{5}\eta(3\eta - 2)\phi g_o) + \tfrac{6}{5}\eta \mu_b\right\}\boldsymbol{S}. \end{aligned} \tag{9}$$

Pseudo-thermal energy flux vector

$$\boldsymbol{q} = -\frac{\lambda^*}{g_o}\left\{(1 + \tfrac{12}{5}\eta \phi g_o)\left(1 + \tfrac{12}{5}\eta^2 (4\eta - 3)\phi g_o\right) + \frac{64}{25\pi}(41 - 33\eta)\eta^2 \phi^2 g_o^2\right\}\nabla T, \tag{10}$$

$$\boldsymbol{S} = \tfrac{1}{2}(\nabla \boldsymbol{v} + (\nabla \boldsymbol{v})^T) - \tfrac{1}{3}(\nabla \cdot \boldsymbol{v})\boldsymbol{I}. \tag{11}$$

Rate of dissipation of pseudo-thermal energy

$$J_{coll} = \frac{48}{\sqrt{\pi}}\eta(1-\eta)\frac{\rho_s \phi^2}{d} g_o T^{3/2}, \tag{12}$$

$$\mu^* = \frac{\mu}{1 + \dfrac{2\beta\mu}{(\rho_s \phi)^2 g_o T}}, \quad \lambda^* = \frac{\lambda}{1 + \dfrac{6\beta\lambda}{5(\rho_s \phi)^2 g_o T}}, \tag{13}$$

$$\mu = \frac{5\rho_s d\sqrt{\pi T}}{96}, \quad \mu_b = \frac{256\mu\phi^2 g_o}{5\pi}, \quad \lambda = \frac{75\rho_s d\sqrt{\pi T}}{48\eta(41 - 33\eta)}, \quad \eta = \frac{(1+e_p)}{2}, \tag{14}$$

$$g_o = \frac{1}{1 - (\phi/\phi_{max})^{1/3}}, \quad \phi_{max} = 0.65, \quad \alpha = 1.6, \tag{15}$$

$$J_{vis} = 3\beta T, \quad \Gamma_{slip} = \frac{81\phi\mu_g^2 |\boldsymbol{u} - \boldsymbol{v}|^2}{g_o d^3 \rho_s \sqrt{\pi T}}. \tag{16}$$

Boundary conditions for particulate phase (Johnson & Jackson 1987)

$$\boldsymbol{n} \cdot \boldsymbol{\sigma}_s \cdot \boldsymbol{t} + \frac{\pi}{2\sqrt{3}\phi_{\max}}\phi' \rho_s \phi g_o T^{1/2} \boldsymbol{v}_{sl} = 0, \tag{17}$$

$$\boldsymbol{n} \cdot \boldsymbol{q} = \frac{\pi\sqrt{3}}{6\phi_{\max}}\phi' \rho_s \phi g_o T^{1/2} |\boldsymbol{v}_{sl}|^2 - \frac{\pi\sqrt{3}}{4\phi_{\max}}(1 - e_w^2)\rho_s \phi g_o T^{3/2}, \tag{18}$$

$$\boldsymbol{v}_{sl} = \boldsymbol{v} - \boldsymbol{v}_w.$$

TABLE 1. Model equations for gas–particle flows.

The solids-phase stress, the PTE flux and the rate of dissipation of PTE due to inelastic collisions are expressed in a manner very similar to that proposed by Lun *et al.* (1984), see (9)–(15). The particles are assumed to be smooth hard spheres of diameter d and only binary interactions (characterized by a single parameter, namely the coefficient of normal restitution, e_p) are considered. The role of the interstitial fluid was not considered by Lun *et al.* (1984), but has been studied by several researchers since (S. B. Savage 1987, personal communication; Koch 1990; Ma & Ahmadi 1988; Gidaspow 1994; Balzer, Boelle & Simonin 1995; Boelle, Balzer & Simonin 1995; Koch & Sangani 1999). Following Savage (1987), Ma & Ahmadi (1988), Balzer *et al.* (1995) and Boelle *et al.* (1995), we have accounted for the role of the interstitial fluid in these expressions through the terms μ^* and λ^*, see (13). The expressions for the granular viscosities (μ and μ_b) and thermal conductivity (λ) given in (14) are the same as those in Lun *et al.* (1984).

The rate of dissipation of PTE by viscous damping is modelled in most of our simulations following Gidaspow (1994), see (16). We will also present some results obtained using an alternative model for this term proposed by Koch & Sangani (1999),

$$\left.\begin{aligned} J_{vis} &= \frac{54\phi\mu_g T}{d^2} R_{diss}, \\ R_{diss} &= 1+\frac{3\phi^{1/2}}{\sqrt{2}}+\frac{135}{64}\phi\ln\phi+11.26\phi(1-5.1\phi+16.57\phi^2-21.77\phi^3)-\phi g_o \ln\varepsilon_m, \end{aligned}\right\} \tag{19}$$

where $\varepsilon_m = 0.01$ and demonstrate that the major findings of our study are not sensitive to the differences between the two different choices for J_{vis}.

The expression shown in (16) for the rate of production of PTE by gas–particle slip, Γ_{slip}, without the g_o term appearing there, was derived by Koch (1990) for dilute systems. More recently, Koch & Sangani (1999) have proposed that

$$\Gamma_{slip} = \frac{81\phi\mu_g^2|\boldsymbol{u}-\boldsymbol{v}|}{g_o d^3 \rho_s \sqrt{\pi T}}\Psi \tag{20}$$

where

$$\Psi = \frac{R_d^2}{(1+3.5\phi^{1/2}+5.9\phi)},$$

$$R_d = \begin{cases} \dfrac{1+3(\phi/2)^{1/2}+(135/64)\phi\ln\phi+17.14\phi}{1+0.681\phi-8.48\phi^2+8.16\phi^3}, & \phi < 0.4 \\ \dfrac{10\phi}{(1-\phi)^3}+0.7, & \phi \geqslant 0.4. \end{cases} \tag{21}$$

The expression for Γ_{slip} given in (16) simply corresponds to setting Ψ to unity. Most of our simulations are based on (16), and we will demonstrate that including the correction factor, Ψ changes the results quantitatively but not qualitatively.

Equation (6) is a simple Newtonian closure for the effective gas phase stress. In the regime investigated in the present study, $\rho_s\phi \gg \rho_g(1-\phi)$, and the contribution due to the deviatoric part of the gas-phase stress is negligible. This will be demonstrated by considering several different models for the effective viscosity of the gas phase, $\hat{\mu}_g$.

In our analysis, it is assumed that the gas–particle interaction force, $\boldsymbol{f}$, is only due to drag. Equations (7) and (8) are the drag correlation used in our simulations (Wen

d	Particle diameter	7.5×10^{-3} cm
ρ_s	Solids density	$1.5\,\mathrm{g\,cm^{-3}}$
ρ_g	Gas density	$1.3 \times 10^{-3}\,\mathrm{g\,cm^{-3}}$
μ_g	Gas viscosity	$1.8 \times 10^{-4}\,\mathrm{g\,cm^{-1}\,s^{-1}}$

TABLE 2. Physical properties of gas and solids used in simulations.

& Yu 1966). It can be shown readily that this model for drag, when applied to the problem of uniform sedimentation of particles in a fluid, yields a Richardson–Zaki (1954) coefficient of 4.65 at low Reynolds number, Re_p ($= \rho_g v_t d/\mu$) and 2.325 at high Re_p. Typical physical properties of systems considered in our study are shown in table 2. For such systems, $Re_p \sim O(1)$ and the drag coefficient estimated from (8) and (9) is not very different from

$$\frac{18\mu_g\phi(1-\phi)^{-2.65}}{d^2}.$$

As we will see later, in our simulations, $T^{1/2} \sim 0.1 v_t$, and hence the Stokes number (St), based on ρ_s, d, $T^{1/2}$ and μ_g (e.g. see Wylie & Koch 2000), is $O(10^2)$. At such large values of St, $\mu^* \sim \mu$, $\lambda^* \sim \lambda$. The Froude number, $Fr_p (= v_t^2/gd)$, is ~ 60 for the combination of physical parameters shown in table 2. It is well known that dense fluidized beds of such particles bubble (Wilhelm & Kwauk 1948).

We will demonstrate in this paper that this system of equations is able to capture the meso-scale structures in gas–solid flows in a qualitatively correct manner. To this end we will discuss in the next section previous work on this problem and trace the origin of these structures. It will become clear that the meso-scale structures are driven by inherent instabilities and not macro-scale shear associated with boundaries.

Most of the results discussed in this paper are concerned with simulations performed in spatially periodic domains. However, we will present a few simulation results to demonstrate that the meso-scale structures persist even in the presence of solid boundaries. At such solid boundaries, we cover a range of possible scenarios by considering three different choices of boundary conditions – no slip, free slip and partial slip. Partial slip boundary conditions for particle–wall interactions have been discussed in the literature by a number of researchers (for example, see Johnson & Jackson 1987; Jenkins 1992; Jenkins & Louge 1997; Jenkins & Richman 1986). As a simple example of partial slip boundary condition, we have employed (17) and (18) (table 1) proposed by Johnson & Jackson (1987), where e_w is the particle–wall coefficient of restitution and ϕ' is the specularity coefficient.

Upon casting these equations in a dimensionless form using ρ_s, v_t and v_t^2/g as characteristic density, velocity and length, respectively, the following dimensionless groups result: Re_p, Fr_p, ρ_g/ρ_s and $\hat{\mu}_g/\mu_g$. The analysis described in this paper is restricted to $Re_p \sim O(1)$ or smaller, $Fr_p \gg 1$ and $\rho_g/\rho_s \ll 1$, which is representative of most gas–particle flows encountered in risers, where we also have $St \gg 1$.

2.1. *Previous work on continuum models for riser flows*

Sinclair & Jackson (1989) examined whether the continuity and momentum equations for the two phases coupled with the pseudo-thermal energy balance equation ((1)–(5) in Table 1) can predict a non-uniform distribution of particles over the cross-section of a vertical pipe under steady and fully developed flow conditions. In their analysis, they neglected the possible consequences of persistent fluctuations and the presence

of clusters and streamers. This model was able to yield rather good agreement with experimental data under some restrictive assumptions about the dissipation of PTE (Sinclair & Jackson 1989; Pita & Sundaresan 1991, 1993; Yasuna *et al.* 1995). Louge, Mastorakos & Jenkins (1991) and Bolio & Sinclair (1995) expanded this model by adding the effect of gas-phase turbulence and found that even in very dilute particle-laden flows where the flow patterns are largely dictated by the turbulent gas flow, particle–particle interactions can play a significant role.

Dasgupta, Jackson & Sundaresan (1994) viewed the fluctuations associated with the clusters as 'particle phase turbulence' and derived time-averaged equations of motion for the fully developed flow of the two phases by Reynolds averaging equations (1)–(4). Their analysis revealed that particles are driven to regions having a low intensity of particle-phase velocity fluctuations from regions of high intensity at rates proportional to the gradients in the intensity of fluctuations. These authors employed a speculative K–ε model for the particle-phase turbulence in order to illustrate the occurrence of segregation. Hrenya & Sinclair (1997) have expanded this work by integrating kinetic theory for granular materials and a model for particle-phase turbulence. Collectively, these studies have helped establish that meso- and macro-scale fluctuations occurring on length scales much larger than that of individual particles must be included in any model for gas–particle flows designed to capture the non-uniform distribution of particles over the cross-section of the riser.

At the same time, various research groups (Enwald & Almstedt 1999; Enwald, Peirano & Almstedt 1997; Enwald *et al.* 1999; Nieuwland *et al.* 1995, 1996; Samuelsberg & Hjertager 1996; Tsuo & Gidaspow 1990; Gidaspow 1993, 1994) have pursued research on simulation of riser flows through direct numerical integration of the locally averaged equations. These simulations do reveal the presence of persistent fluctuations and particle clusters. Such an approach where one tries to capture the time-averaged flow patterns through transient integration of the locally averaged equations is computationally very intensive. Furthermore, the sheer size of the problem, and that of the duct through which the gas–particle mixture is flowing, necessitate the use of coarse grids in the numerical calculations. Such calculations reveal large-scale spatial patterns occurring on a length scale larger than the grid size. It will be shown in this paper that when one uses finer and finer meshes in an attempt to test for grid-size independence of the results, it is invariably found that the features of the flow continue to change at all length and time scales. Therefore, it is not always clear if the computed results are the true consequences of the differential equation models that one is trying to solve. An example to highlight the effect of grid size on the results will be presented later in this paper.

The effect of grid size reveals clearly that unresolved details of flow in a given simulation have an influence on the features occurring on a scale larger than the grid size. The lessons learned from these different attempts to model riser flow using volume-averaged equations of motion can be summarized as follows:

If one wishes to simulate the events occurring at meso- and macro-scale in their entirety, direct numerical integration of the governing equations is the obvious route; however, a fully resolved simulation where the results are independent of the grid size is yet to be demonstrated.

Spatial non-uniformities that are present in a time-averaged sense may be captured by a system of steady-state equations derived by time-averaging the volume-averaged equations of motion. The meso-scale structures and the macro-scale spatio-temporal patterns are erased through such an averaging procedure, but their consequences appear in the final equations as additional terms for which closure relations must be

postulated. K–ε models fall in this category. Although some progress has been made in this type of modelling approach, the reliability of these models for simulation of developing flows has not been validated.

Intermediate to these two approaches is the coarse-grid simulation of two-phase flow (the analogue of large-eddy simulation of single-phase turbulent flow), where one simulates spatial and spatio-temporal patterns occurring at the macro-scale, but accounts for the effects of meso-scale structures occurring at a scale smaller than the grid size through additional closure relations.

One can immediately recognize that the three approaches are practised in simulations of single-phase turbulent flow. The cascade of energy associated with fluctuations in single-phase flow and two-phase flow are very different. In the former the energy flow is predominantly from large scale to small scale, while in the latter it is more complicated. Meso-scale structures, such as clusters and streamers, form initially at small length and time scales and grow into larger scales, so there is almost certainly some energy flow from the very small scale to larger scales. One may also anticipate a flow of energy from large scale to smaller scales, just as in the case of single-phase flow. Understanding the origin and nature of clusters and streamers in riser flow of gas–particle mixtures will pave the way for the development of better closures for the correlations appearing in the Reynolds-averaged model and the coarse-grid simulation model, and will also help us determine the requirements for a fully resolved direct numerical integration of the locally averaged equations such as those summarized in Table 1.

3. Origin of clusters in gas–particle flows

Risers are most commonly encountered as components of circulating fluidized beds (CFBs) in industrial practice. The interaction of the various components of a CFB is known to give rise to instabilities which propagate through the loop. It is therefore useful to inquire if meso-scale structures such as clusters and streamers observed in risers are manifestations of local events or are directly attributable to phenomena associated with the entire loop. It is clear from experimental studies on the dynamics of gas–particle mixtures in a circulating fluidized bed (Srivastava *et al.* 1998; Zhang, Jiang & Fan 1998) that the loop instability manifested itself as low-frequency oscillations in pressure and hold-up. The propagation of this instability through the loop can be recognized from the pressure signals gathered at different locations in the loop. Zhang *et al.* (1998) have shown that the low-frequency components of the oscillations observed at different locations of their CFB apparatus were correlated, while the high-frequency components of the fluctuations (in pressure) at different locations were not. High-frequency fluctuations persist even under conditions where loop instability was not observed (Srivastava *et al.* 1998). It follows that clusters and streamers, which are most likely to be associated with the high-frequency fluctuations, arise from local processes and not because of the loop instability. It is therefore reasonable to conclude that the origin and nature of the clusters can be probed by considering a small segment of the riser.

3.1. *Riser flow simulations*

To probe the origin of clusters further, we performed two-dimensional simulations of gas–particle flow in a segment of a vertical channel, as described below. The MFIX code (Syamlal, Rogers & O'Brien 1993) was modified extensively for solving the system of equations described in table 1. In order to isolate a section of the riser,

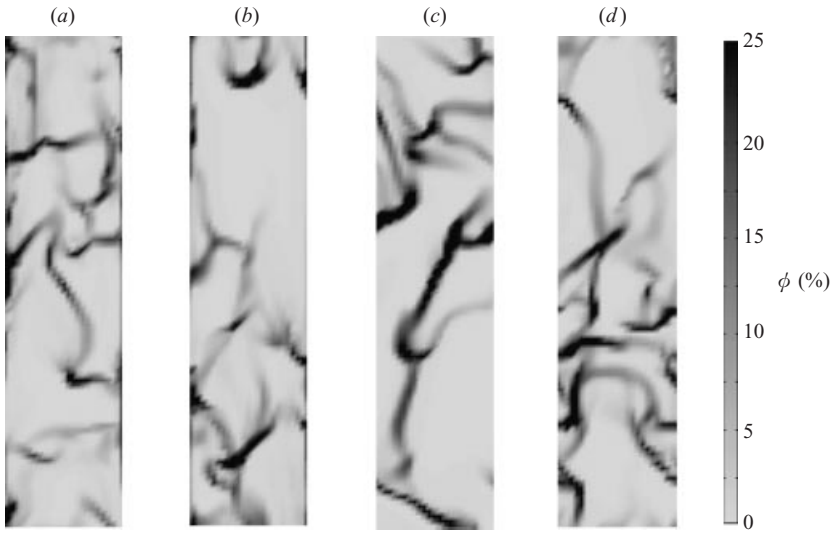

FIGURE 1. Instantaneous greyscale plots of solids volume fraction. 25×100 grids. $Fr_h = 0.0972$; $e_p = 0.9$; $Fr_p = 64.8$; $Re_p = 1.18$; $A = 4$. Average solids volume fraction = 0.05. Gas is allowed to slip freely at the walls. Boundary conditions for the particle phase: (*a*) partial slip (specularity coefficient, $\phi' = 0.5$; $e_w = 0.9$); (*b*) free slip; (*c*) doubly periodic domain; (*d*) doubly periodic domain and fixed T. In (*a*) the pressure drop in the gas phase is 99% of the weight of bed, while in (*b*)–(*d*) the pressure drop balances the weight of the bed.

periodic boundary conditions were imposed in the axial (vertical) direction. Two-dimensional simulation results for a domain with an aspect ratio, A(= height/width), of 4 and an average solids volume fraction of 0.05 are presented in figure 1. In dimensionless form, the width of the box, Δ_h, translates to the inverse of a Froude number, $Fr_h = v_t^2/g\Delta_h$. In these simulations, $Fr_h = 0.0972$. (For the combination of parameters in table 1, this translates to a domain width of 5 cm. Note that even though this is a rather small domain when compared to the typical size of risers, the total number of particles is already prohibitively large to track the motion of each and every particle through a Lagrangian simulation. Thus, structures visible in this figure can be examined realistically only through solution of continuum equations of motion.) This figure shows a grey-scale plot of solids volume fraction at one instant of time and for four different wall boundary conditions. In all these simulations, both the solid and gas phases were initially at rest and the volume fraction of solids was uniform at 0.05. Transient integration was then carried out using four different wall boundary conditions and the evolution of non-uniform structure was followed. Figure 1(*a*) shows a snapshot obtained when a partial slip boundary condition proposed by Johnson & Jackson (1987), see table 1, was used for the particle phase, while allowing the gas to slip freely at the wall. Figure 1(*b*) presents a snapshot obtained when both the gas and solid phases were allowed to slip freely at the wall (but not penetrate it). Similar results were obtained with no-slip boundary conditions as well (not shown). It is thus clear that details of the particle–wall interactions are not essential for producing these meso-scale structures.

We then replaced the walls of the channel with periodic boundary conditions (figure 1*c*), so that both the particles and the gas could penetrate the virtual wall and reappear at the other side. Figure 1(*d*) describes a snapshot obtained when only the continuity and momentum balance equations were solved using periodic boundary conditions in both directions, while fixing the value of the granular temperature at the

value corresponding to the uniformly fluidized state and treating it as independent of time and position. While a direct comparison cannot be made between the four parts of figure 1, all of them show the presence of non-uniform strand and cluster-like structures.

These results indicate that, in this class of flow problems, macroscopic shear arising from the presence of boundaries is not required to induce meso-scale structures. Therefore, one should be able to identify the different routes that lead to cluster formation by simply examining the stability of uniform flow of gas–particle mixtures in unbounded domains.

4. Various routes to formation of clusters in gas–particle flows

Although attractive inter-particle forces can give rise to aggregation of fine particles, this is not likely to be a dominant route to cluster formation under the high-velocity, rapid shear flow conditions encountered in typical riser applications. Therefore, it is reasonable to focus our attention on flow-induced inhomogeneities and ask if such structures arise as a result of instabilities that can be recognized by a stability analysis of the averaged equations of motion. To this end we briefly review the stability of several simple, idealized flows.

4.1. *Stability of the uniformly fluidized state*

Returning to equations (1)–(4), consider first the uniformly fluidized state of a gas–particle suspension. This problem has been investigated by a number of researchers who have sought to elucidate the origin of bubbles in *dense* fluidized beds and the distinction between bubbling and non-bubbling systems. A detailed discussion of this stability analysis, including the history, can be found in recent articles by Anderson, Sundaresan & Jackson (1995) and Glasser, Kevrekidis & Sundaresan (1996, 1997). Focusing on gas–particle systems, it can now be asserted that dense fluidized beds are most unstable to vertically travelling wavefronts having no horizontal structure, and that bubbles emerge through a loss of stability of these wavefronts to horizontal perturbations. In these analyses, a simple Newtonian form has been assumed for the particle- and fluid-phase stress tensors, where the particle-phase pressure, p_s, and viscosity, μ_s, were taken to be monotonically increasing functions of the solids volume fraction, ϕ, and the effective viscosity of the gas phase was simply set to be that of the gas itself. The gas was assumed to be incompressible and the gas-phase pressure p_g was found by solving the equations of motion. The drag coefficient was modelled using the Richardson–Zaki equation (Richardson & Zaki 1954).

Glasser, Sundaresan & Kevrekidis (1998) have extended this stability analysis to uniformly fluidized suspensions covering the entire range from dense fluidized beds to dilute systems representative of riser flow. It was found that for every value of particle volume fraction the uniformly fluidized state is most unstable to vertically travelling wavefronts having no horizontal structure. Furthermore, a loss of stability of this vertically travelling wavefront to transverse perturbations gives rise to a travelling wave having a lateral structure in exactly the same manner, irrespective of whether we are considering a dense fluidized bed or a dilute gas–particle suspension. The structure of solutions having both vertical and lateral non-uniformities in the velocity and particle volume fraction fields changes smoothly from a bubble in the case of a dense fluidized bed to a cluster of particles in the case of a dilute suspension. Thus, it has been shown that bubbles in dense beds and clusters in dilute systems emerge through the same instability and that the averaged equations (1)–(4) with simple phenomenological closures can capture the formation of these structures. These

structures arise because of an interaction between inertia associated with the particle phase, gravity and gas–particle drag. Their dominant length scale, L, is given by $L = (\mu_s v_t/\rho_s g)^{1/2}$. Physically, this particular route to cluster formation arises because of the existence of a relative motion between the particles and the gas. Redistribution of a uniform suspension of particles into clusters surrounded by a region containing a comparatively lower concentration of particles creates a path of lower resistance for the particles to fall down under the action of gravity and the gas to rise.

4.2. *Non-uniform structures arising from inelastic collisions*

Clusters form as a result of inelastic collisions both in granular materials under rapid shear and in the cooling of granular gas. Hopkins & Louge (1991) noted in their simulation of plane shear flow of inelastic disks that a non-uniform microstructure could arise when the collisions between the disks are sufficiently inelastic. This work has spawned particle dynamics simulations (e.g. see Goldhirsch, Tan & Zanetti 1993; McNamara & Young 1996; Tan & Goldhirsch 1997) and experiments (e.g. see Kudrolli & Gollub 1997) on clustering due to inelastic collisions.

The extent to which the formation of clusters as a result of inelastic collisions between particles can be captured by continuum equations of motion for the granular material has also been investigated extensively (e.g. see Savage 1992; Tan 1995; McNamara & Young 1996; Tan & Goldhirsch 1997; Nott *et al.* 1999). Collectively, these studies suggest that the kinetic theory of granular materials does reveal the existence of such clustering.

Given that inelastic collisions and inertial instability associated with fluidization can individually give rise to clusters and streamers, it is hardly surprising that these two mechanisms, when acting together, can also lead to such structures. When an interstitial fluid is present, the damping of the fluctuating motion of the particles by this fluid augments the tendency to form clusters (Wylie & Koch 2000).

Several researchers have investigated the dynamics of fluidized beds and circulating fluidized beds, using discrete particle simulation (or the discrete simulation Monte Carlo method) to follow the motion of the particles and an averaged equation of motion for the gas (Ito *et al.* 1998; Hoomans *et al.* 1996; Ouyang & Li 1999; Tanaka, Yonemura & Tsuji 1995; Tanaka *et al.* 1997; Tsuji, Kawaguchi & Tanaka 1993; Tsuji, Tanaka & Yonemura 1998). Structures, such as bubbles and slugs in dense fluidized beds and clusters in dilute systems, form readily in these simulations. Thus, the meso-scale structures seen in our transient integration of a continuum hydrodynamic model are indeed physical entities.

Let us now return to the problem of gas–particle flows in risers and take stock of what one can say with some degree of confidence. High-velocity gas–particle flows in risers do show persistent fluctuations and are accompanied by the presence of clusters and streamers. Figure 1 presented earlier has confirmed the ability of the averaged equations of motion for two-phase flow, coupled with an additional equation for the particle-phase kinetic energy, described in table 1 (henceforth referred to as micro-scale equations), to capture clusters and streamers, and predict persistent fluctuations in velocity and particle concentration fields. It is also clear that these non-uniform structures arise as a result of local instabilities and not because of instabilities associated with the entire circulation loop of CFBs. Furthermore, the presence of tube walls is not required for the formation of these structures (figure 1). Instead, they arise because of (*a*) instability associated with the relative motion between the gas and particle phases and (*b*) dissipation of fluctuating energy of particles by inelastic collisions between particles and viscous damping.

While the micro-scale equations summarized in table 1 are not exact, they do seem to capture qualitatively the known routes to meso-scale structures. It would therefore seem reasonable to expect that the numerical integration of these equations, using a sufficiently fine grid structure, should reveal the flow behaviour at both meso- and macro-scales. The typical length scale of meso-scale structures estimated from a stability analysis of the micro-scale equations is of the order of 10–50 particle diameters. This is consistent with the cluster sizes reported by Horio (1995). Therefore, if we truly wish to resolve these meso-scale structures in a numerical integration of the micro-scale equations, the grid size should be of the order of a few particle diameters. Such a highly resolved simulation is simply impractical and will not be a useful design tool for industrial applications.

One is usually most interested in the macro-scale structures and how changes in process design influence them. At the same time, meso-scale structures cannot be ignored as these have a significant effect on the macro-scale features and structures seen in process units such as riser reactors. Indeed some researchers have found that the pressure drop in a FCC riser could not be predicted by their *coarse-grid* simulations unless an apparent particle size (larger than or equal to the true size), parameterized in terms of a Reynolds number and void fraction, was used in the drag law (O'Brien & Syamlal 1994).

Let us now take a closer look at what is implicitly assumed in every coarse-grid simulation of a riser. In the finite volume method, which is the most commonly used method to solve such equations, the domain of interest is divided into a number of cells and balance equations are written for each cell. In simulations of industrial scale risers, the cells are typically hundreds of particle diameters in each direction.

In coarse-grid simulations being performed today, the dependent variables are assumed to be uniform inside such cells. We know, however, that meso-scale structures can and will form in riser flows (see figure 1) and that they are only a few tens of particle diameters in size, which is much smaller than the typical computational cell size. These structures will not be resolved in the coarse-grid simulation.

It is worthwhile to digress at this point to turbulent flow of an incompressible single-phase fluid where no sub-grid-scale instability is present to induce sub-grid flow structure. The dissipative sub-grid-scale processes convert mechanical energy to thermal energy, and therefore, to sustain the sub-grid structure, kinetic energy associated with macro-scale (i.e. a length scale larger than the grid size) motion must be converted continually to that associated with sub-grid-scale flow. This is possible only when macro-scale shear is present. Indeed, the effective viscosity in large-eddy simulations depends on the grid size and the macro-scale shear rate (e.g. see Ferziger & Peri 1996; Smagorinsky 1963). Returning to the present two-phase flow problem, it is therefore natural to expect the corrections to the effective stresses and the inter-phase interaction force to depend on the macro-scale shear rates in the particle and gas phases. However, the presence of a macro-scale shear is *not* necessary for inducing a sub-grid structure in our problem.

5. Some results on effects of meso-scale structures

The meso-scale structures due to local instabilities can be understood better by performing highly resolved simulations of a small region of a riser. Furthermore, as the presence of boundaries is not necessary to induce the formation of meso-scale structures, one can isolate a region of the riser by simply utilizing periodic boundary conditions in all directions. With this in mind, we performed a number of two- and

three-dimensional simulations† of the equations in table 1 in rectangular domains and invoked periodic boundary conditions in both lateral and vertical directions. (Such statistical properties may also be gathered by particle dynamics simulations.)

In these simulations, the gas pressure varied periodically in the lateral direction, while in the vertical direction it was partitioned into a periodic part and a linear part. The linear part contributed to a mean pressure gradient in the vertical direction whose value was chosen to balance the total gravitational force acting on the suspension. Henceforth, when we say that periodic boundary conditions are imposed in the axial direction, it is implicitly understood that gas pressure is treated in this manner.

Before discussing results gathered from our simulations in periodic domains, it is important to reiterate the connection between these simulations and a coarse-grid CFD simulation of gas–particle flows in a large riser. The coarse-grid simulations do not resolve the meso-scale structures which are smaller than the grid size. Our ultimate goal is to devise a sub-grid model to account for the role of the sub-grid-scale structure. Our present objective is to bring forth the general features of the sub-grid model. The sub-grid structure is dictated by a combination of sub-grid-scale instabilities and macro-scale shear. We focus first on the former and briefly touch upon the latter at a later stage.

We consider below gas–particle flows in periodic domains whose dimensions are comparable to the grid size in typical coarse-grid CFD simulations, and perform as highly resolved simulations (using a second-order discretization scheme, see Syamlal 1998) as we can with our computational resources. From these computations we have gathered statistical data on the effects of meso-scale structures.

We first present in figure 2 an example to demonstrate that as one increases the resolution, finer and finer structures are revealed. The average solids volume fraction in the domain is 0.05. The initial conditions represent a very slight perturbation of the uniform solution afforded by the equations of motion in table 1. Figure 2(*a*) shows a (representative) snapshot of the solid volume fraction field at one particular instant of time obtained in a simulation using 25×10 equally sized grids. As we increased the resolution, meso-scale structure in the form of many thin strands and clusters were observed. Figure 2(*b*) shows a snapshot obtained with 25×100 grids, while that in (*c*) corresponds to 50×200 grids. The simulation in (*a*) clearly smears the fine-scale features seen in (*b*) and (*c*).

5.1. *Effect of meso-scale structure on drag and pseudo-thermal energy production/dissipation*

It is natural to inquire if the meso-scale structure, which may get resolved by fine-grid simulations, really has any bearing on quantities averaged over the domain. To

† Ideally, one should perform only three-dimensional simulations; however, each three-dimensional simulation of the type we would like to carry out requires nearly 100 times more CPU time than a corresponding two-dimensional calculation. As we need to perform many sets of simulations to bring out the fundamental ideas discussed in this paper, three-dimensional simulations are simply beyond our current resources. While the two-dimensional calculations are less satisfactory than the three-dimensional simulations, they suffice to make a convincing case for the need for sub-grid models. It should be noted that two-dimensional simulations are not useful in single-phase calculations, as there is no meaningful equivalent of vortices (eddies) in two-dimensions. In the case of the present two-phase flow problem, the large-wavenumber portion of the energy spectrum is primarily controlled by the local instabilities. As all the known local instabilities in the gas–solid systems are revealed by the equations at the two-dimensional level itself, there is some basis for hoping that two-dimensional simulations can provide an initial glimpse of the sub-grid model.

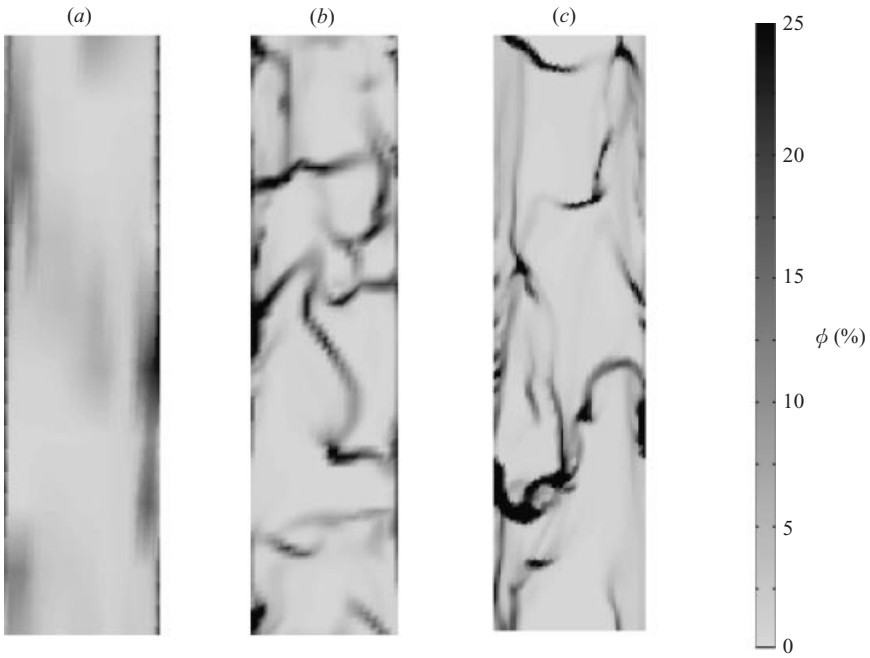

FIGURE 2. Instantaneous greyscale plots of solids volume fraction. $Fr_h = 0.0972$; $e_p = 0.9$; $Fr_p = 64.8$; $Re_p = 1.18$; $A = 4$. Average solids volume fraction = 0.05. Number of grids: (*a*) 25×10; (*b*) 25×100; (*c*) 50×200.

address this issue, consider the results of a simulation presented in figure 3. The parameters are the same as in figure 2(*c*). Figure 3(*a*) shows the temporal evolution of the spatially Favre-averaged granular temperature. (Henceforth, we refer to such an average as the *domain-average*.) After an initial induction period (whose duration depends on the initial conditions), the domain-average temperature shows persistent fluctuations. Typical time step in these simulations is 10^{-2} dimensionless units. The average temperature for this fluctuating state is quite different from that in the uniform state (which was the starting value of the temperature in this figure). Such averaging is typically done for a minimum of 50 units of dimensionless time. (Henceforth, we refer to the time-averaged value of any domain-average quantity simply as the *average* value of that quantity.) The corresponding spatially Favre-averaged velocities of the gas and particle phases in the vertical directions were also calculated as functions of time. The difference between these two velocities, i.e. the domain-average slip velocity, is plotted in figure 3(*b*). Again we see that the average slip velocity in the fluctuating state is substantially different from that in the (initial) uniform state. Stated differently, the slip velocity needed to produce a specified amount of drag force is larger in the presence of meso-scale structure when compared to a corresponding uniform structure. It is also important to note that the instantaneous value of the domain-average slip velocity fluctuates appreciably in the statistical steady state, indicating the dynamic nature of the meso-scale structures.

The two panels on the right are the same as those on the left except that the so-called model B, where the gas-phase pressure gradient appears only in the gas-phase momentum balance, was used for the micro-scale equations. The inter-phase interaction term in model B will differ from that of model A by a factor $(1 - \phi)$ (Bouillard, Lyczkowski & Gidaspow 1989), so both models yield identical uniform

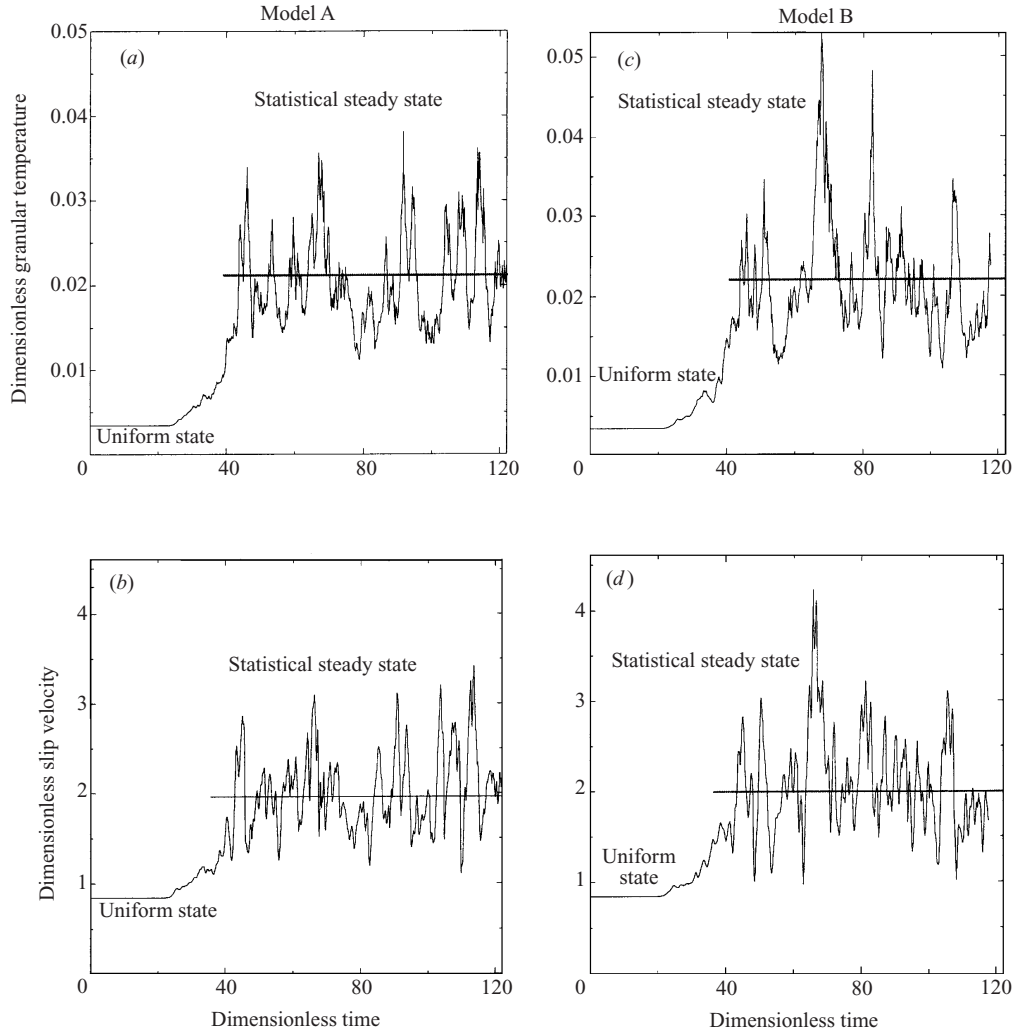

FIGURE 3. Temporal evolution of the Favre-averaged granular temperature and the Favre-averaged axial slip velocity. (a, b) Model A; (c, d) Model B: 50×200 grids. $Fr_h = 0.0972$; $e_p = 0.9$; $Fr_p = 64.8$; $Re_p = 1.18$; $A = 4$. Average solids volume fraction $= 0.05$.

state solutions. In the absence of viscous terms, model A is ill-posed, while model B is not. It is clear from figure 3 that both models A and B predict persistent fluctuations. Indeed the average granular temperature and the slip velocity are almost the same in the two cases.

Figure 4 illustrates the effect of grid resolution on the average slip velocity, W_{slip}, and the average granular temperature. As the grid size is decreased, the meso-scale structures are better resolved, resulting in appreciable changes in the slip velocity and average granular temperature. Both the average granular temperature and W_{slip} become roughly independent of grid resolution, as the meso-scale structures become better and better resolved. The small grid-size dependence seen in figure 4 at the three smallest grid sizes is much smaller than the standard deviation of the temporal fluctuations (e.g. see figure 3). Examination of the power spectra of the variable fields also indicates convergence: as the resolution is increased the power spectra at the

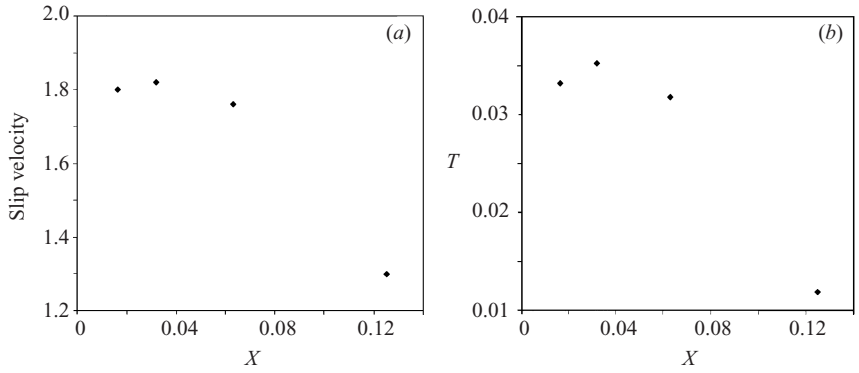

FIGURE 4. Effect of resolution on domain-averaged quantities. $Fr_h = 0.486$; $e_p = 0.9$; $Fr_p = 64.8$; $Re_p = 1.18$; $A = 1$. Average solids volume fraction = 0.05. (*a*) Dimensionless slip velocity; (*b*) dimensionless granular temperature. X denotes $1/N$, where N is the number of grid points in each direction. $X = 1$ corresponds to uniform state, where $W_{slip} = 0.85$ and $T = 0.0034$.

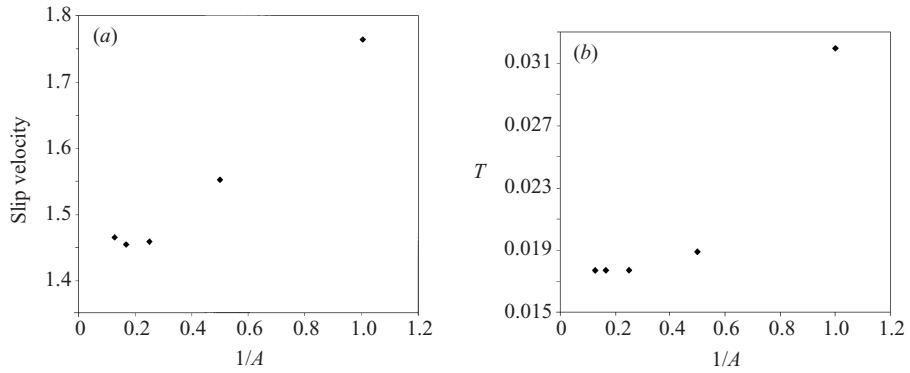

FIGURE 5. Effect of aspect ratio on domain-averaged quantities. $Fr_h = 0.486$; $e_p = 0.9$; $Fr_p = 64.8$. $Re_p = 1.18$. Average solids volume fraction = 0.05. (*a*) Dimensionless slip velocity; (*b*) dimensionless granular temperature. Resolution: $(16 \times 16A)$ grids. At the uniform state, $W_{slip} = 0.85$ and $T = 0.0034$.

lower wavenumbers do not change (Agrawal 2000). It can therefore be said with confidence that meso-scale structures begin to appear at modest grid resolution, and they persist as we continue to increase the grid resolution. Thus, the effects of the meso-scale structures seen in our simulations are not numerical artifacts.

Figure 5(*a*, *b*) shows that the average temperature and slip velocity decrease upon increasing the aspect ratio, and become essentially independent of A for $A \gtrsim 4$. Snapshots of particle volume fraction field, presented in figure 6, clearly show that the meso-scale structures obtained at different aspect ratios are very similar.

We have carried out two-dimensional simulations such as the one shown in figures 3–5 (using model A) for several different combinations of parameters. After each simulation has been run for a long enough duration to ensure that a statistical steady state has been reached (typically at least 50 units of dimensionless time), statistics on a variety of fluctuating quantities have been obtained. The effect of e_p on various domain-averaged quantities is illustrated in table 3. This table presents the magnitude of each quantity at the uniformly fluidized state and its average value obtained from transient simulations in a periodic domain with an aspect ratio of 4 and $Fr_h = 0.486$

	Uniform state					Statistically steady state				
e_p	0.8	0.9	0.9*	0.9**	0.99	0.8	0.9	0.9*	0.9**	0.99
W_{slip}	0.85	0.85	0.85	0.85	0.85	1.60	1.46	1.49	1.68	1.27
T	0.0032	0.0034	—	.0041	.0036	0.015	0.018	0.016	0.017	0.025
$J_{coll}(\times 10^{-4})$	1.11	0.63	—	.83	0.07	73.58	52.78	50.71	59.14	8.5
$J_{vis}(\times 10^{-4})$	5.5	5.77	—	10.29	6.14	32.36	39.16	35.54	85.6	52.2
$\Gamma_{shear}(\times 10^{-4})$	0	0	—	0	0	101.7	88.27	86.25	129.18	57.33
$\Gamma_{slip}(\times 10^{-4})$	6.4	6.58	—	11.12	6.21	4.21	3.68	—	15.56	3.41
$P_{s,KT}$	0.0002	0.00023	—	0.00026	0.00024	0.0019	0.0022	0.0021	0.0024	0.0029
$P_{s,meso,x}$	—	—	—	—	—	0.028	0.032	0.031	0.032	0.020
$P_{s,meso,y}$	—	—	—	—	—	0.018	0.015	0.016	0.025	0.012

TABLE 3. Effect of coefficient of restitution on dimensionless domain-averaged quantities obtained from two-dimensional simulations. $Fr_h = 0.486$; $Fr_p = 64.8$; $Re_p = 1.18$; $A = 4$. Average solids volume fraction = 0.05. Here, subscripts x and y denote the horizontal and vertical directions, respectively. Resolution: 16×64.

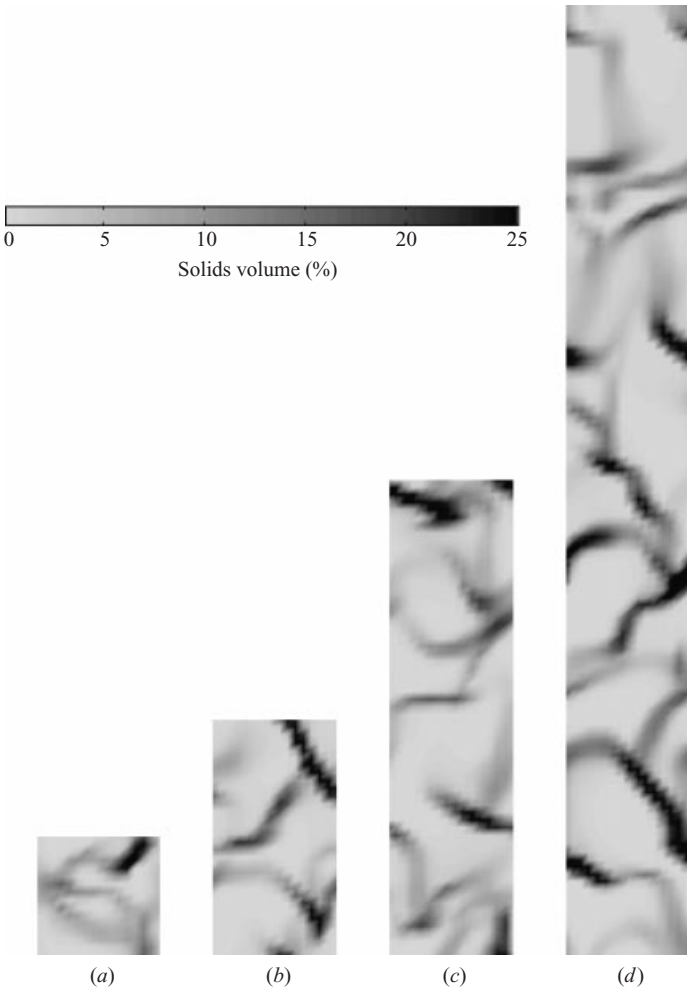

FIGURE 6. Instantaneous greyscale plots of solids volume fraction, revealing meso-scale structures. $Fr_h = 0.486$; $e_p = 0.9$; $Fr_p = 64.8$; $Re_p = 1.18$; (*a*) $A = 1$; (*b*) $A = 2$; (*c*) $A = 4$; (*d*) $A = 8$. Resolution: $(16 \times 16A)$ grids.

using 16×64 grids. According to the model, the slip velocity in the uniform state is independent of e_p, while this is not the case in the statistical steady state. Furthermore, the granular temperature in the statistical steady state is appreciably larger than that in the uniform state in the entire range of e_p values shown in table 3. It should be noted that the closure relations for the stresses, conductivity of PTE and the rate of dissipation due to inelastic collisions derived by Lun *et al.* (1984) are valid for only slightly inelastic collisions. We have explored a somewhat wider range of e_p values in table 3 to demonstrate that the effect of e_p on the average quantities is only gradual.

It is also interesting to discuss at this stage the relative importance of the different routes for production and dissipation of PTE. Let us first consider the production of PTE due to gas–particle slip (see (16) in table 1). In the absence of this term, the PTE of the particles in a uniformly fluidized suspension is zero. Thus, this term gives the particle phase in a uniformly fluidized suspension a small, but non-zero, PTE, which, in turn, imparts the particle phase with a non-zero pressure and viscosity. Once the

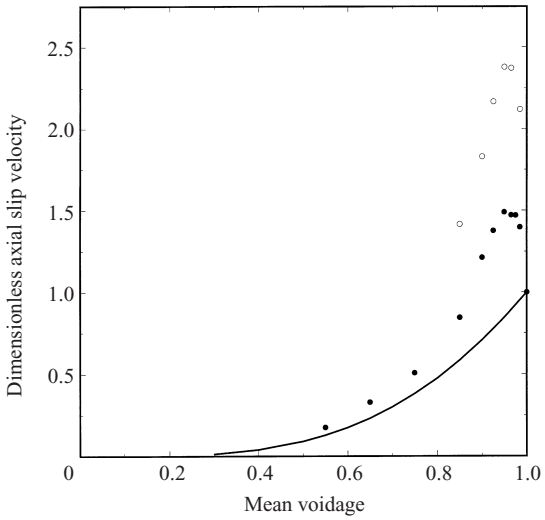

FIGURE 7. Variation of effective slip velocity with voidage. Both are domain-averaged quantities. $e_p = 0.9$; $Fr_p = 64.8$; $Re_p = 1.18$. ●, $Fr_h = 0.486$; $A = 4$; resolution: 16×64. ○, $Fr_h = 0.243$; $A = 2$; resolution: 32×64. Solid line: uniform state.

uniform state of the mixture has given way to a non-uniform distribution consisting of meso-scale structures, production of PTE occurs predominantly through shear (see rows labelled Γ_{shear} and Γ_{slip} in table 3).

In one simulation, with $e_p = 0.9$, the slip-production of PTE was turned off after the system developed a non-uniform structure and the simulation was continued for a sufficiently long period of time to gather statistics. The results obtained in this numerical experiment are shown in table 3 as a separate column (labelled 9^*). Also show in this table are the results obtained in another numerical experiment (also at $e_p = 0.9$) where the full expressions for Γ_{slip} and J_{vis} proposed by Koch & Sangani (1999), described earlier in (19)–(21) were used (see column labelled 9^{**}). A comparison of the entries in the three columns labelled $e_p = 0.9$ reveals clearly that slip is of secondary importance in the system being simulated.

Table 3 also summarizes the statistical average values of the rates of PTE dissipation by gas–particle slip and by inelastic collisions. In the uniform state and $\phi = 0.05$, $J_{vis} \gg J_{coll}$. In contrast, both routes are equally important in the statistical steady state. It is intuitively obvious that as the loading level decreases, the viscous damping will become increasingly more important, and vice versa. It can also be seen from this table that the average rate of dissipation in a state of non-uniform microstructure is actually larger than that in the corresponding uniform state. Thus, a higher average granular temperature is sustained in the non-uniform state through enhanced rate of production of PTE by shear and not because of a lowering of the rate of dissipation. Comparing the statistical steady states shown in the three columns labelled 9, 9^* and 9^{**}, we see that the expression derived recently by Koch & Sangani (1999) predicts a considerably larger J_{vis} than the simpler expression we used in the bulk of our simulations. Simultaneously, W_{slip} is also larger, possibly due to larger clusters and streamers, which, in turn, causes larger magnitudes of velocity gradients and larger Γ_{slip}.

Let us now return to the question of what is needed to properly simulate gas–particle flows in large vessels. It is clear from the examples described above that coarse-grid simulations which completely ignore the sub-grid microstructure will overestimate the

drag force and underestimate the rates of production and dissipation of PTE. A rather simple correction for the drag force term may be determined as follows. Suppose we wish to simulate gas–particle flow in a large process unit using grids of a particular size. Taking this grid size to be used in the coarse-grid simulation of the large unit as the *domain size*, and imposing periodic boundary conditions in all directions, one can carry out simulations of the type described above for various mean volume fractions. The average values of the slip velocity at various particle loading levels may then be used to extract an approximate drag law. This is illustrated in figure 7, where the statistical average slip velocities obtained in simulations carried out over a doubly periodic domain with $Fr_h = 0.486$ and $A = 4$ are shown by filled circles. These data can be captured satisfactorily by some expression of the form $\langle v \rangle / v_t = F_1(\phi)$, where v_t is the terminal velocity of a single particle. A plausible functional representation of the apparent drag, which directly utilizes $F_1(\phi)$, is given in Appendix A. (It should, however, be noted that a proper representation of the effective interaction force between the gas and particle phases, which must be used in coarse-grid simulations, should include both mean and fluctuating components. This may necessitate the use of a stochastic model. See Appendix A for further details.)

The variation of the apparent slip velocity as a function of voidage (shown in figure 7 by filled circles) is quite different from that for the uniform state (the solid line in figure 7). The apparent slip velocity first increases as the voidage decreases. This is a result of the formation of denser clusters for higher mean solids volume fraction (see figure 8*a*, *b*). The denser clusters fall faster relative to the surroundings. Gas bypassing the clusters is clearly evident in figure 9. But as the voidage is decreased further, the clusters start interacting and intersecting one another, making it more difficult for the gas to bypass the dense regions (see figure 8*d*). As a result, the slip velocity starts decreasing with decreasing voidage. At a certain voidage there is a transition from the formation of clusters to the formation of voids (see figure 8*e*). For lower voidages still, the system forms voids, or bubbles, instead of clusters (see figure 8*f*). It should be emphasized at this stage that the apparent slip velocity for a specified mean solids fraction is dependent on grid size to be used in the coarse-grid simulations. To highlight this point, we have also included in figure 7 the apparent slip velocities obtained for some simulations in a doubly periodic domain that is twice as wide (open circles in figure 7). The domain height is the same for both cases. The apparent slip velocities in this case are larger than those for the narrower domain; the trend, however, is similar.

As the size of the domain decreases, the apparent slip velocity decreases towards the value corresponding to a uniform state (equivalently, the apparent particle size decreases toward the true particle size). Needless to say, the *sub-grid* model for apparent drag obtained in this manner by simply averaging over the domain is crude and closer scrutiny of the details of the meso-scale structure is needed for more fundamental sub-grid models. It should be emphasized, however, that even the crude sub-grid model sketched above for the apparent drag is a rational improvement over an utter disregard of the meso-scale structure.

We performed a limited number of three-dimensional simulations in periodic domains to demonstrate that the meso-scale structures and their effects are not artifacts of two-dimensional simulations. Figure 10 shows a vector plot of gas velocity, superimposed on a three-dimensional density plot of solids volume fraction field. The tendency of the gas to bypass the dense regions is clearly evident. Figure 11 shows surface plots of solids volume fraction, revealing a gradual transition from clusters to bubbles as the mean solids volume fraction increases.

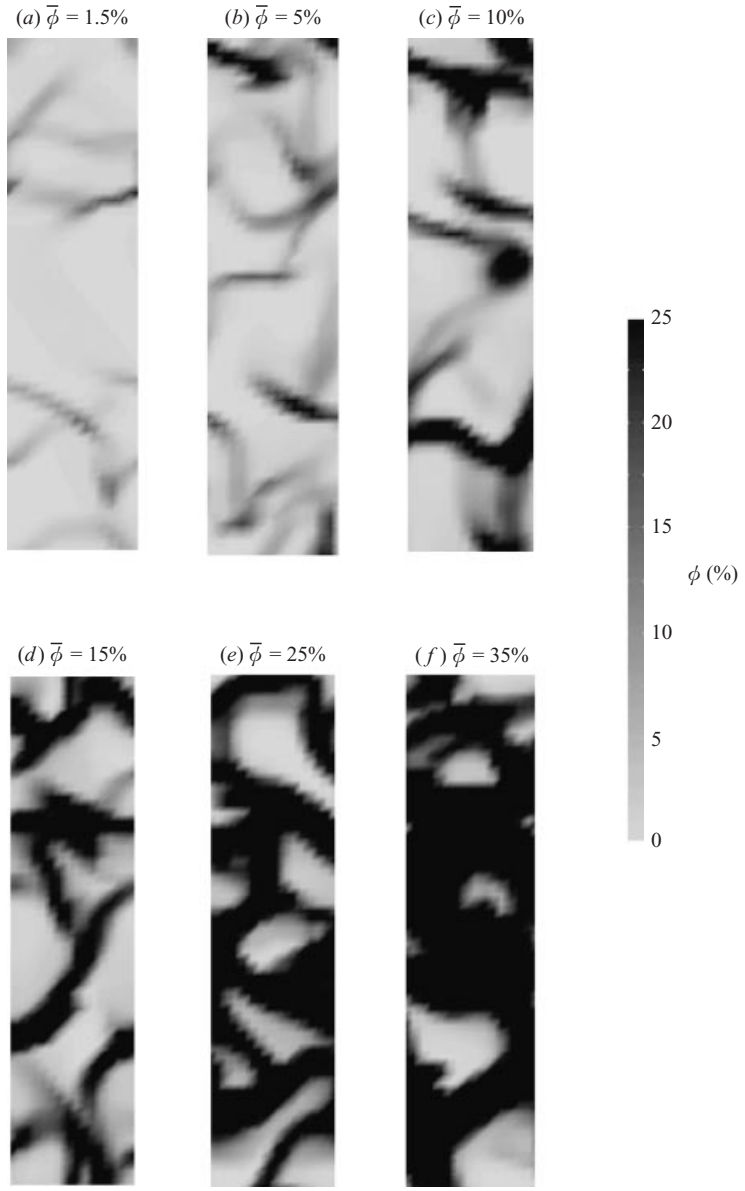

FIGURE 8. Instantaneous greyscale plots of solids volume fraction at various mean solids volume fraction levels. $e_p = 0.9$; $Fr_p = 64.8$; $Re_p = 1.18$; $Fr_h = 0.486$; $A = 4$. Resolution: 16×64.

A comparison of the average axial slip velocities at various values of mean voidages obtained in two-dimensional and three-dimensional simulations at a comparable resolution is presented in figure 12. It is abundantly clear that the effect seen in two-dimensional simulations earlier (figure 7) is present in three-dimensional as well. It is easier for the gas to bypass clusters in three than in two dimensions, making the effect more pronounced in the former. In spite of the quantitative differences, it is apparent that two-dimensional simulations do capture the effect of meso-scale structures qualitatively.

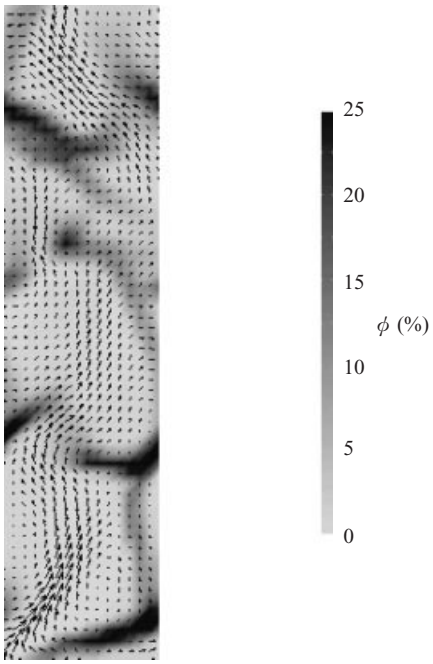

FIGURE 9. Gas bypassing clusters and strands. Snapshot at one instant of time. Vector plot of gas velocity field is superimposed on greyscale plot of solids volume fraction. $e_p = 0.9$; $Fr_p = 64.8$; $Re_p = 1.18$; $Fr_h = 0.486$; $A = 4$. Resolution: 16×64. Average solids volume fraction $= 0.05$.

5.2. *Role of meso-scale structure on effective stresses*

The effective gas- and particle-phase stresses in coarse-grid simulation of gas–particle flows in large vessels should include the micro-scale stresses (appearing in equations (3) and (4) in table 1) and those due to the sub-grid-scale structures. In large-eddy simulation of single-phase turbulent flow, the latter usually dominates the former. We will now illustrate that this is indeed the case in our problem as well.

Dimensionless meso-scale normal stresses, $P_{s,meso,x}$ and $P_{s,meso,y}$, and microscale pressure, $P_{s,kt}$, in two-dimensional simulations were computed as follows. The domain-averaged values of $\boldsymbol{\sigma}_s$ and $\phi \boldsymbol{vv}$ were first computed as functions of time. These were then time-averaged to obtain $\langle \boldsymbol{\sigma}_s \rangle$ and $\langle \phi \boldsymbol{vv} \rangle$, respectively. Finally,

$$P_{s,meso,x} = \langle \phi v_x v_x \rangle - \bar{\phi} \tilde{v}_x \tilde{v}_x + \langle \sigma_{s,xx} \rangle, \quad P_{s,meso,y} = \langle \phi v_y v_y \rangle - \bar{\phi} \tilde{v}_y \tilde{v}_y + \langle \sigma_{s,yy} \rangle,$$

where $\bar{\phi}$ is the average solids volume fraction in the domain and $\tilde{\boldsymbol{v}}$ is the Favre-average velocity of the particle phase with respect to the mass-average velocity of the mixture (the averaging being done over both space and time). The values of $P_{s,kt}$ (defined as $(1/3)\ \mathrm{tr}\langle \boldsymbol{\sigma}_s \rangle$), $P_{s,meso,x}$ and $P_{s,meso,y}$ for a representative set of simulations are shown in table 3. The generation of PTE by shear associated with meso-scale structures increases the value of $P_{s,kt}$ by an order of magnitude over the value at the uniform state. $P_{s,meso,x}$ and $P_{s,meso,y}$ are even larger, showing that fluctuations associated with the meso-scale structures contribute significantly to the effective normal stresses in coarse-grid simulations.

Figure 13(a, b) summarizes $P_{s,meso,x}$, $P_{s,meso,y}$ and $P_{s,kt}$ values obtained for several different values of $\bar{\phi}$, corresponding to the conditions shown by filled circles in figure 12. At every value of $\bar{\phi}$ shown in figure 13(a, b), $P_{s,meso,x}$ and $P_{s,meso,y}$ are

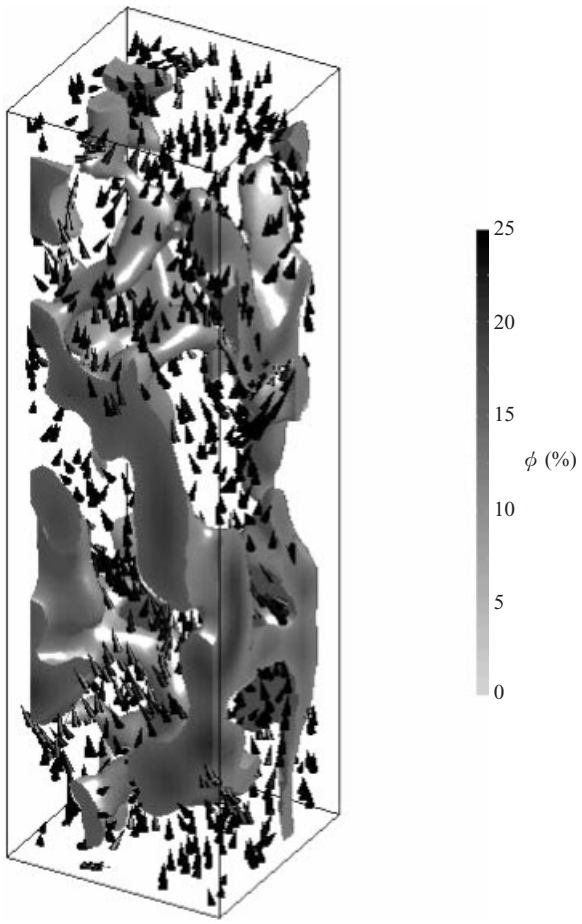

FIGURE 10. Snapshot of solids volume fraction and gas velocity fields in a three-dimensional simulation. Cones represent gas velocity, with orientation and length indicating direction and magnitude, respectively. A contour plot of surface in the interior of the domain where $\phi = 0.05$ is shown. The solids volume fraction at points on the faces is as in the greyscale (provided ϕ here exceeds 0.05). Mean solids volume fraction = 0.05. $e_p = 0.9$; $Fr_p = 64.8$; $Re_p = 1.18$; $Fr_h = 0.486$. Resolution: $16 \times 16 \times 64$. Aspect ratio of the box 1 : 1 : 4.

significantly larger than $P_{s,kt}$ (which, in turn, is much larger than $P_{s,kt}$ corresponding to the uniform state).

The values of horizontal and vertical meso-scale stresses and $P_{s,kt}$ obtained in three-dimensional simulations at various values of $\bar{\phi}$, corresponding to the conditions presented earlier by open circles in figure 12, are shown in figure 14(a, b). The horizontal normal stress in three dimensions is noticeably smaller than that in two dimensions, while $P_{s,kt}$ (three-dimensional) is larger than that in two dimensions. Recall that, in our simulations, the shear due to the meso-scale structures produced PTE and gave rise to $P_{s,kt}$. If the meso-scale structures were not resolved in the simulations, the value of $P_{s,kt}$ would have been much smaller (see columns marked 'uniform state' in table 2). Therefore, it can be concluded that coarse-grid simulations, which do not account for the particle-phase pressure due to the sub-grid-scale clusters and streamers, are grossly inaccurate.

The contribution of the meso-scale structure to the effective gas-phase pressure is

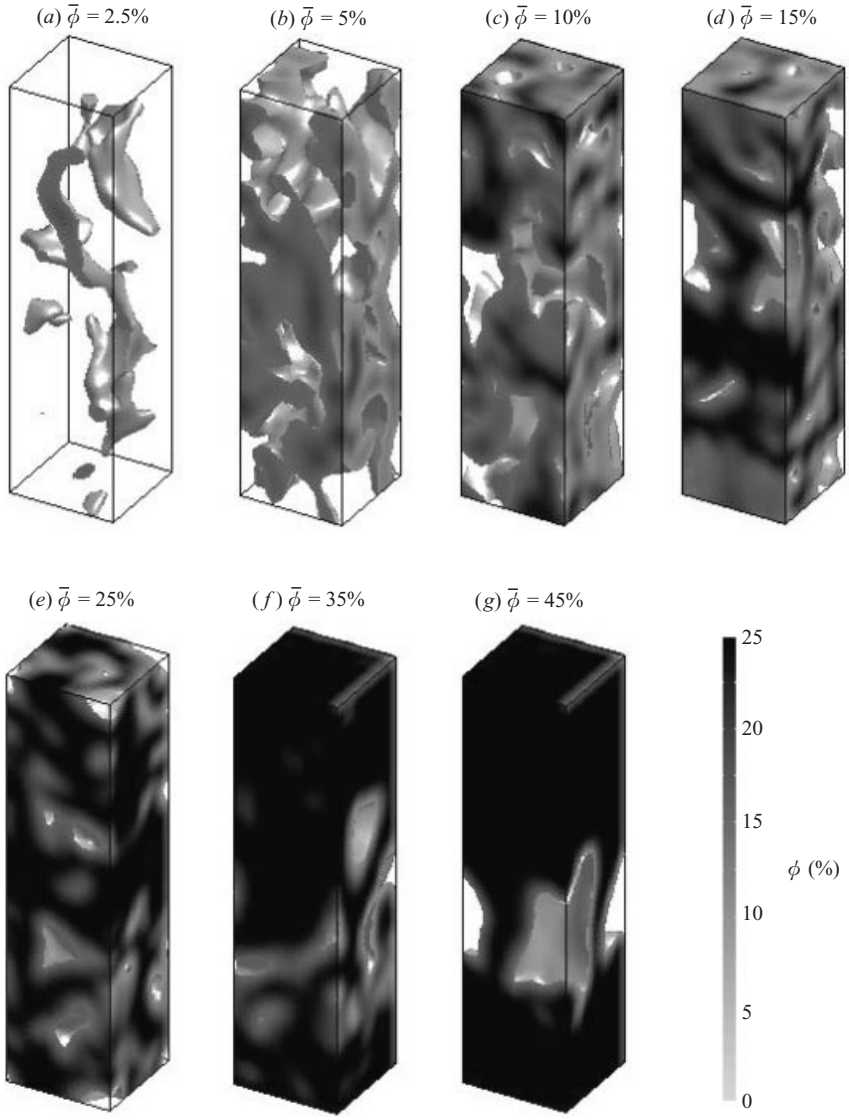

FIGURE 11. Snapshots of solids volume fraction fields in a three-dimensional simulation. A contour plot of surface in the interior of the domain where $\phi = 0.05$ is shown. The solids volume fraction at points on the faces is as in the greyscale (provided ϕ here exceeds 0.05). $e_p = 0.9$; $Fr_p = 64.8$; $Re_p = 1.18$; $Fr_h = 0.486$. Resolution: $16 \times 16 \times 64$. Aspect ratio of the box 1 : 1 : 4.

not included in table 2. As we have treated the gas phase as incompressible, the gas pressure is solved to satisfy incompressibility and the meso-scale contribution to the pressure ($P_{g,meso}$) can simply be absorbed into the pressure term. Strictly speaking, this term needs to be included in the effective pressure in the gas phase in compressible flow problems.

Table 4 presents an illustration of the sensitivity of the values of various average quantities to the choice of model for the effective viscosity of the gas phase. In all the simulations discussed thus far, the effective viscosity of the gas phase was simply taken to be that of the gas itself, and the results obtained with this choice

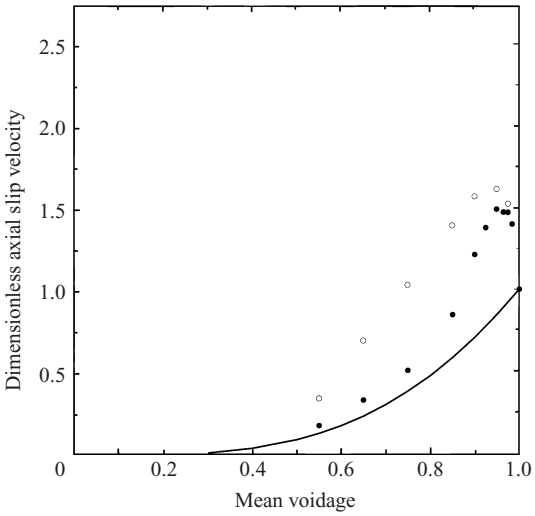

FIGURE 12. Variation of effective slip velocity with voidage. Both are domain-averaged quantities. $e_p = 0.9$, $Fr_h = 0.486$. ●, two-dimensional; aspect ratio 1 : 4; resolution: 16 × 64. ○, three-dimensional; aspect ratio 1 : 1 : 4; resolution: 16 × 16 × 64. Solid line: uniform state.

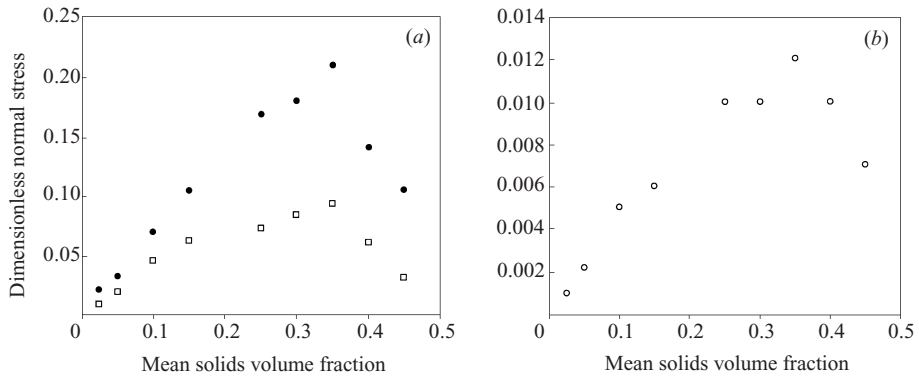

FIGURE 13. Variation of two-dimensional (*a*) meso-scale normal stresses $P_{s,meso,x}$ (●) and $P_{s,meso,y}$ (□), and (*b*) $P_{s,kt}$ (○) with average solids fraction. $e_p = 0.9$; $Fr_p = 64.8$; $Re_p = 1.18$; $Fr_h = 0.486$. Aspect ratio 1 : 4. Resolution: 16 × 64. Here, subscripts x and y denote horizontal and vertical directions, respectively.

are shown as the first column of numbers in this table. The next column employs a standard Smagorinsky (1963) model for viscosity. It is clear from a comparison of these two columns that the average quantities shown there are hardly sensitive to the value of $\hat{\mu}_g$. The final column of numbers was obtained by arbitrarily increasing the Smagorinsky viscosity by a factor of ten, where a small, but detectable, effect of the effective gas-phase viscosity is apparent.

In addition to generating a meso-scale pressure, the meso-scale structures also serve to generate additional deviatoric stresses in the two phases when macro-scale shear is present. We have carried out two-dimensional and three-dimensional simulations in periodic domains, while allowing for the presence of macro-scale shear. In gas–solid flows in vertical risers, axial variation of lateral velocity is present only in a transient fashion but not in a time-averaged sense, whereas lateral variation of axial velocity

	$\hat{\mu}_g = \mu_g$	$\hat{\mu}_g = \mu_g + \mu_{g,t}$	$\hat{\mu}_g = \mu_g + \mu_{g,t}$
W_{slip}	1.46	1.48	1.52
T	0.018	0.018	0.018
$P_{s,KT}$	0.0022	0.0023	0.0024
$P_{s,meso,x}$	0.032	0.033	0.030
$P_{s,meso,y}$	0.015	0.016	0.018

TABLE 4. Dependence of various domain-averaged quantities on the effective viscosity for the gas phase. $Fr_h = 0.486$; $e_p = 0.9$; $Fr_p = 64.8$; $Re_p = 1.18$; $A = 4$. Average solids volume fraction = 0.05. Simulations were carried out in two-dimensional periodic domains. Here, subscripts x and y denote the horizontal and vertical directions, respectively. Resolution: 16×64. In the second and third columns of numbers, gas-phase viscosity (dimensional quantity) is given by $\mu_{g,t} = \rho_g (C\Delta)^2 (\boldsymbol{S}_g : \boldsymbol{S}_g)^{1/2}$.

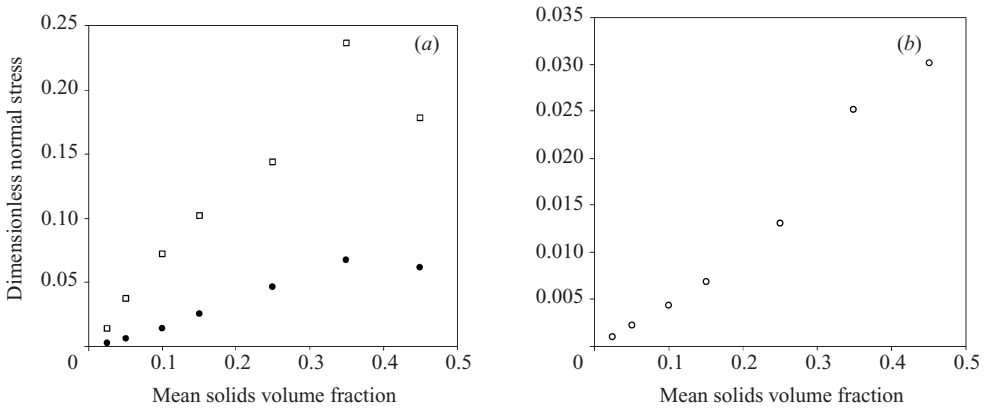

FIGURE 14. Variation of three-dimensional (*a*) meso-scale normal stresses $P_{s,meso,x,z}$ (●) and $P_{s,meso,y}$ (□), and (*b*) $P_{s,kt}$ (○) with average solids fraction. $e_p = 0.9$; $Fr_p = 64.8$; $Re_p = 1.18$; $Fr_h = 0.486$. Aspect ratio 1 : 1 : 4. Resolution: $16 \times 16 \times 64$. Here, subscripts x and z denote horizontal and vertical directions, respectively, while y denotes the vertical direction. $P_{s,meso,x} = P_{s,meso,z} \equiv P_{s,meso,x,z}$.

exists even in a time-averaged sense. This consideration prompted us to focus for the time being only on macroscopic shear in the form of lateral variation of axial velocities of the gas and solid phases.

A schematic of such a simulation in two dimensions is shown in figure 15. From such simulations, we determined $\langle \boldsymbol{\sigma}_s \rangle$, and $\langle \phi \boldsymbol{vv} \rangle$, which were then used to compute $P_{s,meso,x}$, $P_{s,meso,y}$, $P_{s,kt}$ $\mu_{,kt}$ and $\mu_{,meso}$. Here,

$$\mu_{s,kt} = -\frac{1}{\tilde{\gamma}} \langle \sigma_{s,yx} \rangle, \quad \mu_{s,meso} = -\frac{1}{\tilde{\gamma}} \langle \phi v_x v_y \rangle + \mu_{s,kt}.$$

Both $\mu_{s,kt}$ and $\mu_{s,meso}$ are dimensionless quantities, where corresponding dimensional quantities have been scaled in terms of a characteristic viscosity, $\rho_s v_t^3 / g$. $\tilde{\gamma}$ denotes a dimensionless shear rate ($= \gamma v_t / g$ where γ is the shear rate). In general, these viscosities were difficult to compute accurately, requiring long periods of integration (typically over 100 units of dimensionless time). This difficulty stemmed from the large temporal fluctuations of the domain-averaged meso-scale deviatoric stress.

Figure 16(*a–d*) shows the effect of $\tilde{\gamma}$ on W_{slip}, T, $P_{s,kt}$ and μ_{kt}, for three different values of $\bar{\phi}$. Here, μ_{kt} is defined as the average value of kinetic theory viscosity. This is, in general, different from $\mu_{s,kt}$. However, μ_{kt} and $\mu_{s,kt}$ were found to be within a

FIGURE 15. Schematic representation of two-dimensional simulations in periodic domains with imposed shear.

factor of two in our exploratory simulations. For example, at $\phi = 0.05$, $\tilde{\gamma} = 1.113$ and all other parameters as in figure 16, $\mu_{kt} = 1.96 \times 10^{-4}$ and $\mu_{s,kt} = 1.0 \times 10^{-4}$. Therefore, we simply report in figure 16(d) only μ_{kt} (which could be evaluated more accurately). At low shear rates, all four quantities increase modestly with $\tilde{\gamma}$. The fact that these quantities change only modestly with shear rate clearly illustrates that the meso-scale structures arose in these simulations because of inherent instabilities, and were modified by the imposed macro-scale shear. Figure 17(a, b) shows the dependence of $P_{s,meso,x}$ and $P_{s,meso,y}$ on the dimensionless shear rate. The former decreases with $\tilde{\gamma}$, while the latter increases with $\tilde{\gamma}$.

Figure 17(c) shows the effect of $\tilde{\gamma}$ on $\mu_{s,meso}$. It is clear from figures 16(d) and 17(c) that $\mu_{s,meso}$ is larger than μ_{kt} by more than an order of magnitude. Thus, the meso-scale fluctuations cause the system to be more 'viscous' on the macro-scale. It can be shown readily from the equations in table 1 that μ_{kt} of a gas–particle mixture with uniform ϕ increases with shear rate (i.e. shear thickening). When this uniform system gives way to a non-uniform time-dependent structure, the apparent viscosity, $\mu_{s,meso}$, becomes scale-dependent (i.e. dependent on Fr_h and A) and for the combination of Fr_h and A corresponding to figures 16 and 17, it overwhelms μ_{kt}. There is also a qualitative change, namely that at the meso-scale the system now shows a shear-thinning behaviour.

Qualitatively similar behavior is obtained in three-dimensional simulations as well. This is illustrated by the results presented in figure 17(a–c) as filled triangles. Our finding that the meso-scale normal stresses and viscosity overwhelm the corresponding quantities at the particle level clearly shows that the dynamics of the meso-scale structures (characterized by the cluster velocity variance and the associated correlation time) is most relevant for estimating the effective rheological quantities.

The above discussion on the meso-scale stresses clearly suggests that coarse-grid simulations that do not recognize the rather large apparent normal stress and viscosity of the particle phase resulting from sub-grid-scale structure are grossly inaccurate.

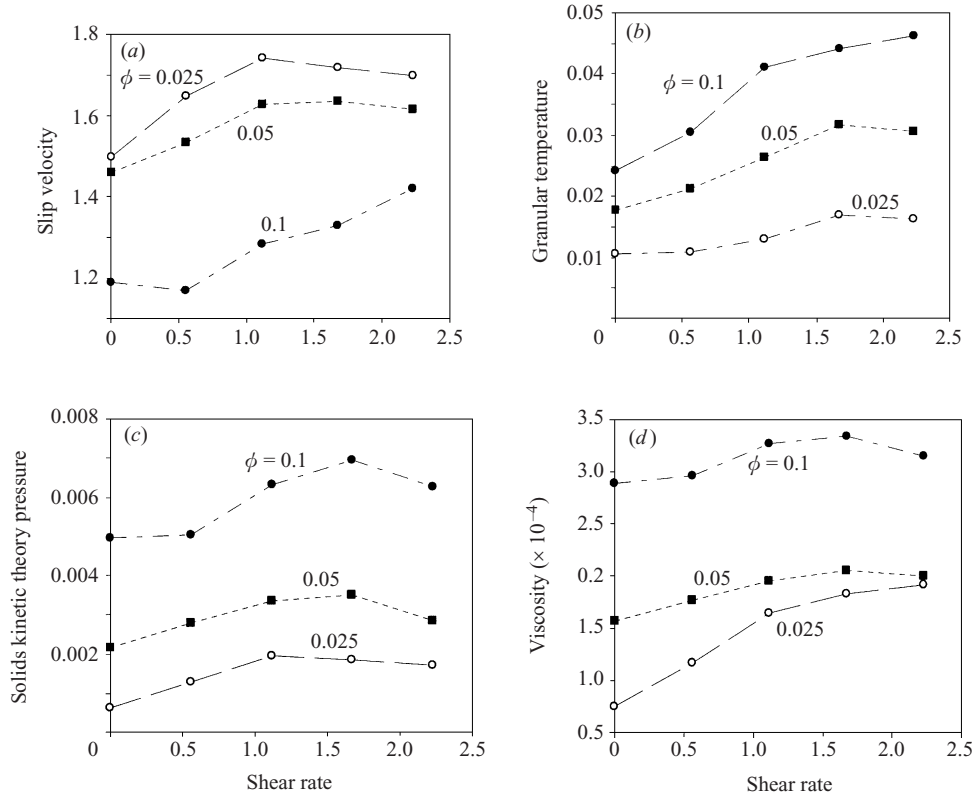

FIGURE 16. Effect of shear rate on (*a*) W_{slip}, (*b*) T, (*c*) $P_{s,kt}$ and (*d*) μ_{kt}, for three different values of $\bar{\phi}$. $e_p = 0.9$; $Fr_p = 64.8$; $Re_p = 1.18$; $Fr_h = 0.486$. Aspect ratio 1 : 4. Resolution: 16×64. ○, $\bar{\phi} = 0.025$; ■, $\bar{\phi} = 0.05$; ●, $\bar{\phi} = 0.10$.

One can readily anticipate that the apparent (meso-scale) viscosity of the gas phase will also be significantly larger than the viscosity used in the detailed simulations. Our efforts to estimate the apparent viscosity of the gas phase due to meso-scale structures, $\mu_{app,g}$, were often unsuccessful because of large (temporal) fluctuation in the domain-averaged value of the $(1-\phi)u_x u_y$. In any case, there is no doubt that in all our simulations, $\mu_{app,g}$ is much smaller than $\mu_{s,meso}$.

The observed effects of shear rate on meso-scale normal stresses and viscosity are easy to rationalize. At low shear rates the streamers are oriented in a more random fashion and they swing sideways more readily. As the shear rate is increased, they exhibit an increased tendency to orient themselves in the vertical direction.

We performed a limited number of two-dimensional simulations to explore how the average quantities are affected by various dimensionless groups appearing in the model equations.

The dimensionless particle size ($1/Fr_p$) enters the model in several places:

(i) In the class of flow problems studied here, the local dimensionless slip velocity is typically $O(1)$. Hence, the importance of Fr_p on the drag term can be assessed by considering a situation where the local slip velocity is close to the terminal velocity. In the limit of Stokes drag ($Re_g \ll 1$) and when $Re_g > 1000$, Fr_p does not appear in the interphase drag term in the dimensionless equations of motion. In these limits,

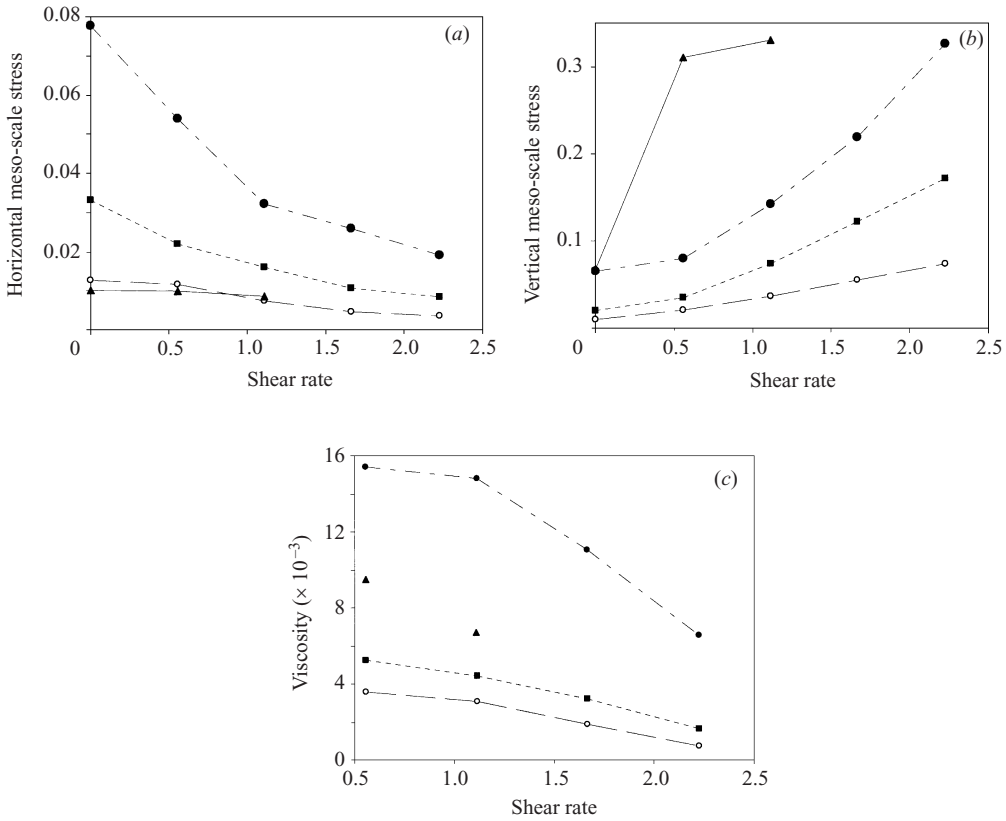

FIGURE 17. Effect of shear rate on the meso-scale normal stresses and viscosity. $e_p = 0.9$; $Fr_p = 64.8$; $Re_p = 1.18$; $Fr_h = 0.486$: ○, two-dimensional; aspect ratio 1 : 4; resolution: 16 × 64. $\bar{\phi} = 0.025$; ■, two-dimensional; aspect ratio 1 : 4; resolution: 16 × 64. $\bar{\phi} = 0.05$; ●, two-dimensional; aspect ratio 1 : 4; resolution: 16 × 64. $\bar{\phi} = 0.10$; ▲, three-dimensional with aspect ratio 1 : 1 : 4; resolution: 16 × 16 × 64. $\bar{\phi} = 0.10$. (*a*) Horizontal meso-scale normal stress, $P_{s,meso,x}$. (*b*) Vertical meso-scale normal stress, $P_{s,meso,y}$. (*c*) Meso-scale viscosity, $\mu_{s,meso}$.

the drag force model described in table 1 can be rewritten formally in terms of the terminal velocity and Richardson–Zaki: exponent (n):

$$\boldsymbol{f} = \beta(\boldsymbol{u} - \boldsymbol{v}), \quad \beta = \frac{(\rho_s - \rho_g)g\phi}{v_t(1-\phi)^{n-2}},$$

with n assuming values of 4.65 and 2.325 at the two limits, respectively. When this is cast in dimensionless form, the only dimensionless group which will appear in this term is $(\Delta\rho)/\rho_s$, which is close to unity in the gas–solid flow problems. At intermediate values of Re_g and a drag model as in table 1, Fr_p does appear in the dimensionless interphase drag force term. However, it is easy to argue that its influence is quite weak for modest changes in Fr_p.

(ii) It appears through the kinetic theory viscosity (μ), conductivity (λ) and the terms representing generation and dissipation of PTE, see table 1. Our computational experiments suggest that the effect of dimensionless particle size on the meso-scale characteristics through the second route is also weak.

This is illustrated in table 5, where we have presented various average quantities for three different values of Fr_p and a fixed value of Fr_h. In these simulations, Re_p is

Fr_p	97.19	64.79	48.59
W_{slip}	1.46	1.46	1.48
T	0.018	0.018	0.021
$P_{s,KT}$	0.0023	0.0022	0.0026
$P_{s,meso,x}$	0.032	0.032	0.030
$P_{s,meso,y}$	0.015	0.015	0.017

TABLE 5. Effect of Fr_p on dimensionless domain-averaged quantities obtained from two-dimensional simulations. $Fr_h = 0.486$; $Re_p = 1.18$; $A = 4$. Average solids volume fraction = 0.05. Here, subscripts x and y denote the horizontal and vertical directions, respectively. Resolution: 16×64.

still $O(1)$. This demonstrates that the effect of particle size (dimensional quantity) is felt largely through its effect on settling velocity (dimensional quantity) and how it changes the value of Fr_h (for a given dimensional box width).

In typical riser flows, the mass loading of particles is much larger than unity, and consequently gas-phase inertia plays only a secondary role; in this regime of flow, the density ratio also has only a small influence on the meso-scale structures. The Reynolds number appears in the model only through the drag correlation and as such its effect is felt primarily via the terminal velocity. Therefore, its direct influence on the meso-scale structures is minimal.

Therefore, the average values of various quantities are determined largely by the values of ϕ, A, Fr_h and $\tilde{\gamma}$. As discussed earlier, for sufficiently large A (which is typically the case in almost all riser flow simulations), the average quantities are only weakly dependent on A, leaving ϕ, Fr_h and $\tilde{\gamma}$ as the main parameters.

We have carried out a limited number of two-dimensional simulations to explore the effect of Fr_h on slip velocity, granular temperature, meso-scale normal stresses and viscosity, and the results are summarized in figure 18(*a–e*). (A typical range of Fr_h relevant in riser simulations is 0.05–1.0, with the explored range of 0.2–0.5 being more common.) In the range of volume fractions shown in this figure, the granular temperature, meso-scale stresses and meso-scale viscosity clearly increase with particle volume fraction. In contrast, the effective slip velocity reveals a more complex dependence, which can be easily traced to the fact that the particle volume fraction at which the maximum slip velocity occurs (e.g. see figure 7 or 12) changes with Fr_h.

All the data shown in figure 18, with the exception of those shown as filled symbols, suggest that, as the domain size increases ($Fr_h \to 0$), the effects of the meso-scale structures reach finite asymptotic values. Physically, the existence of such limits may be interpreted as the saturation of quantities, such as velocity variance and correlation time, that characterize the meso-scale structures. On the other hand, the data shown as filled symbols suggest a more complex Fr_h scaling. Many more simulations need to be performed before the Fr_h-dependence of all of these quantities can be determined with confidence.

6. Summary

Meso-scale structures that take the form of clusters and strands, which have been observed in gas–particle flows, can be captured qualitatively through transient integration of continuum equations for the gas and particle phases. These structures arise as a result of two instability mechanisms, both of which are accounted for in a

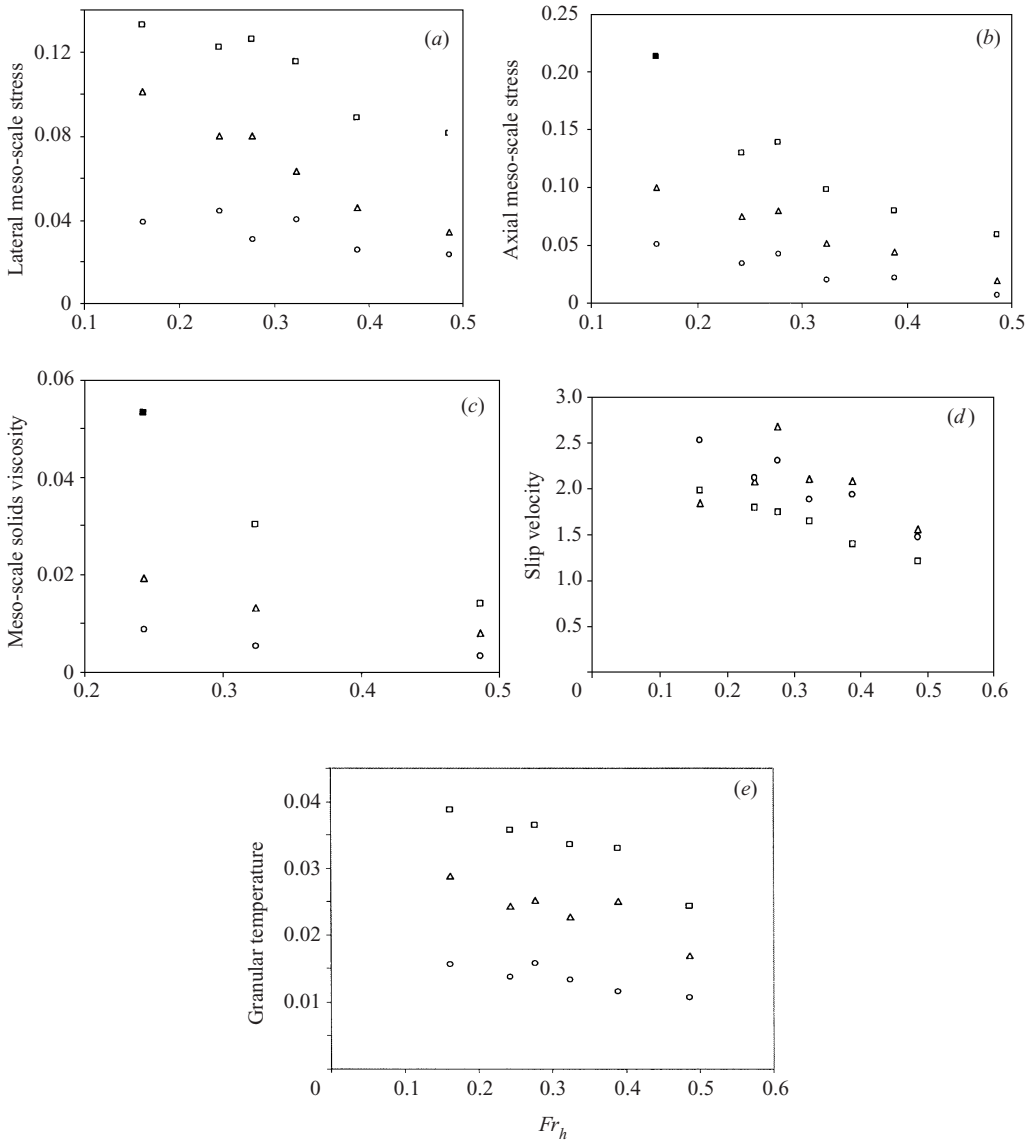

FIGURE 18. Effect of Fr_h on domain-averaged quantities. $e_p = 0.9$; $Fr_p = 64.8$; $Re_p = 1.18$; two-dimensional. Aspect ratio 1 : 4. Resolution: 16×64. ○, $\bar{\phi} = 0.025$; △, $\bar{\phi} = 0.05$; □, $\bar{\phi} = 0.10$. No macro-scale shear was imposed. (*a*) Slip velocity. (*b*) Granular temperature. (*c*) Horizontal meso-scale normal stress, $P_{s,meso,x}$. (*d*) Vertical meso-scale normal stress, $P_{s,meso,y}$. (*e*) Meso-scale viscosity of the solid phase, $\mu_{s,meso}$.

rheological model deduced in the literature by adapting the kinetic theory of gases to gas–particle mixtures. These meso-scale structures are too small to be resolved in simulations of flow in large process vessels, and are invariably invisible in the coarse-grid simulations. Yet, they affect the flow characteristics profoundly; in particular, they alter the effective interaction force that couples the gas and particle phases, and dramatically increase the effective viscosities of the two phases and the normal stresses in the particle phase. In this paper, we have presented examples to illustrate these points.

In large-eddy simulations of turbulent flow of an incompressible single-phase fluid, the sub-grid structure is sustained through macroscopic shear. In the gas–solid flow problem studied here, sub-grid-scale structure arises spontaneously through a sub-grid-scale instability and can be sustained even in the absence of macro-scale shear. We have taken a closer look at instability-driven sub-grid structure and have shown that it does alter the effective drag, viscosities and particle-phase pressure appreciably. We have also presented some calculations which include the effect of macro-scale shear. These results suggest that at low shear rates the sub-grid-scale structure and fluctuations are influenced predominantly by the sub-grid instability and not the macro-scale shear. At higher shear rates, the macro-scale shear alters the fluctuation characteristics substantially by serving to align the meso-scale structure in the axial direction. This leads to a highly anisotropic meso-scale normal stress and a shear-thinning behaviour. Our work demonstrates the need for a sub-grid model to account for the effect of the sub-grid structure, and also outlines a possible approach to developing such a model.

We close by reiterating the practical value of the present line of investigation. Coarse-grid simulation of multiphase flows is highly desirable for exploring the effects of choices made in process design/redesign, as it allows us to analyse the problem with a manageable number of spatial nodes which, in turn, permits much larger time steps to be taken when compared to the simulations with very high spatial resolution (since the maximum time step is related to the grid size through a Courant instability criterion). At the same time, the results of a coarse-grid simulation that ignores the sub-grid processes cannot be trusted as true solutions of the model equations for rapid gas–particle flows one is trying solve. Given the complex nature of the sub-grid processes, it appears doubtful if simple extensions of classical K–ε models will be able to account for the effect of meso-scale structures discussed here. Thus, a physically sound sub-grid model is not simply interesting, but is a must.

This work was supported by the National Science Foundation (CTS-9421661), Exxon Research & Engineering Company, Sandia National Laboratory, and more recently by US Department of Energy CDE-FC26-00NT40971. We are grateful to Thomas O'Brien at the National Energy Technology Laboratory and Roy Jackson for their support and helpful suggestions.

Appendix

Consider, for illustration, a two-dimensional simulation of gas–particle flow in a vertical riser. Let us suppose that we discretize the domain using equally sized, but coarse, grids. Let us further suppose that the system of equations given in table 1 is the *microscopic* model we wish to simulate. The continuity and momentum balance equations of the corresponding coarse-grid model, obtained by Favre averaging over the meso-scale (sub-grid) structures, will have a form identical to equations (1)–(4) in table 1, but $\boldsymbol{\sigma}_s$, $\boldsymbol{\sigma}_g$, and $\boldsymbol{f}$ appearing in these equations will be replaced by $\boldsymbol{\sigma}_s^*$, $\boldsymbol{\sigma}_g^*$ and $\boldsymbol{f}^*$, representing the effective quantities.

In order to construct a simple sub-grid model for the effect of meso-scale structures resulting from sub-grid-scale instabilities, one can perform highly resolved simulations of the type described in the text in a doubly periodic domain whose size is exactly the same as the grid size of the coarse-grid simulation. Such simulations are performed for various mean solids volume fractions and various shear rates. The results are then used to compute effective slip velocity, $\boldsymbol{P}_{s,meso}$, $\mu_{s,meso}$ and $\mu_{app,g}$ as functions of the mean solids volume fraction and shear rates.

The slip velocity data are then correlated, as illustrated in figure 6 for the case $\gamma = 0$. One can then write an effective drag law of the form

$$\boldsymbol{f}^* = \beta^*(\boldsymbol{u} - \boldsymbol{v}), \quad \beta^* = \frac{(\rho_s - \rho_g)g(1-\phi)\phi}{v_t F_1(\phi)}. \tag{A 1}$$

Similar calculations can be performed at various shear rates to include the effect of shear.

As described in the text, solid-phase stress induced by the meso-scale fluctuations is significantly larger than the kinetic theory stress and so the latter can be neglected. This, of course, does *not* mean that the kinetic theory stress plays no role in the macro-scale features of gas–particle flow. It simply means that the primary role of the stress due to the micro-scale fluctuations, captured by the kinetic theory, is confined to the sub-grid processes; these micro-scale fluctuations control the meso-scale structure and, therefore, appear indirectly in the macro-scale through the solid-phase stress induced by the meso-scale fluctuations. A simple model for $\boldsymbol{\sigma}_s^*$ is then written as

$$\boldsymbol{\sigma}_s^* = \boldsymbol{P}_{s,meso} - 2\mu_{s,meso}\boldsymbol{S},$$

which is similar in form to that used by Tsuo & Gidaspow (1989). $\boldsymbol{P}_{s,meso}$ (a diagonal tensor) and $\mu_{s,meso}$ are empirical expressions obtained by fitting the data obtained in the highly resolved simulations alluded to above. The expressions should account for the dependence on the solids volume fraction and the rate of deformation.

Following the same approach, we can express $\boldsymbol{\sigma}_g^*$ as

$$\boldsymbol{\sigma}_g^* = p_g\boldsymbol{I} - 2\mu_{app,g}\boldsymbol{S}_g$$

where p_g is simply the gas pressure, $\mu_{app,g}$, and will depend on the solids volume fraction and the rate of deformation.

In this simple model, it is not necessary to include the PTE balance in the coarse-grid simulations, as long as the grid size is sufficiently large that the PTE balance is relevant only at the sub-grid level.

Note that such an approach focuses on time-averaged (sub-grid-scale) quantities, which fluctuate rapidly around a statistical mean (e.g. see figure 3). Time-averaged quantities suffice only if a complete separation of scales exists between the meso- and macro-scales. Figure 3 suggests that such a separation of scales may not exist, and so it is possible that the fluctuating nature of the interphase interaction force and the effective stresses must be accounted for in coarse-grid simulations. Recall that, in our problem, instabilities begin at a small scale and grow to larger scales. Introducing (stochastic) terms to capture the fluctuating nature of the interphase interaction force and the effective stresses (arising from spatio-temporal meso-scale structures) may allow us to initiate and sustain fluctuations in coarse-grid simulations.

It appears reasonable to retain the inflow and outflow boundary conditions that are currently used in CFD simulations. At bounding walls, the normal velocity of the two phases should obviously equal that of the wall. Wall boundary conditions for the tangential components of gas and particle velocities, suitable for coarse-grid simulations, remain a challenge. Nevertheless, for the specific problem of gas–particle flow in wide risers, it seems adequate to use simple free-slip boundary conditions for both phases, as the wall resistance is known to contribute only minimally.

It is straightforward to extend this idea to three-dimensional simulations with equally sized grids.

When the grids are unequally sized, the approach outlined here becomes much harder, as one now has to do highly resolved simulations for large number of domain

sizes. This clearly shows why a more elegant and fundamentally based sub-grid model that explicitly accounts for the coarse grid size, and does not require the highly resolved simulations, must be developed.

REFERENCES

Agrawal, K. 2000 The role of meso-scale structures in rapid gas-solid flows. PhD Dissertation, Princeton University.

Anderson, T. B. & Jackson, R. 1967 Fluid mechanical description of fluidized beds. Equations of motion. *Indust. Engng Chem. Fundam.* **6**, 527–539.

Anderson, K., Sundaresan, S. & Jackson, R. 1995 Instabilities and the formation of bubbles in fluidized beds. *J. Fluid Mech.* **303**, 327–366.

Bader, R., Findlay, J. & Knowlton, T. M. 1988 Gas/solid flow patterns in a 30.5 cm diameter circulating fluidized bed. In *Circulating Fluidized Bed Technology II* (ed. P. Basu & J. F. Large), pp. 123–137. Pergamon.

Balzer, G., Boelle, A. & Simonin, O. 1995 Eulerian gas-solid flow modelling of dense fluidized beds. In *Fluidization VIII*, p. 1125.

Boelle, A., Balzer, G. & Simonin, O. 1995 Gas-solid flows. In *Gas-particle Flows*. ASME FED, vol. 228, p. 9.

Bolio, E. & Sinclair, J. 1995 Gas turbulence modulation in the pneumatic conveying of massive particles in vertical tubes. *Intl J. Multiphase Flow* **21**, 985–1001.

Bouillard, J. X., Lyczkowski, R. W. & Gidaspow, D. 1989 Porosity distributions in a fluidized bed with an immersed obstacle. *AIChE J.* **35**, 908–922.

Dasgupta, S., Jackson, R. & Sundaresan, S. 1994 Turbulent gas–particle flow in vertical risers. *AIChE J.* **40**, 215–228.

Enwald, H. & Almstedt, A. E. 1999 Fluid dynamics of a pressurized fluidized bed: comparison between numerical solutions from two-fluid models and experimental results. *Chem. Engng Sci.* **54**, 32–342.

Enwald, H., Peirano, E. & Almstedt, A. E. 1997 Eulerian two-phase theory applied to fluidization. *Intl J. Multiphase Flow* **22**, Suppl., 21–66.

Enwald, H., Peirano, E., Almstedt, A. E. & Leckner, B. 1999 Simulation of the fluid dynamics of a bubbling fluidized bed. Experimental validation of the two-fluid model and evaluation of a parallel multiblock solver. *Chem. Engng Sci.* **54**, 31-328.

Ferziger, J. H. & Peri, M. 1996 *Computational Methods for Fluid Dynamics*. Springer.

Gidaspow, D. 1993 Hydrodynamic modelling of circulating and bubbling fluidized beds. In *Particulate Two-Phase Flow* (ed. M. C. Roco), pp. 778–810. Butterworth-Heinemann.

Gidaspow, D. 1994 *Multiphase Flow and Fluidization*, pp. 31–58, 197–238. Academic.

Glasser, B. J., Kevrekidis, I. G. & Sundaresan, S. 1996 One- and two-dimensional travelling wave solutions in gas-fluidized beds. *J. Fluid Mech.* **306**, 183–221.

Glasser, B. J., Kevrekidis, I. G. & Sundaresan, S. 1997 Fully developed travelling wave solutions and bubble formation in fluidized beds. *J. Fluid Mech.* **334**, 157–188.

Glasser, B.J., Sundaresan, S. & Kevrekidis, I.G. 1998 From bubbles to clusters in fluidized beds. *Phys. Rev. Lett.* **81**, 1849–1852.

Goldhirsch, I., Tan, M.-L. & Zanetti, G. 1993 A molecular dynamical study of granular fluids I: The unforced granular gas in two dimensions. *J. Sci. Comput.* **8**, 1–40.

Grace, J. R. & Tuot, J. 1979 A theory for cluster formation in vertically conveyed suspensions of intermediate density. *Trans. Inst. Chem. Engrs* **57**, 49–54.

Hoomans, B. P. B., Kuipers, J. A. M., Briels, W. J. & Van Swaaij, W. P. M. 1996 Discrete particle simulation of bubble and slug formation in a two-dimensional gas-fluidized bed: A hard-sphere approach. *Chem. Engng Sci.* **51**, 99–108.

Hopkins, M. A. & Louge, M. Y. 1991 Inelastic microstructure in rapid granular flows of smooth disks. *Phys. Fluids* A **3**, 47–57.

Horio, M. 1995 Cluster and agglomerate formation in fluidized suspensions. *Proc. 2nd Intl Conf. on Multiphase Flows, Kyoto, 3–7 April 1995*, vol. 3 (ed. A. Serizawa, T. Fukano & J. Bataille), FB1-1.

Hrenya, C. M. & Sinclair, J. L. 1997 Effects of particle-phase turbulence in gas-solid flows. *AIChE J.* **43**, 853–869.

Ito, M., Tsukada, M., Shimamura, J. & Horio, M. 1998 Prediction of cluster size and slip velocity in circulating fluidized beds by a DSMC model. In *Fluidization IX* (ed. L.-S. Fan & T. M. Knowlton), pp. 526–532. Engineering Foundation Publication.

Jenkins, J. T. 1992 Boundary conditions for rapid granular flow: Flat, frictional wall. *Trans ASME: J. Appl. Mech.* **114**, 120–127.

Jenkins, J. T. & Louge, M. Y. 1997 On the flux of fluctuation energy in a collisional grain flow at a flat, frictional wall. *Phys. Fluids* **9**, 2835–2840.

Jenkins, J. T. & Richman, M. W. 1985 Grad's 13-moment system for a dense gas of inelastic spheres. *Arch. Rat. Mech. Anal.* **87**, 355–377.

Jenkins, J. T. & Richman, M. W. 1986 Boundary conditions for plane flows of smooth, nearly elastic circular disks. *J. Fluid Mech.* **171**, 53–69.

Johnson, P. C. & Jackson, R. 1987 Frictional-collisional constitutive relations for granular materials, with applications to plane shearing. *J. Fluid Mech.* **130**, 187–202.

Koch, D. L. 1990 Kinetic theory for a monodisperse gas-solid suspension. *Phys. Fluids* A **2**, 1711–1723.

Koch, D. L. & Sangani, A. S. 1999 Particle pressure and marginal stability limits for a homogeneous monodisperse gas fluidized bed: kinetic theory and numerical simulations. *J. Fluid Mech.* **400**, 229–263.

Kudrolli, A. & Gollub, J. P. 1997 Studies of cluster formation due to collisions in granular material. *Powders & Grains 97* (ed. R. Behringer & J. Jenkins), pp. 535–538. Balkema, Rotterdam.

Louge, M., Mastorakos, E. & Jenkins, J. T. 1991 The role of particle collisions in pneumatic transport. *J. Fluid Mech.* **231**, 345–359.

Lun, C. K. K., Savage, S. B., Jeffrey, D. J. & Chepurniy, N. 1984 Kinetic theories of granular flows: inelastic particles in Couette flow and slightly inelastic particles in a general flow field. *J. Fluid Mech.* **140**, 223–256.

Ma, D. & Ahmadi, G. 1988 A kinetic model for rapid granular flows of nearly elastic particles including interstitial fluid effects. *Powder Technol.* **56**, 191–207.

McNamara, S. & Young, W. R. 1996 Dynamics of a freely evolving two-dimensional granular medium. *Phys. Rev.* B **53**, 5089–5100.

Nieuwland, J. J., Annaland M. V., Kuipers, J. A. M. & van Swaaij, W. P. M. 1996 Hydrodynamic modelling of gas/particle flows in riser reactors. *AIChE J.* **42**, 1569–1582.

Nieuwland, J. J., Huizenga, J. J. P., Kuipers, J. A. M. & van Swaaij, W. P. M. 1995 Hydrodynamic modelling of circulating fluidized beds. *Chem. Engng Sci.* **49**, 5803–5811.

Nott, P. R., Alam, M. A., Agrawal, K., Jackson, R. & Sundaresan, S. 1999 The effect of boundaries on the plane Couette flow of granular materials: a bifurcation analysis. *J. Fluid Mech.* **397**, 203–229.

O'Brien, T. J. & Syamlal, M. 1994 Particle cluster effects in the numerical simulation of a circulating fluidized bed. In *Circulating Fluidized Bed Technology IV* (ed. A. A. Avidan), pp. 345–350. The Secretariat of the International Conference on Circulating Fluid Beds.

Ouyang, J. & Li, J. 1999 Discrete simulation of heterogeneous structure and dynamic behavior in gas-solid fluidization. *Chem. Engng Sci.* **54**, 5427–5440.

Pita, J. A. & Sundaresan, S. 1991 Gas-solid flow in vertical tubes. *AIChE J.* **37**, 1009–1018.

Pita, J. A. & Sundaresan, S. 1993 Developing flow of a gas–particle mixture in a vertical riser. *AIChE J.* **39**, 541–552.

Richardson, J. F. & Zaki, W. N. 1954 Sedimentation and fluidization: Part I. *Trans. Inst. Chem. Engrs* **32**, 35–53.

Samuelsberg, A. & Hjertager, B. 1996 Computational modelling of gas/particle flow in a riser. *AIChE J.* **42**, 1536–1546.

Savage, S. B. 1992 Instability of unbounded uniform granular shear flow. *J. Fluid Mech.* **241**, 109–123.

Schnitzlein, M. G. & Weinstein, H. 1988 Flow characterization in high-velocity fluidized beds using pressure fluctuations. *Chem. Engng Sci.* **43**, 2605–2614.

Sinclair, J. L. & Jackson, R. 1989 Gas-particle flow in a vertical pipe with particle-particle interaction. *AIChE J.* **35**, 1473–1486.

Smagorinsky, J. 1963 General circulation experiments with the primitive equations: Part I, the basic experiment. *Mon. Wea. Rev.* **91**, 99–164.

Srivastava, A., Agrawal, K., Sundaresan, S., Reddy Karri, S. B. & Knowlton, T. M. 1998 Dynamics of gas–particle flow in circulating fluidized beds. *Powder Technol.* **100**, 173–182.

Syamlal, M. 1998 *MFIX Documentation: Numerical Techniques.* DOE/MC-31346-5824. NTIS/DE98002029.

Syamlal, M. Rogers, W. & O'Brien, T. J. 1993 *MFIX Documentation.* US Department of Energy, Federal Energy Technology Center, Morgantown.

Tan, M.-L. 1995 Micro-structures and macro-structures in rapid granular flow. PhD dissertation, Princeton University.

Tan, M.-L. & Goldhirsch, I. 1997 Intercluster interactions is rapid granular shear flows. *Phys. Fluids* **9**, 856–869.

Tanaka, T., Yonemura, S., Kiribayashi, K & Tsuji, Y. 1996 Cluster formation and particle-induced instability in gas-solid flows predicted by the DSMC method. *JSME Intl J.* B **39**, 239–245.

Tanaka, T., Yonemura, S. & Tsuji, Y. 1995 Effects of particle properties on the structure of clusters. In *Gas-particle Flows.* ASME FED, vol. 228, pp. 297–302.

Tsuji, Y., Kawaguchi, T. & Tanaka, T. 1993 Discrete particle simulation of two-dimensional fluidized bed. *Powder Technol.* **77**, 79–87.

Tsuji, Y., Tanaka, T. & Yonemura, S. 1998 Cluster patterns in circulating fluidized beds predicted by numerical simulation: Discrete particle model vs. two-fluid model. *Powder Technol.* **95**, 254–264.

Tsukada, M. 1995 Fluidized bed hydrodynamics, heat transfer and high temperature process developments. PhD Dissertation, Tokyo University of Agriculture and Technology, Tokyo, Japan.

Tsuo, Y. P. & Gidaspow, D. 1990 Computation of flow patterns in circulating fluidized beds. *AIChE J.* **36**, 885–896.

Weinstein, H., Shao, M. & Schnitzlein, M., 1986 Radial variation in solid density in high velocity fluidization. In *Circulating Fluidized Bed Technology I* (ed. P. Basu), pp. 201–206. Pergamon.

Wen, C. Y. & Yu, Y. H. 1966 Mechanics of Fluidization. *Chem. Engng Prog. Symp. Ser.* **62**, 100–111.

Wilhelm, R. H. & Kwauk, M. 1948 Fluidization of solid particles. *Chem. Engng. Prog.* **44**, 201–218.

Wylie, J. J. & Koch, D. L. 2000 Particle clustering due to hydrodynamic interactions. *Phys. Fluids* **12**, 964–970.

Yasuna, J., Moyer, H., Elliot, S. & Sinclair, J. 1995 Quantitative predictions of gas–particle flow in a vertical pipe with particle-particle interactions. *Powder Technol.* **84**, 23–34.

Zhang, J., Jiang, P. & Fan, L.-S. 1998 Flow behaviour in transients of solid flow rates in a circulating fluidized bed system. In *Fluidization IX* (ed. L.-S. Fan & T. M. Knowlton). Engineering Foundation Publication.

Coarse-grid simulation of reacting and non-reacting gas-particle flows

Final Technical Report

Award # DE-FC26-00NT409071

DOE Vision 21 Virtual Demonstration Initiative

Appendix B

Annu. Rev. Fluid Mech. 2003. 35:63–88
doi: 10.1146/annurev.fluid.35.101101.161151

INSTABILITIES IN FLUIDIZED BEDS

Sankaran Sundaresan
Department of Chemical Engineering, Princeton University, Princeton, New Jersey 08544; email: sundar@princeton.edu

Key Words fluidization, stability, bubbles, yield stress, waves

■ **Abstract** This paper reviews recent advances in our understanding of the origin and hierarchy of organized flow structures in fluidized beds, distinction between bubbling and nonbubbling systems, and stages of bubble evolution. Experimental data and theory suggest that, at high particle concentrations, the particle-phase pressure arising from flow-induced velocity fluctuations decreases with increasing concentration of particles. This, in turn, implies that nonhydrodynamic stresses must be present to impart stability to a uniformly fluidized bed at very high particle concentrations. There is ample evidence to support an argument that, in commonly encountered gas-fluidized beds, yield stresses associated with enduring particle networks are present in the window of stable bed expansion, where the particles are essentially immobile until bubbling commences. However, some recent data on gas-fluidized beds of agglomerates of cohesive particles suggest that there exists a window of bed expansion where the bed does manifest a smooth appearance to the naked eye and the particles are mobile; at higher gas velocities the bed bubbles visibly. The mechanics of such beds remain to be fully explained.

1. INTRODUCTION

Fluidized beds are commonly classified on the basis of their appearance as either bubbling (aggregative) or nonbubbling (particulate). Particulate beds maintain a smooth appearance and expand progressively as the fluid flow rate is increased. In contrast, aggregatively fluidized beds are traversed by rising pockets of fluid, which are reminiscent of gas bubbles in liquids. Typical examples of particulate and aggregative beds are 1-mm glass beads fluidized by water and 200-μm glass beads fluidized by ambient air, respectively. Over 50 years ago, Wilhelm & Kwauk (1948) concluded on the basis of their experimental observations that a fluidized bed manifested particulate behavior if $Fr_m = u_m^2/gd_p \ll 1$, where u_m is the minimum fluidization velocity and d_p is the particle diameter. The transition from particulate to aggregative behavior as the Froude number, Fr_m, is increased has been a subject of much research in the past 50 years.

It turns out that the mechanics of fluidized beds is much more complex than the simple classification by Wilhelm & Kwauk (1948). Careful fluidization and sedimentation experiments have revealed that liquid-fluidized beds, which were

termed particulate by Wilhelm & Kwauk, display fascinating organized flow structures, whereas some aggregative gas-fluidized beds manifest a region of stable bed expansion before they start to bubble. This article reviews our current understanding of (*a*) the various stages of bubble evolution, (*b*) the origin and hierarchy of the organized flow structures in liquid-fluidized beds, (*c*) the distinction between bubbling and nonbubbling fluidized beds, and (*d*) the true nature of a gas-fluidized bed in the interval of stable bed expansion.

Early attempts to distinguish between bubbling and nonbubbling fluidized beds were based on linear stability analysis of the uniformly stabilized state (Jackson 1963), and an in-depth review of these studies can be found elsewhere (Jackson 2000). It now appears that this distinction is linked to high-amplitude solutions (Anderson et al. 1995, Glasser et al. 1997, Homsy 1998, Duru & Guazzelli 2002), so this review concentrates on various stages of evolution of nonuniform structures.

In general, evolution of nonuniform structures occurs very rapidly in ground-based gas-fluidized beds. In contrast, it occurs sufficiently slowly in liquid-fluidized beds so that ground-based experimental interrogation is feasible. Indeed, tremendous insight has emerged in recent years through studies of liquid-fluidized beds (see Section 2). The state of a gas-fluidized bed of particles in the interval of stable bed expansion has been studied quite extensively in the past decade to probe the origin of stability (Section 3). Section 4 summarizes the highlights and outstanding questions.

2. STUDIES ON LIQUID-SOLID SYSTEMS

2.1. Experiments on the Hierarchy of Nonuniform Structures

Anderson & Jackson (1969) observed that a bed of 2-mm glass beads fluidized by water (in a 1.5″ ID vertical cylindrical tube) was traversed by a succession of essentially one-dimensional traveling voidage wavefronts (1-DTWs) having no horizontal structure. They also observed that the amplitude of these waves initially increased exponentially with distance from the distributor, establishing that they arose owing to an instability and that this bed, which fell in the category by Wilhelm & Kwauk of particulate beds, was by no means truly uniform beyond a modest extent of bed expansion. Figure 1 (taken from Duru et al. 2002) illustrates a spatiotemporal plot of voidage in the 1-DTWs forced at 1 Hz through an oscillatory motion of the distributor.

El-Kaissy & Homsy (1976) and Didwania & Homsy (1981) conducted experiments in a two-dimensional liquid-fluidized bed and observed two-dimensional destabilization of the 1-DTWs leading to a brief appearance of bubble-like voidage pockets. More recently, using water as the fluidizing medium, Duru & Guazzelli (2002) conducted similar experiments with various particles. Figure 2, recorded by Duru & Guazzelli (2002) in a bed of 685-μm glass beads ($\rho_p = 2.55$ g/cm^3, $Fr_t = u_t^2/gd_p \approx 1.58$, $Fr_m \approx 0.0045$, $St_m = \rho_p u_m d_p/\mu_f \approx 10.7$, and $\mathrm{Re}_m = \rho_f u_m d_p/\mu_f \approx 4.2$, where St_m and Re_m denote Stokes and Reynolds numbers, respectively,

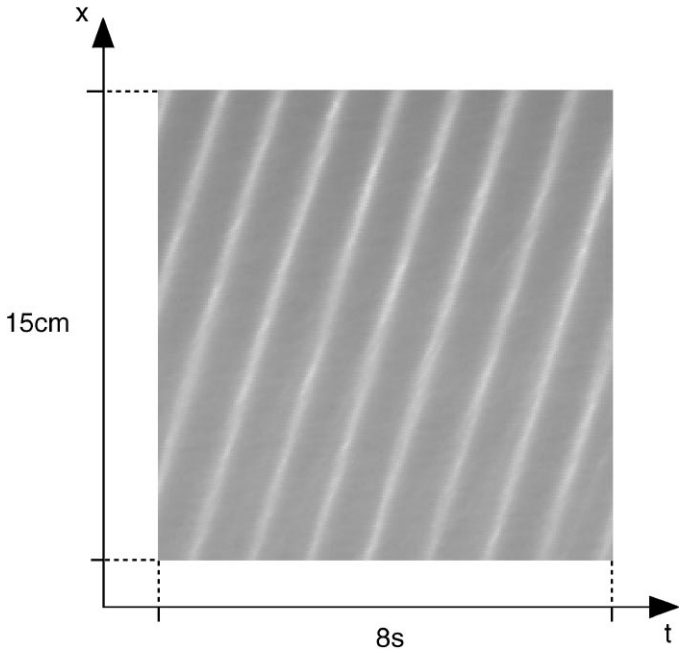

Figure 1 Spatiotemporal plot of one-dimensional traveling waves in a bed of 1220-μm glass beads fluidized by 35-wt% glycerol-water mixture. $\rho_s = 4.08\ \mathrm{g \cdot cm^{-3}}$; bed diameter = 3 cm; $\rho_f = 1.1\ \mathrm{g \cdot cm^{-3}}$; $\mu_f = 3$ cP. $\phi_o = 0.540$. The wave was forced at 1 Hz. Only 15 cm of the bed, shot during 8 s, is shown. Lighter shade of gray indicates regions of higher voidage. Source: Duru et al. (2002). Reprinted with permission from The Cambridge University Press.

evaluated using the minimum fluidization velocity, Fr_t is a Froude number based on terminal velocity, ρ_p and ρ_f are the densities of particles and fluid, and μ_f is the viscosity of the fluid), illustrates the smooth evolution of transverse modulation of 1-DTWs. Two-dimensional destabilization also occurred in a water-fluidized bed of 1220-μm beads ($\rho_p = 4.084\ \mathrm{g/cm^3}$, $Fr_t \approx 3.68$, $Fr_m \approx 0.033$, $St_m \approx 110.6$, $\mathrm{Re}_m \approx 27$), where a more complex set of events could be observed (Duru & Guazzelli 2002) (see Figure 3). After an initial period of growth of the amplitude of the 1-DTW (Figure 3*a*), the waves buckled, and relatively higher voidage "holes" appeared (Figure 3*b*,*c*) and accelerated upward. At higher elevations in the bed, the "holes" disappeared (Figure 3*d*–*f*), and the resulting state did not have any recognizable structure. At slightly higher flow rates, the two-dimensional destabilization proceeded as in Figure 3, but at higher elevations in the bed, a structure reminiscent of oblique traveling waves (Figure 4) emerged.

Duru & Guazzelli (2002) observed that two-dimensional destabilization of 1-DTWs in a bed of 1-mm stainless beads ($\rho_p = 7.96\ \mathrm{g/cm^3}$, $Fr_t \approx 12.8$, $Fr_m \approx 0.092$,

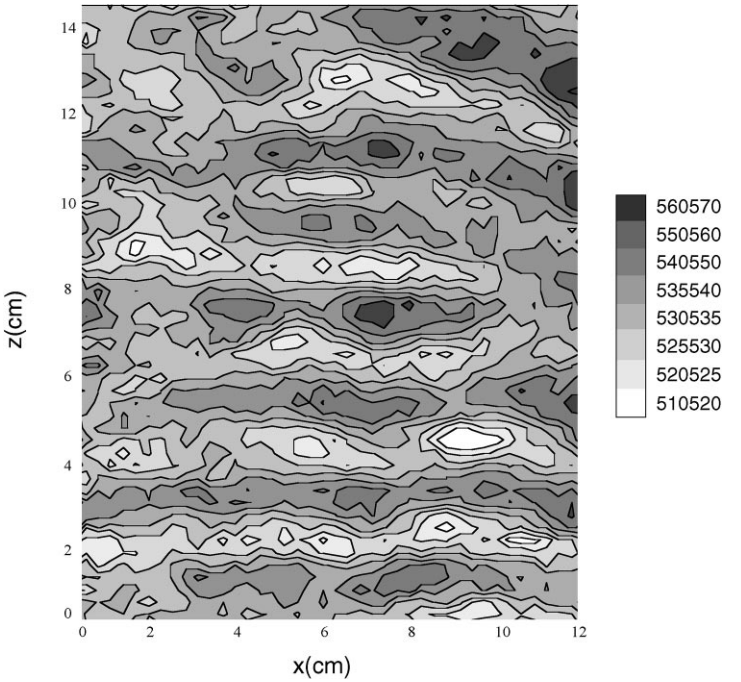

Figure 2 Grayscale plot showing transverse modulation of 1-DTWs. The position z = 0 is arbitrary and does not correspond to the bottom of the bed. $\phi_o = 0.538$. In the legend, 560570 stands for $0.560 < \phi < 0.570$ and so on. Source: Duru & Guazzelli (2002). Reprinted with permission from The Cambridge University Press.

$St_m \approx 265$, $\mathrm{Re}_m \approx 33$) led to bubble-like voids that persisted (see Figure 5). Thus, we now have direct experimental evidence for the hierarchy of structures in liquid-fluidized beds. One-dimensional traveling waves emerge even at extremely small values of Fr_m. For $Fr_m \sim O(10^{-3})$, two-dimensional destabilization of the 1-DTWs invariably occurs, unless suppressed by using narrow beds. For $Fr_m \sim O(10^{-3})$, the two-dimensional structure evolves smoothly and appears to saturate. When $Fr_m \sim O(10^{-2})$, bubble-like voids appear briefly after the two-dimensional destabilization but disappear subsequently, yielding a state with no recognizable structure; however, it appears that the final attractor may be oblique traveling waves. For $Fr_m \sim O(10^{-1})$ or larger, the bubble-like voids persist.

2.2. Particle-Phase Stress and Stability of a Uniformly Fluidized Bed

Through a linear stability analysis of a continuum model where the particles and the fluid are treated as interpenetrating continua, Anderson & Jackson (1967,

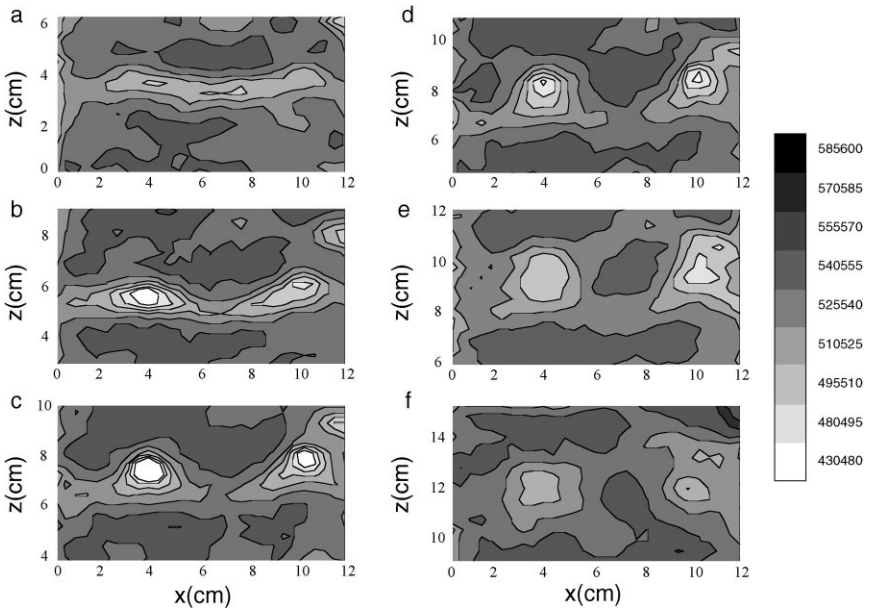

Figure 3 Grayscale plot showing two-dimensional destabilization of 1-DTWs at a superficial velocity of 3.1 cm/s. The position z = 0 is arbitrary and does not correspond to the bottom of the bed. $\phi_o = 0.550$. (*a*) t = 0 s, (*b*) t = 0.16 s, (*c*) t = 0.28 s, (*d*) t = 0.32 s, (*e*) t = 0.40 s, and (*f*) t = 0.56 s. In the legend, 585600 stands for $0.585 < \phi < 0.600$ and so on. Source: Duru & Guazzelli (2002). Reprinted with permission from The Cambridge University Press.

1968) concluded that the state of uniform fluidization is most unstable to vertically traveling wavefronts that have no horizontal structure. Indeed, experiments on liquid-fluidized beds have shown conclusively that the development of such 1-DTWs is the first stage in the growth of nonuniform structures in fluidized beds. It is now well understood that this instability is driven by particle inertia (associated with the relative motion between particles and the fluid) as well as the dependence of drag on particle volume fraction and that the uniform state can be stabilized by a sufficiently large particle-phase bulk elasticity (Garg & Pritchett 1975, Batchelor 1988). The relative motion between the particles and the fluid in a uniformly fluidized state can be expected to impart to the particles a fluctuating velocity that, in turn, endows the particle phase with bulk elasticity. Batchelor (1988) proposed a second source of bulk elasticity arising from hydrodynamic dispersion and suggested that the hydrodynamic dispersion contributes more significantly than the velocity fluctuations to bulk elasticity. Ham et al. (1990) performed fluidization experiments using a variety of particles and liquids, examined the frequency of the traveling waves at various flow rates to accurately pinpoint the conditions at which

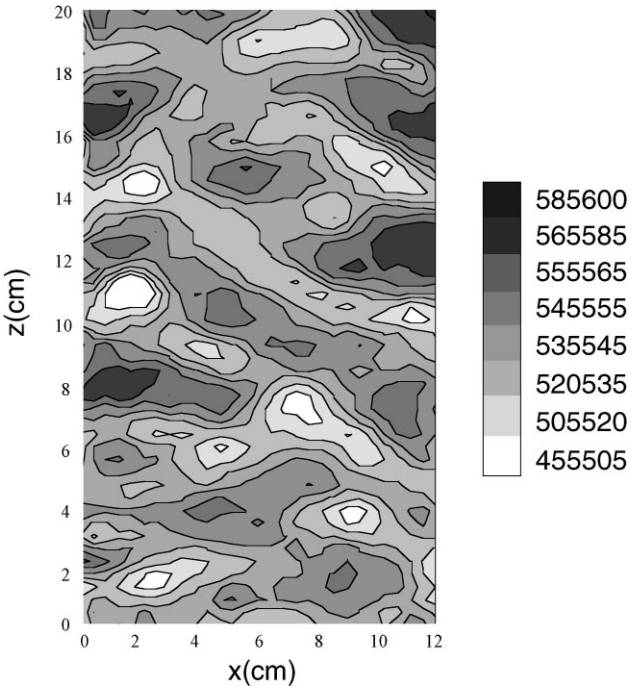

Figure 4 Grayscale plot showing oblique traveling waves resulting from two-dimensional destabilization of 1-DTWs. Same bed as in Figure 3, except with the superficial velocity of 3.3 cm/s. The position z = 0 is arbitrary and does not correspond to the bottom of the bed. $\phi_o = 0.536$. In the legend, 585600 stands for $0.585 < \phi < 0.600$ and so on. Source: Duru & Guazzelli (2002). Reprinted with permission from The Cambridge University Press.

the beds first became unstable, and concluded that hydrodynamically generated bulk elasticity arose mostly from the velocity fluctuations, contrary to Batchelor's suggestion.

The velocity fluctuations endow the particle phase with a pressure (p_s) and a viscosity (μ_s). When a uniform state is perturbed, the spatial variation of particle-phase pressure resulting from variations in voidage and the relative velocity between the two phases drive a redistribution of the particles and thus contribute to either stabilization or destabilization (Koch & Sangani 1999). At the simplest

Figure 5 Transverse destabilization of a 1-DTW leading to the formation of a bubble. (*a*) t = 0.0 s, (*b*) t = 0.12 s, (*c*) t = 0.20 s, (*d*) t = 0.32 s, and (*e*) t = 0.4 s. Each white spot is the individual reflection from a single bead. Source: Duru & Guazzelli (2002). Reprinted with permission from The Cambridge University Press.

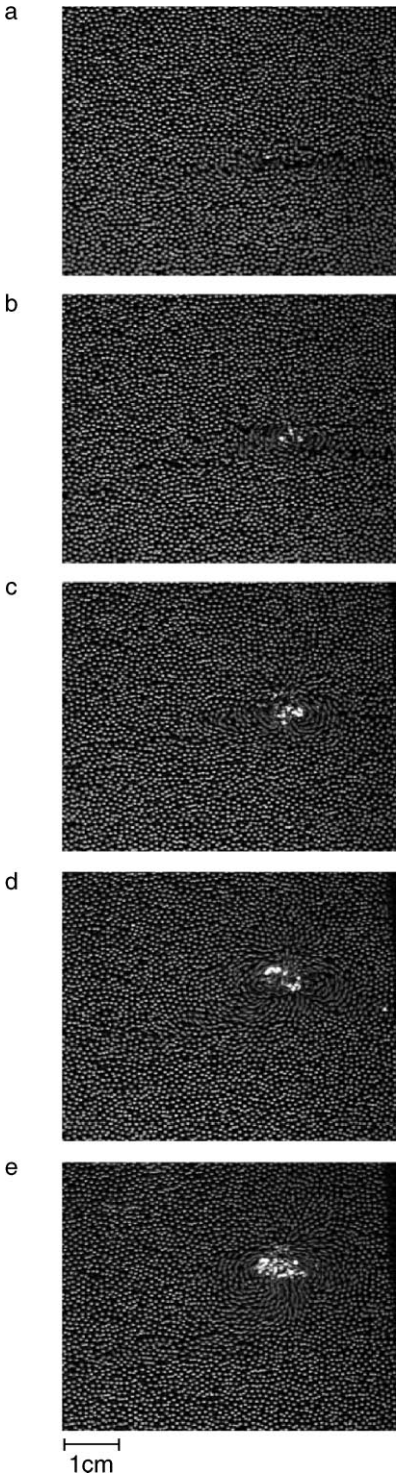
a
b
c
d
e
1cm

phenomenological level, the spatial variation of p_s and μ_s is captured through $p_s = p_s(\phi)$ and $\mu_s = \mu_s(\phi)$, where ϕ is the volume fraction of the particles and $dp_s/d\phi$ is the bulk elasticity mentioned earlier. By demanding that their experimental data on saturated 1-DTWs (generated by periodically forcing the distributor plate in liquid-fluidized beds operated with several different particles and fluids) be captured by a continuum model of the type used by Anderson et al. (1995), Duru et al. (2002) found that (*a*) $\mu_s(\phi) \approx 0.18\,\rho_p u_t d_p/(\phi_{rlp} - \phi)$, where ϕ_{rlp} denotes the particle volume fraction at random loose packing, and (*b*) $dp_s/d\phi \approx 0.2\rho_p u_t^2$ or $0.7\rho_f u_t^2$, which is roughly independent of ϕ, for $\phi_o - \phi$ in the range (0, 0.08). In the region $\phi > \phi_o$, $dp_s/d\phi$ decreased rapidly and even became negative. Here ϕ_o refers to the average solids fraction in the fluidized bed, and the experiments covered ϕ_o values in the range 0.50–0.57. The two choices for $dp_s/d\phi$ in terms of solid or fluid density reflect the uncertainty in the measurement and analysis as well as the fact that the densities of the particles used in their experiments fell in a narrow range (2.48–4.08 g · cm^{-3}). The ϕ_o dependence observed in this study is curious and not understood.

Zenit et al. (1997) measured collisional pressure in beads of glass, plastic, and steel particles of various sizes fluidized by water ($\mathrm{Re}_t = 440$–$3{,}665$; $St_t = 630$–$28{,}500$, where Re_t and St_t are the Reynolds and Stokes numbers, respectively, based on the terminal velocity of the particles), using a flush-mounted piezoelectric pressure transducer. In a later publication, Zenit & Hunt (2000) analyzed voidage fluctuations measured in the same experimental unit and found the low-frequency voidage fluctuations to be reminiscent of traveling waves, whereas the high-frequency component appeared to be random. They observed that the root mean square (RMS) value of the high-frequency fluctuations ($\delta\phi_{hf}$) increased systematically with increasing St_t, getting closer and closer to an expression based on the Enskog model for dense gases:

$$\delta\phi_{hf}^2 = \phi^2 \left[1 + \left(\frac{\phi}{\phi_{rlp}}\right)^{1/3}\right]\left[1 + \frac{1}{3}\left(\frac{(\phi/\phi_{rlp})^{1/3}}{1 - (\phi/\phi_{rlp})^{1/3}}\right)\right]^{-1}.$$

The RMS value of the total fluctuations was roughly twice $\delta\phi_{hf}$ for $0.05 < \phi < 0.40$, was somewhat larger in the range $0.40 < \phi < 0.50$, and rapidly decreased to $\delta\phi_{hf}$ at higher values of ϕ.

The normalized collisional pressure, $p_s/(0.5\rho_p u_t^2)$, determined by Zenit et al. (1997), increased almost exponentially with ϕ for $0.1 < \phi < 0.3$ and decreased with increasing ϕ for $\phi > \sim 0.5$. Their results obtained with glass beads of various sizes suggest that the normalized collisional pressure increased monotonically with St_t. The theory developed by Koch & Sangani (1999) for uniformly fluidized suspensions of elastic particles with $St_t \gg 1$ and $\mathrm{Re}_t \ll 1$ predicts much smaller particle-phase pressures and, more strikingly, a decrease in the normalized particle-phase pressure with increasing St_t. Currently, a theory does not exist for particle-phase pressure in fluidized suspensions where both St_t and Re_t are large, corresponding to the conditions encountered in the experiments of Zenit

et al. (1997). As noted by Zenit et al. (1997), the extent to which the presence of traveling waves contributed to the measured collisional pressure is unknown. Campbell & Wang (1991) showed that the particle-phase pressure measured in a bubbling gas-fluidized bed by a wall-mounted probe correlated with bubble rise velocity, which suggests that traveling waves could have contributed appreciably to the collisional pressure measured by Zenit et al. (1997).

In spite of these uncertainties, it seems reasonable to conclude from the experimental data by Zenit et al. (1997) and Duru et al. (2002) and the theoretical work by Koch & Sangani (1999) that the normalized particle-phase pressure in a fluidized bed increases with ϕ for small ϕ, reaches a maximum value at some $\phi(=\phi^*,$ say), and decreases with increasing ϕ for $\phi > \phi^*$. There is considerable uncertainty about the value of ϕ^*. The analysis by Koch & Sangani (1999) suggests that $\phi^* \approx 0.5$. Duru et al. (2002) obtained a somewhat larger estimate for $\phi^*(\approx 0.52–0.59)$, but they found ϕ^* to depend on ϕ_o. Zenit et al. (1997) observed in their experiments with glass beads of various diameters that ϕ^* increased with St_t, although their values of ϕ^* were smaller ($\approx 0.4–0.5$).

It is well known that an unbounded uniformly fluidized bed can be linearly stable only if $dp_s/d\phi$ is greater than zero and is sufficiently large to overcome the destabilizing effect resulting from particle inertia and the voidage dependence of the drag. Thus, one can readily conclude that a uniformly fluidized bed cannot be stabilized purely by hydrodynamically generated particle-phase pressure for any $\phi_o > \phi^*$; such a bed will give way to traveling waves containing domains with even more compact assemblies of particles until the compaction is stopped by formation of particle networks where nonhydrodynamic stresses become important. A stable fluidized bed at $\phi_o > \phi^*$ is therefore possible only if nonhydrodynamic stresses become active.

In general, in a fluidized (or sedimenting) suspension of noncohesive particles, hydrodynamic (kinetic and collisional) stresses will be the dominant contributors to the particle-phase stress for ϕ below some threshold value, $\phi_{\min}$. For $\phi_{\min} < \phi < \phi_{cp}$, where ϕ_{cp} denotes particle volume fraction at close packing, the relative importance of the hydrodynamic and frictional contact stresses will depend on the prevailing intensity of fluctuating motion available to break the networks (Savage 1998). Our current understanding of the stresses in the region where the presence of velocity fluctuations interferes with the formation of particle networks is primitive. As we learn more about the state of the particle assembly in a stable fluidized bed and in the dense plugs in traveling waves, we will perhaps better understand the stresses in this frictional-collisional regime.

2.3. Two-Dimensional Destabilization of 1-DTWs

Batchelor (1993) and Batchelor & Nitsche (1991, 1993) explained two-dimensional destabilization of 1-DTWs as a gravitational overturning instability and proposed this as the second stage of the development of nonuniform structures in fluidized beds. Through an analysis of the linear stability of 1-DTWs against

two-dimensional perturbations, Anderson et al. (1995), Göz (1995), and Glasser et al. (1996, 1997) verified the existence of the overturning instability. The early experiments by El-Kaissy & Homsy (1976) and the more recent results by Duru & Guazzelli (2002) provide conclusive evidence for this stage of structure evolution. Glasser et al. (1996, 1997) found the overturning instability mechanism to be robust, independent of the closure relations for $p_s(\phi)$ and $\mu_s(\phi)$.

The manner in which the structure evolves following two-dimensional destabilization has been probed by Anderson et al. (1995) and Glasser et al. (1996, 1997) through transient integration of two-phase equations of motion in periodic domains; the latter authors also computed the fully developed solutions through bifurcation analysis and numerical continuation. The numerical simulations by these authors do capture several features seen in the experiments by Duru & Guazzelli (2002). The development of bubble-like voids following two-dimensional destabilization and the upward acceleration of these voids, leading to a state with no recognizable structure, as shown in Figure 3 for a nonbubbling system, were predicted by the transient integration of two-phase equations of motion coupled with simple closures (see Figure 6). Even the manner in which the voids disappear is predicted correctly; see Anderson et al. (1995) for a detailed discussion. These simulations postulated center symmetry in the periodic domain and thereby suppressed oblique traveling waves. However, the experiments suggest that the ultimate attractor may very well be an oblique traveling wave; so it will be interesting to repeat the computational analysis by allowing oblique waves to develop (using the experimentally determined closures).

Batchelor postulated the emergence of bubble-like voids with an internal fluid circulation as the third stage of bubble development. Bubble-like voids are seen in Figures 3, 4, and 5, but it is not known if internal fluid circulation occurred in these voids (although it seems reasonable to expect such a circulation). As noted by Anderson et al. (1995) and Duru & Guazzelli (2002), in a nonbubbling system, the rate at which particles enter the voids from the top exceeds the rate at which they leave the void at the bottom, hence the voids fill back.

In a bubbling system, more particles leave the void than enter, and the bubble becomes progressively more depleted of particles. Batchelor & Nitsche (1994) attributed this to the expulsion of particles from the buoyant blob by centrifugal action and referred to this expulsion as the fourth stage of bubble development. Glasser et al. (1997) sought to identify the parameter in the two-phase flow model that serves to differentiate between bubbling and nonbubbling systems. They concluded that the particle-phase pressure determined the critical bed expansion level above which nonuniform structures emerged, but not whether the system bubbled. On the other hand, the viscosity of the particle phase did not affect the critical bed expansion level, but rather contributed to the differentiation between bubbling and nonbubbling systems. Glasser et al. (1997) employed a closure of the form $\mu_s(\phi) = \Psi \rho_p u_t d_p \phi / (1 - (\phi/\phi_{cp})^{1/3})$, where Ψ was a parameter. This form differs from the expression deduced by Duru et al. (2002), but by comparing these two functional forms, $\Psi \approx 0.16$–0.20 for $0.50 < \phi < 0.60$. Glasser et al. (1997) also

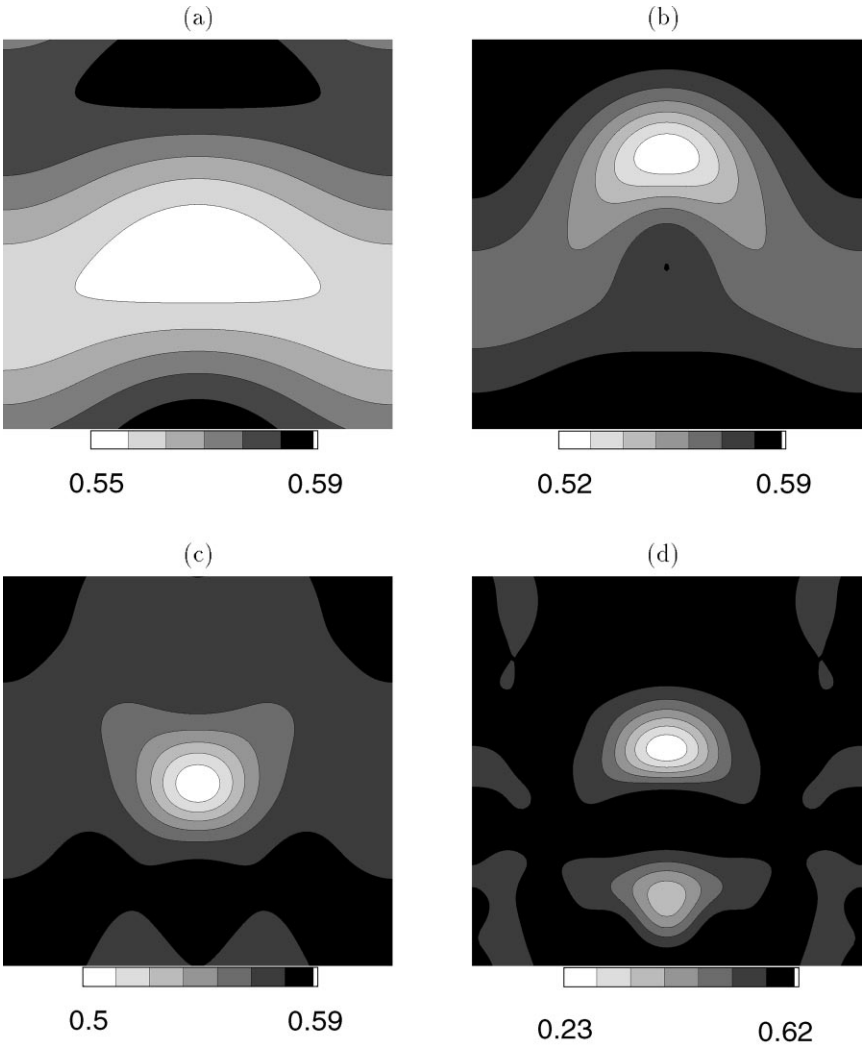

Figure 6 Grayscale plots showing the growth of a two-dimensional perturbation of the uniform state for 1-mm glass beads ($\rho_p = 2.2\ \mathrm{g \cdot cm^{-3}}$) fluidized by water. $\phi_o = 0.57$. Simulations were performed in a periodic box. Snapshots at four different times during the destabilization: (*a*) buckling of a 1-DTW, wave speed, $c = 0.201u_t$; (*b*) the formation of a bubble-like void that begins to accelerate, $c = 0.209u_t$; (*c*) depletion of particles in the void, leading to further acceleration, $c = 0.243u_t$; and (*d*) breakup of the void into two pieces, one of which begins to fade, while the other is still accelerating, $c = 0.262u_t$. The upper void is more depleted of particles, but it is also slowly shrinking. Source: Glasser et al. (1997). Reprinted with permission from The Cambridge University Press.

found that bubbles developed easily when $Fr_t \gg 100\Psi$ and that bubble-like voids appeared only briefly (if at all) when $Fr_t \ll 100\Psi$. Inserting the above estimate for Ψ, we get $Fr_t \approx 16$–20 as a rough cut-off separating bubbling and nonbubbling systems. Duru & Guazzelli (2002) found experimentally that beds with Fr_t of 12.8 and 3.58 bubbled and did not bubble, respectively. Although the estimate made by Glasser et al. (1997) is close, it is not satisfactory. The added mass term, not included in the analysis by Glasser et al., may be responsible for the discrepancy between the experiments and computations.

It will be interesting to conduct experiments of the type performed by Duru et al. (2002) and Duru & Guazzelli (2002) for gas-solid systems under reduced gravity conditions so that one can observe the evolution of nonuniform structures in them.

3. STUDIES ON GAS-SOLID SYSTEMS

Most gas-fluidized beds operate at a pressure of a few bars and employ 50–150-μm particles. For these particles, $St_m, St_t \gg 1$, and particle-particle collisions can occur readily. In a dense bed made up of such particles, the slip velocity is sufficiently small that $\mathrm{Re}_m \ll 1$, even though $\mathrm{Re}_t = \rho_f u_t d_p/\mu_f = O(10^{0-1})$. Therefore it seems reasonable to use the theory developed by Koch & Sangani (1999), which is valid for $St_t \gg 1$ and $\mathrm{Re}_t \ll 1$, to estimate the particle-phase pressure and viscosity (arising from hydrodynamically generated velocity fluctuations) in a uniform fluidized bed at moderate to high ϕ. Koch & Sangani (1999) concluded that when $St_t \gg 1$ and $\mathrm{Re}_t \ll 1$, and the particles are subject only to hydrodynamic interactions and fast binary collisions, an unbounded gas-fluidized bed is unstable except at the very dilute limit. However, it is now clear that contact stresses play an important role in generating an interval of stable bed expansion in commonly encountered gas-fluidized beds.

In his classic paper, Geldart (1973) classified gas-fluidized beds into four categories. Very fine particles (group C) are cohesive and are difficult to fluidize. Beds of somewhat larger particles (group A) manifest an interval of stable bed expansion before bubbling commences. Even larger particles (group B) bubble immediately after fluidization. Whereas typical, bubble rise velocities in beds of particles belonging to groups A and B are larger than the interstitial gas velocity in the dense phase, the opposite is true in beds of very large particles belonging to group D. As a consequence, the mixing pattern in bubbling beds of group-D particles differs significantly from those in bubbling beds of particles of groups A and B.

Geldart (1973) observed that the range of gas velocities for which stable bed expansion could be achieved for group-A particles decreased as the particle size was increased. He defined the A-B boundary as the locus of particle diameters for various gas-solid systems (simply characterized by $\rho_p - \rho_f$), where this window becomes unobservably small. The origin of stable bed expansion for group-A

particles in the interval (u_{mf}, u_{mb}), where u_{mb} is the gas superficial velocity at which bubbles first appear spontaneously and in a sustained manner, has been a subject of much debate (Jackson 2000). Rietema (1973), Mutsers & Rietema (1977a,b), and Rietema & Piepers (1990) attributed it to cohesive forces at particle-particle contact. Mutsers & Rietema (1977a) argued that their fluidization data obtained with various gases are consistent with a stabilizing force whose origin is enduring contact between particles. Although Rietema's papers were focused on cohesive force, we now know that cohesion per se is not required to generate a window of stable bed expansion and that a compressive yield strength that can arise simply because of frictional contact between particles in an assembly and wall friction is sufficient.

Tsinontides & Jackson (1993) fluidized cracking catalyst particles with dry and humid air. They also measured pressure drop and bed height as functions of gas flow rate as well as voidage variation as a function of bed depth at various gas flow rates. On the basis of these data and the hysteretic behavior recorded during fluidization and defluidization, they concluded that the bed exhibited yield stress throughout the range of stable bed expansion. Cody et al. (1996) measured acoustic shot noise in air-fluidized beds of Cataphote glass beads of various diameters (63–595 μm) and narrow size distributions and found the RMS fluctuating velocity of the particles to be essentially zero until the beds began to bubble. Diffusing wave spectroscopy measurements led Menon & Durian (1997) to the same conclusion. All these studies strongly point to yield stress resulting from sustained contact between particles as the most likely mechanism for stable bed expansion.

The manner in which the yield-stress characteristics of a given material change as one increases the particle size from group A to group B and the associated changes in the fluidization behavior have been studied by Loezos et al. (2002). Figure 7 shows the pressure drop and bed height in a 1.0″ ID tube as functions of gas (dry air) velocity for glass beads sieved between 58 and 75 μm. Starting from a fully defluidized bed, as the gas velocity, u, was increased from zero, an essentially linear relationship between pressure drop and u resulted in the fluidization branch, while the bed height remained constant. Then, at $u = u_c$, the pressure drop decreased abruptly and this was accompanied by a sudden increase in bed height. Tsinontides & Jackson (1993) have described the dynamics associated with this bed expansion in narrow tubes. The bed expansion begins with a lift-off and upward acceleration of the entire bed as a plug; as this plug rises, particles erode from the bottom, settle down on the distributor, and form a new bed.

For all the particles studied by Loezos et al. (2002), spanning average diameters in the range 63–210 μm, the maximum pressure drop achieved at u_c exceeded the bed weight per unit cross-sectional area (mg). Beyond $u = u_c$, the bed height increased steadily with u until u_{mb}. In the interval $u_c < u < u_{mb}$, the bed maintained a smooth appearance with no sustained bubbling.

These authors also performed identical experiments in 0.5″ and 2.0″ ID tubes and found that the pressure-drop overshoot decreased with increasing tube diameter, D. Indeed, the overshoot appeared to become essentially zero as $D \rightarrow \infty$

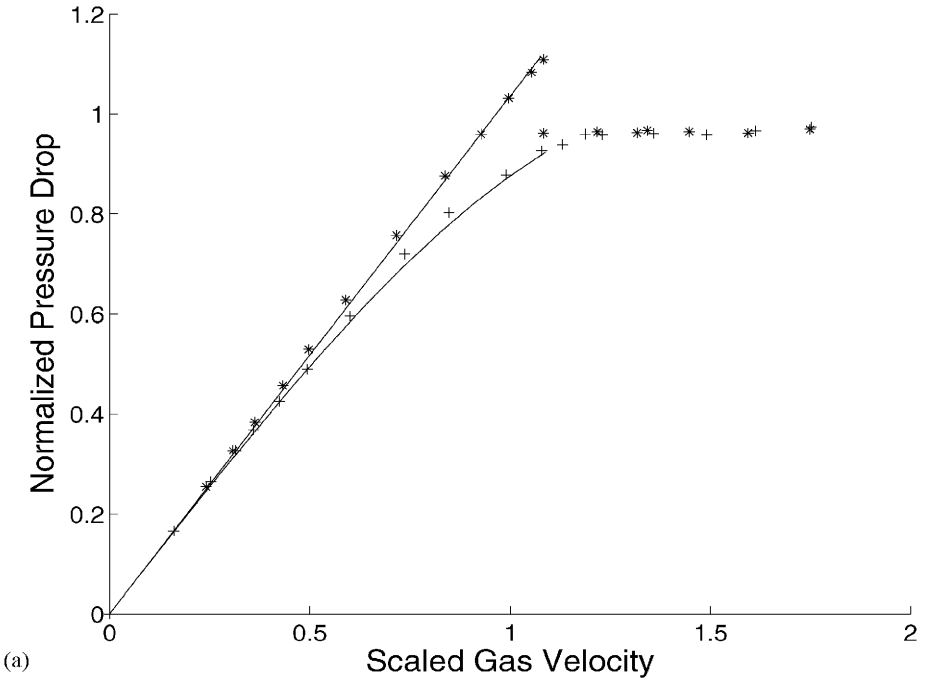
Normalized Pressure Drop
Scaled Gas Velocity
0
0.2
0.4
0.6
0.8
1
1.2
0.5
1.5
2

(a)

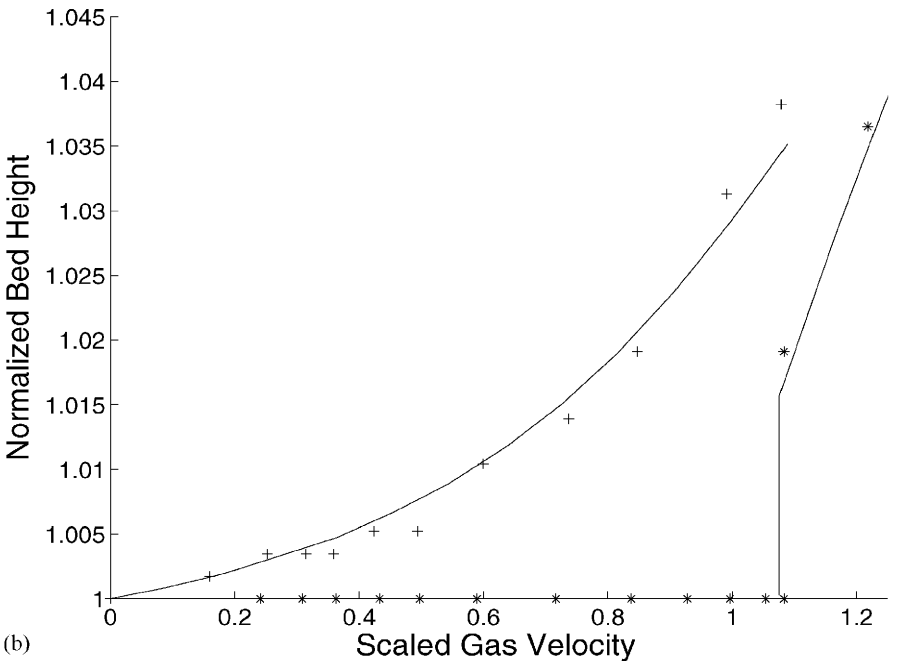
Normalized Bed Height
Scaled Gas Velocity
1
1.005
1.01
1.015
1.02
1.025
1.03
1.035
1.04
1.045
0.2
0.4
0.6
0.8
1
1.2

(b)

for all the particles, which led them to attribute the overshoot entirely to wall friction (see Figure 8). Tsinontides & Jackson (1993) found the overshoot to depend on tube diameter for fluid cracking catalyst (FCC) particles. Srivastava & Sundaresan (2002) found similar results for glass beads with a wide size distribution, a mean size of $\sim$50 μm, and a density of 2.35 g $\cdot$ cm^{-3}. In contrast, Valverde et al. (1998), who worked with very fine particles (discussed below), and Ojha et al. (2000) found the overshoot to be independent of tube diameter. So, additional work remains to be done before the effect of wall friction on pressure-drop overshoot can be established concretely.

Loezos et al. (2002) found the average solids fraction in the bed at u_{mb}, ϕ_{mb} to be roughly independent of tube diameter, suggesting that by the time the bed began to bubble freely the wall effect had become too small to have a measurable influence.

Starting from a bubbling bed, and by gradually decreasing the gas flow rate, Loezos et al. (2002) traced the behavior of the bed in the defluidization branch as well (see Figure 7). Within the confidence limits of their experiments, u_{mb} was the same in the fluidization and defluidization branches. As u was decreased below u_{mb}, the bed entered a regime of stable expansion. The bed height and pressure drop obtained in this range of stable bed expansion were very different in the fluidization and defluidization branches (see Figure 7). This behavior has been noted previously (see Tsinontides & Jackson 1993). Loezos et al. (2002) found the defluidization branches obtained with different tube diameters to be rather close, suggesting that wall friction played only a weak role in defluidization branch, in stark contrast to what was observed in the fluidization branch.

The hysteretic behavior displayed in Figure 7 has been examined in a much more detailed manner by Tsinontides & Jackson (1993). For example, they did a number of partial defluidization/fluidization cycles, where the gas flow rate was decreased gradually along the defluidization branch to some minimum (but nonzero) value and then increased gradually. Such experiments demonstrated unequivocally that bed characteristics including the particle-phase stress were path dependent and provided direct evidence that nonhydrodynamic stresses were involved in a significant way.

Jackson (1998, 2000) developed a one-dimensional model for pressure drop, bed expansion, and the particle-phase stress profile in a fluidized bed, allowing for particle-phase compressive yield stress and wall friction. He postulated that in the

←

Figure 7 (*a*) Normalized pressure drop ($\Delta p/mg$) versus scaled gas velocity (u/u_r). (*b*) Normalized bed height (H/H_o) versus scaled gas velocity (u/u_r). *, fluidization branch; +, defluidization branch. *mg* denotes weight of particle per unit cross-sectional area. u_r is a reference velocity (equal to 0.52 cm/s). Tube diameter = 1.0″. $u_c \approx 0.60$ cm/s. $u_{mb} \approx 0.62$ cm/s. $\phi_{mb} \approx 0.529$. Glass beads sieved between 58 and 75 μm. $\rho_p = 2.55$ g $\cdot$ cm^{-3}. Solid lines represent model predictions. Source: Loezos et al. (2002). Reprinted with permission from the authors.

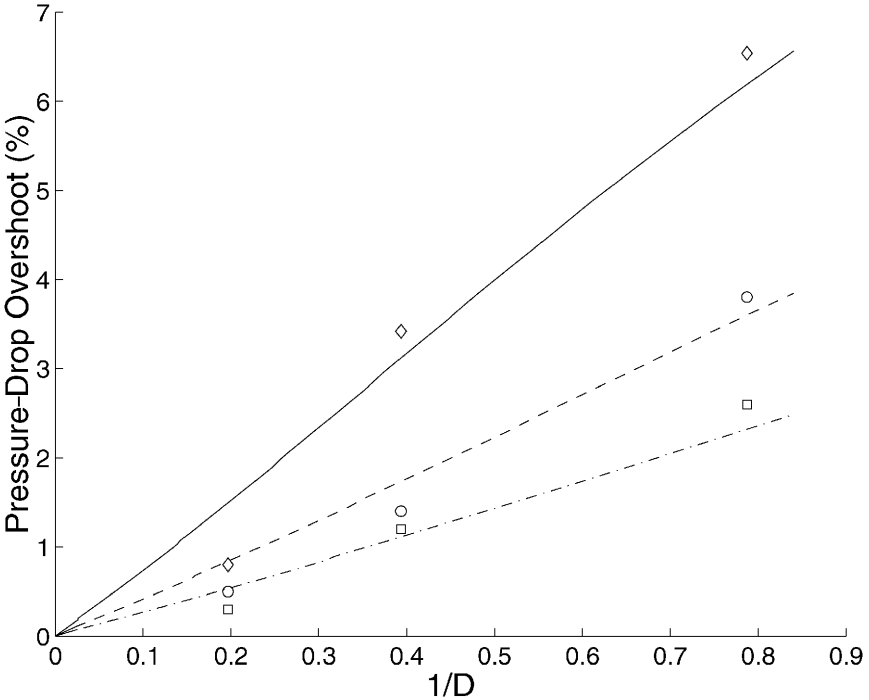

Figure 8 Pressure-drop overshoot (%) versus (1/D), where D is the tube diameter in centimeters. Cataphote particles. $\rho_p = 2.46\ \mathrm{g \cdot cm^{-3}}$. (◊) 63-$\mu$m data; (○) 88-$\mu$m data; (□) 105-$\mu$m data. Model predictions: (—) 63 μm; (- - -) 88 μm; (- · · ·) 105 μm. Source: Loezos et al. (2002). Reprinted with permission from the authors.

defluidization branch the particle assembly was at compressive yield everywhere and that a simple relationship existed between the particle-phase normal stress along the vertical direction, σ_s, and particle volume fraction, ϕ. In the packed-bed state of the fluidization branch (i.e., before the pressure-drop overshoot), the ϕ-profile was frozen, whereas the σ_s-profile was allowed to change with gas flow rate. [The same ideas, but without wall friction effects, were introduced by Tsinontides & Jackson (1993).]

For noncohesive particles, $u = u_c$ is defined as the condition when σ_s first becomes zero at the bottom of the bed (as u is gradually increased). Jackson (1998) demonstrated how wall friction could give rise to pressure-drop overshoot at $u = u_c$, even for noncohesive materials. For these materials, Jackson (1998) suggested that the bed height for $u > u_c$ in the fluidization branch could be estimated to a good approximation by simply treating this region as an ideal fluidized bed.

Loezos et al. (2002) found that all the trends observed in their experiments performed with a number of different particles (with size > 60 μm) and three different tube diameters could be captured reasonably well using Jackson's model

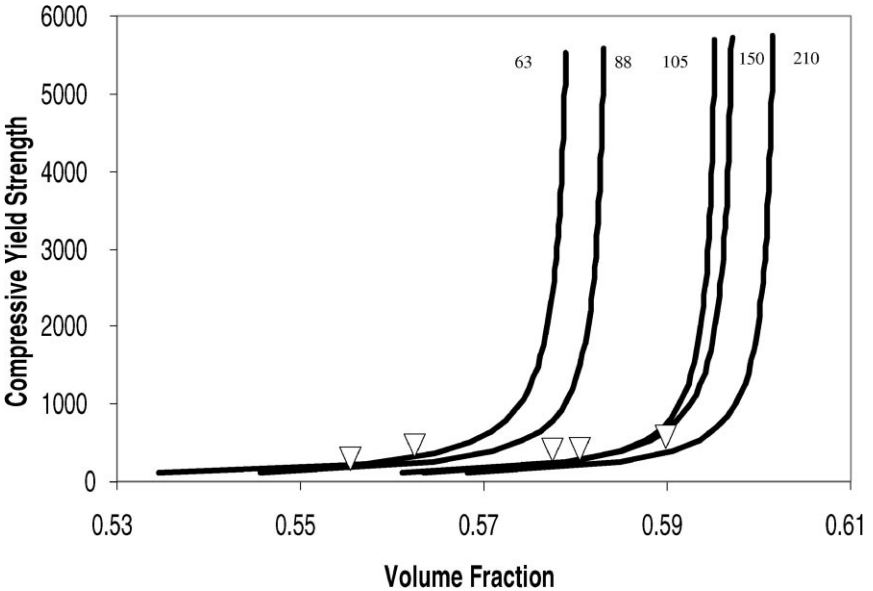

Figure 9 Compressive yield strength (in N/m^2) versus particle volume fraction, ϕ. Cataphote particles. $\rho_p = 2.46\ g \cdot cm^{-3}$. ($\Delta$) ϕ_{mb}. Source: Loezos et al. (2002). Reprinted with permission from the authors.

(see solid lines in Figures 7 and 8). These authors determined independently the compressive yield strength, $\sigma_c(\phi)$, of assemblies of the various particles used in their studies, using a method presented by Valverde et al. (1998). Figure 9 shows curve fits of the $\sigma_c(\phi)$ data by Valverde et al. for Cataphote glass beads of various diameters. At low ϕ values, σ_c is quite small; as ϕ increases, σ_c increases slowly at first and then very rapidly for all these particles. For this family of particles and another family of glass beads, the maximum value of ϕ achieved upon defluidization, $\phi_{\max}$, increases with particle diameter. In contrast, Ojho et al. (2000) found $\phi_{\max}$ to be 0.590 ± 0.004 independent of both tube diameter (0.5″, 1.0″ & 2.0″) and particle size (50–350 μm). Because of such variances between results reported by different research groups, very little can be said in a definitive manner at this stage about the dependence of $\phi_{\max}$ on d_p. The origin of this dependence on particle size, should this prove to be real, also remains to be understood.

We now return to the issue of stability of the bed against sustained bubbling. When the fluid density is much smaller than that of the particles, a uniformly fluidized bed of infinite extent is linearly stable (Jackson 2000) if

$$\left.\frac{dp_s}{d\phi}\right|_{\phi_o} > \rho_p u_t^2 n^2 \phi_o^2 (1-\phi_o)^{2(n-1)},$$

where ϕ_o is the particle volume fraction in the uniform state, n is the Richardson-Zaki (1954) index, and p_s is the reversible pressure (associated with the elastic deformation) of the particle phase. For elasto-plastic materials, one expects that

$$\frac{dp_s}{d\phi} > \frac{d\sigma_c}{d\phi}.$$

For hard particles, this inequality is expected to be a strong one (i.e., $\gg$). One can find an upper bound (ϕ_u) for the critical particle volume fraction (ϕ_{crit}) above which the uniform state is linearly stable by setting

$$\left.\frac{d\sigma_c}{d\phi}\right|_{\phi_u} = \rho_p u_t^2 n^2 (\phi_u)^2 (1-\phi_u)^{2(n-1)}.$$

Loezos et al. (2002) correlated their experimental data on compressive yield strength as

$$\sigma_c(\phi) = C\frac{(\phi-\phi_{\min})^a}{(\phi_{\max}-\phi)^b},$$

where C, a, b, $\phi_{\min}$, and $\phi_{\max}$ are positive adjustable parameters. They found that ϕ_u was only marginally higher than $\phi_{\min}$ for all the particles analyzed. Furthermore, the value of ϕ_{mb} recorded experimentally (*triangles* in Figure 9) was considerably larger than ϕ_u in every system, which further confirmed that the onset of bubbling in their system could not be captured by such a linear stability analysis. They also did not see stable expansion in any system at $\phi < \phi_{\min}$. These authors suggested that bubbling sets in when the yield stress in the bed has become small enough to be overcome by fluctuations in the gas flow rate (and hence gas drag), but a definitive explanation is still missing.

3.1. Cohesive Particles

We now return to fluidization-defluidization experiments and reexamine the pressure-drop overshoot observed at $u = u_c$. When the particles interact with each other and with the distributor plate cohesively, σ_s at the bottom of the bed must become sufficiently negative (i.e., tensile) to overcome this cohesion before the abrupt change at $u = u_c$ can occur. The larger the tensile stress is, the greater the pressure-drop overshoot at $u = u_c$ will be. There is some ambiguity as to what this tensile stress really represents. If the particle-particle cohesion is much stronger than that between the particle assembly and the distributor plate, the relevant cohesive stress is that resulting from the interaction between the particles and the distributor; in this case, the tensile stress extracted from the experiments simply provides a lower bound for the cohesive strength of the particle assembly. On the other hand, if the particle-distributor interaction is more cohesive than that between the particles, a monolayer (or a thin layer) of particles will remain stuck to the distributor, and the estimated tensile strength may be taken as a measure of the cohesive strength of the particles (Valverde et al. 1998). Tsinontides & Jackson

(1993) knew that the overshoot was partly due to wall friction and estimated an upper bound for the cohesive strength of the FCC particles used in their experiments by attributing the overshoot entirely to cohesion.

Valverde et al. (1998) performed extensive measurements on the compressive yield and tensile strengths of two different styrene-butadiene copolymer (xerographic toner) particles with average sizes of 8.5 and 12.7 μm. They measured the compressive yield strength of the particle assemblies at various volume fractions, $\sigma_c(\phi)$, by measuring the heights of defluidized beds containing various masses of particles. Such measurements performed in tubes of different cross-sectional areas did not reveal any systematic variation, although there was a fair amount of scatter when the data gathered in various tubes were plotted together. Therefore, Valverde et al. (1998) assumed that wall friction was negligible and attributed the entire pressure-drop overshoot upon fluidization to cohesive stress at the bottom of the bed. They observed that a layer of particles remained stuck to the distributor upon lift-off, concluded that the tensile stress is a measure of cohesion between the particles in the assembly, and used the pressure-drop overshoot to estimate the tensile strength of the assembly at different volume fractions, $\sigma_t(\phi)$. They examined the effect of adding various amounts of fine silica particles on $\sigma_c(\phi)$ and $\sigma_t(\phi)$ for assemblies of toner particles. The silica nano-particles formed 40–60-nm agglomerates, which, in turn, adhered to the polymer particles. The effect of these silica agglomerates on the toner particles was to alter the effective interaction between the polymer particles, and this was reflected in a systematic variation of $\sigma_c(\phi)$ and $\sigma_t(\phi)$ with the level of silica addition. In particular, silica decreased the level of cohesive interaction between particles, which allowed the toner particles to pack at a higher ϕ for a given compaction stress. Valverde et al. (1998) also found the tensile strength to be proportional to consolidation stress for all the samples, and $\sigma_t(\phi)/\sigma_c(\phi)$ decreased steadily with increasing silica content. This paper is an excellent demonstration of the use of fluidization measurements to learn about the particle-particle interactions. In particular, the experiments with different levels of silica on the toner particles illustrate the relevance of nonhydrodynamic stresses in fluidization.

In summary, Koch & Sangani (1999) concluded that hydrodynamically generated stresses are not strong enough to stabilize an unbounded, homogeneous gas-fluidized bed except at very dilute conditions. Experiments by Mutsers & Rietema (1977a), Rietema & Piepers (1990), Tsinontides & Jackson (1993), Cody et al. (1996), Menon & Durian (1977), and Loezos et al. (2002) indicate that nonhydrodynamic stresses are responsible for stable bed expansion in gas-fluidized beds with particles of sizes greater than about 60 μm. However, recent results by Valverde et al. (2001) seem to suggest that in gas-fluidized beds of finer particles there exists a window of bed expansion where the bed manifests a smooth appearance to the eye while the particles are highly mobile.

Valverde et al. (2001) fluidized with dry nitrogen a mixture of yellow and magenta toner particles with an average diameter of 8.53 ± 2.53 μm in a rectangular fluidized bed. The particles tended to form aggregates, so the effective aggregate

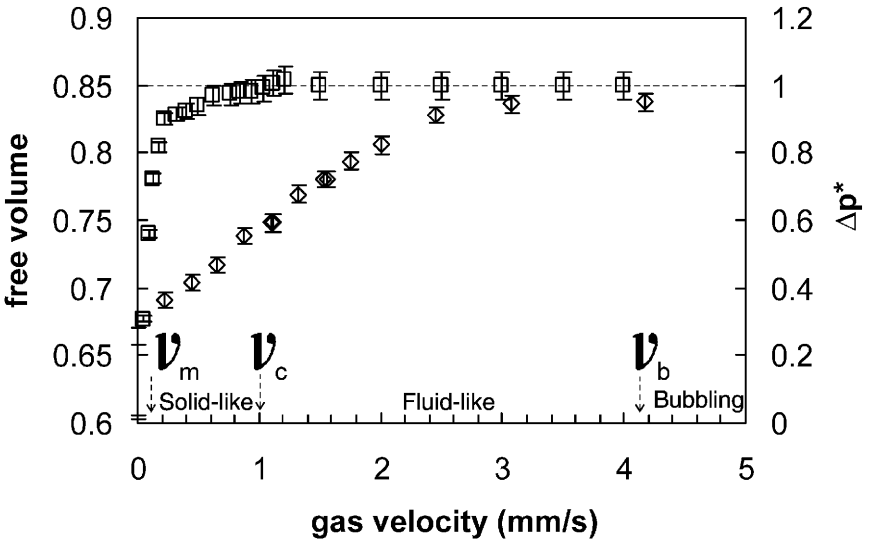

Figure 10 Behavior of a fluidized bed composed of 50% magenta and 50% yellow toner particles. The gas pressure drop (□) is normalized by bed weight per unit cross-sectional area. Average primary particle diameter = 8.53 μm. $\rho_p = 1.199\ \mathrm{g \cdot cm^{-3}}$. Free volume (◊) is the bed voidage. v_m, v_c, and v_b denote gas velocities at which regime transition occurs. Source: Valverde et al. (2001).

size of the particles is larger. Figure 10 shows the pressure drop and free volume (i.e., voidage) as functions of gas velocity in the defluidization branch (the fluidization branch was not reported). They also determined the diffusion coefficient of the magenta particles (see Figure 11). The pressure drop across the bed was essentially equal to the weight of the bed per unit cross-sectional area for 1 mm/s $< u <$ 4 mm/s, where the bed maintained a homogeneous appearance and expanded smoothly with increasing u (see Figure 10). In this region, the scaled diffusivity $D^* = (D/ud_p)$ increased with u almost exponentially at first and then reached a plateau value (see Figure 11). In contrast, for $u <$ 1 mm/s, the pressure drop was less than bed weight per unit cross-sectional area, and the diffusivity was essentially zero. Based on the diffusivity data, these authors labeled the regions $u <$ 1 mm/s and 1 mm/s $< u <$ 4 mm/s as solid-like and fluid-like, respectively. The bed bubbled visibly for $u >$ 4 mm/s.

Figure 12, supplied by J.M. Valverde, M.A.S. Quintanilla & A. Castellanos (private communication), reveals another interesting feature; this figure shows the average solids fractions in two different fluidized beds as functions of gas velocity. Toner particles (15.4 μm) having two different levels of surface coverage with silica nano-particles were examined in these experiments. Both beds manifested solid-like, fluid-like, and bubbling regions. As noted earlier, the higher the silica content, the less cohesive the particles are and the smaller σ_c at a given value of

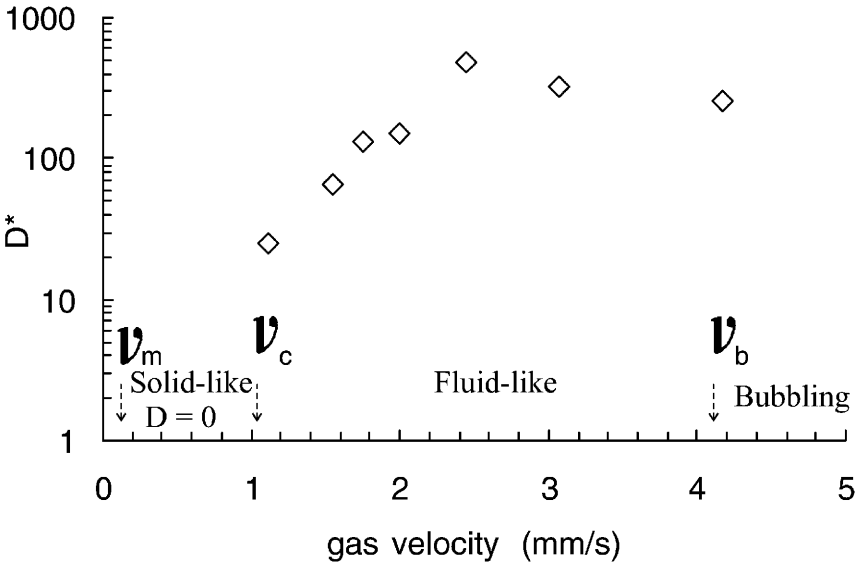

Figure 11 Dimensionless diffusion coefficient, $D^* = (D/ud_p)$, as a function of gas velocity estimated from the mixing of the magenta toner particles. Here D denotes diffusivity, u is gas velocity, and d_p is primary particle diameter. Particle properties are as in Figure 10. Source: Valverde et al. (2001).

ϕ is; therefore, the bed of particles having a higher silica content packed more compactly in the solid-like region (see Figure 12). The behavior was opposite in the fluid-like region (where permanent networks were broken), which may be rationalized as follows: The toner particles with a lower silica content would form larger aggregates, and the drag on the larger agglomerates would be smaller, so the bed expansion would be smaller for the bed with a lower silica content. This crossover of the bed-expansion characteristics across the boundary separating the solid-like and fluid-like regions appears to corroborate further a change in the structure of the particle assembly across this boundary. Castellanos et al. (2001) estimated that the agglomerates had a fractal structure and their size was in the range of 30–45 μm. It will be revealing to perform experiments with primary nonagglomerating particles in this size range and contrast their behavior with those of a bed of agglomerated particles.

Let us set aside for the moment the cohesive interaction between the agglomerates and simply look at the stability problem on the basis of a Froude number criterion. For 30- and 45-μm agglomerates with an effective density 0.72 g $\cdot$ cm^{-3}, where it has been assumed that the porosity of the agglomerates are $\sim$40%, the terminal settling velocities are $\sim$2 and 4.4 cm/s, respectively. Fr_t for these agglomerates are then $\sim$1.4 and 4.4 cm/s, respectively. The data on liquid-fluidized beds by Duru & Guazzelli (2002) suggest that such beds fall in the nonbubbling

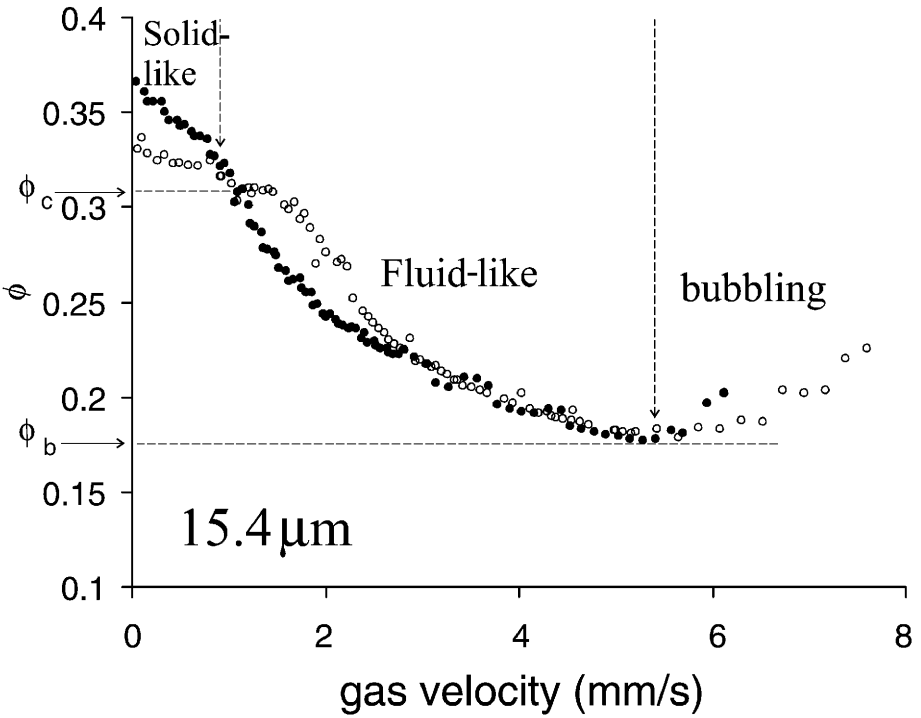

Figure 12 Particle volume fraction, ϕ, versus superficial gas velocity. Approximate surface coverage of silica agglomerates over the polymer toner particles: (●) 32%; (○) 8%. Volume fractions at the regime transitions are marked in the figure. Average toner particle size is 15.4 μm. Source: J.M. Valverde, M.A.S. Quintanilla & A. Castellanos (private communication).

category but will manifest spatiotemporal structures. Indeed, very recent fiber-optic probe measurements by Valverde et al. (2002) reveal small-scale spatiotemporal structures in the fluid-like region, whose characteristic temporal frequency gradually increases with gas velocity. Thus, even though the bed manifested a smooth appearance (to the naked eye) in the fluid-like region (Valverde et al. 2001), it may not be truly stable after all. This, however, does not explain why visible bubbles appear at higher gas velocities (see Figure 10). In any case, there is much still to be learned from careful measurements of the behavior of gas-fluidized beds of particles in the 10–60-μm range.

As was mentioned in the Introduction, a number of researchers have attempted to explain the distinction between bubbling and nonbubbling systems through a linear stability analysis of the uniformly fluidized state. This article focuses on nonlinear effects, where the linear stability analysis is either inadequate to get the full picture (as in the liquid-fluidized beds) or inapplicable (as in the case of gas-solid systems

where yield stresses are present). It would, however, be incomplete to close the review without drawing attention to a puzzling criterion for instability deduced by Foscolo & Gibilaro (1984) through a linear stability analysis. These authors argued that the fluid-particle drag force should include a (stabilizing) term proportional to the gradient in the voidage; however, the physical basis for such a term has been questioned (Batchelor 1988). Using this term and no other terms for hydrodynamic or nonhydrodynamic particle-phase pressure, the following condition was obtained for instability of a uniform state at $\phi = \phi_o$:

$$\left(\frac{\rho_p - \rho_f}{\rho_p Fr_t}\right)^{1/2} < 0.56 n \phi_o^{1/2} (1 - \phi_o)^{n-1}.$$

The right-hand side of this inequality vanishes for $\phi_o = 0$ and 1 and assumes its maximum value ($\mathrm{RHS_{max}}$) at some intermediate ϕ_o value. If $\mathrm{RHS_{max}}$ is smaller than the left-hand side of the inequality, the bed is stable (according to this criterion) for all ϕ_o values; however, some liquid-fluidized beds, which are predicted to be stable by this condition, manifest primary instability leading to voidage waves (e.g., see Tsinontides & Jackson 1993). When $\mathrm{RHS_{max}}$ is larger than the left-hand side of the above inequality, there exists a range of ϕ_o values, $\phi_{low} < \phi_o < \phi_{up}$, for which the bed is unstable. If $\phi_{up} < \phi_{mf}$, then there will be a window of stable bed expansion past the point of incipient fluidization. A criterion for the Geldart A-B transition may then be deduced by demanding that $\phi_{up} = \phi_{mf}$, i.e.,

$$\left(\frac{\rho_p - \rho_f}{\rho_p Fr_t}\right)^{1/2} = 0.56 n \phi_{mf}^{1/2} (1 - \phi_{mf})^{n-1}.$$

This criterion lies in the general vicinity of the empirical A-B transition of Geldart (1973), which is a surprising finding. Given that all the experimental evidence points to the presence of appreciable yield stress in the window of stable bed expansion, it is really puzzling how a criterion that does not address yield stress at all can come so close to capturing the A-B transition.

4. SUMMARY

This review focuses specifically on dense fluidized beds, i.e., beds with a high volume fraction of solids. There is much interest in the nature of the instabilities and structures observed in suspensions at low and intermediate levels of particle loading (e.g., see Agrawal et al. 2001), but these are not discussed here.

Experiments probing the nature of the voidage waves in liquid-fluidized beds have been instrumental in establishing that one-dimensional traveling waves first emerge as manifestations of primary instability then develop into two-dimensional structures. The manner in which nonuniform structures evolve beyond that stage depends (at least) on the Froude number. Computational studies do seem to capture these features qualitatively. The stages of bubble evolution beyond the initial evolution of the two-dimensional structure are also understood reasonably well. But

quantitative prediction remains elusive. This is due to the limited progress in the development of theories for particle-phase stresses in fluidized suspensions. The bulk of the theoretical advances on hydrodynamically generated stresses come from the work by Koch & Sangani, which is restricted to $\mathrm{Re}_t \ll 1$ and $St_t \gg 1$. Every liquid-fluidized bed experiment, where one has probed the evolution of nonuniform structure, lies outside this restricted range of Re_t and St_t. Closures for the hydrodynamic stresses when $\mathrm{Re}_t \approx O(1)$ or larger are sorely needed.

It appears that the hydrodynamically generated stresses need to be supplemented with nonhydrodynamic contact stresses to get a truly stable fluidized bed, but a definitive statement cannot be made at this time. Closures for the stresses, when collisional interaction between particles is supplemented with a combination of short- and long-lived particle networks, are also needed.

The theory by Koch & Sangani (1999) indicates that commonly encountered gas-fluidized beds cannot be stabilized purely by hydrodynamically generated stresses. There is ample experimental data showing that beds with solid particles whose size is larger than $\sim$60 μm manifest a window of stable expansion only when contact stresses are important. In this region of stable bed expansion, the particles are essentially immobile.

Gas-fluidized beds of much smaller particles, where cohesive interactions become important and particles form agglomerates, seem to manifest a window of expansion where the particles are mobile and small-scale flow nonuniformities exist. At larger gas flow rates, these beds bubble. Much remains to be learned about the mechanics of such beds.

ACKNOWLEDGMENTS

I am grateful to P. Duru, E. Guazzelli, J.M. Valverde, and A. Castellanos for sharing preprints of their recent research and supplying the figures.

The *Annual Review of Fluid Mechanics* is online at http://fluid.annualreviews.org

LITERATURE CITED

Agrawal K, Loezos PN, Syamlal M, Sundaresan S. 2001. The role of meso-scale structures in rapid gas-solid flows. *J. Fluid Mech.* 445: 151–85

Anderson TB, Jackson R. 1967. Fluid mechanical description of fluidized beds. Equations of motion. *Ind. Eng. Chem. Fundam.* 6:527–39

Anderson TB, Jackson R. 1968. Fluid mechanical description of fluidized beds. Stability of the state of uniform fluidization. *Ind. Eng. Chem. Fundam.* 7:12–21

Anderson TB, Jackson R. 1969. Fluid mechanical description of fluidized beds. Comparison of theory and experiments. *Ind. Eng. Chem. Fundam.* 8:137–44

Anderson K, Sundaresan S, Jackson R. 1995. Instabilities and the formation of bubbles in fluidized beds. *J. Fluid Mech.* 303:327–66

Batchelor GK. 1988. A new theory of the instability of a uniformly fluidized bed. *J. Fluid Mech.* 193:75–110

Batchelor GK. 1993. Secondary instability of a gas-fluidized bed. *J. Fluid Mech.* 257:359–71

Batchelor GK, Nitsche JM. 1991. Instability of a stationary unbounded stratified fluid. *J. Fluid Mech.* 227:357–91

Batchelor GK, Nitsche JM. 1993. Instability of a stratified fluid in a vertical cylinder. *J. Fluid Mech.* 252:419–48

Batchelor GK, Nitsche JM. 1994. Expulsion of particles from a buoyant blob in a fluidized bed. *J. Fluid Mech.* 278:63–81

Campbell CS, Wang DG. 1991. Particle pressures in gas-fluidized beds. *J. Fluid Mech.* 227:495–508

Castellanos A, Valverde JM, Quintanilla. 2001. Aggregation and sedimentation in gas-fluidized beds of cohesive powders. *Phys. Rev. E* 64:041304

Cody GD, Goldfarb DJ, Storch GV, Norris AN. 1996. Particle granular temperature in gas-fluidized beds. *Powder Technol.* 87:211–32

Didwania AK, Homsy GM. 1981. Flow regime and flow transitions in liquid-fluidized beds. *Int. J. Multiph. Flow* 7:563–80

Duru P, Guazzelli E. 2002. Experimental investigation of a secondary instability of liquid-fluidized beds and the formation of bubbles. *J. Fluid Mech.* Submitted

Duru P, Nicolas M, Hinch J, Guazzelli E. 2002. Constitutive laws in liquid-fluidized beds. *J. Fluid Mech.* 452:371–404

El-Kaissy MM, Homsy GM. 1976. Instability waves and the origin of bubbles fluidized beds. Part 1: experiments. *Int. J. Multiph. Flow* 2:379–95

Foscolo PU, Gibilaro LG. 1984. A fully predictive criterion for the transition between particulate and aggregative fluidization. *Chem. Eng. Sci.* 39:1667–75

Garg SK, Pritchett JW. 1975. Dynamics of gas-fluidized beds. *J. Appl. Phys.* 46:4493–500

Geldart D. 1973. Types of gas fluidization. *Powder Technol.* 7:285–92

Glasser BJ, Kevrekidis IG, Sundaresan S. 1996. One- and two-dimensional traveling wave solutions in gas-fluidized beds. *J. Fluid Mech.* 306:183–221

Glasser BJ, Kevrekidis IG, Sundaresan S. 1997. Fully developed traveling wave solutions and bubble formation in fluidized beds. *J. Fluid Mech.* 334:157–88

Göz MF. 1995. Transverse instability of plane voidage wavetrains in gas-fluidized beds. *J. Fluid Mech.* 303:55–81

Ham JM, Thomas S, Guazzelli E, Homsy GM, Anselmet MC. 1990. An experimental study of the stability of liquid-fluidized beds. *Int. J. Multiph. Flow* 16:171–85

Homsy GM. 1998. Nonlinear waves and the origin of bubbles in fluidized beds. *Appl. Sci. Res.* 58:251–74

Jackson R. 1963. The mechanics of fluidized beds. *Trans. Inst. Chem. Eng.* 41:13–28

Jackson R. 1998. The nature and role of effective stress in fluidized systems. In *Fluidization IX*, ed. LS Fan, TM Kowlton, pp. 1–13. Charlottesville, VA: Eng. Found. Publ.

Jackson R. 2000. *Dynamics of Fluidized Particles*. Cambridge, MA: Cambridge Univ. Press

Koch DL, Sangani AS. 1999. Particle pressure and marginal stability limits for a homogeneous monodisperse gas fluidized bed: kinetic theory and numerical simulations. *J. Fluid Mech.* 400:229–63

Loezos PN, Costamagna P, Sundaresan S. 2002. The role of contact stresses and wall friction on fluidization. *Chem. Eng. Sci.* In press

Menon N, Durian DJ. 1997. Particle motions in a gas-fluidized bed of sand. *Phys. Rev. Lett.* 79:3407–10

Mutsers SMP, Rietema K. 1977a. Gas-solid fluidization in a centrifugal field. The effect of gravity upon bed expansion. *Powder Technol.* 18:249–56

Mutsers SMP, Rietema K. 1977b. The effect of inter-particle forces on the expansion of a homogeneous gas-fluidized bed. *Powder Technol.* 18:239–48

Ojha R, Menon N, Durian DJ. 2000. Hysteresis and packing in gas-fluidized beds. *Phys. Rev. E* 62:4442–45

Richardson JF, Zaki WN. 1954. Sedimentation and fluidization. Part 1. *Trans. Inst. Chem. Eng.* 32:35–53

Rietema K. 1973. The effect of interparticle forces on the expansion of a homogeneous

gas-fluidized bed. *Chem. Eng. Sci.* 28:1493–97

Rietema K, Piepers HW. 1990. The effect of inter-particle forces on the stability of gas-fluidized beds. I. Experimental evidence. *Chem. Eng. Sci.* 45:1627–39

Savage SB. 1998. Analyses of slow high-concentration flows of granular materials. *J. Fluid Mech.* 377:1–26

Srivastava A, Sundaresan S. 2002. Role of wall friction in fluidization and standpipe flow. *Powder Technol.* 124:45–54

Tsinontides SC, Jackson R. 1993. The mechanics of gas-fluidized beds with an interval of fluidization. *J. Fluid Mech.* 255:237–74

Valverde JM, Castellanos A, Quintanilla MAS. 2001. Self-diffusion in a gas-fluidized bed of fine powder. *Phys. Rev. Lett.* 86:3020–23

Valverde JM, Quintanilla MAS, Castellanos A, Mills P. 2002. Experimental study on the dynamics of gas-fluidized beds. *Phys. Rev. Lett.* Submitted

Valverde JM, Ramos A, Castellanos A, Watson PK. 1998. The tensile strength of cohesive powders and its relationship to consolidation, free volume and cohesivity. *Powder Technol.* 97:237–45

Wilhelm RH, Kwauk M. 1948. Fluidization of solid particles. *Chem. Eng. Prog.* 44:201–18

Zenit R, Hunt M, Brennen CE. 1997. Collisional particle pressure measurements in solid-liquid flows. *J. Fluid Mech.* 353:261–83

Zenit R, Hunt ML. 2000. Solid fraction fluctuations in solid-liquid flows. *Int. J. Multiph. Flow* 26:763–81

Coarse-grid simulation of reacting and non-reacting gas-particle flows

Final Technical Report

Award # DE-FC26-00NT409071

DOE Vision 21 Virtual Demonstration Initiative

Appendix C

Coarse-grid Simulation of Gas-Particle Flows in Vertical Risers

Arthur T. Andrews IV, Peter N. Loezos and Sankaran Sundaresan*

Princeton University

Princeton, New Jersey

Submitted for Publication to I & EC Research

August 2004

*Address correspondences to Sundaresan: sundar@princeton.edu

Abstract

It is well known that continuum model equations for unsteady gas-particle flows in devices such as fluidized beds and circulating fluidized bed risers contain unstable modes whose length scale is of the order of ten particle diameters. Yet, because of limited computational resources, these flows are routinely simulated by solving the discretized version of continuum models over coarse spatial grids. These simulations resolve the large-scale flow structures, but not the finer scale structures. In most industrial applications involving large devices, it is impractical to resolve all the fine-scale structures and therefore the effects of the unresolved structures must be addressed through suitable sub-grid models. Using gas-particle flows in a wide and very tall vertical channel as an example, we have demonstrated in this study that the results obtained in coarse-grid integration of the microscopic equations for gas-particle flows change appreciably if sub-grid corrections to account for the effects of unresolved structures are included. The addition of a simple time-averaged sub-grid model for the effective drag coefficient, and particle phase viscosity and pressure led to a qualitative change in the simulation results. Our simulations revealed a lack of separation of time scales between the resolved and unresolved structures. This led us to formulate a stochastic sub-grid model for the drag coefficient and investigate its consequence. The addition of a stochastic correction made quantitative, but not qualitative, changes to the simulation results.

Keywords: riser flow, gas-particle flow, kinetic theory, CFD, sub-grid model, simulation

Introduction

It is well known that gas-particle flows in vertical risers are inherently unstable, and that they manifest fluctuations over a wide range of length and time scales. There is a substantial body of literature where researchers have sought to capture these fluctuations through numerical simulation of continuum equations for gas-particle flows.[1-17] It is well known that continuum models for such flows, coupled with either simple phenomenological closures for drag and effective stresses[18] or closures obtained by extending the kinetic theory of granular materials to account for the presence of the interstitial fluid,[9,19,20] reveal unstable modes whose length scale is as small as ten particle diameters. Yet, because of limited computational resources, riser flows in large units are routinely simulated by solving discretized versions of the continuum models over a coarse spatial grid. Such coarse grid simulations do not resolve the small-scale spatial structures which, according to the continuum equations, do indeed exist. The accuracy of these simulation results is therefore questionable.[21] Such unresolved structures commonly arise in single phase turbulent flow, where large eddy simulations strive to incorporate the influence of the unresolved structures on those resolved in the simulations through sub-grid models; however, such sub-grid corrections have not received much attention in the context of heavily loaded gas-particle flows. Our study is aimed at exposing the most important ingredients of sub-grid models for coarse-grid simulation of typical circulating fluidized bed riser flows.

Agrawal *et al.*[20] have examined in detail the fate of a uniform suspension of particles fluidized by a gas through highly resolved simulations of continuum model

equations in two-dimensional and three-dimensional periodic domains, whose size is of the order of the typical grid sizes employed in coarse-grid simulation of large scale risers and fluidized beds. In their analysis, they employed a kinetic theory closure for the particle phase stress,[9,19,22] and a drag force model proposed by Wen & Yu.[23] They found that the uniformly fluidized state was unstable and that it quickly gave way to persistent, time-dependent, mesoscale structures, which assumed the form of clusters and streamers at low particle volume fractions and bubbles at high particle loadings. They found that the effective drag coefficient obtained by averaging the results over the periodic domain (a) was appreciably smaller than that corresponding to a homogeneous state, (b) was dependent on the size of the domain and (c) manifested a rather complex, but understandable dependence on particle volume fraction. They also found that the effective viscosity of and the normal stresses in the particle phase obtained by averaging over the mesoscale structures were (a) appreciably larger than those corresponding to the homogeneously fluidized state (given by the kinetic theory), and (b) depended on the size of the domain. Based on these findings, they concluded that unresolved mesoscale structures could contribute appreciably to results predicted by coarse-grid simulations.

The purpose of the present study is to investigate the influence of sub-grid models on the results obtained in coarse-grid simulations. We will demonstrate in this paper that one must include sub-grid corrections (for drag coefficient and particle phase effective viscosity and pressure), and that because of a lack of separation of time scales between resolved and unresolved structures one should, in a strict sense, employ stochastic sub-grid models. However, simple deterministic sub-grid models seem to capture much of the large-scale flow structures obtained with stochastic sub-grid models.

It is appropriate to mention, at least in passing, that it has long been recognized in industrial practice that CFD simulations based on averaged equations of motion underestimate the holdup in fluidized beds and riser flows, unless an apparent particle cluster size, which is typically two to ten times the true size of the particles, is used in the calculations. Such a larger cluster size leads to a smaller drag coefficient than what would be obtained if the true particle size is employed. Thus, one can indeed view the use of an apparent particle cluster size as a simple sub-grid model for the drag coefficient. Apparent cluster size is sometimes used as a tuning parameter to match the simulation results with experimental data.[24] A method to estimate the cluster size via an energy-minimization-multi-scale model has been presented in the literature recently.[25] Our study differs from these approaches in the sense that we have focused on identifying the relationship between the level of sophistication of the sub-grid models and the results obtained in coarse grid simulations.

Approach to coarse-grid simulations

The purpose of the simulations described in this study is to examine the flow behavior of a gas-particle suspension in a vertical channel, whose geometrical details are presented later. The starting point of the analysis is a kinetic theory based continuum model for gas-particle flow, see Table 1 (and appendix A for a brief description). A detailed discussion of these equations can be found in Agrawal *et al*.[20] and will not be repeated here. This model consists of continuity and momentum equations for the gas and particle phases, and an additional scalar equation for the fluctuation energy per unit mass of the particle phase. Henceforth, we will refer to these equations as microscopic (or kinetic theory) equations. Table 2 shows typical particle and gas properties. According to

this system of microscopic equations, homogeneously fluidized suspensions (with properties shown in Table 2) are unstable with dominant instabilities occurring at a length scale of the order of ten particle diameters.[26] We consider only those situations, where the dimensions of the riser are too large to make numerical simulations with grid sizes of the order of ten particle diameters impractical even in two-dimensional simulations. (Virtually every commercial or medium-scale pilot unit falls in this category.) Consequently, if one carries out coarse-grid integration of these microscopic equations employing a practically affordable grid resolution, there are bound to be small structures which have not been resolved and whose influence is not properly recognized in the simulations. This rather obvious point is well known in the literature on single-phase turbulent flow and turbulent flow with very dilute loading of particles. Yet, very little has been done about the sub-grid scale modeling in the context of densely loaded gas-particle flows. (In fact, the very need for sub-grid models has not been widely recognized and discussed.) In this manuscript we compare results obtained in simulation of the microscopic equations discretized using coarse grids with those obtained in coarse grid simulations where the microscopic equations have been augmented with sub-grid models of different levels of sophistication. A question of fundamental importance in two-phase flows problems is the accuracy of the postulated microscopic equations in capturing the microscale physics behind the flow. [The present study does not address this question. Instead, we begin with a reasonable set of microscopic equations developed in the literature, which captures the known instabilities in simple test problems, and examine issues associated with the integration of this *given* set of equations using coarse grids.]

Agrawal *et al.*[20] have already pointed out that the origin of the small-scale structures in gas-particle flows through risers is very different from those in single-phase turbulent flow. In the latter, the small-scale eddies are dissipative and are largely sustained by energy cascade from larger eddies. In contrast, small-scale structures arise in riser flows primarily through local instabilities associated with fluidization; energy to sustain these structures comes largely from the mean relative motion between the particle and gas phases. Consequently, one should not directly apply the sub-grid models, which have been developed in single-phase turbulent flows, to the riser flow problem. Agrawal *et al.*[20] proposed a simple, preliminary approach where highly resolved simulations of the microscopic equations are performed in small periodic domains which are commensurate with the grid sizes to be used in the coarse-grid simulations. This is precisely the approach we have examined here.

Although all the results will be presented in dimensionless form, it is useful to first present some quantities, such as riser dimensions and typical grid size that would be employed in coarse grid simulations, to motivate the specific combination of dimensionless variables employed in our test simulations. The vertical channel through which the gas-particle mixture flows is 76 cm wide and 30 m tall. In the coarse-grid simulation of flow described in this manuscript, the riser is discretized using 2 cm x 8 cm grids. These are fairly typical of industrial scale risers whose diameters range from 0.5 – 2.0 m and height ranges from 20 – 90 m. Three-dimensional simulations invariably employ even coarser grids.

The microscopic equations were made dimensionless using particle density (ρ_s), terminal velocity $\left(v_t\right)$ and $\left(\frac{v_t^2}{g}\right)$ as characteristic density, velocity and length (as in Agrawal *et al.*[20]). It then follows that the characteristic time and stress are $\left(\frac{v_t}{g}\right)$ and $\left(\rho_s v_t^2\right)$, respectively. The particle size then appears in the microscopic equations as $\frac{dg}{v_t^2}\left(=\frac{1}{Fr_p}\right)$. The aspect ratio of the grid, vertical height $\left(\Delta_v\right)$ / horizontal width $\left(\Delta_h\right)$, is A. The width of the grid in dimensionless form is $\frac{\Delta_h g}{v_t^2}\left(=\frac{1}{Fr_h}\right)$. Using the dimensional quantities presented above as an illustration, A = 4, Fr_p ~ 65 and Fr_h ~ 0.2434. The larger the difference between Fr_p and Fr_h, the more important the contributions of the sub-grid corrections will be. Indeed, Agrawal et al.[20] found that as Fr_h decreased, the effects of the mesoscale structures assumed greater and greater importance.

Simulations to estimate sub-grid corrections

Agrawal *et al.*[20] proposed that, as an initial approach to constructing sub-grid models, one perform highly resolved simulations of the microscopic equations in small periodic domains, whose dimensions are commensurate with the grid dimensions of the planned coarse-grid simulations. Such calculations begin with a uniformly fluidized suspension of particles, and simulate the evolution of non-uniform structures through instabilities inherent to the fluidization problem. Details of such simulations are described in Agrawal *et al.*,[20] and will not be repeated here. We simply note that the computations

were performed using the MFIX code,[27,28] which is based on discretization using staggered Cartesian grids and a finite volume method. Spatial and temporal derivatives were approximated using a second order discretization scheme and an implicit Euler scheme, respectively. As non-uniform structures evolve, the gas will bypass regions rich in particles, and the domain-averaged slip velocity between the gas and the particles (defined as the difference between domain average values of volume fraction-weighted gas and particle phase velocities) required to support the weight of the particles will take on a larger value than that for the uniformly fluidized state. The non-uniform structures are dynamic in nature, and so will the domain-average slip velocity be. This is illustrated in Figure 1, which presents the instantaneous domain-averaged dimensionless slip velocity as a function of dimensionless time in one such periodic domain calculation. In such simulations, the pressure drop across the bed is chosen to balance the weight of the suspension, and therefore the instantaneous domain-averaged dimensionless drag coefficient (defined such that the domain-averaged dimensionless drag coefficient multiplied by the domain-averaged dimensionless slip velocity is simply the effective dimensionless drag force per unit volume in the domain) can readily be extracted from the results shown in figure 1. It can be seen from figure 1 that after an initial transient period, the flow settles into a statistical steady state with persistent fluctuations. By averaging the results obtained in the statistical steady state, one can obtain a time-averaged value for the domain-averaged slip velocity (shown by the horizontal line in this figure) and then a corresponding time-averaged value for the domain-averaged drag coefficient. Agrawal *et al*.[20] have already examined the dependence of the time-averaged values of the domain-averaged quantities on the grid resolution used in the simulations;

we simply note here that we employed 32x128 grids in the simulations presented in figure, which was found to be adequate by Agrawal *et al*.[20]

By repeating simulations of the type shown in figure 1 for different average particle volume fractions in the domain and imposed shear rates, one can create a look-up table or a simple curve-fit function for the time-averaged drag coefficient in terms of the average particle volume fraction and dimensionless shear rate. We found the shear dependence of the effective drag coefficient to be weak for typical shear rates encountered in riser flows, so that the effective drag coefficient was simply taken as a function of the particle volume fraction in the domain. This function will change with Fr_h; however, the value of Fr_h was not changed in our simulations. Agrawal *et al*.[20] found that the domain-averaged quantities had only a weak dependence (if any) on the aspect ratio, A, for $A > \sim 4$. In all our coarse grid simulations, A was four.

Agrawal *et al*.[20] proposed the use of the look-up table or the curve-fit function for the effective (time-averaged) drag coefficient discussed in the previous paragraph in coarse-grid simulations, as a simple model for the effect of the unresolved structures on the interphase interaction force. We have examined the impact of such a sub-grid model for drag coefficient in our coarse-grid simulations (described later). Such an approach has its limitations; for example, its validity in the vicinity of boundaries such as solid walls is arguable. Nevertheless, we have applied a sub-grid model generated through this approach everywhere in the flow domain, as fluctuations in gas-particle flows in risers do not appear to be driven by shear at bounding surfaces – more on this later.

Note that the instantaneous domain-averaged slip velocity, and hence the instantaneous domain-averaged drag coefficient, fluctuate with time, and the basis for

using time-averaged values for these quantities to construct a sub-grid model is reasonable if and only if the characteristic fluctuation time scale observed in the coarse-grid simulation is much larger than that in the sub-grid calculations illustrated in figure 1. When a clear separation of time scales does not exist, the consequences of the fluctuating drag coefficient seen in the statistical steady state (illustrated in figure 1) should be brought into the coarse-grid simulations. We will however, begin with time-averaged sub-grid models and evaluate if a separation of time scale exists or not.

As discussed in detail by Agrawal *et al.*,[20] one can also extract effective particle phase normal stresses in the vertical and lateral directions, and effective particle phase viscosity from such highly resolved simulations. Once again, one can raise the issue as to whether time-averaged sub-grid models for these quantities (which take the form of look-up tables or curve-fit functions) are adequate if there is no clear separation of time scales.

Table 3 contains the time-averaged sub-grid models for the specific values of Fr_h and A used in our illustrative examples. The effective dimensionless drag coefficient, $\overline{\beta}$, is simply a function of local particle volume fraction, i.e. $\overline{\beta} = \overline{\beta}(\phi)$, where ϕ is the instantaneous volume fraction of particles at any node in the coarse grid simulation (and equal to the average volume fraction of particles in the domain in the sub-grid model calculations described in this section). The time-averaged dimensionless sub-grid horizontal normal stress and effective sub-grid particle phase viscosity ($P_{s,meso}$ and $\mu_{s,meso}$, respectively) depended both on ϕ and the prevailing macroscale shear rate (see expressions in Table 3, where $|\tilde{\gamma}|$ denotes dimensionless $\left|\frac{dv_y}{dx}\right|$, where v_y is the vertical velocity and x is the lateral position). Both of these quantities decreased with increasing

shear rate, indicating a tendency of the shear to orient the clusters and hinder their lateral fluctuations. This shear dependence is exactly opposite of what one obtains in single-phase turbulent flows where sub-grid viscosity and stresses increase with shear rate. The contribution of the vertical normal stress in riser flow simulations is, in general, a very small correction to the convective momentum flux, and hence can be ignored with little loss of accuracy.

One can readily observe that the expressions described here are simple *ad hoc* sub-grid models. Fundamentally based models for the sub-grid corrections are certainly more desirable and should indeed be developed. However, the goal of the present study is to simply investigate if the inclusion of sub-grid models affects the predicted results in a significant way, thus establishing whether or not a need exists for an in-depth study of sub-grid models in the future. This goal can be achieved using the *ad hoc* sub-grid models presented in Table 3. We will demonstrate below that sub-grid models do affect the predicted results profoundly.

Coarse-grid simulations of riser flow

We have performed two-dimensional coarse-grid simulations of gas-particle flows in a vertical channel equipped with a horizontal splash plate at the top, shown schematically in figure 2. [While 3 – D simulations are more desirable, the computational costs are prohibitive. Unlike single phase turbulent flow, nonuniform structures in the gas-particle flow studied here arise primarily through local instabilities, which are already captured in 2 – D analysis. Indeed, Agrawal et al.[20] have shown that both 2 – D and 3 – D simulations of flows in small periodic domains yield similar results, so that there is some reason to expect that the 2 – D and 3 – D coarse-grid simulations will also lead to similar

findings.] Gas and particles entered the channel at the bottom and exited through two symmetric openings on the sides, located near the top of the riser. The exit pressure (in dimensional units) was set to be atmospheric. The gas and particle velocities at the inlet were independent of lateral position, and equal to 27.47 and 16.67 dimensionless units, respectively. The aspect ratio of the grids used in the coarse grid simulations was 4, and the Froude number based on the grid width, Fr_h, was 0.2434. These are exactly the same as the values of A and Fr_h used in the sub-grid model calculations outlined in the previous section.

The coarse-grid simulations employed the effective drag coefficients determined from the sub-grid calculations. We have simply used the sub-grid model for the horizontal normal stress as the effective mesoscale pressure model, i.e. the anisotropy in the horizontal and vertical sub-grid normal stresses was ignored. This particular choice is a reasonable first approximation as the influence of the effective particle phase normal stress is unimportant in the vertical momentum balance.

Agrawal et al.[20] have already shown through quantitative examples that, for the type of two-phase flow problems addressed here, the contribution from the gas phase deviatoric stress – both laminar and turbulent contributions – is negligible when compared to that due to the particle phase. Therefore, we did not include any sub-grid correction for the effective viscosity of the gas phase.

The coarse-grid model retains the general form presented in equations (1) – (4). The fluid phase stress tensor is still given by (6). The interphase interaction force is written as $\underline{f} = \overline{\beta}(\underline{u} - \underline{v})$, where $\overline{\beta}$ is given in Table 3. The effective particle phase pressure

is now written as $\underline{\underline{\sigma_s}} = P_{s,meso}\underline{\underline{I}} - 2\mu_{s,meso}\underline{\underline{S}}$, and the expressions for $P_{s,meso}$ and $\mu_{s,meso}$ are summarized in Table 3.

Very little is known about appropriate wall boundary conditions in *coarse-grid* simulations of densely loaded gas-particle flows. In high-velocity flows of densely loaded gas-particle mixtures through vertical pipes, the shear stress transmitted through the particle phase is generally much larger than that due to the gas; indeed, numerical experiments suggest that there is hardly any difference between results obtained with no-slip and free-slip boundary conditions for the gas phase. Thus, in the class of problems addressed here, the gas phase boundary condition at the walls is not a critical factor. Visual observations of flows through vertical pipes indicate that particles do slip near the wall, and hence a partial or free-slip boundary condition for the particle phase is indicated. It is generally believed that in high-velocity flows of densely loaded gas-particle mixtures through large risers the vertical pressure gradient is largely due to the particle holdup and that wall shear is only weakly relevant.[29] Thus, the correct boundary condition for the large channel flow problem studied here is quite possibly a partial-slip condition, which is not far from a free-slip boundary condition. In the simulations described in this manuscript, we have examined both no-slip and free-slip boundary conditions for the particle and gas-phases at the bounding walls. These two extremes serve as bounds (within which the true boundary condition should lie) and thus give an idea about the extent of the changes in the mean flow characteristics that can come about upon altering the boundary conditions. It also helps us assess whether the need for (and the influence of) sub-grid models is dependent on the wall boundary conditions employed.

Agrawal *et al*.[20] noted that the kinetic theory stresses were dwarfed by the mesoscale corrections when Fr_p exceeded Fr_h by a factor of ~100, which was indeed the case here. Consequently, one need not consider the fluctuation energy equation at all in the coarse-grid simulations. Therefore, the issue of appropriate boundary conditions for the granular energy equation becomes irrelevant for the present coarse-grid simulations.

The coarse-grid simulation was always carried out for a long duration (typically several thousand units of dimensionless time) and a statistical steady state was allowed to establish itself before data on various flow characteristics were gathered. The time-averaged data presented here were obtained by averaging the simulation results over ~ 3000 dimensionless units of time.

Figures 3a and 3b show the time dependence of the slip velocity between the gas and particle phases and the particle volume fraction at an arbitrarily chosen location in the riser. This location, marked as X in figure 2, is 86.3 dimensionless units of length away from the left side riser wall and at an elevation of 2301 dimensionless units of length from the bottom inlet. As expected, persistent fluctuations in all the dependent variables were observed throughout the riser – figures 3a and 3b are simply typical examples. Figure 3c shows the power spectrum corresponding to the results shown in figure 3a. Although a single dominant frequency could not be identified from this figure, the range of frequencies over which most of the fluctuations occurred in the coarse-grid simulations could readily be identified. Very similar results were obtained in coarse-grid simulations using free-slip boundary conditions. Thus, the fluctuations seen here are not due to the same mechanism that drives turbulent pipe flow of a single-phase fluid.

In order to examine if there was indeed a separation of time scale between the sub-grid scale simulations (figure 1) and the coarse-grid scale simulations (figure 3), we present in figure 4 further details of a representative sub-grid scale simulation. The simulation conditions are exactly as in figure 1. Figure 4a shows the instantaneous domain-averaged drag coefficient (related inversely to the slip velocity shown in figure 1) as a function of dimensionless time. The characteristic time used to make the results dimensionless is exactly the same in sub-grid and coarse-grid simulations. Figure 4b shows the power spectrum corresponding to figure 4a. It is readily apparent from a comparison of figures 3c and 4b that the range of dimensionless frequencies is comparable in both cases. Thus, there is no basis for ignoring in the coarse-grid simulations the fluctuations in the sub-grid drag coefficient. In other words, the use of a time-averaged sub-grid model for effective drag coefficient is, in a formal sense, not correct.

This lack of separation of time scales suggests that the fluctuations observed in the sub-grid and coarse-grid simulations are driven by the same mode of instability. Given that the sub-grid scale simulations considered only the fluidization instability, it is reasonable to attribute the persistent fluctuations seen in the coarse-grid simulations to a local instability associated with particle phase inertia, gravity and the dependence of the drag coefficient on particle volume fraction. In this physical picture, small-scale structures arise as a result of local instabilities and coalesce to produce large scale fluctuations observed in coarse-grid simulations.

In sub-grid simulations (such as those shown in figures 1 and 4), mesoscale structures are repeatedly formed and destroyed, and the fluctuations in the slip velocity

(and other mesoscale quantities) are tied to the fluctuations in the configuration of the mesoscale structure. Thus, the need to include the effect of sub-grid drag coefficient fluctuations in the coarse-grid simulations can be interpreted as a need to recognize the fact that the instantaneous sub-grid mesoscale structure can vary about a mean configuration. It then follows that a proper sub-grid model for the fluctuations should try to capture the evolution of the sub-grid structure. As this structure is being convected by the flow, it is reasonable to anticipate that a full-fledged sub-grid model for the fluctuations should be a dynamic model including convective derivatives. Such a dynamic model is rather complex and we have not pursued it in the present study. Instead, we consider a very simple localized sub-grid model that treats the fluctuations in the effective drag coefficient (see figure 4a) as a random stochastic event.

Figure 4c shows that the probability distribution function for $\left(1 \big/ \beta_{meso} \right)$ in the statistical steady state, corresponding to the results presented in figure 4a, is essentially Gaussian. This Gaussian distribution suggests that the formation and breakup of clusters and streamers, which drive the fluctuations in the drag coefficient, are essentially uncorrelated random events. Figure 4c suggests that, as a simple approximation, one can write

$$\left(\frac{1}{\beta_{meso}} \right) = \left(\frac{1+f}{\bar{\beta}} \right)$$

where *f* is a zero-mean Gaussian random variable with suitably chosen variance, and $\overline{\beta}$ is the average drag coefficient shown in figure 4a by the horizontal line. The broken line shown in figure 4c confirms that such a functional representation does capture the pdf.

Stochastic sub-grid model

In order to examine the possible consequence of a lack of separation of time scales between the coarse-grid and sub-grid fluctuations, we constructed a simple time-dependent sub-grid model for the effective drag coefficient. Accordingly, the drag coefficient at each node of the coarse-grid simulation was treated as an independent stochastic random variable modeled via an Uhlenbeck-Ornstein process.[30] Thus, the instantaneous drag coefficient, $\beta_{meso,j}(t)$, of the j[th] node was written as

$$\left(\frac{1}{\beta_{meso,j}}\right)=\left(\frac{1+f_j(t)}{\overline{\beta}\left(\phi_j(t)\right)}\right)$$

where $\phi_j(t)$ is the instantaneous particle volume fraction at that node, $\overline{\beta}$ is the sub-grid model for the time-averaged drag coefficient and f_j is a stochastic random variable with zero-mean. The Uhlenbeck-Ornstein (U-O) model to evolve a stochastic random variable *f* can be summarized as follows.

If f_t denotes the value of a random variable *f* at time *t*, its value at time $t+\Delta t$, $f_{t+\Delta t}$, is set to be $f_{t+\Delta t}=(\alpha_1)\,f_t+(\alpha_2\sigma)\,Rn$, where $\alpha_1=\exp(-\Delta t/\tau^*)$ and $\alpha_2=\sqrt{1-\alpha_1^2}$. Here τ^* and σ are model parameters; Rn is a random number with a Gaussian distribution, $\langle Rn\rangle=0$, and $\langle Rn^2\rangle=1$. The random variable *f*, evolved in time

according to this rule, satisfies $\langle f \rangle = 0, \left\langle f^2 \right\rangle = \sigma^2$ and $\left\langle f_t f_{t+\Delta t} \right\rangle = \sigma^2 \exp(-\Delta t / \tau^*)$, where $\langle\ \rangle$ denotes time averaging.

The stochastic model parameters τ^* and σ represent fluctuation time scale and standard deviation, respectively. Measurements of dominant fluctuation frequency (figure 4b) and sample variance in the meso-scale drag coefficient led to estimates for τ^* and σ. Figure 5 illustrates the stochastic sub-grid model for drag coefficient, applied to the conditions simulated earlier in figure 4. It is remarkable that the simple U-O process produces fluctuations similar to those seen in the detailed sub-grid scale flow simulations. Thus, it is reasonable to hope that such a stochastic sub-grid model for the drag coefficient can be used as a simple vehicle to investigate the possible effect of a lack of separation of time scale between the sub-grid and coarse-grid simulations. We found that the standard deviation σ and the characteristic time τ^* varied somewhat with particle volume fraction. However, for the sake of simplicity, we have assumed in the coarse-grid simulations described below that they are approximately constant [$\sigma = 0.25$; $\tau^* = 1.12$, both being dimensionless], as this is sufficient to investigate the consequences of a lack of separation of time scales.

In what follows, when we talk about coarse-grid simulations with a *stochastic* sub-grid model for riser flows, we refer to coarse-grid simulations employing a stochastic sub-grid model for the drag coefficient along with time-averaged sub-grid models for particle-phase pressure and viscosity. We focused primarily on the drag coefficient, as the interphase interaction force term, particle inertia and the gravitational force term are the most dominant terms in the vertical momentum balance. Similarly, when we discuss coarse-grid simulations using a *time-averaged* sub-grid model, we refer to coarse-grid

simulations employing time-averaged sub-grid models for the drag coefficient, and particle-phase pressure and viscosity. Finally, coarse-grid simulations with *no* sub-grid model refer to results obtained by simply solving the microscopic equations (kinetic theory model) on a coarse grid without including any sub-grid correction.

Coarse-grid simulations with different sub-grid models

We repeated the coarse-grid simulation described earlier in figures 2 and 3, using the stochastic sub-grid model. We also performed an identical simulation where no sub-grid corrections were made. Figures 6a – 6c obtained with the stochastic sub-grid model are analogous to figures 3a – 3c discussed earlier in the context of time-averaged sub-grid model.

It is clear that the addition of a stochastic fluctuation in the drag coefficient has not produced any qualitative difference in the fluctuations. Instantaneous snapshots of particle volume fraction profiles between these two models also appeared qualitatively similar – compare figures 7a and 7b. The same was true for the velocity fields as well. Thus, no qualitatively new feature appeared in the simulation results because of the addition of the stochastic correction.

Surprisingly, however, when no-sub-grid model was included, large-scale nonuniformities could not be sustained even if we began our simulations with highly nonuniform initial conditions in the riser. For example, we carried out coarse-grid simulations using a stochastic sub-grid model and allowed a statistical steady state to evolve. We then stopped the simulation at different times in the statistical steady state, turned off the sub-grid model, and continued the simulation. We found that over a few multiples of the residence time in the riser the inhomogeneities washed out of the riser

and a nearly homogeneous state with small fluctuations resulted. Thus, in this example, inhomogeneities could not be sustained without adding sub-grid models.

From our coarse-grid simulations, we have obtained the time-averaged profiles of various quantities in the statistical steady state, some of which are illustrated below. Figure 8 shows the laterally averaged particle volume fraction as a function of riser elevation for the three cases: no sub-grid, time-averaged sub-grid, and stochastic sub-grid models. We performed simulations with two different initial conditions, one where the channel was initially devoid of particles and another where the channel was initially filled with a non-uniform distribution of particles. The time-averaged results representing a statistical steady state showed no significant dependence on the initial condition. (Some small difference was invariably present; however, as the difference decreased with increasing sampling time, it was taken as an indication that the data had not been averaged for a sufficiently long duration.)

The result obtained in the *no sub-grid model* case is qualitatively different from those in the other two cases. It proved to be deficient in the sense that it did not reproduce the generally known, large scale fluctuations. The axial profiles for the other two cases manifest peaks in the laterally averaged particle volume fraction at an intermediate elevation in the riser (~ 15% of riser height from the bottom). In simulations with both the time-averaged and stochastic sub-grid models, particle rich regions are more commonly seen near the wall, and they slowly descend, causing an accumulation near the bottom of the riser. However, the upward flow from the inlet tends to push the accumulated solids upwards, and these two opposing effects are responsible for the peak at the intermediate elevation. It is clear from figure 8 that the time-averaged and

stochastic sub-grid models lead to quantitatively different results near the inlet but converge at higher riser elevations. Figure 9 shows the lateral profiles of particle volume fraction and dimensionless particle flux at an elevation of 80% of the riser height, where the laterally averaged particle volume fractions obtained with the stochastic and time-averaged sub-grid models are fairly close. It is clear from this figure that both models predict enrichment of particle concentration and downflow near the wall region. The results are quantitatively different, but the difference is not very large. Although we do not attempt any comparison with experimental data in this study, we suspect that the uncertainties in the experimental data will be at least as large as the differences between these two model predictions and that discrimination between these two models by comparison with experimental data in the upper elevation of risers is unlikely. On the other hand, discrimination may be possible at the lower elevations. However, the details of flow at the bottom are probably very sensitive to the spatial nonuniformities and fluctuations in the inlet flow (discussed later), and proper discrimination between models on the basis of experimental data will be difficult unless one carefully measures the inlet flow characteristics.

In any case, there is no doubt that the addition of a sub-grid model (be it the time-averaged sub-grid model or the stochastic sub-grid model) has dramatically altered the simulation results, establishing that results obtained by integrating the microscopic equations without any sub-grid correction are suspect.

Coarse-grid simulations with free-slip boundary conditions

As discussed earlier, no-slip boundary condition at the solid walls (used in the simulations described above) is by no means accurate and a partial slip boundary condition (which is not too far from free slip) is probably more realistic. We explored the sensitivity of the coarse grid simulation results to the wall boundary conditions by repeating a number of simulations using free slip boundary conditions for both phases. Specifically, we started from a highly nonuniform initial state obtained via coarse grid simulation using the time-averaged or the stochastic sub-grid model and no-slip boundary conditions, and continued the simulation with free slip boundary conditions and desired sub-grid model. Once again, the fluctuations were washed out of the channel when no sub-grid model was included. With the time-averaged and stochastic sub-grid models, fluctuations persisted. Figures 10a and 10b show snapshots of simulations with free slip boundary conditions; no dramatic, qualitative difference between the time-averaged and stochastic sub-grid models is apparent. Indeed, these snapshots are not much different from those obtained with no-slip boundary conditions, suggesting that the gross features of the fluctuating flow pattern in a statistical steady state are not driven by specific choice of wall boundary conditions.

Coarse grid simulations with free slip boundary conditions manifested sensitivity to the initial condition. When the above simulations were repeated, starting from an initially empty channel, nonuniform distribution of particles and persistent large-scale fluctuations in particle concentration did not develop with both sub-grid models. This suggested that there are at least two attractors for simulations with free slip boundary conditions. Such a multiplicity has not been reported in any experimental study and is

therefore likely to be unphysical. In practice, the inlet at the bottom is neither perfectly uniform nor steady, and spatial nonuniformities and temporal fluctuations are inevitable at the bottom inlet. Indeed, when we introduced stochastic, lateral variation in axial particle mass flux at the inlet to a simulation with stochastic sub-grid model, the nonuniform distribution of particles and persistent large-scale fluctuations readily developed even from a uniform initial condition.[31] Thus, nonuniformities or fluctuations at the inlet and/or some resistance at the solid walls to flow serve to eliminate spurious solutions.

Figure 11 presents the axial variation of laterally averaged particle volume fraction in the statistical steady state for simulations with free slip boundary conditions, a highly nonuniform initial condition, and uniform inlet. Once again, we see that the results obtained with the time-averaged and stochastic sub-grid models are qualitatively similar, while the result obtained in simulations with no sub-grid correction is grossly different. Comparison of figures 8 (no slip) and 11 (free slip) reveal no qualitative differences; however, the wall boundary conditions do seem to have a quantitative effect on the predicted holdup profile.

Figures 12a and 12b show lateral variation of particle volume fraction and dimensionless particle flux at an elevation of 80% of riser height. It is clear that the time-averaged and stochastic sub-grid models yield nearly the same results. Comparison of these figures with figures 9a and 9b reveals that a change in wall boundary conditions only contributes to a small quantitative change near the wall region.

Discussion

Our simulations show clearly that the dominant fluctuations occurred at comparable dimensionless frequencies (which are much smaller than the inverse of dimensionless time step) in both coarse-grid and mesoscale calculations. This suggests that fluctuations derive from the same process at both scales. As fluctuations do occur in mesoscale simulations even in the absence of macroscale shear and in coarse-grid simulations with free-slip boundary conditions, we begin by examining instabilities associated with the governing equations of motion (without requiring an active role for the macroscale shear or exit configuration). In the absence of shear and exit effect, the governing equations support a simple solution where the gas-particle mixture travels up the channel homogeneously with the slip velocity being adequate to support the weight of the particle – that is, the simplest version of riser flow is a vertically traveling homogeneous fluidized bed. It is well known that the dominant instability in homogeneously fluidized beds, as predicted by the averaged equations of motion with simple phenomenological closures where the particle phase pressure and viscosity are only functions of particle volume fraction, take the form of one-dimensional, vertically traveling wavefronts having no horizontal structure.[32] Two-dimensional linear stability analysis of a uniformly fluidized bed of infinite extent based on the microscopic (kinetic theory) equations used in the present study[26] revealed that the most unstable mode is an oblique wave, with the horizontal wavenumber being much smaller than the vertical wavenumber. Hence it is sufficient to focus our discussion on growth rates of vertically traveling wavefronts having no horizontal structure and the amplification of disturbances

introduced at the bottom of the riser and convected upwards by the flow. The time available for amplification is comparable to the residence time of the mixture in the riser.

According to the microscopic (kinetic theory) equations, the homogeneously fluidized state is unstable to vertically traveling horizontal wavefronts whose wavelength is larger than a few particle diameters and the dominant mode has a wavelength of ten or so particle diameters. The growth rate of perturbations whose wavelength is much larger than that of the dominant mode is *much* smaller than that of the dominant mode. Thus, a homogeneously fluidized bed gives way to nonuniform structures in coarse-grid simulations much more slowly (provided it is not stabilized by numerical viscosity), than in highly resolved simulations. As a result, appreciable amplification of the initial disturbances (which, in turn, can give way to lateral nonuniformities through secondary gravitational overturning instability,[18,33-35] does not occur in the coarse-grid simulations with free-slip boundaries within the time available in the riser flow and the disturbance gets washed out of the riser. Our observation that a highly nonuniform initial state (coupled with uniform inlet conditions) could not sustain the fluctuating state suggests that the basin of attraction for the homogeneous state is fairly large and/or that a fluctuating statistical steady state does not exist for the microscopic equations discretized on a coarse grid.

When modest stochastic, lateral variation was introduced in axial particle mass flux at the inlet, the fluctuations persisted in the riser (in our simulations of the microscopic equations discretized on a coarse grid coupled with free-slip boundary conditions); however, the time-averaged solution was only marginally different from that

obtained without stochastic fluctuations, clearly suggesting that this solution was only a mild perturbation of the homogeneous solution.

Note that in our riser simulations the gas-particle mixture entered the riser in a plug flow manner. When no-slip boundary conditions are employed, both the fluid and the particles are forced to slow down near the wall and an increase in particle volume fraction must occur purely because of kinematic effect. This represents another form of lateral nonuniformity that can, in principle, develop into a fluctuating state. However, the particle phase viscosity in the homogeneous state is very small (when no sub-grid correction is included). Therefore, the boundary layer near the channel walls did not grow rapidly with distance from the inlet in our coarse-grid simulation examples (without any sub-grid correction) and the particle concentration near the channel walls did not grow appreciably with height. Thus, lateral perturbation to the homogeneously fluidized state by the presence of the sidewalls was not large enough to give rise to and sustain the highly nonuniform fluctuating state.

Our computational experiments indicate that nonuniform solutions with sustained fluctuations and lateral segregations *may* develop in coarse-grid simulations of the microscopic equations only if pronounced nonuniformity is present at the inlet (such as side entrance, large scale fluctuations at the inlet, etc.).

Adding the time-averaged closure expressions in Table 3 to the microscopic model equations did *not* lead to an increase in the growth rate of perturbations to a homogeneously fluidized bed – if anything, the addition of a large mesoscale particle phase viscosity should decrease the growth rate! Thus, the difference in the outcome of the coarse-grid simulations with and without sub-grid models is *not* due to a larger

growth rate of disturbances in the presence of sub-grid models. This is consistent with our observation that the fluctuating state could not be reached from uniform initial conditions (and uniform inlet conditions) when free slip boundary conditions were employed. The observation that the fluctuating state could be sustained if the simulations began with a nonuniform initial condition reveals coexistence of a homogeneous solution and a high-amplitude nonuniform solution. [Such coexistence of solutions for these equations has been demonstrated previously, see Glasser *et al.*[34,35]] We found that adding stochastic, lateral fluctuations in particle mass flux at the inlet could eliminate the homogeneous state; thus, the homogeneous solution appears to have a small attractor basin. When no-slip boundary conditions are used in the simulations using sub-grid corrections, the boundary layer grows more rapidly than in the no sub-grid case, as the particle phase viscosity is much larger when a sub-grid model is used. Consequently, particle accumulation near the wall region is more pronounced when a sub-grid model is used and this lateral nonuniformity is apparently enough to take the system into the basin of attraction for the fluctuating state.

Summary

It is clear from the examples presented here that the results obtained in coarse-grid integration of the microscopic equations for gas-particle flows in large process vessels can change appreciably if sub-grid corrections to account for the effects of unresolved structures are included. The most dramatic difference occurred in our simulations when a simple *time-averaged* sub-grid model was added to the *no sub-grid* model case. In view of this sensitivity, the results published in the literature where researchers have simply solved the continuum equations without corrections for sub-grid

structures should be re-evaluated. Although the level of sophistication of the sub-grid model did make a difference in the quantitative results in our simulations, even a simple time-averaged sub-grid model appeared to capture the main qualitative effects.

The simple time-averaged sub-grid model is, in a strict sense, flawed, as there is no separation of time scales between the unresolved (sub-grid) structures and those resolved in the coarse-grid simulations. To account for this lack of separation of time scale, a rather simple enhancement of the time-averaged sub-grid model that took the form of a stochastic correction to the drag coefficient was implemented. It was found that such a stochastic sub-grid model yielded qualitatively the same results as the time-averaged sub-grid model. Thus the lack of separation of time scales does not appear to be a severe deficiency.

The approach employed in the present study to construct sub-grid models is clearly *ad hoc*. Such an approach is adequate, in our opinion, for our study as our primary goal is to expose the potential importance of sub-grid corrections. More in-depth study of the processes occurring at small scales is needed to develop meaningful and broadly useful sub-grid models.

It should also be emphasized that the present analysis only considered a static interphase interaction force – even though the stochastic part introduced a time-dependent character, it does not capture dynamic effects of the type examined by Zhang & VanderHeyden,[36] who argued that the mesoscale structures can lead to an appreciable added mass correction. Additional work is required to verify the existence of such a dynamic term – if it does exist, it may slow down the coarse-grid fluctuations appreciably and eliminate the need for a stochastic sub-grid model for the drag coefficient.

Acknowledgements

This work was supported by the US Department of Energy CDE-FC26-00NT40971.

References

(1) Benyahia, S., Arastoopour, H. & Knowlton, T. M. Simulation of particles and gas flow behavior in the riser section of a circulating fluidized bed using the kinetic theory approach for the particulate phase. *Powder Technol.* **2000**, *112*, 24 – 33.

(2) Benyahia, S., Arastoopour, H. & Knowlton, T. M. Two-dimensional transient numerical simulation of solids and gas flow in the riser section of a circulating fluidized bed. *Chem. Eng. Commun*. **2002**, *189*, 510 – 527.

(3) Ding, J. & Gidaspow, D. A Bubbling Fluidization Model Using Kinetic-Theory of Granular Flow. *AIChE J*. **1990**, *36*, 523 – 538.

(4) Enwald, H., Peirano, E. & Almstedt, A. E. Eulerian two-phase theory applied to fluidization. *Int. J. Multiphase Flow.* **1997,** *22*, Suppl., 21-66.

(5) Enwald, H., Peirano, E., Almstedt, A. E. & Leckner, B. Simulation of the fluid dynamics of a bubbling fluidized bed. Experimental validation of the two-fluid model and evaluation of a parallel multiblock solver. *Chem. Eng. Sci.*, **1999**, *54*, 311-328.

(6) Enwald, H. & Almstedt, A. E. Fluid dynamics of a pressurized fluidized bed: comparison between numerical solutions from two-fluid models and experimental results. *Chem. Eng. Sci.* **1999**, *54*, 329-342.

(7) Nieuwland, J. J., Huizenga, J. J. P., Kuipers, J. A. M. & van Swaaij, W. P. M. Hydrodynamic modelling of circulating fluidized beds. *Chem. Eng. Sci.* **1995**, *49*, 5803 – 5811.

(8) Nieuwland, J. J., Annaland M. V., Kuipers, J. A. M. & van Swaaij, W. P. M. Hydrodynamic modelling of gas/particle flows in riser reactors. *AIChE J.* **1996,** *42*, 1569 – 1582.

(9) Gidaspow, D. *Multiphase Flow and Fluidization*. Academic Press: CA, 1994.

(10) Lu, H. L. & Gidaspow, D. Hydrodynamic simulations of gas-solid flow in a riser. *Ind. Eng. Chem. Res.* **2003**, *42*, 2390 – 2398.

(11) Goldschmidt, M. J. V., Kuipers, J. A. M. & van Swaaij, W. P. M. Hydrodynamic modeling of dense gas-fluidized beds using the kinetic theory of granular flow: Effect of restitution coefficient on bed dynamics. *Chem. Eng. Sci.* , **2001**, *56*, 571 – 578.

(12) Neri, A. & Gidaspow, D. Riser hydrodynamics: Simulation using kinetic theory. *AIChE J*. **2000**, *46*, 52 – 67.

(13) Samuelsberg, A. & Hjertager, B. Computational modelling of gas/particle flow in a riser. *AIChE J.* **1996**, *42*, 1536 – 1546.

(14) Sun, B. & Gidaspow, D. Computation of circulating fluidized bed riser flow for the Fluidization VIII benchmark test. *Ind. Eng. Chem. Res.* **1999**, *38*, 787 – 792

(15) Tsuo, Y. P. & Gidaspow, D. Computation of flow patterns in circulating fluidized beds. *AIChE J.* **1990**, *36*, 885 – 896.

(16) Van Wachem, B. G. M., Schouten, J. C., van den Bleek, C. M., Krishna, R. & Sinclair, J. L. Comaparative analysis of CFD models of dense gas-solid systems. *AIChE J*. **2001**, *47*, 1035 – 1051.

(17) Zhang, D. Z. & VanderHeyden, W. B., High-resolution three-dimensional numerical simulation of a circulating fluidized bed. *Powder Technol*. **2001**, *116*, 133 – 141.

(18) Glasser, B. J., Sundaresan, S. & Kevrekidis, I. G. From bubbles to clusters in fluidized beds. *Phys. Rev. Lett*. **1998**, *81*, 1849 – 1852.

(19) Koch, D. L. & Sangani, A. S. Particle pressure and marginal stability limits for a homogeneous monodisperse gas fluidized bed: kinetic theory and numerical simulations. *J. Fluid Mech.* **1999**, *400*, 229 – 263.

(20) Agrawal, K., Loezos, P. N., Syamlal, M. & Sundaresan, S. The Role of Meso-scale Structures in Rapid Gas-solid Flows. *J. Fluid Mech.* **2001**, *445*, 151 – 185.

(21) Sundaresan, S. Perspective: Modeling the Hydrodynamics of Multiphase Flow Reactors: Current Status and Challenges. *AIChE J*. **2000**, *46*, 1102 – 1105.

(22) Lun, C. K. K., Savage, S. B., Jeffrey, D. J. & Chepurniy, N. Kinetic theories of granular flows: inelastic particles in Couette flow and slightly inelastic particles in a general flow field. *J. Fluid Mech.* **1984**, *140*, 223 – 256.

(23) Wen, C. Y. & Yu, Y. H. Mechanics of Fluidization. *Chem. Eng. Prog. Symp. Ser.* **1966**, *62*, 100 – 111.

(24) McKeen, T. and T. Pugsley. Simulation and Experimental Validation of a Freely Bubbling Bed of FCC Catalyst. *Powder Technology*. **2003**, 129(1-3), 139-152.

(25) Yang. N., Wang, W., Ge, W. & Li, J. CFD Simulation of Concurrent-up Gas-Solid Flow in Circulating fluidized beds with Structure-dependent Drag Coefficient. *Chem. Eng. J.* **2003**, 96, 71-80.

(26) Tan, J. *2 – D stability analysis of gas-particle flows in risers*. BSE Thesis, Department of Chemical Engineering: Princeton University, Princeton, New Jersey, 2000.

(27) Syamlal, M. *MFIX Documentation: Numerical Techniques*. DOE/MC-31346-5824. NTIS/DE98002029. December 1998.

(28) Syamlal, M., Rogers, W. & O'Brien, T. J. *MFIX Documentation*. U.S. Department of Energy, Federal Energy Technology Center: Morgantown, WV, 1993.

(29) Chang, H. & Louge, M. Fluid Dynamic Similarity of Circulating Fluidized-Beds. *Powder Technol.* **1992**, *70*, 259 – 270.

(30) Uhlenbeck, G. E. & Ornstein, L. S. On the theory of Brownian motion. *Phys Rev*. **1930**, *36*, 823 – 841.

(31) Andrews, A. T. Unpublished results. 2003.

(32) Jackson, R. *The dynamics of fluidized particles*. Cambridge University Press, 2000.

(33) Batchelor, G. K. Secondary Instability of a Gas-Fluidized Bed. *J. Fluid Mech.* **1993**, *445*, 151 – 185

(34) Glasser, B. J., Kevrekidis, I. G. & Sundaresan, S. One- and two-dimensional travelling wave solutions in gas-fluidized beds. *J. Fluid Mech*. **1996**, *306*, 183 – 221.

(35) Glasser, B. J., Kevrekidis, I. G. & Sundaresan, S. Fully developed travelling wave solutions and bubble formation in fluidized beds. *J. Fluid mech*. **1997**, *334*, 157 – 188.

(36) Zhang, D. Z. & VanderHeyden, W. B. The effects of mesoscale structures on the macroscopic momentum equations for two-phase flows. *Int. J. Multiphase Flow*. **2002**, *28*, 805 – 822.

Appendix A

Eqs. (1) – (4) describe the continuity and momentum balance equations for the particle and gas phases. Here, ϕ is the volume fraction of particles; $\underline{v}$ and $\underline{u}$ are the local average velocities of the particle and gas phases, respectively; ρ_s and ρ_g are the densities; $\underline{\underline{\sigma}}_s$ and $\underline{\underline{\sigma}}_g$ are the stress tensors associated with the two phases expressed in a compressive sense; $\underline{f}$ is the interaction force between the phases per unit volume of the bed; and $\underline{g}$ is the specific gravity force. Eq. (5) is the pseudothermal energy (PTE) balance, where T is the granular temperature – in this equation, $\underline{q}$ is the diffusive flux of PTE; the second and third terms on the right hand side quantify the rates of production of PTE by shear and gas-particle slip, respectively. The fourth and the fifth terms account for the rates of dissipation of PTE through inelastic collisions and viscous damping, respectively.

Eq. (6) describes a simple Newtonian closure for the effective gas phase stress. Here p_g and $\hat{\mu}_g$ denote fluid phase pressure and effective viscosity, respectively. In the regime investigated in the present study, namely, $\rho_s\phi >> \rho_g(1-\phi)$, the contribution due to the deviatoric part of the gas phase stress is negligible.

The gas-particle interaction force, $\underline{f}$, is, for all practical purposes, only due to drag. Eq. (7) describes the drag correlation used in our simulations.[23] Here β, C_D, d, μ_g and Re_g denote an effective drag coefficient for the suspension, single particle drag coefficient, particle diameter, fluid viscosity and Reynolds number, respectively.

Eq. (8) summarizes a kinetic theory closure for the particle phase stress in the fluid-particle mixture. An expanded discussion of this closure can be found in Agrawal et

al.[20] Here e_p denotes the coefficient of restitution for particle-particle collisions, and the spheres are assumed to be smooth. Eq. (9) is the corresponding closure for the diffusive flux of PTE.

Eq. (10) is the kinetic theory closure for the rate of dissipation of PTE through inelastic collisions, while eq. (11) represents the closure due to Koch & Sangani[19] for the rate of dissipation of PTE by viscous dissipation in the fluid phase.

Table 1: MODEL EQUATIONS FOR GAS-PARTICLE FLOWS

$$\frac{\partial \rho_s \phi}{\partial t} + \nabla \cdot (\rho_s \phi \underline{v}) = 0 \tag{1}$$

$$\frac{\partial \left(\rho_g (1-\phi) \right)}{\partial t} + \nabla \cdot \left[\rho_g (1-\phi) \underline{u} \right] = 0 \tag{2}$$

$$\left[\frac{\partial (\rho_s \phi \underline{v})}{\partial t} + \nabla \cdot \left(\rho_s \phi \underline{v} \underline{v} \right) \right] = \quad -\nabla \cdot \underline{\underline{\sigma}}_s \quad - \quad \phi \nabla \cdot \underline{\underline{\sigma}}_g \quad + \quad \underline{f} \quad + \quad \rho_s \phi \underline{g} \tag{3}$$

$$\left[\frac{\partial \left(\rho_g (1-\phi) \underline{u} \right)}{\partial t} + \nabla \cdot \left(\rho_g (1-\phi) \underline{u} \underline{u} \right) \right] = \quad -(1-\phi) \nabla \cdot \underline{\underline{\sigma}}_g \quad - \quad \underline{f} \quad + \rho_g (1-\phi) \underline{g} \tag{4}$$

$$\left[\frac{\partial \left(\frac{3}{2} \rho_s \phi T \right)}{\partial t} + \nabla \cdot \left(\frac{3}{2} \rho_s \phi T \underline{v} \right) \right] = \quad -\nabla \cdot \underline{q} \quad - \quad \underline{\underline{\sigma}}_s : \nabla \underline{v} \tag{5}$$

$$+ \Gamma_{slip} \; - \; J_{coll} \; - \; J_{vis}$$

Gas phase stress tensor

$$\underline{\underline{\sigma}}_g = p_g \underline{\underline{I}} - \hat{\mu}_g \left[\nabla \underline{u} + (\nabla \underline{u})^T - \frac{2}{3} (\nabla \cdot \underline{u}) \underline{\underline{I}} \right] \tag{6}$$

Gas-particle drag (Wen & Yu,[23] Gidaspow[9])

$$\underline{f} = \beta (\underline{u} - \underline{v}) \;\; ; \;\; \beta = \frac{3}{4} C_D \frac{\rho_g (1-\phi) \phi |\underline{u} - \underline{v}|}{d} (1-\phi)^{-2.65} \tag{7}$$

$$C_D = \begin{cases} \frac{24}{Re_g} \left(1 + 0.15 Re_g^{\,0.687} \right) & Re_g < 1000 \\ 0.44 & Re_g \geq 1000 \end{cases} \quad ; \quad Re_g = \frac{(1-\phi) \rho_g d |\underline{u} - \underline{v}|}{\mu_g}$$

Table 1 – continued

Particle phase stress

$$\underline{\underline{\sigma_s}} = \left[\rho_s \phi \left(1 + 4\eta\phi g_o\right)\ \mathrm{T} - \eta\mu_b \left(\nabla \cdot \underline{\mathrm{v}}\right)\right]\ \underline{\underline{\mathrm{I}}}$$
$$-\left(\frac{2+\alpha}{3}\right)\left\{\frac{2\mu^*}{g_o\eta\left(2-\eta\right)}\left(1+\frac{8}{5}\phi\eta g_o\right)\ \left(1+\frac{8}{5}\eta\left(3\eta-2\right)\ \phi\ g_o\right)+\frac{6}{5}\eta\mu_b\right\}\underline{\underline{\mathrm{S}}} \qquad (8)$$

where $\underline{\underline{S}} = \frac{1}{2}\left(\nabla \underline{\mathrm{v}} + \left(\nabla \underline{\mathrm{v}}\right)^{\mathrm{T}}\right) - \frac{1}{3}\left(\nabla \cdot \underline{\mathrm{v}}\right)\underline{\underline{\mathrm{I}}}$

$$\mu^* = \frac{\mu}{1+\frac{2\beta\mu}{\left(\rho_s\phi\right)^2 g_o \mathrm{T}}} \quad ;\mu = \frac{5\rho_s d\sqrt{\pi \mathrm{T}}}{96} \quad ;$$

$$\mu_b = \frac{256\mu\phi^2 g_o}{5\pi} \quad ; \quad \eta = \frac{\left(1+e_p\right)}{2}; g_o = \frac{1}{1-\left(\phi/\phi_{\max}\right)^{1/3}} \quad ; \quad \phi_{\max} = 0.65; \alpha = 1.6$$

Pseudo-thermal energy flux

$$\underline{\mathrm{q}} = -\frac{\lambda^*}{g_o}\left\{\left(1+\frac{12}{5}\eta\phi g_o\right)\ \left(1+\frac{12}{5}\eta^2(4\eta-3)\phi g_o\right)+\frac{64}{25\pi}\left(41-33\eta\right)\ \eta^2\phi^2 g_o^2\right\}\ \nabla \mathrm{T} \quad (9)$$

where $\lambda^* = \frac{\lambda}{1+\frac{6\beta\lambda}{5\left(\rho_s\phi\right)^2 g_o \mathrm{T}}}; \lambda = \frac{75\rho_s d\sqrt{\pi \mathrm{T}}}{48\eta\left(41-33\eta\right)}$

Rate of dissipation of pseudo-thermal energy through collisions

$$\mathrm{J}_{\mathrm{coll}} = \frac{48}{\sqrt{\pi}}\eta\left(1-\eta\right)\frac{\rho_s\phi^2}{\mathrm{d}} g_o \mathrm{T}^{3/2} \qquad (10)$$

Table 1 – continued

Effect of fluid on particle phase fluctuation energy (Koch & Sangani[19])

$$J_{vis} = \frac{54\ \phi\mu_g T}{d^2} R_{diss}, \quad \text{where}$$
$$R_{diss} = 1+\frac{3\phi^{1/2}}{\sqrt{2}}+\frac{135}{64}\phi\ln\phi+11.26\phi\ (1-5.1\phi+16.57\phi^2-21.77\phi^3)\text{-}\phi g_o \ln(0.01) \tag{11}$$

$$\Gamma_{slip} = \frac{81\phi\mu_g^2\left|\underline{u}-\underline{v}\right|}{g_o d^3 \rho_s \sqrt{\pi T}}\Psi, \quad \text{where} \tag{12}$$

$$\Psi = \frac{R_d^2}{(1+3.5\phi^{1/2}+5.9\phi)},$$

$$R_d = \begin{cases} \dfrac{1+3(\phi/2)^{1/2}+(135/64)\phi\ln\phi+17.14\phi}{1+0.681\phi-8.48\phi^2+8.16\phi^3}, & \phi < 0.4 \\ \dfrac{10\phi}{(1\text{-}\phi)^3}+0.7, & \phi \geq 0.4 \end{cases}$$

Table 2: Physical properties of gas and solids

d	particle diameter	7.5×10^{-3} cm
ρ_s	particle density	1.5 g/cm^3
ρ_g	Gas density	1.3×10^{-3} g/cm^3
μ_g	Gas viscosity	1.8×10^{-4} g/cm·s
e_p	Coefficient of restitution	0.9
v_t	Terminal settling velocity	21.84 cm/s
$\frac{v_t^2}{g}$	Characteristic length	0.487 cm
$\frac{v_t}{g}$	Characteristic time	0.0223 s
$\rho_s v_t^2$	Characteristic stress	715.5 g/cm.s^2

Table 3: Computationally generated *ad hoc* sub-grid model for various dimensionless quantities

---

$$P_{s,meso} = 1.54\phi \exp(-.701|\tilde{\gamma}|)$$

$$\mu_{s,meso} = \begin{cases} \left(0.0121|\tilde{\gamma}|^3 - 0.0605|\tilde{\gamma}|^2 + 0.0314|\tilde{\gamma}| + .130\right)\dfrac{\phi}{0.398} & \text{for} \quad |\tilde{\gamma}| < 2.45 \\ 0.0546\phi \quad \text{for} \quad |\tilde{\gamma}| \geq 2.45 \end{cases}$$

$$\overline{\beta} = \left(1 - \frac{\rho_g}{\rho_s}\right)\frac{\phi(1-\phi)}{F}, \text{ where}$$

$$F = \begin{cases} \left(396\phi^2 - 30.8\phi + 1\right) & \text{for} \quad \phi < 0.0375 \\ \left(.151\ln(\phi) + .898\right) & \text{for} \quad \phi \geq 0.0375 \end{cases}$$

Figure Captions

Figure 1: Domain-averaged dimensionless slip velocity calculated in a doubly periodic domain with Fr_h = 0.2434; A = 4; Average particle volume fraction in the domain = 0.05; Reynolds number based on particle diameter and terminal settling velocity, Re_p = 1.18. Highly resolved simulation of flow in this periodic domain was performed using 32 x 128 grids. Time-averaged slip velocity shown as a superimposed line, and was calculated between 200 and 800 dimensionless time units. The imposed shear rate in the periodic domain is zero. See Agrawal et al.[20] for details on the introduction of macroscale shear in the periodic domain calculations. The dominant period of the oscillations is ~ 10 dimensionless units of time. For the parameter values listed in Table 2, this translates to a period of 0.223 s.

Figure 2: Schematic diagram showing the geometry used in 2D coarse grid simulations. Riser half-width, W = 78.1; Riser height, H = 6164; Exit opening height, B = 102.7 (all in dimensionless units). Volume fraction of particles at the inlet = 0.04. Simulations were done using 38 x 375 grids. The location designated by "X" will be referred to later.

Figure 3: Results obtained from a coarse grid simulation with time-averaged sub-grid models for drag coefficient and the stresses. (a) Dimensionless slip velocity and (b) particle volume fraction as functions of dimensionless time at the location marked as X in figure 2. (c) The power spectrum of slip velocity shown in figure 3a.

Figure 4: (a) Dimensionless drag coefficient, β_{meso}, vs. dimensionless time. (b) Power spectrum of drag coefficient shown in figure 4a. (c) Probability distribution function

vs. $(1 / \beta_{meso})$ corresponding to figure 4a. Geometry and conditions are the same as in figure 1.

Figure 5: Temporal fluctuations in drag coefficient modeled as a Uhlenbeck-Ornstein process. U-O model parameters: characteristic time, $\tau^* = 1.12$ dimensionless time units; $\sigma = 0.25$. Particle volume fraction = 0.05. The time-averaged drag coefficient is set to be same as that in figure 4a. (a) Dimensionless drag coefficient, β_{meso}, vs. dimensionless time. (b) Power spectrum of drag coefficient shown in figure 5a. (c) Probability distribution function vs. $(1/ \beta_{meso})$ corresponding to figure 5a.

Figure 6: Results obtained from a coarse grid simulation with stochastic sub-grid model for drag coefficient and time-averaged sub-grid models for the stresses. (a) Dimensionless slip velocity and (b) particle volume fraction as functions of dimensionless time at the location marked as X in figure 2. (c) The power spectrum of slip velocity in figure 6a.

Figure 7: Snapshots of particle volume fractions obtained in the coarse-grid simulations. (a) Time-averaged sub-grid model, (b) stochastic sub-grid model. No-slip boundary conditions for both phases.

Figure 8: Axial variation of laterally averaged particle volume fraction corresponding to statistical steady state. Results obtained from coarse-grid simulations with stochastic (+) and time-averaged (o) sub-grid models are compared. Also shown as (x) are results corresponding to kinetic theory (i.e. with no sub-grid models). No slip boundary conditions. Uniform inlet conditions. The riser geometry and conditions are the same as in figures 2 and 3.

Figure 9: Lateral variations of (a) particle volume fraction and (b) dimensionless particle flux at an elevation of 80% of the riser height. Results obtained from coarse-grid simulations with stochastic (+) and time-averaged (o) sub-grid models are compared. Also shown as (x) are results corresponding to kinetic theory (i.e. with no sub-grid models). No slip boundary conditions. Uniform inlet conditions. The riser geometry and conditions are the same as in figures 2 and 3.

Figure 10: Snapshots of particle volume fractions obtained in the coarse-grid simulations. (a) Time-averaged sub-grid model, (b) stochastic sub-grid model. Free-slip boundary conditions for both phases.

Figure 11: Axial variation of laterally averaged particle volume fraction corresponding to statistical steady state. Results obtained from coarse-grid simulations with stochastic (+) and time-averaged (o) sub-grid models are compared. Also shown as (x) are results corresponding to kinetic theory (i.e. with no sub-grid models). Free-slip boundary conditions. Uniform inlet conditions. The riser geometry and conditions are the same as in figures 2 and 3.

Figure 12: Lateral variations of (a) particle volume fraction and (b) dimensionless particle flux at an elevation of 80% of the riser height. Results obtained from coarse-grid simulations with stochastic (+) and time-averaged (o) sub-grid models are compared. Also shown as (x) are results corresponding to kinetic theory (i.e. with no sub-grid models). No slip boundary conditions. Uniform inlet conditions. The riser geometry and conditions are the same as in figures 2 and 3.

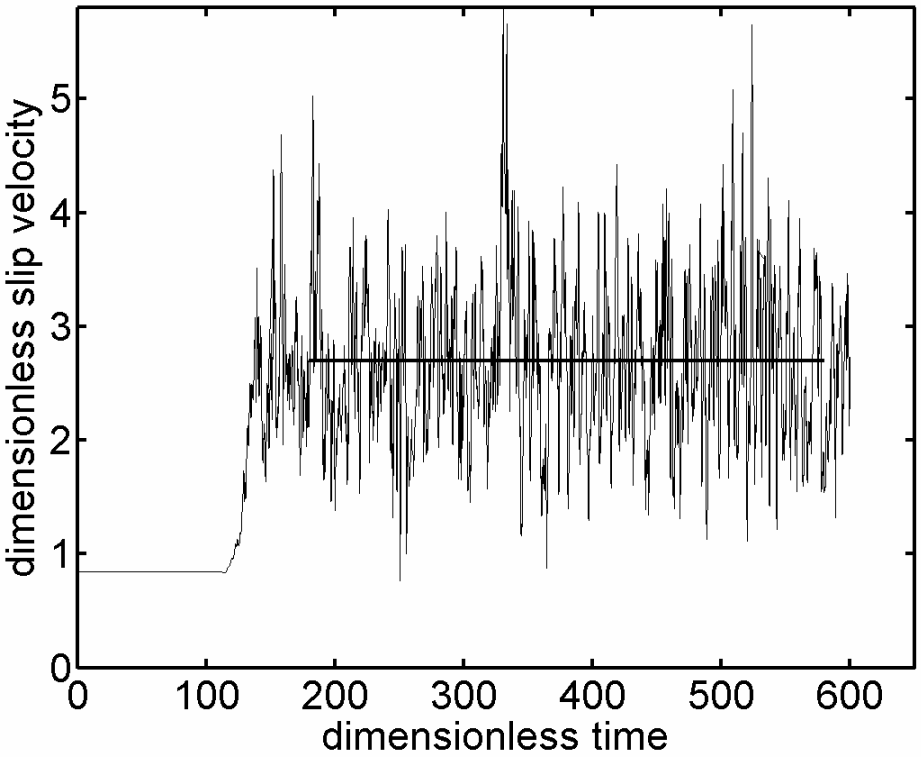
dimensionless slip velocity
0
1
2
3
4
5
0
100
200
300
400
500
600
dimensionless time

Figure 1

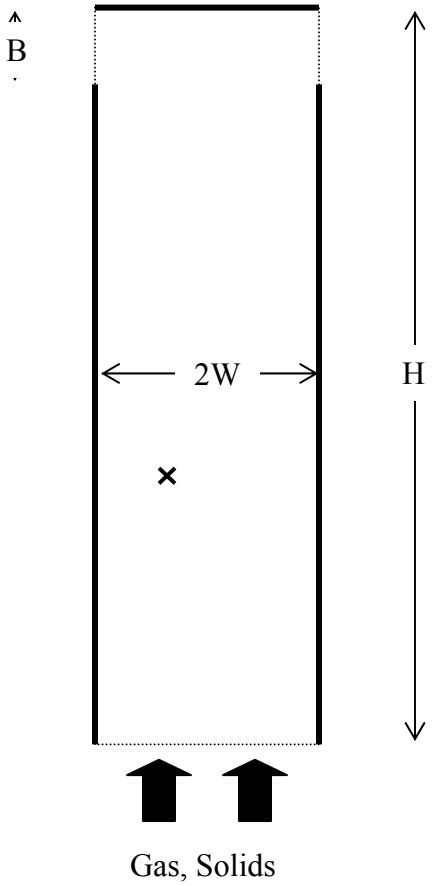

Figure 2

a

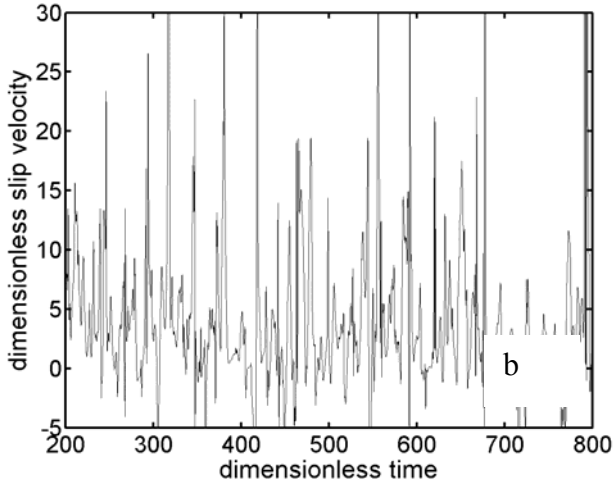
dimensionless slip velocity
dimensionless time
b

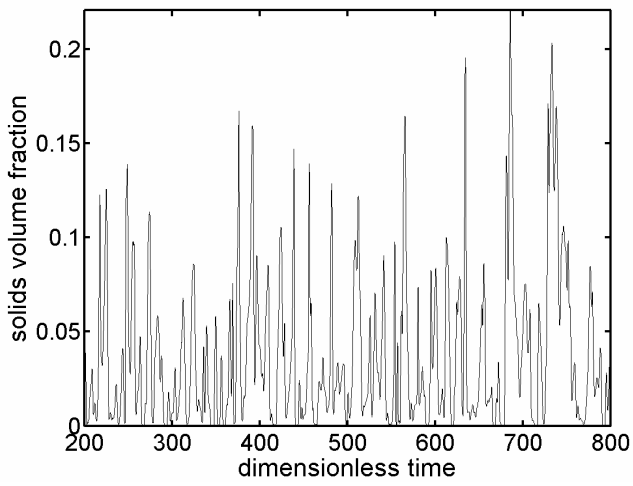
solids volume fraction
dimensionless time

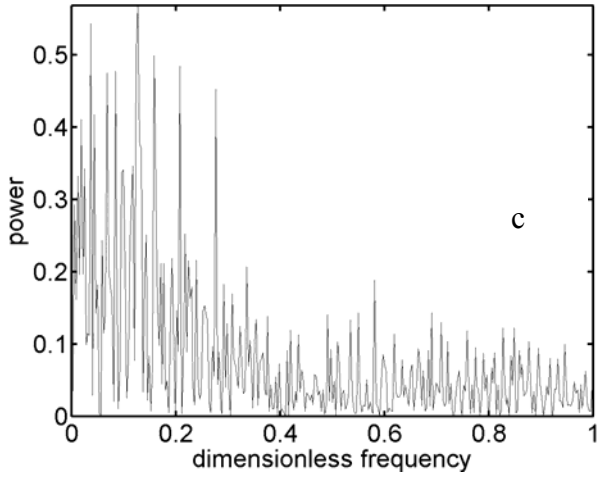
power
dimensionless frequency
c

Figure 3

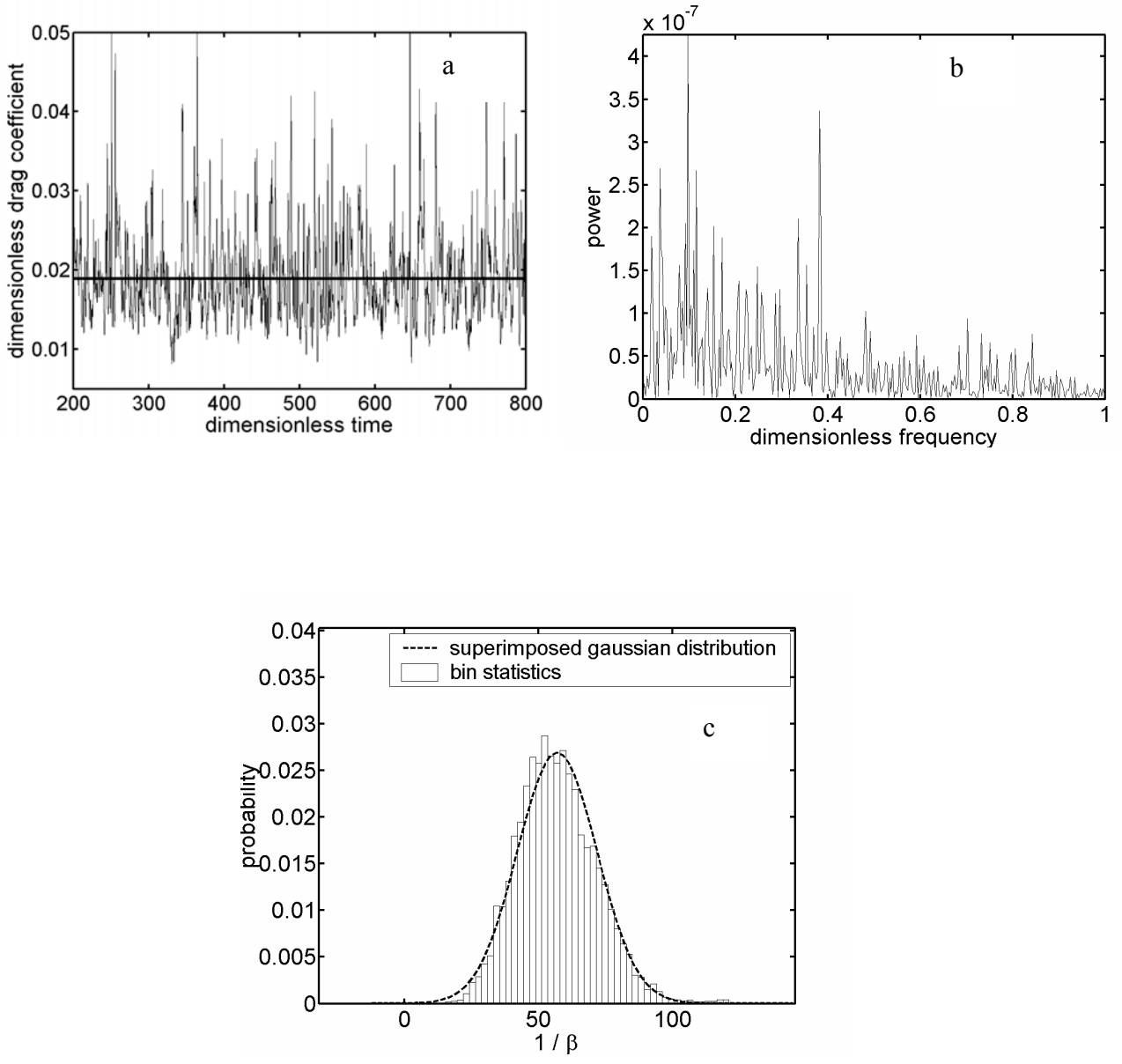
a
dimensionless drag coefficient
dimensionless time
b
x 10^-7
power
dimensionless frequency
c
superimposed gaussian distribution
bin statistics
probability
1 / β

Figure 4

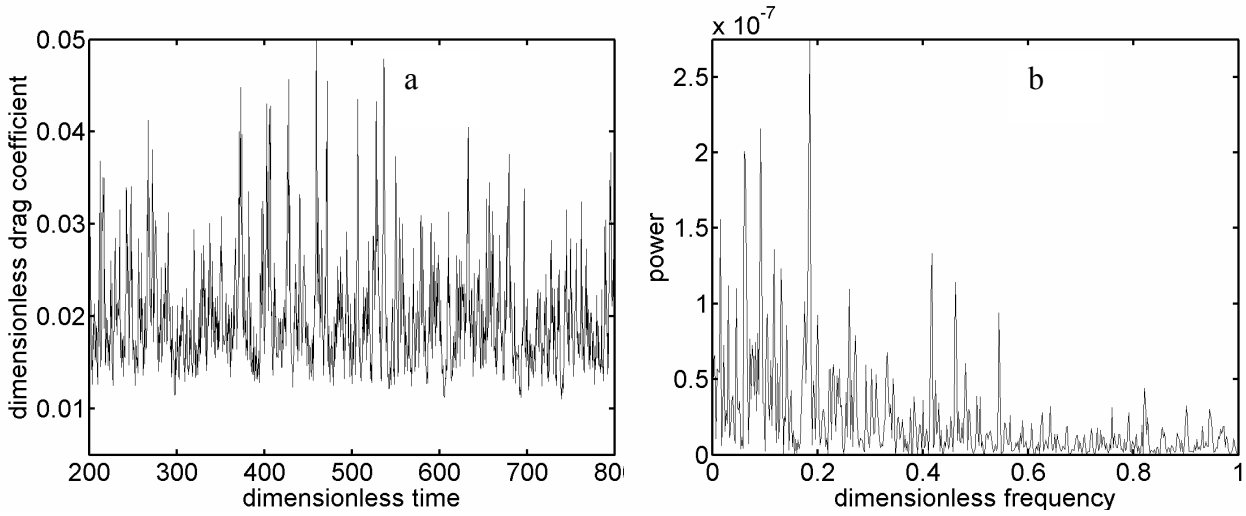
a
b
dimensionless drag coefficient
dimensionless time
power
x 10^-7
dimensionless frequency

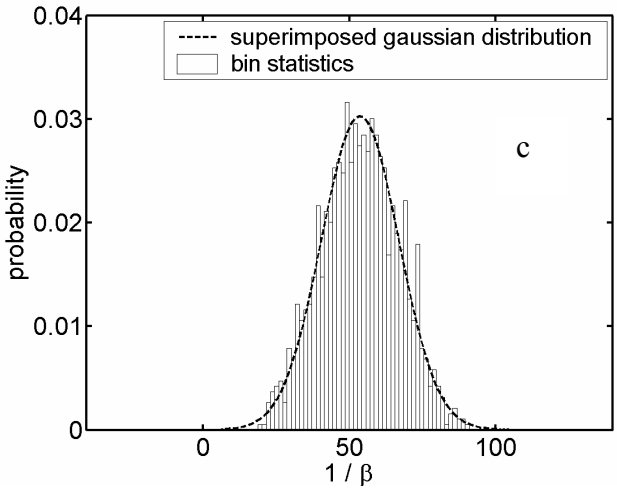
superimposed gaussian distribution
bin statistics
c
probability
1 / β

Figure 5

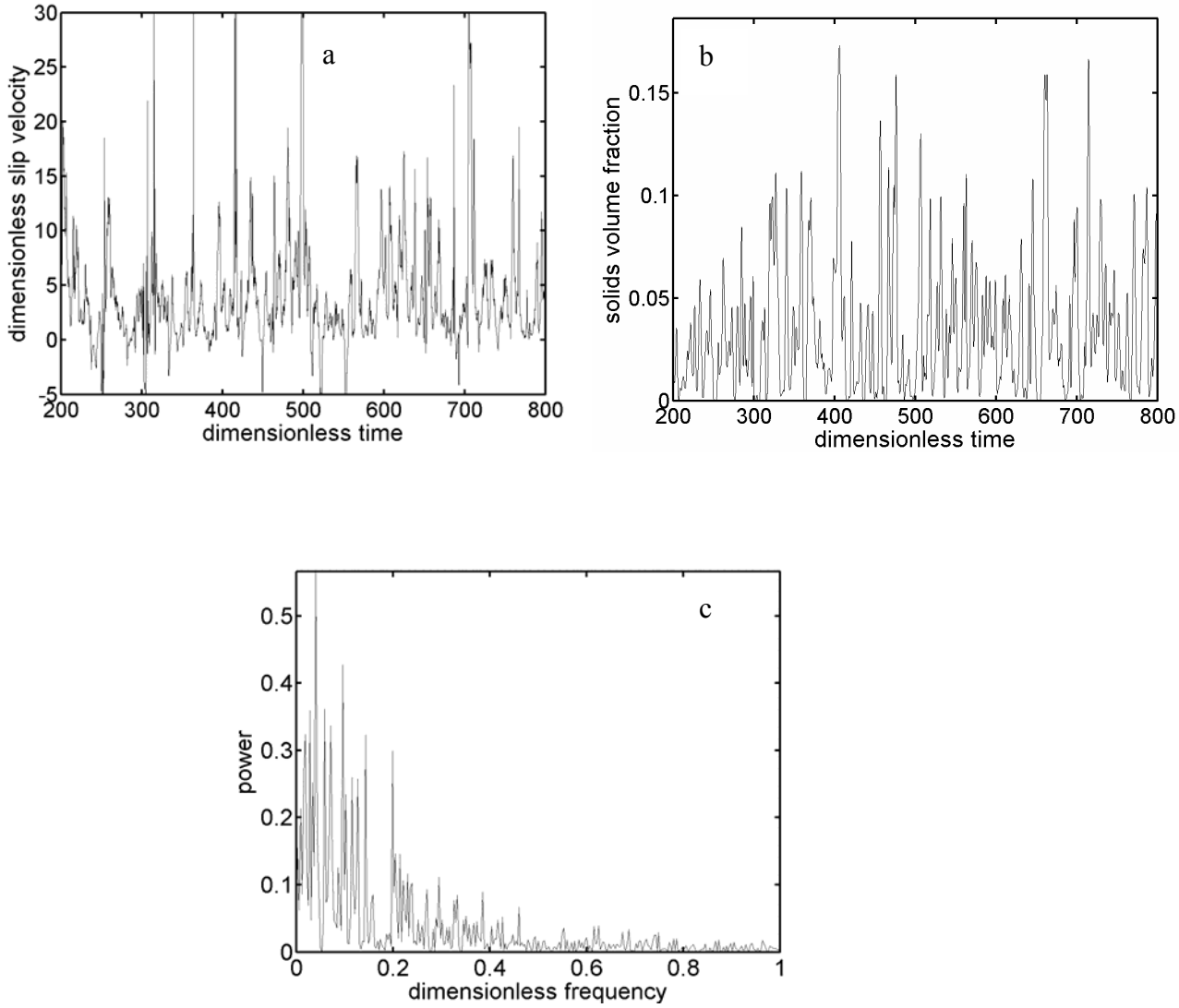
a
dimensionless slip velocity
dimensionless time
b
solids volume fraction
dimensionless time
c
power
dimensionless frequency

Figure 6

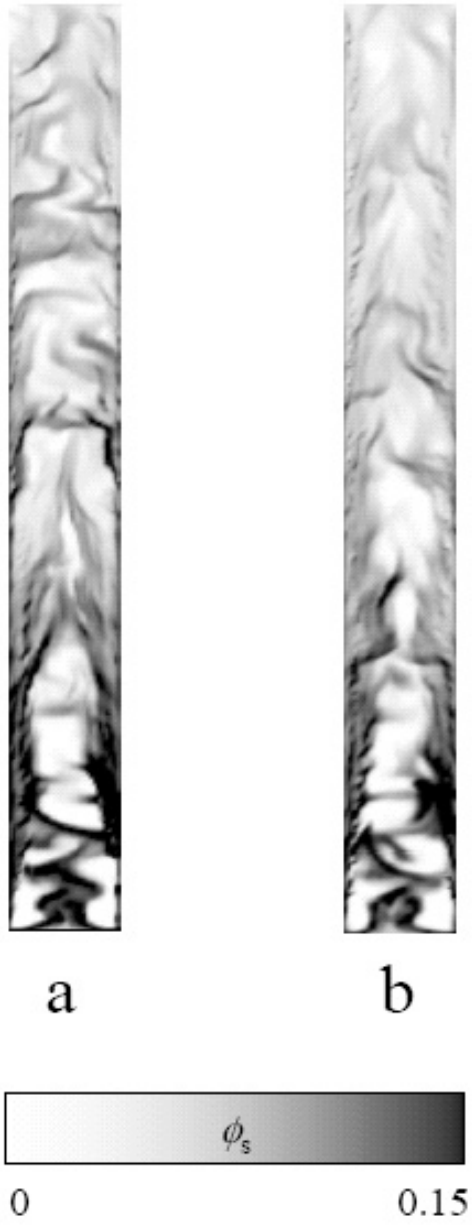

Figure 7

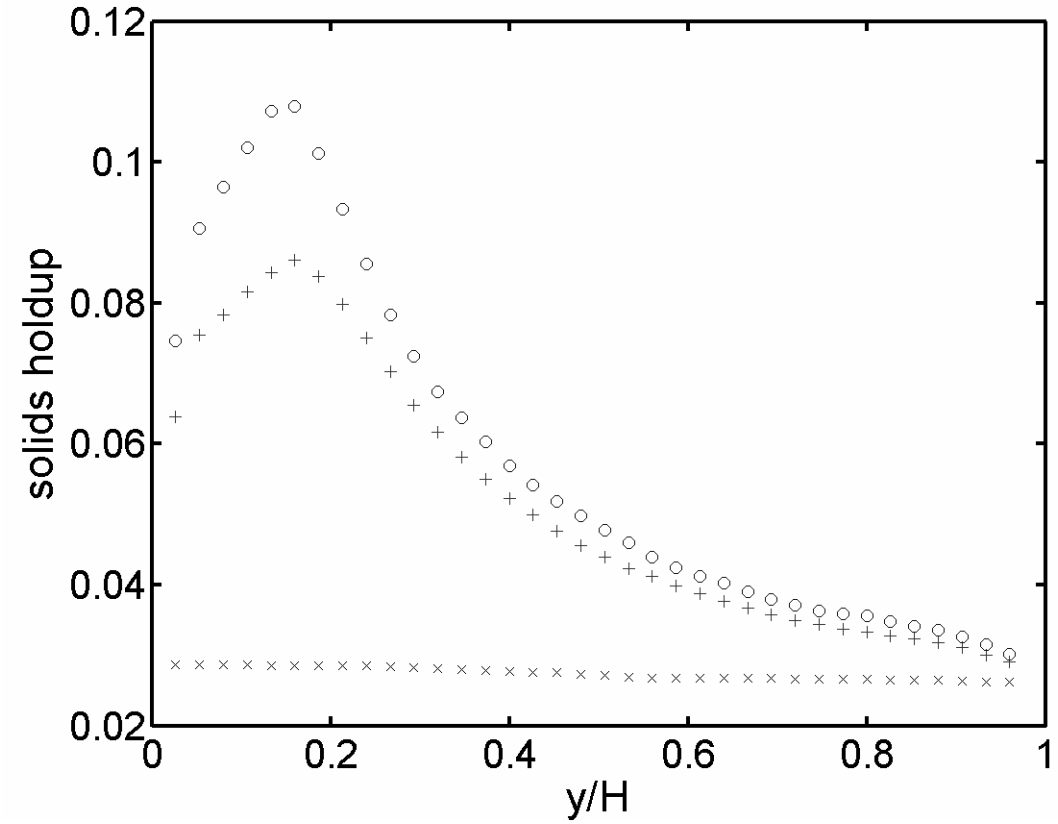

Figure 8

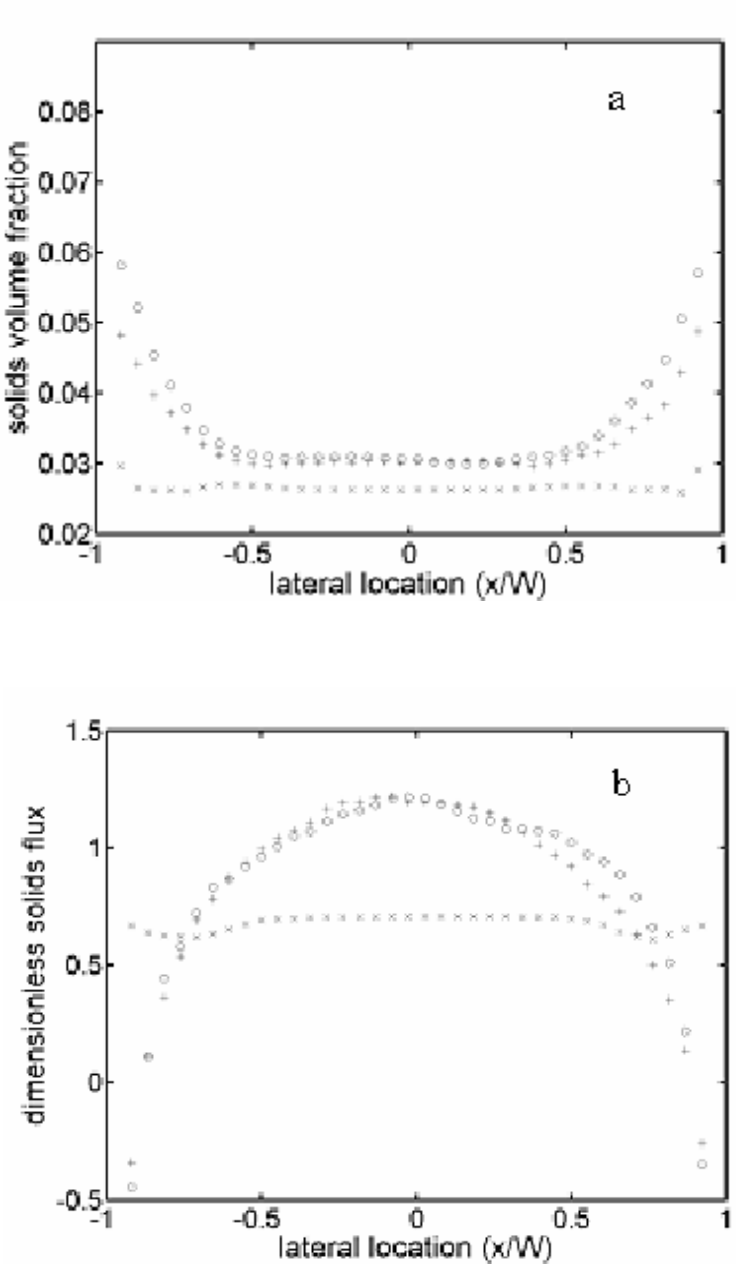
a
solids volume fraction
0.08
0.07
0.06
0.05
0.04
0.03
0.02
-1
-0.5
0
0.5
1
lateral location (x/W)
b
dimensionless solids flux
1.5
1
0.5
0
-0.5
-1
-0.5
0
0.5
1
lateral location (x/W)

Figure 9

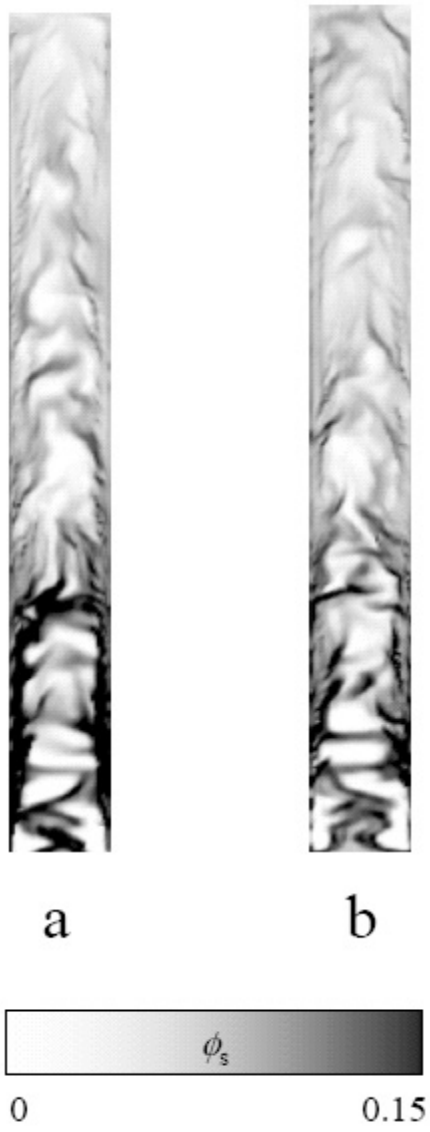

Figure 10

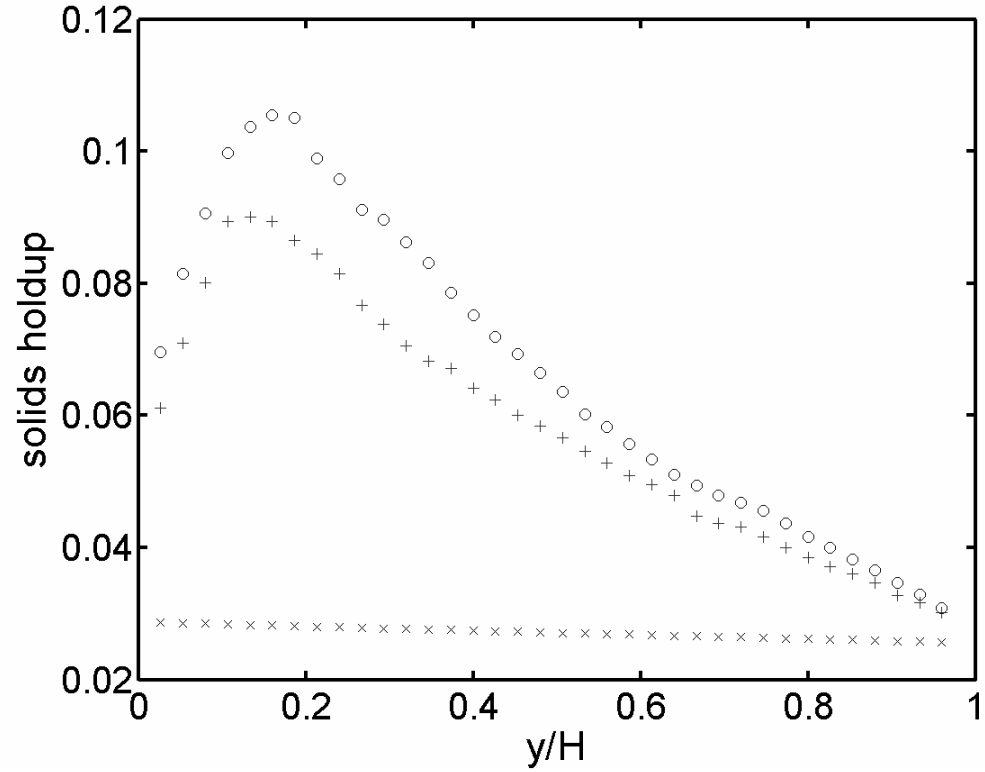

Figure 11

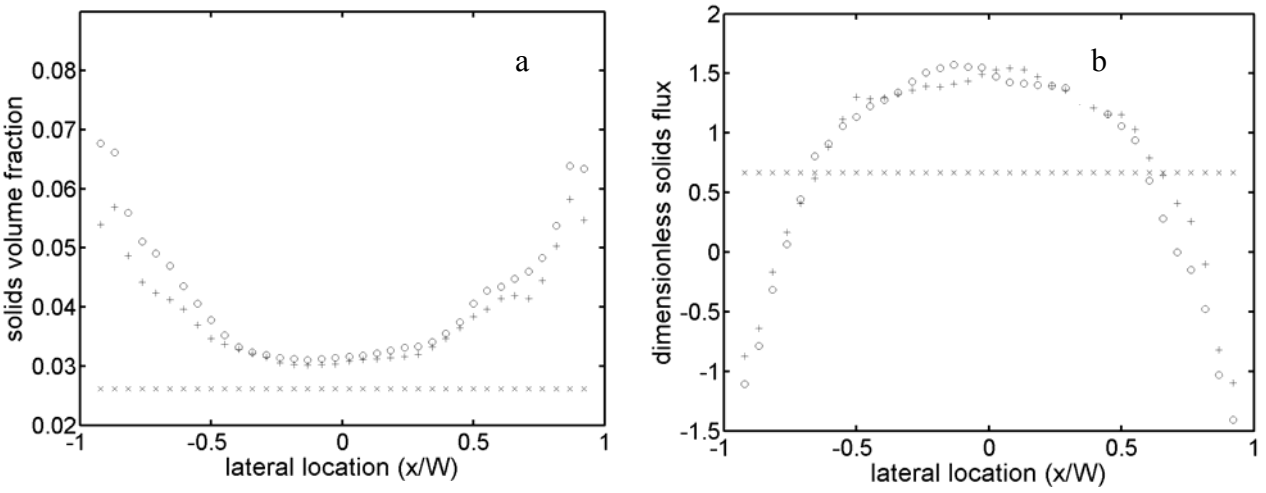
a
solids volume fraction
0.08
0.07
0.06
0.05
0.04
0.03
0.02
-1
-0.5
0
0.5
1
lateral location (x/W)
b
dimensionless solids flux
2
1.5
1
0.5
0
-0.5
-1
-1.5
-1
-0.5
0
0.5
1
lateral location (x/W)

Figure 12

Coarse-grid simulation of reacting and non-reacting gas-particle flows

Final Technical Report

Award # DE-FC26-00NT409071
DOE Vision 21 Virtual Demonstration Initiative

Appendix D

THE ROLE OF MESO-SCALE STRUCTURES ON DISPERSION IN GAS-PARTICLE FLOWS

Peter Loezos and Sankaran Sundaresan
Department of Chemical Engineering
Princeton University
Princeton, NJ, 08544

Abstract

The effect of fluctuations associated with meso-scale structures on the rate of tracer dispersion in gas-particle systems is probed. Coarse-grid simulations of gas-particle flows generally do not recognize the influence of fluctuations associated with meso-scale structures whose size is comparable to or smaller than the grid size. A sub-grid model for effective dispersion resulting from sub-grid scale fluctuations is formulated through computational experiments.

Two-dimensional coarse-grid simulations of hydrodynamics and tracer dispersion in vertical channels of various widths reveals that sub-grid scale fluctuations are important to capture the macro-scale hydrodynamics accurately, while macro-scale tracer dispersion is largely determined by fluctuations which are resolved by the coarse-grid simulations. Apparent lateral Peclet numbers obtained from our simulations are comparable to those reported in the literature.

Introduction

Experimental studies on high-velocity gas-particle flows in vertical pipes have revealed that particles are usually distributed over the cross section in a non-uniform fashion (Bader *et al*. 1988). These non-uniformities exist on a wide range of length scales, ranging from millimeters to meters. Meso-scale structures, namely clusters and streamers of particles, whose characteristic size is of the order of 10-100 particle diameters, have been observed in these flows (Horio 1995). These meso-scale structures arise as result of local hydrodynamic instabilities (Agrawal *et al.* 2001) and they have a strong influence on macro-scale hydrodynamics (Dasgupta *et al.* 1994; Agrawal *et al*. 2001). The present manuscript is concerned with the effects of such meso-scale structures on the rates of dispersion of gas and solid phase tracers in riser flows.

Given that meso-scale structures occur on a continuous spectrum of length scales down to about ten particle diameters, it is impractical to resolve them completely in CFD simulations of flows in large risers where the use of coarse grids is inevitable (Sundaresan 2000). Agrawal *et al.* (2001) have already pointed out the need for sub-grid hydrodynamic models to account for the consequence of the unresolved meso-scale structures on the effective drag and the stresses. In this paper, we explore the dispersion characteristics in these systems. In particular, we have determined through computational experiments effective dispersion coefficients, which characterize transport resulting from sub-grid scale fluctuating motion. These effective dispersion coefficients depend on grid size, particle phase volume fraction (ϕ), the terminal velocity of the particles (v_t) and the macro-scale shear rate. An approximate closure for the dispersion coefficient, generated through our computational experiments, is presented.

Coarse-grid simulations of hydrodynamics and tracer dispersion have been performed, where we have explored the impact of sub-grid corrections on the predicted flow and gas dispersion. In the examples described here, the sub-grid corrections for hydrodynamic quantities, namely drag and stresses, have a profound influence on the results. Sub-grid correction for the effective dispersion coefficient has been found to have a much smaller effect, revealing that tracer dispersion on a macro-scale is largely dictated by the velocity and concentration fluctuations resolved by the coarse-grid simulations. Our coarse-grid, two-dimensional simulations of tracer dispersion in vertical channels suggest that the effective radial Peclet number is only weakly dependent on the channel width.

Computational Experiments on Meso-scale Structures

To probe the effect of meso-scale structures on species dispersion, 2-D simulations were performed in highly resolved doubly periodic domains, as the presence of solid boundaries is not necessary to induce the formation of meso-scale structures (Agrawal *et al*. 2001). A detailed discussion of the hydrodynamic equations used in our study can be found elsewhere (Agrawal *et al.* 2001). These equations were augmented by non-reactive transport equations for gas and solid phase tracers. The MFIX code (Syamlal 1998) was modified to solve these equations. Agrawal *et al*. (2001) found that the domain-averaged hydrodynamic quantities obtained by averaging over the meso-scale structures were essentially independent of the aspect ratio of the domain, A (= height/width), when $A \geq 4$. Therefore all simulations described here were performed using an aspect ratio of 4. In dimensionless form, the width of the box, Δ_h, translates to the inverse of a Froude number, $Fr_h = v_t^2/g\Delta_h$ where g is the specific gravity force. We present below results for two domain sizes, corresponding to Fr_h of 0.486 and 0.243. Typical physical properties for the gas and solids used in our simulations are given in Table 1. For this gas-solid system, Fr_h of 0.486 and 0.243 translate to domain widths of 10 and 20 mm, respectively.

In these simulations, the gas pressure varied periodically in the lateral direction, while in the vertical direction it was partitioned into a periodic part and a linear part. The linear part contributed to a mean pressure gradient in the vertical direction whose value was chosen to balance the total gravitational force acting on the suspension. Lateral gradients in the concentrations of gas and solid phase tracers were imposed in an analogous manner. These simulations were performed using a second order discretization scheme and sufficiently small grid sizes to ensure that the results were independent of grid size. Although the state of uniformly fluidized suspension is a solution for the hydrodynamic equations, it is unstable and rapidly gives way to persistent spatio-temporal (meso-scale) structures. Instantaneous fluxes for both gas and solid phase tracers due to the motion of meso-scale structures were determined from these computations and were time-averaged to obtain mean fluxes, which were then used to a find the effective dispersion coefficients for the two phases (D_g^* , D_s^*).

Effective dispersion coefficients were computed as follows. Domain-averaged gas and solid phase mass fluxes in the lateral direction, f_{ms}^g and f_{ms}^s, were first calculated as functions of time. These fluxes are defined as:

$$f_{ms}^{g} = \left\langle ((1-\phi')\rho_g \chi_g' u_g') + ((D_g(1-\phi')\rho_g \frac{\partial \chi_g'}{\partial x}) \right\rangle; \quad f_{ms}^{s} = \left\langle (\phi' \rho_s \chi_s' u_s') \right\rangle$$

where $\langle\ \rangle$ denotes domain average, x is lateral coordinate, χ_g' and χ_s' are the local gas and solid phase tracer fractions, u_g' and u_s' are the local lateral velocities, D_g is the binary gas-phase diffusion coefficient and ϕ' is the local particle volume fraction. These were then time-averaged (denoted by over-bar) and used to find the effective dispersion coefficients.

$$\overline{f_{ms}^{g}} = D_g^{*} \rho_g (1-\phi) \frac{\partial \tilde{\chi}_g}{\partial x}; \qquad \overline{f_{ms}^{s}} = D_s^{*} \rho_s \phi \frac{\partial \tilde{\chi}_s}{\partial x}$$

where $\tilde{\chi}_g$ and $\tilde{\chi}_s$ are tracer fractions for the respective phases and ϕ is the average solids volume fraction in the periodic domain. The effective dispersion coefficients were made dimensionless using v_t and v_t/g as characteristic velocity and time. The dependence of the effective gas and solid phase dispersion coefficients on ϕ corresponding to $Fr_h = 0.486$ and 0.243 are presented in Figures 1a and 1b, respectively. The estimated values of D_g^{*} are one to two orders of magnitude higher than gD_g/v_t^3. Thus, meso-scale structures indeed serve to enhance the dispersion characteristics in these systems. It is also clear from these figures that the behavior of the gas and solid phase dispersion coefficients are well correlated. This suggests that the effective dispersion in either phase is a direct result of the motion of the meso-scale structures. In the region $0.05 < \phi < \sim 0.30$, the effective dispersion coefficients increase with ϕ, beyond which the trend reverses (Figure 1a). Agrawal *et al.* (2001) found that the rms value of the fluctuation velocities assumed their maximum values at $\phi \sim 0.30$ where cluster-to-bubbling transition begins to set in for this range of Fr_h. An explanation of the behavior seen in Figures 1a and 1b for $\phi < 0.05$ is elusive.

In gas-solid flows in vertical risers, axial variation of lateral velocity is present only in a transient fashion, but not in the time-averaged flow, whereas lateral variation of axial velocity exists even in a time-averaged sense. This consideration prompted us to explore the effects of macro-scale shear in the form of lateral variation of axial velocities of the gas and solid phases.

The effect of dimensionless macro-scale shear rate (γ) on D_g^{*} and D_s^{*} is shown in Table 2 for different values of ϕ and $Fr_h = 0.486$. In these simulations, a prescribed macro-scale shear rate is imposed across the domain. It is clear that the effective dispersion coefficients decrease as γ increases. Physically, this trend can be explained by noting that as γ increases, the meso-scale structures tend to align vertically and the horizontal fluctuations become more restricted.

Figure 2, showing D_g^{*} plotted against D_s^{*}, reveals clearly that these two are highly correlated, establishing that they arise through a common underlying mechanism. Comparing Figures 1a and 1b, we observe that the effective dispersion coefficients are inversely proportional to Fr_h. As Δ_h increases, larger meso-scale structures having higher rms velocities and traveling longer distances form, and consequently the effective dispersion coefficients increase.

For the purpose of coarse-grid simulation of gas-phase tracer dispersion, the values of D_g^* determined through computational experiments described above were correlated as:

$$D_g^* = \frac{f(\phi)h(\gamma)}{\mathrm{Fr_h}} + \frac{\mathrm{D_g g}}{\mathrm{v_t^3}} \qquad (1)$$

where $f(\phi)$ and $h(\gamma)$ are simple curve-fit functions. Sub-grid models for effective drag coefficient, particle phase viscosity and normal stresses were also constructed in a similar manner (Agrawal *et al.,* 2001).

Coarse-Grid Simulations

Coarse-grid two-dimensional simulations of hydrodynamics and gas-phase tracer dispersion in a vertical channel were performed to probe the importance of unresolved meso-scale structures on the overall flow characteristics. To this end, we compare results obtained with and without grid-size dependent sub-grid closures for drag coefficient, effective viscosities, normal stresses and dispersion coefficients. Our simulations, described below, suggest that:

- closure relations for the effects of sub-grid scale structures on the *hydrodynamic* quantities are important to properly characterize the fluctuating motion resolved by the coarse-grid simulations, and
- the macro-scale mixing characteristics depend primarily on flow behavior that are resolved by the coarse-grid simulations and to a lesser extent on the effective dispersion attributable to sub-grid scale fluctuations.

The dimensions of the vertical channel and the operating conditions are shown in Figure 3a. Four test cases, representing two different channel widths (0.75 and 1.0 m) are described below. Uniform inflow conditions were used in the simulations, see Figure 3a. Figure 3a displays a snapshot of particle volume fraction distribution obtained in a coarse-grid simulation of a 1.0 m wide channel using 50x200 cells. Darker regions correspond to regions of higher particle volume fraction. A steady stream of tracer was injected right at the bottom at the centerline of the channel. In the first set of test cases, the effective dispersion coefficient for the gas tracer species (see equation 1) was included in the simulations, while in the second set of simulations only the binary gas diffusion coefficient was used. In all these cases, the sub-grid scale closure for the hydrodynamic quantities were incorporated. We found that flow nonuniformities did not develop in these simulations if the sub-grid scale hydrodynamic corrections were not included.

Figure 3b is an instantaneous gray-scale image of the tracer concentration in a 1.0 m wide channel, revealing rapid lateral spreading of the tracer. Simulation results were averaged over a long period of time to obtain time-averaged tracer concentration distribution. Figure 4a shows the lateral variation of tracer species fraction at different elevations in the 1.0 m wide channel, when the effective dispersion coefficient was included in the simulation. Rapid spreading of the tracer is readily apparent. Our results also reveal a curious pattern near the bottom of the riser, where the tracer fraction first decreases and then increases as we go from the centerline toward the channel wall. This may be a consequence of the combined action of large-scale velocity

fluctuations and downflow (of gas and solids) near the channel walls, which transport gas pockets with high tracer concentration from the centerline to the wall region.

Lateral variation of tracer species fraction at different elevations shown in Figure 4b corresponds to the same conditions employed in figure 4a, with the exception that only the binary gas diffusion coefficient was used in the tracer dispersion calculations. Figures 4a and 4b reveal very similar tracer spreading, suggesting that the features which are resolved by the coarse-grid simulations are principally responsible for macro-scale dispersion.

From plots such as those in figures 4a and 4b, *apparent macro-scale* lateral dispersion coefficients, D^e, may be calculated readily. Experimental data on tracer dispersion are often analyzed by assuming a plug flow of gas and adjusting D^e to fit the data (Werther *et al*. 1992). It is a straightforward exercise to extract D^e from the data (in the vicinity of the centerline) shown in figures 4a and 4b. They were found to be 91 x 10^{-4} and 83 x 10^{-4} m^2/s, respectively. The percentage difference between the apparent dispersion coefficients is quite small, when compared with that between D_g^* and D_g. Therefore, we conclude that the macro-scale dispersion is largely determined by fluctuations resolved by the coarse-grid simulations.

Values for D^e (extracted from simulations using D_g^*) and lateral Peclet number, defined as $Pe = U_g W/D^e$ where U_g is the gas superficial velocity and W is the channel width, are presented in Table 3 for two different channel widths. Note that Pe remains approximately constant independent of W, i.e. the apparent radial dispersion coefficient increases roughly linearly with channel width. We have not made any quantitative comparison of our simulation results with experimental data, but we note that the computed values of Pe are close to the literature values based on experimental data, which lie in the range of 400 – 500 (Werther *et al*. 1992). Simulations were also performed with a narrower channel (W = 0.50 m), where the time-averaged flow pattern and the tracer fraction remained appreciably asymmetric even after a long simulation time; consequently, we could not extract Pe and D^e values for this case.

Conclusions

Fluctuations associated with meso-scale structures serve to enhance the rate of tracer dispersion in gas-particle systems. This may be accounted for in coarse-grid simulations through effective dispersion coefficients for the gas and particle phases, which depend on grid size, macro-scale shear rate and particle phase volume fraction and terminal velocity.

In order to probe the effects of sub-grid scale fluctuations on coarse grid simulation results, two-dimensional simulations of hydrodynamics and tracer dispersion in vertical channels of various widths were performed in the regime of fast fluidization. While sub-grid scale fluctuations are important to capture the hydrodynamics accurately, the effective dispersion directly attributable to sub-grid scale fluctuations has only a secondary effect on macro-scale tracer dispersion. The values of effective meso-scale and apparent macro-scale dispersion coefficients are separated by over an order of magnitude (~5 x 10^{-4} m^2/s for the meso-scale, and ~7 x 10^{-3} m^2/s for the macro-scale). Thus, macro-scale tracer dispersion is largely determined by fluctuations which are resolved by the coarse-grid simulations. Recall that the magnitude of the meso-scale

dispersion coefficient is a function of the grid size. Therefore, if simulations were performed using a large grid size, the effective meso-scale dispersion coefficient would be larger. Assuming our scaling with Fr_h holds, the effective meso-scale dispersion coefficient would be comparable to the apparent macro-scale dispersion coefficient, when $Fr_h \sim .017$. This suggests that structures approximately 0.30 m in length were primarily responsible for dispersion in the flow regime studied. Apparent lateral Peclet numbers obtained from our simulations are comparable to those measured experimentally.

Acknowledgement

This work was supported by ExxonMobil Research & Engineering Company, Millennium Inorganic Chemicals and the US Department of Energy CDE-FC26-00NT40971.

References

Agrawal, K., P. Loezos, M. Syamlal and S. Sundaresan, "The Role of Meso-Scale Structures in Gas-Solid Flows," J. Fluid Mech., **445**, 151-185 (2001).

Dasgupta, S., R. Jackson, and S. Sundaresan, "Turbulent Gas-Particle Flow in Vertical Risers," AIChE J. **40,** 215 – 228 (1994).

Bader, R., J. Findlay and T. M. Knowlton, "Gas/solid Flow Patterns in a 30.5 cm Diameter Circulating Fluidized Bed," In "Circulating Fluidized Bed Technology II", P. Basu, and J. F. Large (EDS.), Pergamon Press, New York, (1988) pp. 123 – 137.

Horio, M., "Cluster and Agglomerate Formation in Fluidized Suspensions," in "Proc. 2nd Int. Conf. On Multiphase Flows, Kyoto" A. Serizawa, T. Fukano and J. Bataille (EDS.), FB1-1 (1995).

Sundaresan, S., "Perspective: Modeling the Hydrodynamics of Multiphase Flow Reactors: Current Status and Challenges," AIChE J., **46**, 1102-1105 (2000).

Syamlal, M., "MFIX Documentation: Numerical Techniques". DOE/MC-31346-5824. NTIS/DE98002029 (1998).

Werther, J., E. –U. Hartage and M. Kruse, "Radial Mixing in the Upper Dilute Core of a Circulating Fluidized Bed," Powder Technology, **70**, 293 – 301 (1992).

d, particle diameter	7.5×10^{-5} m
ρ_s, solids density	1500 kg/m^3
ρ_g, gas density	1.3 kg/m^3
D_g, binary diffusivity	$.165 \times 10^{-4}$ m^2/s
μ_g, gas viscosity	1.8×10^{-5} kg/m·s
v_t, terminal settling velocity	.2183 m/s

Table 1: Physical properties used in simulations

	D_g^*			D_s^*		
ϕ	$\gamma = 0$	$\gamma = 1.12$	$\gamma = 2.23$	$\gamma = 0$	$\gamma = 1.12$	$\gamma = 2.23$
.05	0.54	0.14	0.002	1.05	0.22	0.13
.10	0.60	0.30	0.01	1.0	0.21	0.096
.20	0.73	0.27	0.02	1.24	0.25	0.13

Table 2: Effects of dimensionless shear rate (γ) and particle volume fraction (ϕ) on dimensionless effective gas and solid phase dispersion coefficients

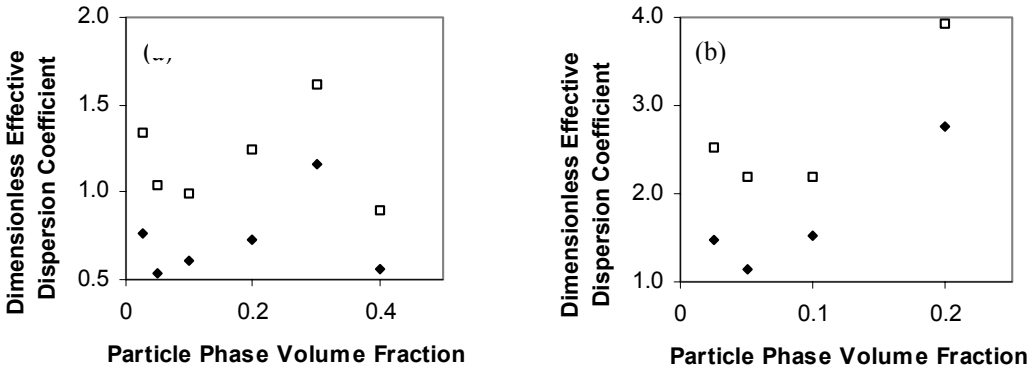

Figure 1: Dimensionless effective dispersion coefficient vs. solid volume fraction for gas (♦) and solid phases (□) for (a) Fr_h =.486, (b) Fr_h = .243. The effective dispersion coefficients were made dimensionless using v_t and v_t/g as characteristic velocity and time, respectively.

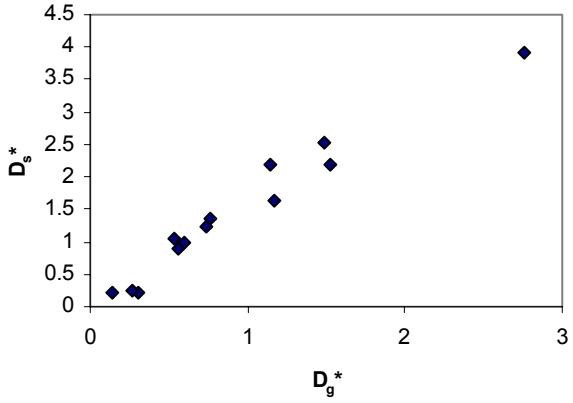

Figure 2: Effective solid-phase dispersion coefficient vs. effective gas-phase dispersion coefficient

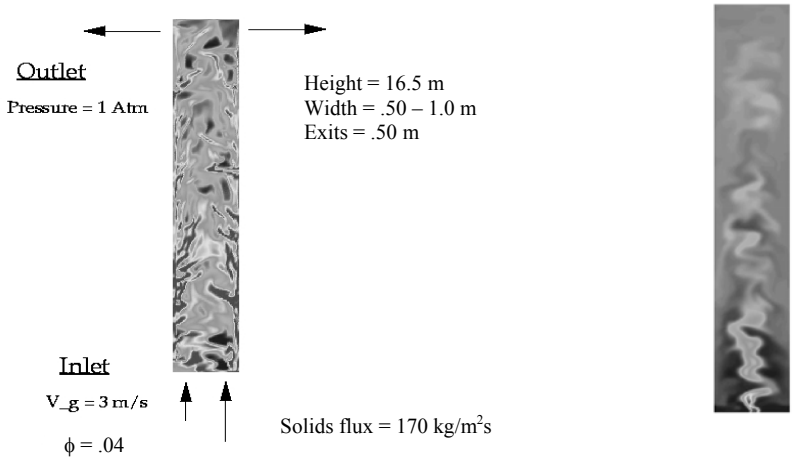

Figure 3: (a) Riser dim...s, (b) gray-scale tracer image

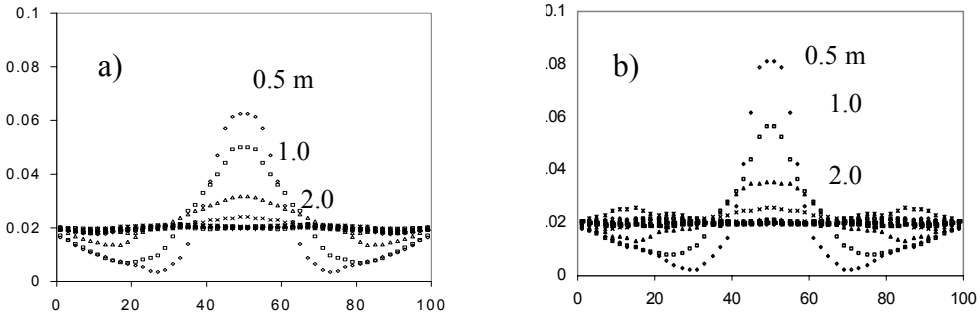

Figure 4: Tracer fraction vs. lateral location at various elevations obtained in simulations using (a) effective meso-scale dispersion coefficient , (b) binary gas diffusion coefficient. W = 1.0 m

W (cm)	D^e (m^2/s)	Pe
75	67×10^{-4}	336
100	91×10^{-4}	330

Table 3: Apparent dispersion coefficient and Peclet number for two different channel widths, U_g = 3.0 m/s

Coarse-grid simulation of reacting and non-reacting gas-particle flows

Final Technical Report

Award # DE-FC26-00NT409071

DOE Vision 21 Virtual Demonstration Initiative

Appendix E

The Effect of Static Electrification on Gas−Solid Flows in Vertical Risers

Mahdi F. Al-Adel, Dudley A. Saville, and Sankaran Sundaresan*

Department of Chemical Engineering, Princeton University, Princeton, New Jersey 08544

Steady, fully developed gas−particle flow in a vertical riser is analyzed. The model consists of axial momentum balances for the gas and particle phases, a radial momentum balance for the particle phase, and Poisson's equation for the electric field. Each particle carries a prescribed charge. Consequently, a radially varying electric field develops spontaneously, and this drives an electrophoretic flux of particles toward the wall. This is balanced by a diffusive particle flux. At steady state, these fluxes balance and produce a radially nonuniform particle volume fraction distribution. This, in turn, affects the axial momentum balance. The model captures important qualitative features of riser flows: core−annular particle distribution, annular particle downflow at low riser gas velocities, and annular upflow at high gas velocities. Furthermore, the model accurately depicts results on riser flows reported by Bader et al.

1. Introduction

Although it has been known widely that static electrification can occur in gas−solid handling devices such as fluidized beds,[1−15] circulating fluidized beds,[16−23] and pneumatic conveying systems,[22−41] progress in understanding the influence of electrostatic charges on the mechanics has remained lethargic. Although considerable progress has been made in understanding charging mechanisms,[42−44] measuring or calculating electrical charges on particles in gas−particle systems is far from simple.[2] The charging is primarily a surface phenomenon, and the magnitude and sign of the charge are quite sensitive to the state of the surface and the characteristics of the ambient gas (e.g., humidity level and temperature).[3,5,6,11,18−21,31,34,37−39] Furthermore, in some systems, all of the particles appear to carry charges of the same sign (commonly referred to as *unipolar charging*); in others, some particles are positively charged, while others are negatively charged (*heteropolar charging*).[11,13,18] In the latter case, particles tend to agglomerate and complicate the hydrodynamics. In both cases, nonuniform particle distributions can arise on a macroscopic scale as a result of static electrification; this further impacts the hydrodynamics. For example, it is well-known that the pressure gradient required for the vertical conveying of particles by a gas depends on the extent of particle charging.[20,22,23,26,29,30,33,37,38] The excess pressure gradient, which can be attributed to the presence of charges on the particles, is often called the "electrostatic pressure gradient". There is ample evidence in the literature that increasing the humidity level (e.g., see ref 20) or adding antistatic agents[16] lowers the pressure gradient required for vertical conveying. In systems with unipolar charging, the electrostatic pressure gradient is intimately related to a nonuniform particle distribution over the pipe cross section.[41]

The nonuniform distribution of particles over the cross section is ubiquitous in gas−solids flows. In horizontal and inclined pneumatic transport lines, nonuniformities arise from gravitational sedimentation in the case of large particles. With finer particles, electrostatics plays a more important role.[32,41] Lateral segregation is also observed in vertical conveying (aka riser flows), and the origin of such segregation has been a subject of much research.[45−52] Gas−solid flows in risers are accompanied by density and velocity fluctuations that vary over a wide range of length and time scales, and these fluctuations cause lateral segregation.[45−52] In fact, all of the modeling efforts in this area have focused on hydrodynamic mechanisms for segregation. We are unaware of any modeling that includes static electrification as a significant driving force, even though the experimental evidence for the influence of electrostatics is striking.

In the present study, we examined the character and extent of lateral segregation arising from static electrification in riser flows. Hydrodynamically driven segregation was deliberately suppressed. A comprehensive model would predict the amount of charge carried by the particles and how it changes with flow conditions. Such a model is beyond the scope of the present study. Instead, we postulate that the particles carry a prescribed charge and then examine the influence of this charge on the hydrodynamics. The results of calculations made with our model are fully consistent with the fully developed flow patterns reported by Bader et al.[46] for FCC particles transported in a vertical riser. The level of unipolar particle charging required to capture the Bader et al.[46] data is comparable to that determined experimentally by Jiang et al.[18] Accordingly, our results demonstrate that electrostatic effects should be considered when analyzing gas−solid flows. At the very least, thorough, quantitative assessments should be made before their influence is ignored. It follows as a corollary that more experimental work probing static electrification in gas−solid flows is needed.

This paper is organized as follows. Section 2 presents a brief summary of literature data on electrostatic charges on particles in gas−solid flows. Here, we conclude that surface charge densities on the order of 10^{-7} C/m^2 (based on exterior surface area) are consistent with data reported by many researchers. Section 3

* To whom correspondence should be addressed. E-mail: sundar@princeton.edu. Phone: (609) 258-4583. Fax: (609) 258-0211.

10.1021/ie010982w CCC: $22.00
Published on Web 00/00/0000 **PAGE EST: 10.4**

Table 1. Summary of Data Reported by Ally and Klinzing[38]

tube material	particles	charge (μC/m^2)	kg of H_2O per kg of solid
copper	P004 glass, 75 μm	500	10^{-3}
	crushed glass, 314 μm	0.5	10^{-2}
	P008 glass, 150 μm	150	10^{-3}
	plexiglas, 145 μm	15	10^{-2}
plexiglas	P004 glass, 75 μm	50	10^{-3}
	P008 glass, 150 μm	15	10^{-3}
	plexiglas, 145 μm	120	10^{-2}
	copper, 196 μm	150	10^{-2}
glass	copper, 196 μm	2000	10^{-2}
	plexiglas, 145 μm	15000	10^{-3}

Table 2. Literature Data on Particle Charge in Pneumatic Conveying

material	charge density (μC/m^2)	reference
Illinois #2 coal (5 μm)	0.01	Gupta et al.[28]
charcoal (5 μm)	1.0	Gupta et al.[28]
latex (100 μm)	1−10	Nieh et al.[41]
alumina (60 μm)	1.0	Nieh et al.[41]
magnesia (30 μm)	0.01	Soo Trezek[40]
polystyrene (1 mm)	1−10	Gajewski[34]
plastic resin (30 μm)	4	Dahn[25]
plastic (20 μm)	0.6	Dahn[25]
flour (40 μm)	25.5	Dahn[25]
HDPE (3 mm)	0.9	Dahn[25]
glass beads (550 μm)	1−2	Nieh and Nguyen[39]
FCC particles (76 μm)	0.1−0.2	Jiang et al.[18]

describes a simple model for the steady, fully developed flow of a gas−particle mixture in a vertical pipe, where we assume that all of the particles are of the same size and carry the same amount of (unipolar) charge. In section 4, we describe our computational results and compare them with the data of Bader et al.[46] The key findings are summarized in section 5.

2. Literature Data on Static Electrification in Gas−Particle Flows

The electrostatic charge content of particles is usually reported in the literature on a mass basis (C/kg). We have converted all of these data to an (exterior) surface charge density using the reported particle size. Table 1 presents a summary of particle charge measured by Ally and Klinzing[38] in their experiments on pneumatic conveying in a 1-in. vertical pipe. It is clear from this table that the charge level depends on the tube material, particles, and humidity level.

Nieh and Nguyen[39] studied horizontal pneumatic transport of 550-μm glass beads in a 2-in. Cu pipe and found that the charge level increased with gas velocity and decreased with increasing humidity. A typical value for the surface charge density reported by these authors is 1 μC/m^2.

It is well-known that the variation of the pressure gradient with gas velocity (at a fixed particle flux) in vertical pneumatic conveying is U-shaped. Joseph and Klinzing[20] found that the location of the left limb was sensitive to the relative humidity (RH), which could be attributed to the dependence of the extent of static electrification on RH.

Table 2 summarizes data on charge accumulation on various materials during pneumatic conveying applications. Table 3 presents similar results obtained in the freeboard region of fluidized beds.

Chang and Louge[16] presented striking evidence for the effect of an antistatic agent on riser flow. At a specified combination of gas and plastic particle fluxes, the holdup of particles in the riser decreased appreciably (by over a factor of 2) upon the addition of an antistatic agent.

Table 3. Literature Data on Particle Charge in Fluidized Beds

material	charge density (μC/m^2)	reference
glass beads (35 μm)	1	Fasso et al.[15]
porcelain (2 μm)	0.1	Tardos and Pfeffer[14]
glass beads (200−250 μm)	0.1	Fujino et al.[2]
neobeads (200−540 μm)	0.1	Fujino et al.[2]
PMMA (540 μm)	0.1	Fujino et al.[2]
polyamide (75 μm)	0.003	Ali et al.[12]
polystyrene (475 μm)	1−10	Wolny and Kazmierczak[11]

Jiang et al.[18] studied the transport of FCC particles at a gas velocity of 2 m/s in a 10.2-cm-i.d. vertical pipe made of Plexiglas. They found that all of the particles carried the same sign of charge and that the charge level varied from 0.2 μC/m^2 at a RH of 14% to 0.1 μC/m^2 at a RH of 40%. The presence of the electrostatic charge was believed to have decreased the tendency of the particles to form clusters. (In systems such as polymer particles, the particles tend to acquire bipolar charges, and this enhances clustering.[18]) The charge level was found to be roughly independent of particle mass flux over the range studied [5−20 kg/(m^2 s)]. These authors found a measurable difference in the solids holdup profile with humidity level. For example, at a RH of 14% and a solids flux of 16.1 kg/(m^2 s), the volume fractions of particles in the core and wall regions were 0.01 and 0.04, respectively. At a RH of 40% and the same solids flux, the corresponding solids volume fractions were 0.018 and 0.032. Although the precise reason for the dependence of the particle concentration profile on humidity is not known, it is natural to suspect that static electrification might have been responsible. As RH increases, the charge level decreases, and the electrophoretic flux toward the wall is diminished.

It is clear from the data summarized here that the surface charge densities can vary widely from system to system. At the same time, one can also see that a surface charge density of ~0.1 μC/m^2 is on the lower end of the range reported in the literature. It will become clear in section 4 that even such a small surface charge density can give rise to an appreciable radial segregation of particles in riser flows.

3. Model for Steady, Fully Developed Flow in a Riser

We use a simple model of steady, fully developed flow of gas−particle mixtures in a vertical pipe. It is assumed that the particles are uniform in size and that each carries the same amount of charge. Let the charge density (based on external surface area) be σ (C/m^2), so that each particle has a charge of $\pi d^2\sigma$. A radially varying electric field develops in the riser because of the charged particles. The structure of the field follows from the solution of Poisson's equation. This field imparts an electrical force on the particles, which causes them to drift toward the wall. This electrophoretic flux increases the concentration of particles near the wall region and decreases the concentration in the core. This flux is balanced by a diffusive flux of particles from the region of high ϕ (i.e., wall region) to the region of low ϕ

(i.e., tube axis). At steady state, these fluxes balance one another. The particles and the accompanying electrical effects influence the radial momentum balance in two ways. First, the electric field acting on the particles provides a body force. Second, the diffusive flux shows up as a gradient in the particle-phase pressure, $p_s(\phi)$.

The simple model presented here consists of steady-state axial momentum balances for the gas and particle phases, the Poisson equation for the electric potential and the steady-state radial momentum balance for the particle phase. To present these equations in dimensionless form we use the particle density (ρ_s), terminal velocity (v_t), tube radius (R), $\rho_s gR$ and $6R^2\sigma/\epsilon_o d$ as the characteristic density, velocity, length, pressure, and potential, respectively.

The axial momentum balance for the gas phase takes the form

$$-\frac{dp}{dz}+\frac{\phi}{(1-\phi)^{n-1}}(V_s-V_g)=0 \tag{1}$$

where p is the dimensionless pressure in the gas phase; z is the dimensionless axial variable (with the z axis pointing vertically upward); V_g and V_s are dimensionless gas- and solid-phase axial velocities, respectively; and n is the Richardson−Zaki exponent. The deviatoric stress term is not included as its role is negligible in flows with high solids mass loadings (e.g., see Agrawal et al.[52]).

The axial momentum balance for the particle phase takes the form

$$\frac{\phi}{(1-\phi)^{n-1}}(V_g-V_s)-\phi+\frac{1}{\xi}\frac{d}{d\xi}\left[\left(\frac{v_t\mu_s}{\rho_s gR^2}\right)\xi\frac{dV_s}{d\xi}\right]=0 \tag{2}$$

where the three terms represent the gas−particle drag, the body force due to gravity, and the viscous forces, respectively. Here, ξ and μ_s denote the dimensionless radial coordinate and dimensional viscosity associated with fluctuations at all length and time scales, respectively. The Archimedean buoyancy term is negligible in our work as $\rho_s\phi \gg \rho_g(1-\phi)$.

Poisson's equation, in dimensionless form, is

$$\frac{1}{\xi}\frac{d}{d\xi}\left[\epsilon(\phi)\xi\frac{d\Psi}{d\xi}\right]=-\phi \tag{3}$$

where Ψ is the dimensionless potential and $\epsilon(\phi)$ is the effective dielectric constant of the gas−solid mixture. Here, we have used a simple relation $\epsilon(\phi)=1+3.5\phi^{1.25}$ to represent the effect of the particles.The dielectric constant of the solid particles was taken to be 4.5, which is satisfied by this equation. This expression was obtained by curve-fitting the Bruggeman[61] equation for the effective dielectric constant of a mixture. We simply mention that we have repeated our simulations for various functional forms, including $\epsilon(\phi)=1+3.5\phi$ and $\epsilon(\phi)=1$, and verified that the general features of the solutions reported below are not dependent on the specific choice made for $\epsilon(\phi)$.

The radial momentum balance for the particle phase takes the form

$$\phi\left(\frac{36R\sigma^2}{\epsilon_o d^2\rho_s g}\right)\left(\frac{d\Psi}{d\xi}\right)+\left(\frac{1}{\rho_s gR}\right)\frac{dp_s}{d\xi}=0 \tag{4}$$

where the first term represents the force due to the electric field and the second term is the gradient in the particle-phase pressure. Here, the particle-phase pressure includes contributions arising from fluctuations at all velocity scales.

Closures for the particle-phase pressure and viscosity relations are needed before we can proceed further. Riser flows are accompanied by persistent fluctuations covering a wide range of length and time scales.[52] It is known that these fluctuations can give rise to a non-uniform distribution of particles over the cross section of a riser[45−52] even in the absence of any electrostatic effect. Sinclair and Jackson[45] attempted to explain this segregation of particles on the basis of fluctuations at the level of the individual particles. Dasgupta et al.[49] brought into the analysis the effect of velocity fluctuations occurring on a larger length scale through a $K-\epsilon$ model. Hrenya and Sinclair[51] proposed a model that combines the effects of the larger-scale and particle-scale fluctuations. Computational fluid dynamics simulations attempt to simulate the large-scale fluctuations occurring over a slow time scale and average over the fast fluctuations at short length and fast time scales (e.g., see Agrawal et al.[52]). Strictly speaking, if electrostatic effects are important, one should couple the hydrodynamic and electrostatic segregation mechanisms and analyze their combined influence. Here, however, we concentrate exclusively on segregation due to electrostatic effects and suppress all of the hydrodynamic segregation mechanisms. With this in mind, we choose a closure for the particle-phase pressure that curtails segregation in the absence of electrostatics. Accordingly, we employ the following expressions for the effective viscosity and pressure in the particle phase

$$\mu_s \equiv \mu_s^o\langle\phi\rangle = \rho_s\langle\phi\rangle\frac{UR}{300} \tag{5}$$

and

$$p_s=\frac{\rho_s\phi U^2}{400} \tag{6}$$

where U is the riser gas velocity, ϕ is the particle volume fraction (function of radial position), and $\langle\phi\rangle$ is the cross-sectional average particle volume fraction (i.e., holdup). Appendix A describes an analysis of fluctuations at different scales to support the choice of these relations.

Introducing these expressions into eqs 2 and 4, we have

$$\frac{\phi}{(1-\phi)^{n-1}}(V_g-V_s)-\phi+\frac{1}{\xi}\frac{d}{d\xi}\left(M_s^o\langle\phi\rangle\xi\frac{dV_s}{d\xi}\right)=0 \tag{7}$$

$$Q\phi\left(\frac{d\Psi}{d\xi}\right)+\frac{d\phi}{d\xi}=0 \tag{8}$$

where

$$M_s^o=\frac{\mu_s^o v_t}{\rho_s gR^2}=\frac{Uv_t}{300gR} \tag{9}$$

and

$$Q=\frac{(14400)R^2\sigma^2}{\epsilon_o d^2\rho_s U^2}. \tag{10}$$

These equations are supplemented with conditions at the axis of the tube, where center symmetry is enforced, and at the wall, where the electric potential assumes a specified value. As only a spatial derivative of the potential appears in the model, one can take

$$\Psi|_{\xi=1} = 0 \tag{11}$$

without loss of generality.

The particle-phase boundary condition at the wall is not fully understood. Some authors have suggested that the pressure gradient is almost completely associated with holdup in risers of large cross-sectional area;[16,62] thus, a free-slip condition for the particle phase is not unrealistic. Other possibilities, where one demands that the particle phase and/or the gas phase satisfies the no-slip condition (e.g., Gidaspow[50]), have also been discussed in the literature. A partial-slip boundary condition for the particle phase has also been applied (e.g., see Sinclair and Jackson[45]). We investigated both free-slip and no-slip boundary conditions for the particle phase to examine the sensitivity of the results to this boundary condition. The core−annulus flow pattern with downflow in the annular region at low gas velocities and annular upflow at high gas velocities is obtained with either boundary condition (Al-Adel[56]). To illustrate the role of electrostatics, we present results obtained with the free-slip boundary conditions here. With a free-slip boundary, one can readily show that

$$\frac{dp}{dz} = -\langle\phi\rangle$$

The cross-sectional average gas and solids fluxes can be written as

$$U_g^* = \frac{U_g}{v_t} = 2\int_0^1 \xi(1-\phi)V_g(\xi)\,d\xi \tag{12}$$

and

$$U_s^* = \frac{G_s}{\rho_s v_t} = 2\int_0^1 \xi\phi V_s(\xi)\,d\xi \tag{13}$$

where U_g and G_s denote the riser gas velocity and solids mass flux, respectively. The corresponding dimensionless quantities are U_g^* and U_s^*.

One can readily combine eqs 3 and 8, eliminate Ψ, and obtain an equation describing the radial variation of ϕ

$$\frac{1}{\xi}\frac{d}{d\xi}\left(\frac{\epsilon(\phi)}{Q\phi}\xi\frac{d\phi}{d\xi}\right) = -\phi$$

For specified values of Q and $\langle\phi\rangle$, this equation can be solved separately to determine the radial variation of ϕ. Thus, the radial distribution of particles is simply dictated by the charge density and the average holdup and is determined by the radial momentum balance and the Poisson equation. The average holdup for a *specified combination of fluxes* can be found only by solving the axial momentum balance equations.

We solved the complete system of equations 1, 3, 7, 8, 12, and 13 as a boundary-value problem by discretizing the spatial derivatives using a central difference scheme. For specified values of U_g^* and U_s^*, the solutions could be found for a range of values of Q by a simple continuation method. Specifically, starting from the analytical solution for $Q = 0$, the solutions for various Q values were found by changing Q by small increments (using the solution for the previous Q value as the initial guess). The average holdup, $\langle\phi\rangle$, is an output in such calculations. As discussed in the next section, turning points were encountered, with multiple solutions for some values of Q. A slightly different approach, where we specified $\langle\phi\rangle$, determined Q as an output, and performed continuation in $\langle\phi\rangle$, was computationally more expedient for tracing the family of solutions for a range of Q values.

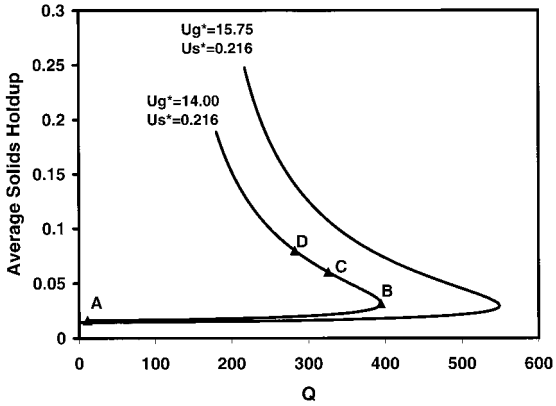

Figure 1. Average solids holdup vs Q for two different gas velocities at a fixed solid flux. See Table 4 for parameter values.

Table 4. Parameter Values Used in the Simulations

particle diameter	76 μm
particle density	1714 kg/m^3
terminal velocity	26.42 cm/s
riser radius	15 cm

Results and Discussion

Figure 1 shows the cross-sectional average holdup of particles in the riser, $\langle\phi\rangle$, as a function of Q for two combinations of U_g^* and U_s^*. The line labeled with four points (A−D) corresponds to conditions for which Bader et al.[46] reported experimental data. These authors studied the transport of FCC particles by ambient air in a 15-cm-i.d. vertical riser. Table 4 summarizes the parameter values corresponding to their experiments. They measured the radial variation of particle volume fraction (using γ-ray densitometry) at a gas velocity of 3.7 m/s and a solids mass flux of 98 kg/(m^2 s), which, in dimensionless form, corresponds to $U_g^* = 14.00$ and $U_s^* = 0.216$. (These authors also reported the radial variation of solids mass flux at another operating condition, which will be discussed later.) As noted in the Introduction, in the present study, we do not attempt to predict the value of σ for any operating conditions. Therefore, we cannot identify a specific value of Q for a specific experiment. It follows from eq 10 that $Q \approx O(10^3)$ when $\sigma \approx 10^{-7}$ C/m^2. Surface charge densities of this magnitude are easily achieved on FCC particles,[18] so the Q values explored in Figure 1 are quite reasonable.

Because we ignore hydrodynamic mechanisms for segregation in our model, the particle concentration is uniform when $Q = 0$. Hence, the velocity profile is uniform when a free-slip boundary condition is employed (and parabolic with a no-slip boundary condition). As Q increases, the average holdup increases (see Figure 1). This increase translates into an increase in

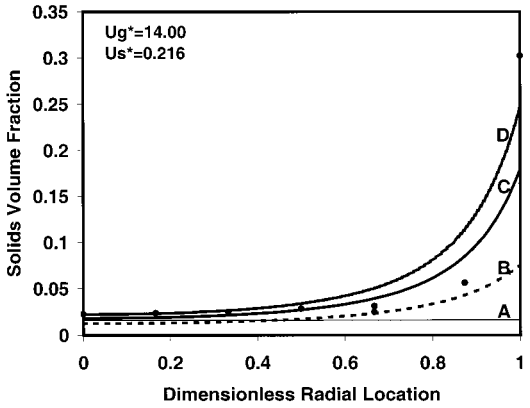

Figure 2. Particle volume fraction as a function of dimensionless radial position corresponding to the points A−D marked in Figure 1. (●) Experimental data of Bader et al.[46]

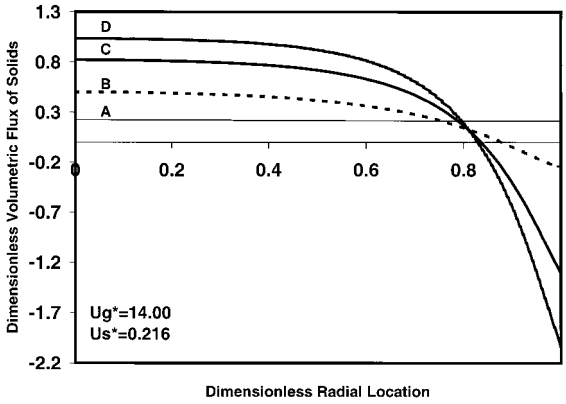

Figure 3. Dimensionless volumetric flux of solids as a function of dimensionless radial position corresponding to the points A−D marked in Figure 1.

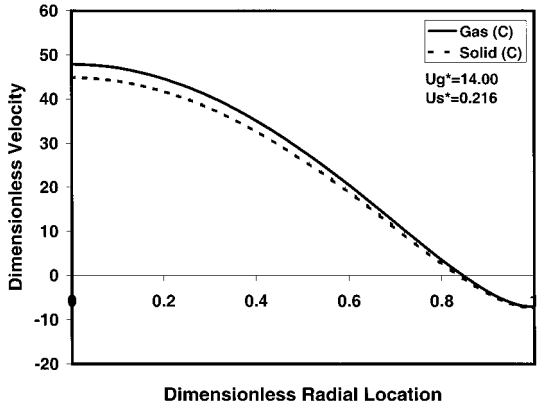

Figure 4. Dimensionless gas and solid velocities as a function of dimensionless radial position for point C in Figure 1.

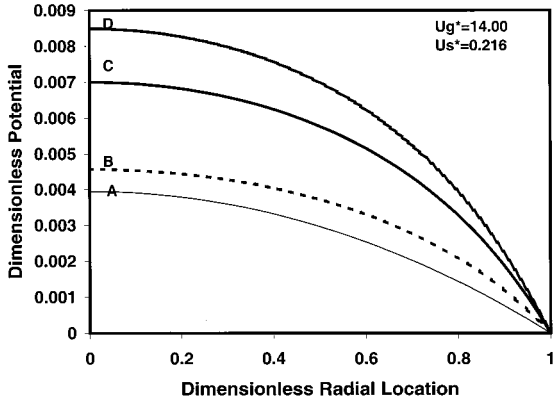

Figure 5. Dimensionless potential as a function of dimensionless radial position corresponding to the points A−D marked in Figure 1.

the pressure gradient, often called the *electrostatic pressure gradient* in pneumatic conveying.[20] Figure 1 shows that a turning point is encountered at a critical value of Q, so one can loosely talk of a lower branch and an upper branch.

The radial variations of the solids volume fraction for the four different points labeled A−D in one of the curves in Figure 1 are presented in Figure 2, along with the experimental data of Bader et al.[46] It is clear from Figure 2 that the extent of particle segregation increases steadily as the holdup increases (from A to D). Moreover, the core−annular flow structure is readily apparent at high segregation levels. The model predictions are qualitatively similar to the experimental data, although a quantitative match is not obtained for any particular value of Q. It should be noted, however, that, although the experimental data on radial variation of particle volume fraction obtained by γ-ray densitometry are qualitatively correct, they are by no means quantitatively accurate.

Figure 3 shows that radial variation of solids flux (ϕV_s) for the conditions shown in Figure 2; Figure 4 describes the gas- and particle-phase velocities for point C. It is clear from Figures 2 and 3 that, as the extent of radial segregation of particles increases, the solids flux becomes increasingly nonuniform. At sufficiently large segregation levels, one obtains downflow in the annular region with this example. Both particle and gas downflows are present as illustrated in Figure 4.

The radial profiles of the dimensionless potential for the cases shown in Figure 2 are displayed in Figure 5, which indicates that the largest magnitude of $d\Psi/d\xi$ occurs at the wall. In terms of dimensional quantities, the largest potential gradient was ~1 kV/cm (for case D in Figure 5), which is well below the field strength where dielectric breakdown occurs. Thus, the results shown in this figure are not unrealistic.

Figure 1 shows the holdup as a function of Q for two different gas velocities at a fixed solid flux. The general trend is clearly robust. As the gas velocity increases, the turning point shifts to larger Q values. Note that the upper branches of the curves in this figure have not been continued beyond some level. The only restriction placed in the mathematical model as presented is that $\phi < 1$. In reality, sustained contact between neighboring particles will occur when the particle volume fraction exceeds a threshold value, and the particle-phase pressure will rise rapidly with volume fraction beyond that point. Furthermore, it will be impossible to compress the assembly beyond some limit without crushing the particles, which is often taken in flow problems to be the volume fraction at random close packing, ϕ_{max}. Strictly speaking, the closures described in eqs 5 and 6 should be modified to capture this restriction; this point will be addressed briefly at the end of this paper. At this stage, we simply note that the curves in Figure 1 were terminated when the particle volume fraction at the wall is equal to ϕ_{max}.

Figure 6 shows the holdup as a function of Q for other operating conditions with the gas velocity held constant for changing solids flux. The shapes of the curves are qualitatively similar to those of Figure 1. The particle flux profile corresponding to four different points in one

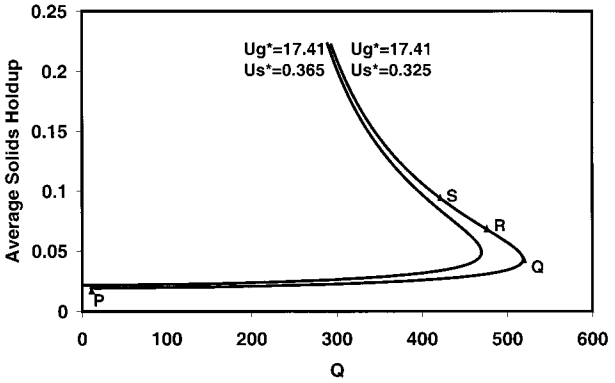

Figure 6. Average solids holdup vs *Q* for two different solid fluxes at a fixed gas velocity. See Table 4 for parameter values.

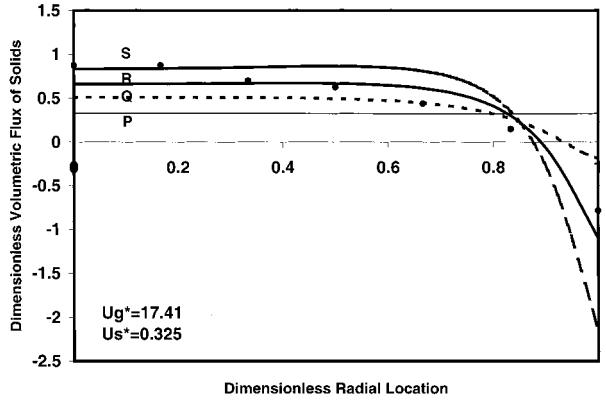

Figure 7. Dimensionless volumetric flux of solids as a function of dimensionless radial position corresponding to the points P−S marked in Figure 6. (●) Experimental data of Bader et al.[46]

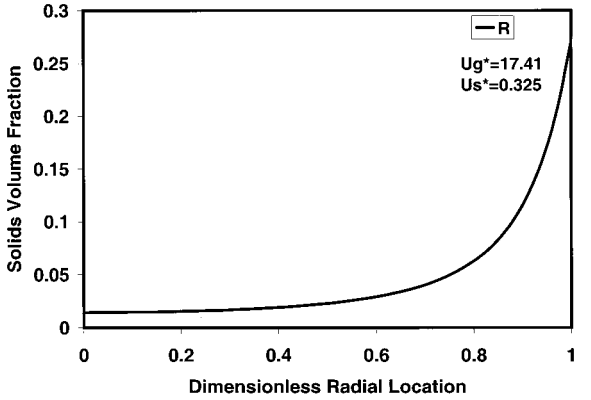

Figure 8. Particle volume fraction as a function of dimensionless radial position corresponding to point R in Figure 6.

of these curves is shown in Figure 7, with the experimental data of Bader et al.[46] The downflow in the annular region recorded by Bader et al. can be captured reasonably well by postulating the presence of an appropriate level of charge (e.g., that corresponding to point R). The solids volume fraction profile for point R in Figure 7 is displayed in Figure 8, where the core−annular flow structure is clearly apparent. The corresponding gas and solid velocity profiles are presented in Figure 9, which shows clearly the downflow of both the gas and the particles near the wall. The radial variation of the dimensionless potential for point R is illustrated in Figure 10; once again, the dimensional potential gradient is well below the dielectric breakdown field strength. Returning to Figure 6, one can see that, as the solids flux is increased at a fixed gas velocity,

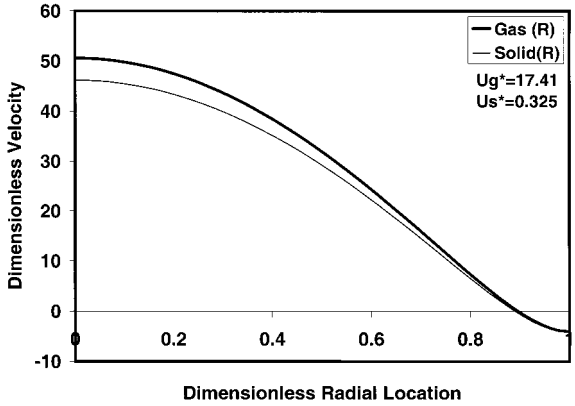

Figure 9. Dimensionless gas and solid velocities as a function of dimensionless radial position for point R in Figure 6.

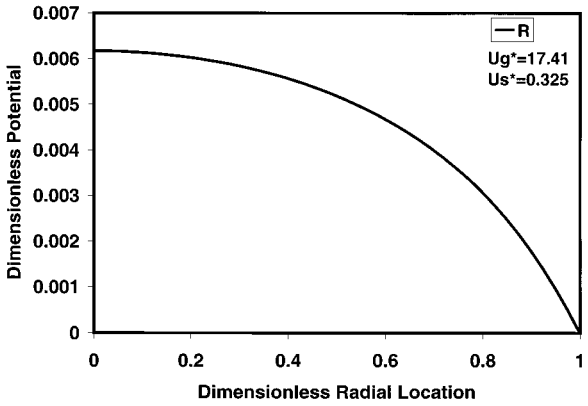

Figure 10. Dimensionless potential as a function of dimensionless radial position corresponding to point R in Figure 6.

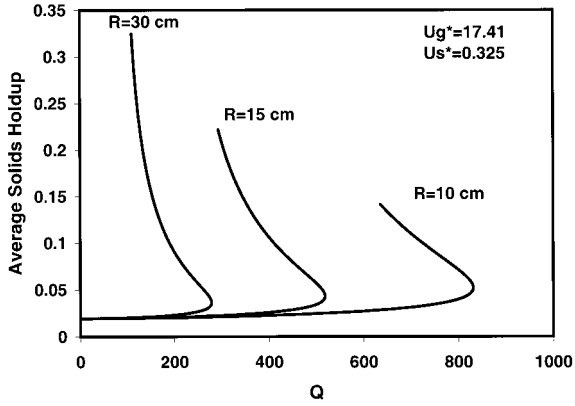

Figure 11. Average solids holdup vs *Q* for fixed gas and solid fluxes. Results are shown for three different tube radii. See Table 4 for parameter values.

the effect of electrostatics is felt at smaller and smaller values of *Q* (or, equivalently, at smaller surface charge densities).

Figure 11 shows the effect of the riser diameter for the same combinations of fluxes described in Figures 7−10. Note that the riser diameter has a systematic effect on the flow and that the effect of electrostatics becomes increasingly important as the tube diameter is increased.

Figure 12 shows the effect of increasing the throughput through the riser while maintaining the ratio of gas and solid fluxes constant. The curve labeled 1.0 corresponds to the combination of fluxes shown as the legend in this figure and has already been discussed in Figures

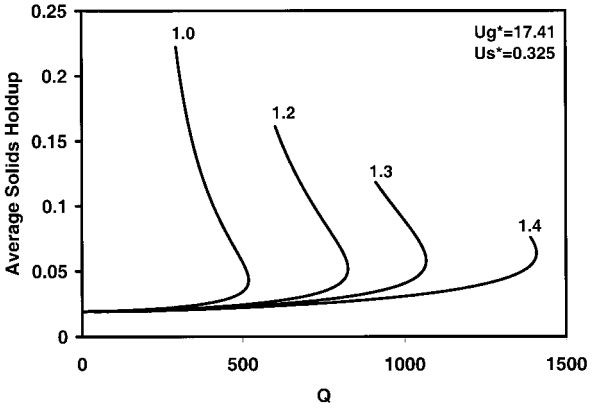

Figure 12. Average solids holdup vs Q for various gas and solid fluxes. The ratio of fluxes is held constant. The curve labelled 1.0 corresponds to the dimensionless gas and solid fluxes of 17.41 and 0.325, respectively. The dimensionless gas and solid fluxes for the other curves are simply obtained by multiplying 17.41 and 0.325 by the factors shown next to the curves. See Table 4 for other parameter values.

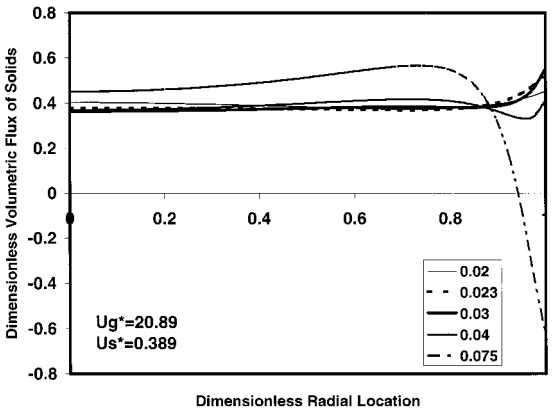

Figure 13. Dimensionless volumetric flux of solids as a function of dimensionless radial position for various points on the curve labeled 1.2 in Figure 12. The legends show the average solids holdups corresponding to the various curves.

7−10. The labels on the other curves simply refer to the multiple by which the fluxes (of both phases) have been increased from this base case. The turning point responds systematically to the throughput. The solids flux profiles corresponding to several different points on curves labeled 1.2 and 1.3 (in Figure 12) are shown in Figures 13 and 14, respectively. These figures reveal a flow feature that has received much attention in the literature recently, namely, annular upflow.[53−55] At modest levels of segregation (corresponding to intermediate holdup values in these figures), the peak flux occurs at the wall, and the peak location shifts inward as the holdup increases. These results should be contrasted with the flow patterns shown in Figures 3 and 7 for lower gas velocities, where the maximum upward flux occurs at the center.

We investigated briefly the effect of changing the closure for the particle-phase pressure given by eq 6. Specifically, we set

$$p_s = \frac{\rho_s \phi U^2}{400} g_o(\phi) \quad \text{where} \quad g_o(\phi) = \left(1 - \frac{\phi}{\phi_{max}}\right)^{-1/3} \tag{14}$$

which represents an ad hoc modification to ensure that the volume fraction of particles remains everywhere below ϕ_{max}. When this constraint is introduced into the

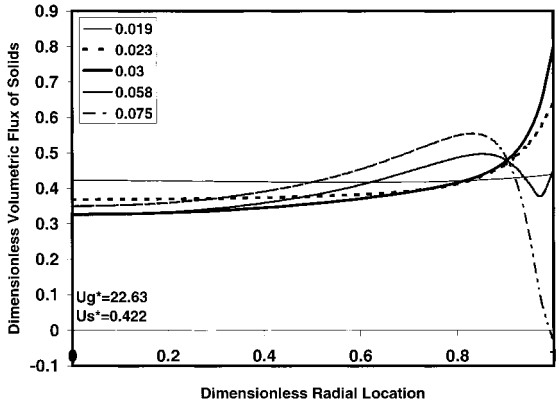

Figure 14. Dimensionless volumetric flux of solids as a function of dimensionless radial position for various points on the curve labeled 1.3 in Figure 12. The legends show the average solids holdups corresponding to the various curves.

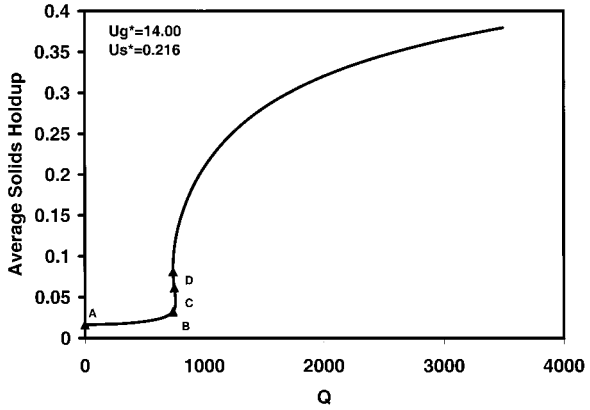

Figure 15. Average solids holdup vs Q for a specific combination of gas and solid fluxes. See Table 4 for parameter values. The particle-phase pressure is given by eq 14.

radial momentum balance, one obtains

$$Q\phi\left(\frac{d\Psi}{d\xi}\right) + \frac{d(\phi g_o)}{d\xi} = 0 \tag{15}$$

Figure 15 shows the variation of the holdup with Q obtained with this closure for the combination of fluxes discussed previously in Figures 1−5. Note that we now have an S-shaped curve in Figure 15, which should be contrasted with the corresponding curve in Figure 1. The points A−D marked in Figure 15 correspond to the same holdup values as in Figure 1 obtained with a simpler closure. The radial variations of the solids volume fraction and solids flux corresponding to these four points marked in Figure 15 are shown in Figures 16 and 17, respectively. These results should be compared with the curves shown in Figures 2 and 3. The addition of the g_o term has flattens the ϕ profile modestly, and its influence is felt in the solids flux profile. It is clear that, even though Figures 1 and 15 look significantly different, the general characteristics of the radial profiles remain robust. We simply note that the *annular upflow* obtained at high fluxes persists with the modified closure as well.

The present study clearly demonstrates that the lateral nonuniformities seen in riser flows can be captured in a qualitatively correct manner with a model that encompasses electrostatic effects. The amount of electrostatic charge required to fit the data is very modest and certainly lies in the lower range of values

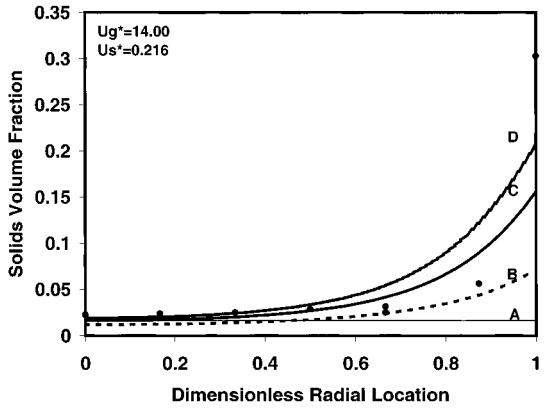

Figure 16. Particle volume fraction as a function of dimensionless radial position corresponding to the points A−D marked in Figure 15. (●) Experimental data of Bader et al.[46]

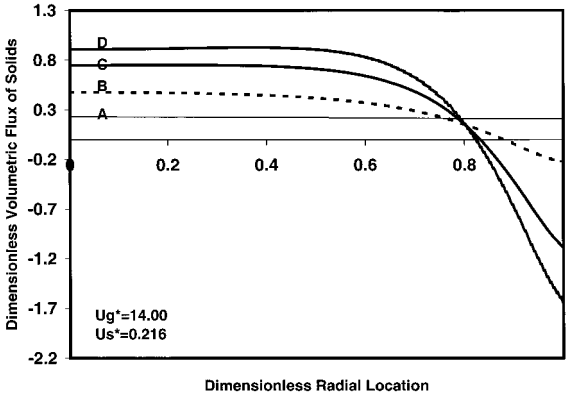

Figure 17. Dimensionless volumetric flux of solids as a function of dimensionless radial position corresponding to the points A−D marked in Figure 15.

reported in the literature. Thus, electrostatics should be considered carefully in future studies of gas−solid flows. In particular, careful experiments that probe the influence of static electrification on flow are needed.

In the present analysis, we suppressed hydrodynamically driven segregation. Thus, a natural extension will be to examine the combined influence of electrostatic and hydrodynamic segregation mechanisms. From the definition of Q, it follows that the effect of electrostatics decreases as particle size increases. Thus, we can anticipate that hydrodynamic segregation will be more relevant for larger particles, whereas electrostatic segregation will assume a greater importance with smaller particles.

A significant weakness of the present analysis derives from our ignorance about the size of the particle charges. At the same time, our study supports the need for more experimental and modeling work on the role of electrostatics in gas−solid flow. An obvious extension of the present model involves methods of describing the rates of generation and neutralization of particle charge, but closures for these processes remain a formidable challenge. In our opinion, experimental work to establish the relevance of electrostatics (or lack thereof) in gas−solid flows such as the riser flow analyzed here assumes a higher priority.

5. Summary

It is shown that electrostatics can be an important driving force for radial particle segregation in risers. Unfortunately, particle charge under a given set of conditions is unknown, and so, fully predictive models are not possible at this time. Consequently, a model of fully developed gas−particle flow was implemented with the charge level left as a model parameter. It was found that known trends, including core−annular flow, annular downflow at low gas velocities, and annular upflow at higher gas velocities, are captured with this model. In particular, experimental data for FCC particles by Bader et al.[46] can be captured by the model. The required charge level is at the lower end of the spectrum of charge levels reported in the literature.

Decades ago, Soo[35,40,41] and Owen[32] concluded that particle charge plays important roles in gas−particle flows with small particles. The results of the present study suggest that the lack of attention to this issue has been a grave oversight.

Appendix A

Simple Model for Particle-Phase Pressure and Viscosity. Consequences of Structures at Different Length Scales. It is well-known that hydrodynamic structures in the form of spatial and temporal nonuniformities in velocities and particle volume fractions are present in riser flows. These fluctuations span a wide range of length and time scales, and the origin of these structures is fairly well understood (e.g., Agrawal et al.[52]). It is also known that the segregation of particles toward the walls of the riser can occur simply because of hydrodynamic effects.[45−52] In this paper, we specifically suppress *hydrodynamically driven segregation* and focus on assessing segregation from electrostatic effects. The role of hydrodynamic fluctuations should not be completely ignored, as they impart the particle phase with an effective viscosity and a pressure. The analysis described below outlines the rationale behind the expressions for particle-phase viscosity and pressure used in the present study.

At the smallest scale, the particles execute a fluctuating motion over and above the mean velocity; this is quantified through the granular temperature.[46,47,50−52,57] The fluctuating motion comes about because of (a) velocity gradients in the riser and (b) relative motion between the particles and the suspending gas (e.g., see Koch and Sangani[58]). An estimate of the fluctuating velocity due to the shear is $2Ud/R$, where U is the average velocity of the gas through the pipe, R is the tube radius, and d is the particle diameter. For typical riser flows with FCC particles (say, $U = 7$ m/s, $d = 75$ μm, and $R = 15$ cm), $2Ud/R = 0.7$ cm/s. Velocity fluctuations arising from the relative motion between the gas and the particles scale with the mean slip velocity,[59] and for dilute systems, this is typically one-tenth of the terminal velocity, v_t.[52] The terminal velocity for the FCC particles considered here is about 25 cm/s. Thus, we anticipate that the "slip motion" is the primary source of fluctuations at the particle scale. The Stokes number for the FCC particles suspended by air is ~O(10^2), and so, we expect that the damping of the fluctuating motion is primarily due to inelastic collisions.[52] The length scale relevant for the estimation of the viscosity is thus the mean free path between collisions. For low particle concentrations, one then finds that

$$\mu_s \approx (\rho_s \phi)(0.1 v_t)\left(\frac{d}{\phi}\right) = 0.1 \rho_s v_t d$$

$$p_s \approx (\rho_s\phi)(0.1v_t)^2 = 0.01\rho_s {v_t}^2$$

It is well-known that a uniform suspension of particles fluidized by a gas is unstable and that nonuniform mesoscale structures form readily.[52] The effective pressure and viscosity due to the mesoscale structures were estimated by Agrawal et al.[52] through computational experiments. Their simulations suggest the following typical values of the effective viscosity and pressure

$$\mu_s \approx 0.5\rho_s {v_t}^3 \frac{\phi}{g}, \quad p_s \approx 0.5\rho_s\phi {v_t}^2$$

which are significantly larger than the microscale viscosity and pressure.

Finally, there are fluctuations at the scale of the riser radius itself. Here, we expect that the scale of the fluctuations will manifest some dependence on the mean flow rate and the riser diameter. Unfortunately, there is no simple way of estimating the consequence of fluctuations at this scale. Detailed models based on particle-phase turbulence have been described in the literature where the hydrodynamic mechanism for segregation is also considered. As mentioned before, we want to consider only a very simple model for the effect of riser scale fluctuations here. Specifically, we wish to set aside the segregation that arises because of hydrodynamics and focus only on the possible segregation due to electrostatics alone. With this in mind, we ignore the lateral variation of the kinetic energy per unit mass associated with these fluctuations.[49,51] Instead, we simply take the fluctuating velocity and the mixing length to be a fraction of the mean gas velocity and the tube radius, respectively.

It is known from tracer gas dispersion measurements[60] that $UR/D_r \approx 300$, where D_r is the average value of the radial dispersion coefficient in the *core region* (where the particle concentration is roughly uniform). One can rationalize this physically as

$$D_r = v'l, \quad v' \approx \frac{U}{20}, \quad l \approx \frac{R}{15}$$

where $\approx$ indicates physically reasonable, typical values. As dispersion is associated with hydrodynamic fluctuations and fluctuations in the gas and particle phases are closely coupled,[52] the particle-phase dispersion coefficient can be expected to be comparable to that for the gas. Furthermore, we expect the effective kinematic viscosity, ν_s, to be roughly equal to the particle-phase dispersion coefficient as well. Thus, $\nu_s \approx v'l$. This suggests an expression for the particle-phase viscosity of the form $\mu_s \approx (\rho_s\phi)v'l$.

From the lessons of single-phase turbulent flow, one can anticipate that the mixing length will decrease as one approaches the wall. In the present two-phase flow problem, the particle concentration increases as one approaches the wall. For the sake of simplicity, we hypothesize that the radial variations of ϕ and l compensate each other and postulate that the particle-phase viscosity is roughly constant, independent of the radial position, and write

$$\mu_s = \rho_s\langle\phi\rangle \frac{UR}{300}$$

where $\langle\phi\rangle$ denotes the cross-sectional average volume fraction (holdup) of particles.

For the transport of FCC particles in a 30-cm-diameter riser at a gas velocity of 5 m/s, the ratio of the intermediate-scale viscosity to the macroscale viscosity is

$$\frac{150{v_t}^3}{URg} = 0.375$$

so that the macroscale viscosity is indeed the most relevant one. At higher gas velocities and tube diameters, the macroscale viscosity becomes even more dominant.

With this in mind, we use the following expression for viscosity in our model

$$\mu_s = \rho_s\langle\phi\rangle \frac{UR}{300} \tag{A1}$$

To be consistent, for the particle-phase pressure, we should use

$$p_s \approx \rho_s\phi(v')^2 = \frac{\rho_s\phi U^2}{400} \tag{A2}$$

It should be emphasized that these functional forms were chosen to ensure that the particle volume fraction will be uniform over the cross section of the riser in the absence of electrostatic effects, i.e., hydrodynamic segregation is not permitted.

It is interesting to compare the pressure obtained from the riser-scale fluctuations with that at the mesoscale. Typically, for riser flows, $U \approx 3-10$ m/s, so that $(U/20) \approx 15-50$ cm/s. At the lower end, this is not much different from the terminal velocity. Thus, the magnitude of the effective pressure due to the macroscale fluctuations is 1−10 times that due to fluctuations at the mesoscale.

The expressions for particle-phase viscosity and pressure described above, eqs A1 and A2, do not include the finite-size effect and thus allow the particle volume fraction at some regions of the riser to exceed the close-packing limit. This can be prevented by forcing the pressure and/or viscosity to become very large (diverge) at some critical volume fraction, ϕ_{max}. The qualitative arguments considered here do not shed any light on how this should be done. In some of the later examples described in this study, we demonstrated how the results will change if we replace eq A2 with

$$p_s = \frac{\rho_s\phi U^2}{400} g_o(\phi) \quad \text{where} \quad g_o(\phi) = \left(1 - \frac{\phi}{\phi_{max}}\right)^{-1/3} \tag{A3}$$

Acknowledgment

This work was supported by the New Jersey Commission on Science and Technology; Merck & Co., Inc.; and the ExxonMobil Research & Engineering Company. Financial support for M.F.A. by Saudi Aramco is gratefully acknowledged.

Nomenclature

d = particle diameter
D_r = radial dispersion coefficient of gas in the core region
g = acceleration due to gravity
g_o = function defined by eq A3
G_s = solids mass flux through the riser

L = characteristic length associated with fluidization instability
M_s^o = dimensionless solid-phase viscosity
n = Richardson−Zaki exponent (4.65)
p = dimensionless gas pressure
p_s = particle-phase pressure
Q = electrodiffusion parameter
R = riser radius
U = riser gas velocity
U_g^*, U_s^*= dimensionless riser gas and solids velocities, respectively
V_g, V_s = dimensionless gas and solid-phase axial velocities, , respectively, where the terminal velocity of the particle is used to make the velocities dimensionless
v_t = terminal velocity of the particle
v' = magnitude of the fluctuating velocity
l = mixing length
β = drag coefficient
ρ_s = particle density
μ_s = particle-phase viscosity
ν_s = particle-phase kinematic viscosity
ϵ = dielectric constant of the gas−solid mixture, a function of ϕ
ϵ_o = permittivity of free space [8.8542×10^{-12} C^2/(N m^2)]
ϕ = particle volume fraction (function of radial position)
$\langle\phi\rangle$ = cross-sectional average particle volume fraction (i.e., holdup)
Ψ = dimensionless electric potential (function of position)
ξ = dimensionless radial coordinate
σ = surface charge density (C/m^2)

Literature Cited

(1) Boland, D.; Al-Salim, Q. A. W.; Geldart, D. Static electrification in fluidized beds. *Chem. Eng. Sci*. **1969**, *24*, 1389−1390.

(2) Fujino, M.; Ogata, S.; Shinohara, H. The electric potential distribution profile in a naturally charged fluidized bed and its effects. *Int. Chem. Eng.* **1985**, *25*, 149−159.

(3) Ciborowski, J.; Woldarski, A. On electrostatic effects in fluidized beds. *Chem. Eng. Sci.* **1962**, *17* (1), 23−32.

(4) Briens, C. L.; Bergougnou, M. A.; Inculet, I. I.; Baron, T.; Hazlett, J. D. Size distribution of particles entrained from fluidized beds: Electrostatic effects. *Powder Technol.* **1992**, *70*, 57−62.

(5) Bafrnec, M.; Bena, J. Quantitative data on the lowering of electrostatic charge in a fluidized bed. *Chem. Eng. Sci*. **1972**, *27*, 1177−1181.

(6) Guardiola, J.; Rojo, V.; Ramos, G. Influence of particle size, fluidization velocity and relative humidity on fluidized bed electrostatics. *J. Electrost.* **1996**, *37*, 1−20.

(7) Park, A.-H. A. Electrostatic charging in gas−solid fluidized beds. M.S. Thesis, University of British Columbia, British Columbia, Canada, 2000.

(8) Katz, H.; Sears, J. T. Electric field phenomena in fluidized and fixed beds. *Can. J. Chem. Eng*. **1969**, *47*, 50−53.

(9) Ali, F. S.; Ali, M. A.; Ali, R. A.; Inculet, I. I. Minority charge separation in falling particles with bipolar charge. *J. Electrost*. **1998**, *45*, 139−155.

(10) Boland, D.; Geldart, D. Electrostatic charging in gas fluidised beds. *Powder Technol*. **1971**, *5*, 289−297.

(11) Wolny, A.; Kazmierczak, W. Triboelectrification in fluidized bed of polystyrene. *Chem. Eng. Sci*. **1989**, *44* (11), 2607−2610.

(12) Ali, F. S.; Inculet, I. I.; Tedoldi, A. Charging of polymer powder inside a metallic fluidized bed. *J. Electrost*. **1999**, *45*, 199−211.

(13) Wolny, A.; Opalinski, I. Electric charge neutralization by addition of fines to a fluidized bed composed of coarse dielectric particles. *J. Electrost*. **1983**, *14*, 279−289.

(14) Tardos, G.; Pfeffer, R. A method to measure electrostatic charge on a granule in a fluidized bed. *Chem. Eng. Commun*. **1980**, *4*, 665−671.

(15) Fasso, L.; Chao, B. T.; Soo, S. L. Measurement of electrostatic charges and concentration of particles in the freeboard of a fluidized bed. *Powder Technol*. **1982**, *33*, 211−221.

(16) Chang, H.; Louge, M. Fluid dynamic similarity of circulating fluidized beds. *Powder Technol*. **1992**, *70*, 259−270.

(17) Jiang, P.; Bi, H.; Liang, S.-C.; Fan, L.-S. Hydrodynamic behavior of circulating fluidized bed with polymeric particles. *AIChE J*. **1994**, *40* (2), 193−206.

(18) Jiang, P.; Zhang, J.; Fan, L.-S. Electrostatic charge effects on the local solids distribution in the upper dilute region of circulating fluidized beds. In *Circulating Fluidized Beds V*; Kwauk, M., Li, J., Eds.; Science Press: Beijing 1997.

(19) Myler, C. A.; Zaltash, A.; Klinzing, G. E. Gas−solid transport in a 0.0508 m pipe at various inclinations with and without electrostatics II: Stability. *J. Powder Bulk Solids Technol.* **1986**, *10*, 13−17.

(20) Joseph, S.; Klinzing, G. E. Vertical gas−solid transition flow with electrostatics. *Powder Technol.* **1983**, *36*, 79−87.

(21) Zhang, Y.-F.; Yang, Y.; Arastoopour, H. Electrostatic effect on the flow behavior of a dilute gas/cohesive particle flow system. *AIChE J*. **1996**, *42* (6), 1590−1599.

(22) Plasynski, S. I.; Klinzing, G. E. High-pressure vertical pneumatic transport investigation. *Powder Technol*. **1994**, *79*, 95−109.

(23) Zaltash, A.; Myler, C.; Klinzing, G. E. Stability of gas−solid transport with electrostatics. *J. Pipelines* **1988**, *7*, 85−100.

(24) Liang, S.-C.; Zhang, J.-P.; Fan, L.-S. Electrostatic characteristics of hydrated lime powder during transport. *Ind. Eng. Chem. Res.* **1996**, *35*, 2748−2755.

(25) Dahn, C. J. Electrostatic hazards of pneumatic conveying of powders. *Saf. Consult. Eng.* **1992**, *11*, 201−204.

(26) Klinzing, G. E. Challenges in pneumatic conveying. *KONO* **2000**, *18*, 81−87.

(27) Lee, R. J.; Fan, L.-S. The effect of solid interaction forces on pneumatic handling of sorbent powders. *AIChE J*. **1993**, *39* (6), 1018−1029.

(28) Gupta, R.; Gidaspow, D.; Wasan, D. T. Electrostatic beneficiation of eastern oil shales. *Chem. Eng. Commun.* **1991**, *108*, 49−66.

(29) Plasynski, S. I.; Dhodapkar, S.; Klinzing, G. E. Observations from electrostatically charged conveying systems. Presented at NEPTIS-3, Kyoto, Japan, Nov 29−Dec 1, 1994.

(30) Dhodapkar, S. V. Flow pattern classification in gas−solid suspensions. Ph.D. Dissertation, University of Pittsburgh, Pittsburgh, PA, 1991; pp 62−76.

(31) Ebadat, V.; Singh, S. Importance of humidity on the control of electrostatic charging of high-density polyethylene powder. Presented at the Fourth International Conference on Pneumatic Conveying Technology, Glasgow, Scotland, Jun 26−28, 1990.

(32) Owen, P. R. Pneumatic transport. *J. Fluid Mech.* **1969**, *39* (2), 407−432.

(33) Klinzing, G. E.; Zaltash, A.; Myler, C. A. Particle velocity measurements through electrostatic field fluctuations using external probes. *Part. Sci. Technol*. **1987**, *5*, 95−104.

(34) Gajewski, A. Measuring the charging tendency of polystyrene particles in pneumatic conveyance. *J. Electrost*. **1989**, *23*, 55−66.

(35) Soo, S. L. Electrostatic hazards in pneumatic conveying. *J. Pipelines* **1981**, *1*, 57−68.

(36) Cole, B. N.; Baum, M. R.; Mobbs, F. R. An investigation of electrostatic charging effects in high-speed gas−solids pipe flows. *Proc. Inst. Mech. Eng.* **1969**, *184*, 77−83.

(37) Smeltzer, E. E.; Weaver, M. L.; Klinzing, G. E. Pressure drop losses due to electrostatic generation in pneumatic transport. *Ind. Eng. Chem. Process Des. Dev*. **1982**, *21*, 390−394.

(38) Ally, M. R.; Klinzing, G. E. Inter-relation of electrostatic charging and pressure drops in pneumatic transport. *Powder Technol*. **1985**, *44*, 85−88.

(39) Nieh, S.; Nguyen, T. Effects of humidity, conveying velocity, and particle size on electrostatic charges of glass beads in a gaseous suspension flow. *J. Electrost.* **1988**, *21*, 99−114.

(40) Soo, L. S.; Trezek, G. J. Turbulent pipe flow of magnesia. *Ind Eng. Chem. Fundam*. **1966**, *5*, 388−392.

(41) Neih, S.; Chao, B. T.; Soo, S. L. Modeling of pipe flow of a gas−solid suspension electrostatic and gravity effects. *J. Pipelines* **1987**, *7*, 73−84.

(42) Bailey, A. G. Electrostatic phenomena during powder handling. *Powder Technol*. **1984**, *37*, 71−85.

(43) Harper, W. R. *Contact and Frictional Electrification*; Oxford University Press: New York, 1967.

(44) Jones, T. B. *Electromechanics of Particles*; Cambridge University Press: New York, 1995.

(45) Sinclair, J. L.; Jackson, R. Gas−particle flow in a vertical pipe with particle−particle interaction. *AIChE J.* **1989**, *35*, 1473−1486.

(46) Bader, R.; Findlay, J.; Knowlton, T. M. Gas/solid flow patterns in a 30.5 cm diameter circulating fluidized bed. In *Circulating Fluidized Bed Technology II*; Basu, P., Large, J. F., Eds.; Permagon Press: New York, 1988; pp 123−137.

(47) Louge, M.; Mastorakos, E.; Jenkins, J. T. The role of particle collisions in pneumatic transport. *J. Fluid Mech.* **1991**, *231*, 345−359.

(48) Pita, J. A.; Sundaresan, S. Gas−solid flow in vertical tubes. *AIChE J.* **1991**, *37*, 1009−1018.

(49) Dasgupta, S.; Jackson, R.; Sundaresan, S. Turbulent gas−particle flow in vertical risers. *AIChE J.* **1994**, *40*, 215−228.

(50) Gidaspow, D. *Multiphase Flow and Fluidization*; Academic Press: New York, 1994.

(51) Hrenya, C. M.; Sinclair, J. L. Effects of particle-phase turbulence in gas−solid flows. *AIChE J.* **1997**, *43*, 853−869.

(52) Agrawal, K.; Loezos, P. N.; Syamlal, M.; Sundaresan, S. The role of meso-scale structures in rapid gas−solid flows. *J. Fluid Mech.* **2001**, *445*, 151−185.

(53) Grace, J. R.; Issangya, A. S.; Bai, D.; Bi, H. Situating the High-Density Circulating Fluidized Bed. *AIChE J.* **1999**, *45*, 2108−2116.

(54) Isangya, A. S.; Grace, J. R.; Bai, D.; Zhu, J. Further measurements of flow dynamics in a high-density circulating fluidized bed riser. *Powder Technol.* **2000**, *111*, 104−113.

(55) Pärssinen, J. H.; Zhu, J.-X. Axial and Radial Solids Distribution in a Long and High-Flux CFB Riser. *AIChE J.* **2001**, *47*, 2197−2205.

(56) Al-Adel. M. Role of Electrostatics on Gas−Particle Flows in Vertical Ducts. M.S. Thesis, Princeton University, Princeton, NJ, 2002, in preparation.

(57) Lun, C. K. K.; Savage, S. B.; Jeffrey, D. J.; Chepurniy, N. Kinetic theories of granular flows: Inelastic particles in Couette flow and slightly inelastic particles in a general flow field. *J. Fluid Mech.* **1984**, *140*, 223−256.

(58) Koch, D. L.; Sangani, A. S. Particle pressure and marginal stability limits for a homogeneous monodisperse gas fluidized bed: Kinetic theory and numerical simulations. *J. Fluid Mech.* **1999**, *400*, 229−263.

(59) Koch, D. L. Kinetic theory for a monodisperse gas−solid suspension. *Phys. Fluids A* **1990**, *2*, 1711−1723.

(60) Grace, J. R.; Avidan, A. A.; Knowlton, T. M. *Circulating Fluidized Beds*; Blackie Academic and Professional: New York, 1997.

(61) Bruggeman, D. A. G. *Ann. Phys.* **1935**, *24*, 636.

(62) Qi, C.; Farag, I. H. Lateral particle motion and its effect on particle concentration distribution in the riser of CFB. *AIChE Symp. Ser.* **1998**, *89* (296), 73−80.

Received for review December 5, 2001
Revised manuscript received January 22, 2002
Accepted January 23, 2002

IE010982W

Coarse-grid simulation of reacting and non-reacting gas-particle flows

Final Technical Report

Award # DE-FC26-00NT409071
DOE Vision 21 Virtual Demonstration Initiative

Appendix F

ELSEVIER

Powder Technology 124 (2002) 45–54

POWDER TECHNOLOGY

www.elsevier.com/locate/powtec

Role of wall friction in fluidization and standpipe flow

Anuj Srivastava, Sankaran Sundaresan*

Department of Chemical Engineering, The Engineering Quadrangle, Princeton University, Princeton, NJ 08544-5263, USA

Received 14 June 2001; received in revised form 14 September 2001; accepted 20 September 2001

Abstract

Fluidization–defluidization experiments have been carried out in beds of three different diameters, using XL glass beads and air as the fluidizing medium. The variation of pressure drop and bed height manifested a hysteretic behavior, which was more pronounced in smaller tubes. Analysis of the results using a one-dimensional model proposed by Jackson revealed that the observed effect of tube diameter may be attributed to wall friction. From this analysis, we extracted a quantitative estimate of the variation of the compressive yield stress of an assembly of particles as a function of particle volume fraction. The standpipe performance data reported by Srivastava et al. [Powder Technol. 100 (1998) 173.] for these glass beads were analyzed on the basis of the estimated compressive yield strength. It was found that the support provided by the standpipe wall could be estimated quantitatively from the standpipe holdup data and the compressive yield strength determined separately from our fluidization–defluidization experiments.

Keywords: Fluidization; Defluidization; Circulating fluidized bed; Standpipe; Wall friction

1. Introduction

Circulating fluidized beds (CFB) have been widely used over many decades for fluid catalytic cracking (FCC), and for roasting and combustion applications. The commercial success of FCC has led to the use of CFB in other industrial applications such as Fischer–Tropsch synthesis in the SASOL synthetic gasoline process, oxidation of *n*-butane to maleic anhydride and calcination of aluminum hydroxide to high-grade alumina [1]. A CFB loop typically consists of a riser, cyclones, fluidized bed and a solids return system, usually comprising a standpipe and a valve. Risers and standpipes are known to exhibit a rich variety of flow behavior. Experimental measurements reveal that particle concentration is non-uniform over the cross-section of a vertical riser with particles being concentrated near the walls [2]. Standpipes are known to exhibit instabilities under certain operating conditions, which lead to inadequate pressure buildup in the pipe [3,4].

Although there have been several studies on gas–particle flow instabilities in the individual components of the CFB circuit, much less is understood about the particle circulation instabilities propagating throughout the CFB loop. Zhang et al. [5] studied the dynamic flow behavior of FCC particles in a CFB circuit through an analysis of pressure fluctuations at various locations of the loop. These authors observed low-frequency oscillatory solids circulation rates under certain operating conditions. Srivastava et al. [6] studied the effect of aeration in the standpipe on flow of gas–particle mixtures in a pilot-scale CFB unit, using electrical capacitance tomography (ECT) to image the cross-sectional particle distribution in the standpipe. Fig. 1 shows the schematic of the pilot-scale CFB unit on which these experiments were conducted. At low aeration rates, a stable dense phase flow was obtained in the standpipe, while at higher aeration rates, the flow became unstable, manifesting low frequency oscillations in the particle circulation rate. For stable flow conditions, a significant portion of the weight of the bed in the standpipe was supported by wall friction. Furthermore, the onset of the oscillatory flow pattern seemed to occur when the contribution of wall friction became negligible.

It is also worthwhile at this juncture to discuss the stability of gas-fluidized beds, which has been the focus of research for a number of decades. Mutsers and Rietema [7] and Rietema and Piepers [8] argued that the stability of a fluidized bed is governed by forces exerted at direct contacts between particles, such as cohesive forces and frictional interactions between particles. As a result of such interac-

* Corresponding author. Tel.: +1-609-258-4583; fax: +1-609-258-0211.
E-mail address: sundar@princeton.edu (S. Sundaresan).

0032-5910/02/$ - see front matter
PII: S0032-5910(01)00471-5

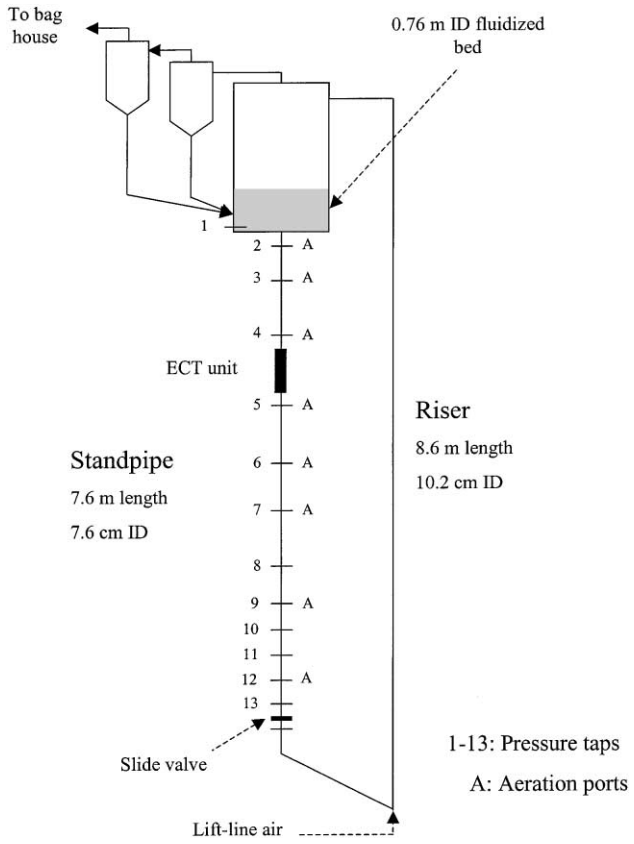

Fig. 1. Schematic of CFB unit used by Srivastava et al. [6].

tions fluidized beds can display a mechanical structure, whose strength decreases with increasing bed expansion. Furthermore, these authors attributed the existence of surpressure at minimum fluidization (i.e. the additional pressure drop in excess of the weight of the bed which is required to initiate the expansion of a packed bed) to particle–particle and particle–wall interactions. Tsinontides and Jackson [9], in experiments involving fluidization and defluidization of cracking catalyst particles in air, observed a marked hysteresis in the fluidization characteristics, and attributed it to a yield stress in the granular assembly resulting from inter-particle and particle–wall interactions.

There is no doubt that stresses resulting from cohesive and/or frictional interactions play an important role in determining the mechanical behavior of granular assemblies such as those found in fluidized beds and standpipes. Yet, quantitative information on the magnitude of such stresses is scanty, thus limiting quantitative understanding of the complex flow behavior observed in circulating fluidized bed experiments.

Jackson [10] has argued that information about the nature and magnitude of contact stresses arising due to frictional interactions can be obtained through simple measurements of bed height and pressure drop during the process of fluidization and defluidization. In the present study, we have performed such fluidization–defluidization experiments in beds of different diameters in order to estimate the magnitude of contact stresses. The particles used in this study are XL glass beads, the same as those used in our earlier CFB experiments [6]. These data provide strong evidence for the effect of wall stresses on fluidization and defluidization characteristics. In this paper, we demonstrate that the simple 1-D model proposed by Jackson is able to capture several aspects of our data. We have also extracted from these data a quantitative estimate for the yield stresses in assemblies of these particles.

Armed with the yield stress information, we have analyzed the standpipe data reported by Srivastava et al. [6]. We find that a simple one-dimensional model of granular flow can capture the general trends observed in our circulating fluidized bed experiments.

This paper is organized as follows. Section 2 outlines the 1-D model for the effect of wall friction described by Jackson [10,11]. The experimental system and procedure employed in our fluidization–defluidization experiments are presented in Section 3. Section 4 describes the fluidized bed data and analysis. In Section 5, we examine the standpipe data of Srivastava et al. [6]. Section 6 summarizes the major results of this study.

2. Theory

An analysis of the role of contact stresses on the mechanical behavior of fluidized beds of non-cohesive particles has been described recently by Jackson [10,11]. The present treatment is a minor modification of his model. Let us consider a bed of particles in a vertical tube of diameter D subject to a uniform upward flow of a gas at a superficial velocity $\bar{u}$. Following Jackson, we consider the classical Janssen's one-dimensional analysis of stress distribution in a packed bed and write the balance of forces in the vertical direction acting on the assembly of particles as

$$\frac{\mathrm{d}\sigma_s}{\mathrm{d}y} = \rho_p \nu g - \beta(\nu)\frac{\bar{u}}{1-\nu} \pm \frac{4}{D}\mu j \sigma_s \qquad (1)$$

where y is the vertical coordinate measured from the upper surface of the bed (with the y-axis pointing downwards). Here, σ_s is the cross-sectional average of the yy-component of the compressive stress in the particle phase, transmitted through sustained contacts between particles. The term on the left-hand side of the equation represents the gradient in this stress. The first term on the right represents the gravitational force acting on the particles where ρ_p is the density of the particles, ν is the volume fraction of particles and g is the specific gravity force. The second term on the right represents the drag exerted by the fluid on the particles, where β is the drag coefficient. The third term on the right represents the frictional force exerted on the particle assem-

bly by the walls of the container. Here, j is the Janssen's coefficient (usually assumed to be a constant) which is the ratio between the normal stress exerted by the particle assembly on the walls and σ_s, while μ is the coefficient of wall friction. The sign of this term depends on the direction in which friction is acting. Therefore, the negative sign applies when the bed is compacting during the process of defluidization while the positive sign applies when the bed is in the process of expansion as is the case during fluidization.

The corresponding force balance on the fluid phase is

$$\frac{dp}{dy} = \beta(\nu)\frac{\bar{u}}{1-\nu} \tag{2}$$

where p is the is the fluid phase pressure. The form for β is assumed to be

$$\beta(\nu) = \frac{\rho_p \nu g}{v_t}\frac{1}{(1-\nu)^{n-1}} \tag{3}$$

where v_t is the terminal velocity of a single particle and n is the Richardson–Zaki [12] index.

Non-cohesive granular material can support only compressive stresses, and the compressive yield stress σ_s^y can be expected to be a monotonically increasing function of ν. Various expressions have been proposed for the functional dependence of σ_s^y on ν, see for example Atkinson and Bransby [13], Schaeffer [14], Prakash and Rao [15] and Johnson et al. [16]. As discussed in a greater detail later, the following simple functional form for σ_s^y, considered by Jackson [10], was found to be adequate for capturing our experimental results

$$\sigma_s^y(\nu)\begin{cases} = F\dfrac{(\nu-\nu_{min})}{(\nu_{max}-\nu)} & \nu_{min} < \nu < \nu_{max} \\ = 0 & \nu < \nu_{min} \end{cases} \tag{4}$$

where F is a constant. This functional form assumes that sustained frictional contact between multiple neighbors does not occur at values of $\nu \le \nu_{min}$. Furthermore, the compressive yield stress is postulated to diverge as $\nu \to \nu_{max}$. (In practice, one can pack the particles at volume fractions exceeding ν_{max} without crushing the particles by mechanical means such as tapping. The above form assumes that such higher packing levels are not attainable in simple fluidization–defluidization processes.)

2.1. Defluidization

Consider a defluidization experiment in which the gas flow rate is reduced in small increments, allowing the bed to equilibrate at each gas flow rate. In such an experiment, the bed height generally decreases monotonically with gas flow rate, so that the bed is progressively compressed by its own weight. An important assumption in the model is that the local volume fraction of the particles is such that the bed is at incipient (compressive) yield everywhere. In other words, $\sigma_{\underline{s}} = \sigma_s^y$. In this case, Eqs. (1) and (3) can be combined to obtain

$$\frac{d\nu}{dy} = \left(\rho_p \nu g - \frac{\rho_p \nu g}{v_t}\frac{1}{(1-\nu)^n}\bar{u} - \frac{4}{D}\mu j \sigma_s^y\right) \Big/ \frac{d\sigma_s^y}{d}. \tag{5}$$

This equation can be integrated numerically, starting at $y=0$ where $\nu = \nu_{min}$ (corresponding to the condition that $\sigma_s = \sigma_s^y = 0$ at the top of the bed) and terminating at the bottom of the bed at $y=H$ such that

$$\rho_p \int_0^H \nu(y)dy = m \tag{6}$$

where m is the specified mass loading of particles per unit cross-sectional area. Once the particle volume fraction profile in the bed is determined, it is straightforward to integrate Eq. (2) to find the overall pressure drop across the bed. In this manner, one can determine the pressure drop and bed height as functions of $\bar{u}$ to generate the theoretical defluidization curve.

The solids volume fraction and stress profiles at the end of the defluidization cycle can be found from Eqs. (5) and (6) by letting $\bar{u}=0$. Let us now consider the process of refluidization from this point onwards.

2.2. Fluidization cycle

When the gas velocity is increased gradually from zero, the pressure drop across the bed increases steadily while the height of the bed remains unaltered until a critical gas velocity, $\bar{u}_c$, is reached. In this regime, as we increase $\bar{u}$ ($\bar{u} < \bar{u}_c$), a larger and larger fraction of the weight of the bed is supported by the upward drag exerted by the gas on the particles. This will necessarily change the stress profile, $\sigma_s(y)$, in the particle phase while the solids volume fraction profile, $\nu(y)$ remains unaltered. Jackson [10] argued that as $\bar{u}$ is progressively increased σ_s at the bottom of the bed must correspondingly take on lower and lower values. He further argued that when $\bar{u} = \bar{u}_c$, σ_s at the bottom of the bed becomes zero. At this point, the bottom of the bed loses contact with the distributor (provided no cohesive interaction between the particle assembly and the distributor exists), and the entire bed is lifted by the fluid. As the bed rises, the particles at the bottom rain down and eventually recompact to form a new bed.

The value of $\bar{u}_c$ can be determined as follows. We combine Eqs. (1) and (3) and write

$$\frac{d\sigma_s}{dy} - \frac{4}{D}\mu j \sigma_s = \rho_p \nu g - \frac{\rho_p \nu g}{v_t}\frac{1}{(1-\nu)^n}\bar{u} \tag{7}$$

with friction acting to oppose the bed expansion. Here, $\nu(y)$ is the particle volume fraction profile determined from defluidization calculations with $\bar{u}=0$. Thus

$$\sigma_s(y=H)e^{-JH}-\sigma_s(y=0)=\rho_p g\int_0^H \nu e^{-Jy}dy-\frac{\rho_p g\bar{u}}{v_t}\int_0^H \frac{\nu}{(1-\nu)^n}e^{-Jy}dy \quad (8)$$

where $J=(4/D)\mu j$. At the point at which the bed rises, σ_s is zero both at the top and at the bottom of the bed, so the left hand side of Eq. (8) vanishes when $\bar{u}=\bar{u}_c$. Therefore, we have

$$\frac{\bar{u}_c}{v_t}=\frac{\int_0^H \nu e^{-Jy}dy}{\int_0^H \frac{\nu}{(1-\nu)^n}e^{-Jy}dy}. \quad (9)$$

For any $\bar{u}\le\bar{u}_c$, one can readily integrate Eqs. (2) and (7) to determine the stress and pressure profiles, respectively. In this manner, we determine how the overall pressure drop across the bed varies with $\bar{u}$ (i.e. the fluidization curve).

Jackson [10] assigned the same value for the Janssen's coefficient j for both fluidization and defluidization, so the role of wall friction was captured by a single parameter J in the entire fluidization–defluidization cycle. If cylindrical symmetry holds, then along the centerline of the cylindrical bed the shear stress will be zero and the vertical and horizontal normal stresses, σ_s and σ_h, respectively, will be the principal stresses. It seems reasonable to expect that during defluidization the vertical normal stress (σ_s) will be larger than the horizontal normal stress (σ_h) (as the bed is gradually being compacted when we progressively lower the gas flow rate). Therefore, during defluidization, at least along the centerline, the vertical stress σ_s will be the major principal stress and

$$\frac{\sigma_h}{\sigma_s}=j_{df}=\frac{1-\sin\varphi}{1+\sin\varphi}$$

where φ is the angle of internal friction for the particles. We have assumed in our analysis that the value of $j=j_{df}$ estimated in this manner from the angle of internal friction applies for the defluidization branch.

In the fluidization branch, the stress profile determines the gas velocity at which the bed will detach from the distributor. As already pointed out by Jackson [10], just before the detachment of the bed from the distributor (i.e. $\bar{u}$ slightly smaller than $\bar{u}_c$), the drag exerted by the gas on the bed exceeds the weight of the bed when wall friction is present. This suggests that σ_s (along the centerline of the bed) should be the minor principal stress at least in the lower part of the bed, where σ_s decreases as y increases. This led us to postulate that $j_f=j_{df}^{-1}$ where j_f is the Janssen's coefficient for the fluidization branch. The model employed in our study differs from that of Jackson [10] in this one regard. This change was also motivated by the fact that we could fit our experimental data (described below) to the 1-D model better when we assumed that $j_f=j_{df}^{-1}$.

In order to understand the role of wall friction on the fluidization and defluidization behavior, and also evaluate the adequacy of the model described here, we performed fluidization and defluidization experiments in tubes of different diameters. These are described below.

3. Experimental

The physical properties of particles used in the experiments, namely XL glass beads, are summarized in Table 1. These are exactly the same particles used by Srivastava et al. [6] in their circulating fluidized bed experiments. The angle of internal friction for the particles was determined via measurements in a Jenike shear cell apparatus.

Fluidization experiments were performed in three different Plexiglas tubes (0.5″, 1.0″ and 2.0″ ID). Following Tsinontides [17], the gas distributors were constructed by sandwiching two layers of fibrous material between two micronic mesh screens. Distributors were rejected as unsatisfactory if any obvious maldistribution of the feed gas was detected. Dry air was further dried by passing it over a packed bed of drying agent and used in all the experiments described below. At each experimental condition, the volumetric flow rate of air exiting at the top of the fluidized bed was measured and was used to compute the superficial velocity of the air through the bed.

The bed height was determined by means of a tape measure attached to the outside of each tube. The pressure drop across the distributor and bed was measured by means of a U-tube manometer filled with red liquid of specific gravity 0.827. The pressure drop across the distributor alone, as a function of the gas flow rate, was determined through separate tests in the empty tubes. The pressure drop across the bed was obtained by subtracting the latter from the former.

The fluidization and defluidization experiments were performed as follows. A fairly deep bed, roughly 30 cm in height, was formed by depositing a known mass of glass beads into the tube. The bed was allowed to bubble gently for a period of time by operating the column at an air flow rate which is slightly larger than that corresponding to the point of minimum bubbling. The air flow rate was then reduced progressively in small steps (all the way down to zero flow rate), allowing the bed to equilibrate at each condition and recording the pressure drop, the bed height,

Table 1
Physical properties of XL glass beads

$d_{p,50}$	Mean particle diameter (μm)	50
ρ_p	Solids density (g/cm^3)	2.35
ϕ	Angle of internal friction	13°

the air flow rate and visual observations of the state of the bed. In this manner, the defluidization branch was mapped out. The fluidization branch was mapped out in a similar manner by progressively increasing the air flow rate in small steps from zero to the minimum bubbling point.

4. Fluidization–defluidization results

Figs. 2a, 3a and 4a show the measured pressure drop across the bed in the 0.5″, 1.0″ and 2.0″ tubes, respectively, as a function of the superficial velocity of the fluidizing air for a complete defluidization–fluidization cycle. Figs. 2b, 3b and 4b show the corresponding bed height data. The smooth curves in these figures represent the model predictions (discussed later), while the points refer to experimental data. The mass of particles loaded per unit cross-sectional area, m, is 36.3 g/cm^2 for all three tubes. The pressure drop has been normalized with respect to mg, the weight of the bed per unit cross-sectional area. A normalized pressure drop of 1.0 thus corresponds to the case where the pressure drop across the bed exactly balances the weight of

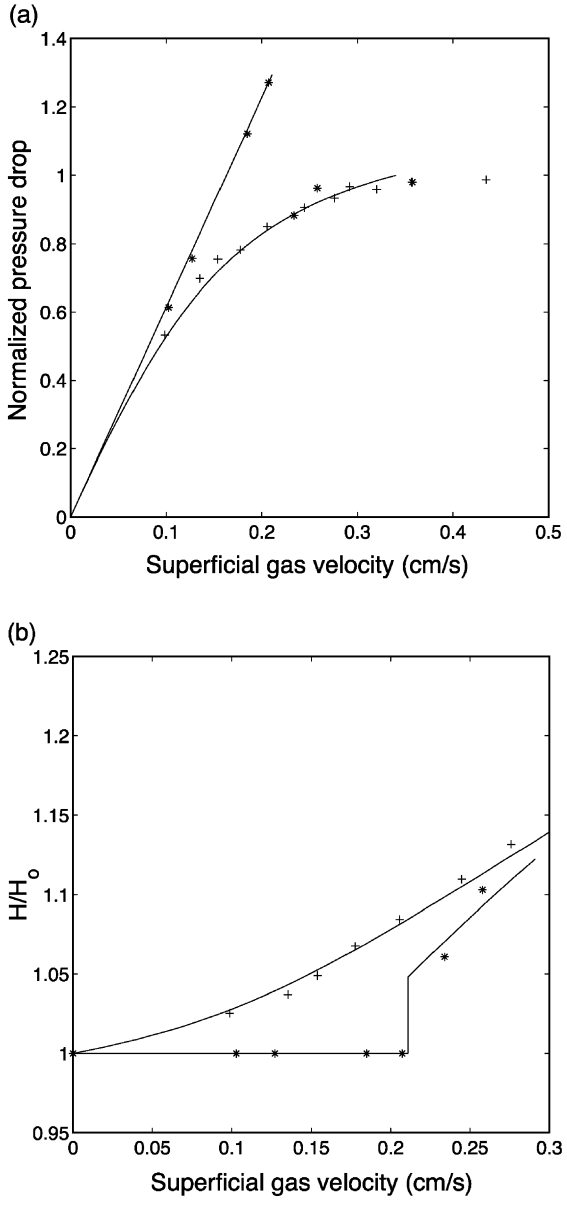

Fig. 2. Dimensionless pressure drop (a) and bed height (b) as functions of the superficial gas velocity, for XL glass beads in a vertical tube of 0.5″ diameter; *, increasing gas flow during fluidization, +, decreasing gas flow during defluidization. The solids curves represent model predictions. Bed height H_0 at zero glass flow rate = 29.6 cm.

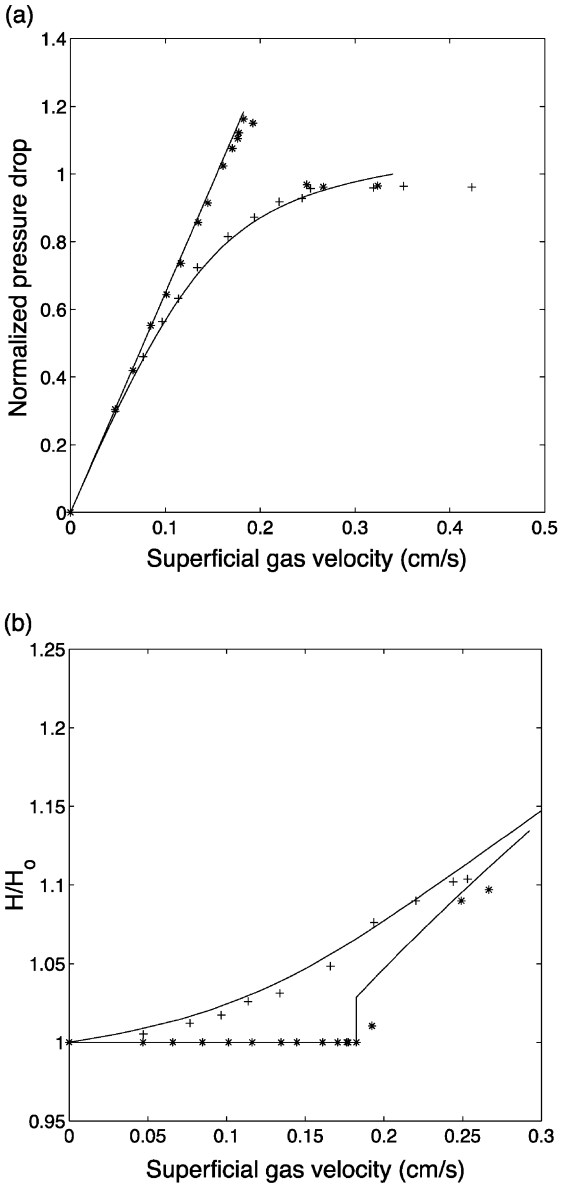

Fig. 3. Dimensionless pressure drop (a) and bed height (b) as functions of the superficial gas velocity, for XL glass beads in a vertical tube of 1″ diameter; *, increasing gas flow during fluidization, +, decreasing gas flow during defluidization. The solids curves represent model predictions. Bed height H_0 at zero glass flow rate = 28.9 cm.

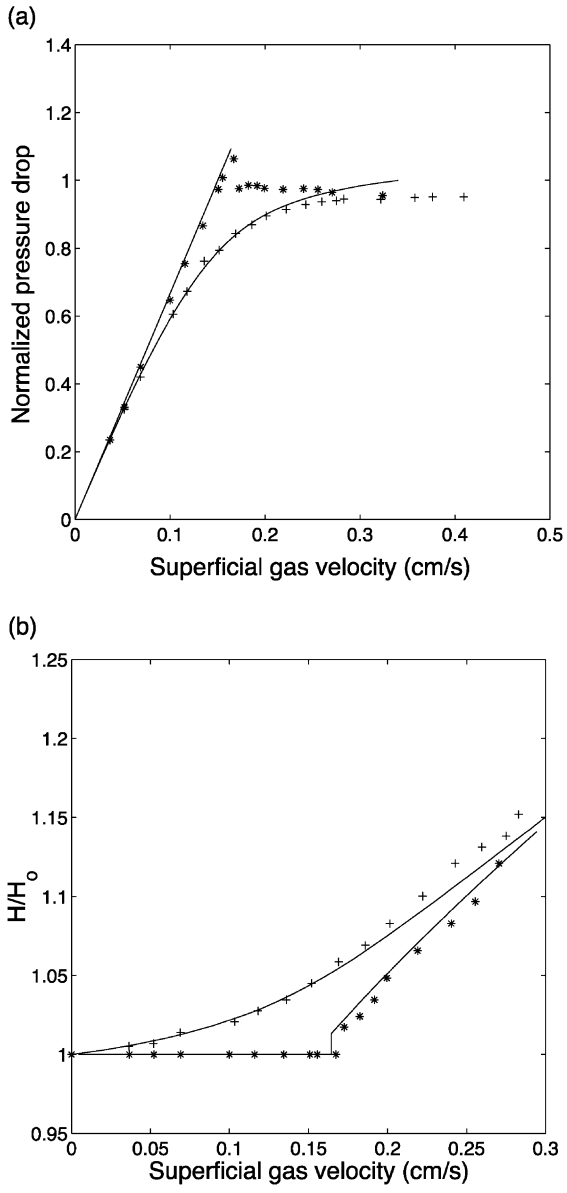

Fig. 4. Dimensionless pressure drop (a) and bed height (b) as functions of the superficial gas velocity, for XL glass beads in a vertical tube of 2″ diameter; *, increasing gas flow during fluidization, +, decreasing gas flow during defluidization. The solids curves represent model predictions. Bed height H_0 at zero glass flow rate = 28.9 cm.

particles. The height of the bed is normalized with respect to height H_0, which is the height of the bed at zero gas flow rate.

It is instructive to first discuss the qualitatively similar features among the three figures in so far as the experimental results go. As the superficial velocity ($\bar{u}$) is increased from zero in the fluidization branch, the pressure drop increases linearly with it. In ideal systems, the bed will become fluidized at a gas superficial velocity U_{mf}, commonly known as the *minimum fluidization* velocity, where the pressure drop first equals the weight of the bed per unit cross-sectional area (mg), and for all $\bar{u} > U_{mf}$, the pressure drop is exactly equal to mg. However, in our system, the pressure drop overshoots mg (see Figs. 2a, 3a and 4a) and continues to increase linearly with $\bar{u}$ until $\bar{u} = \bar{u}_c$. This phenomenon, where $\bar{u}_c > U_{mf}$, occurs when there exist cohesive forces between particles and between the particles and the distributor plate, or when frictional forces at the walls of the bounding tube, or a combination of both [9,10]. The percent overshoot in the pressure drop ($\Delta P/mg^{-1}$) is plotted in Fig. 5 against the inverse of the tube diameter (D). The trend suggests that the overshoot goes to zero as $D \to \infty$. Thus, it appears reasonable to anticipate that the pressure drop overshoot seen in our experiments may be rationalized using a model that considers only wall friction effect.

Beyond $\bar{u}_c$, the pressure drop in the fluidization branch decreases abruptly and this is accompanied by a jump in the bed height. As the gas velocity is further increased, the bed expands without any visible signs of bubbling until the point of minimum bubbling, $\bar{u}_{mb}$, is reached.

In the defluidization branch, as one decreases $\bar{u}$ from $\bar{u}_{mb}$, the pressure drop data remain close to the values recorded in the fluidization experiments initially. With further decreases in $\bar{u}$, the defluidization and fluidization branches separate with the former always lying below the latter. As $\bar{u}$ is progressively brought down to zero, pressure drop readings as well as the height of the bed decrease smoothly down to values corresponding to zero flow of gas.

There is thus a marked hysteresis between the fluidization and defluidization curves in the beds in all the three tubes. The features seen here are very similar to those observed by Tsinontides and Jackson [9] in their experiments with cracking catalyst. We found the hysteresis and the pressure drop overshoot to be more pronounced as tube diameter was decreased (compare Figs. 2a, 3a and 4a).

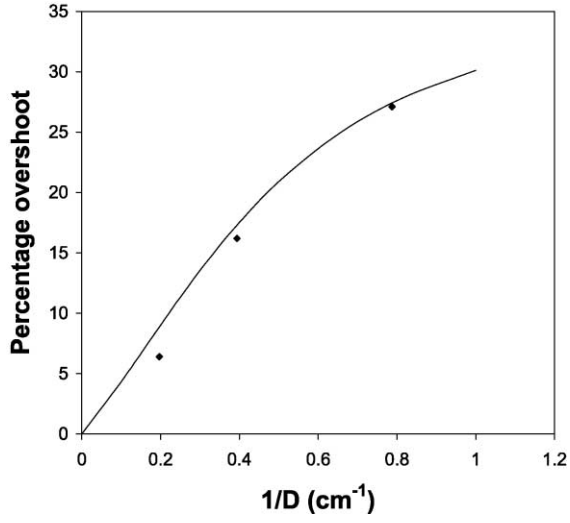

Fig. 5. Percentage overshoot in the pressure drop during fluidization as a function of the inverse of tube diameter; ◆, experimental data points. The solids curve represents model predictions.

These observations are consistent with those of Tsinontides and Jackson [9] and readily suggest that wall friction is important. Another noteworthy feature is the increase in $\bar{u}_c$ with a decrease in the tube diameter; $\bar{u}_c$ is 0.167 cm/s in the 2″ tube, 0.183 cm/s in the 1″ tube and 0.207 cm/s in the 0.5″ tube. Tsinontides and Jackson [9], on the other hand, did not note any such dependence of $\bar{u}_c$ on the confining tube diameter.

Another point of interest is the persistent offset between the pressure drop and *mg*; the asymptotic value of pressure drop is less than *mg* in all the tubes. Such an offset had also been reported elsewhere with different particles; see for example Tsinontides and Jackson [9]. This offset suggests that the beds were not completely fluidized and that a portion of the weight of the bed was still being supported by the distributor plate and/or the frictional stresses acting on the cylindrical walls. The 2″ tube has the largest offset of 5% while the 1″ and 0.5″ tubes have offsets of 4% and 2.5%, respectively. This trend, namely that the offset decreases as tube diameter is decreased, suggests that the offset is not due to wall friction. We conjecture that lateral non-uniformities in bed density become more pronounced as tube diameter increases and is responsible for the observed effect of tube diameter on the offset. The 1-D model described in Section 2 is then a gross simplification and may be used to interpret only *some* of the features of the experimental data. This model simply cannot capture the observed asymptotic offset or its dependence on tube diameter. Consequently, we did not attempt to analyze the pressure data obtained on the fluidization branch for $\bar{u} > \bar{u}_c$ using this model.

The rest of the fluidization–defluidization data were analyzed in terms of the 1-D model as follows. The Richardson–Zaki coefficient, *n*, was estimated from the defluidization data by assuming that the particle volume fraction was uniform everywhere in the bed. (In reality, the particle volume fraction is not uniform; nevertheless ignoring this spatial variation allows us to simplify the parameter estimation process.) It then follows that

$$\frac{\Delta P}{H} \approx \frac{\rho_p \bar{\nu} g}{v_t} \frac{1}{(1-\bar{\nu})^n} \bar{u}$$

where ΔP and H are, respectively, the pressure drop across the bed and the bed height for a particular value of $\bar{u}$ and $\bar{\nu} = m/\rho_p H$. This can be rewritten as

$$\log\left(\frac{\Delta P \bar{u}}{H \rho_p \bar{\nu} g}\right) = n \log(1-\bar{\nu}) - \log v_t.$$

The slope of the best-fit line gives the value of *n*. We found that the data obtained on all three tubes yields a value of ~ 5.0 for *n*. We attempted to estimate the effective terminal velocity, v_t, from the intercept. This led to estimates of 7.25, 7.8 and 5.8 cm/s for v_t from the data obtained in the 0.5″, 1.0″ and 2.0″ tubes, respectively. We suspect that this discrepancy in the estimated value stems from the fact that only a limited region in the $\bar{\nu}$ space is probed by the defluidization branch, with $\bar{\nu}$ typically being between 0.47 and 0.52, and the estimation of v_t requires extrapolation to $\bar{\nu} = 0$. Thus, best-fit lines with even slightly differing slopes yield very different values for v_t. For this reason, v_t was left as an adjustable parameter such that it lies in the range given above.

The other quantity which can be estimated a priori is the limiting value of the solids volume fraction ν_{max}. It is assumed here that this is the solids volume fraction at the bottom of a deep bed upon the end of defluidization. An estimate of this quantity was made by a simple experiment. A known is mass of particles was added to an initially empty bed, the bed was gently fluidized and defluidized, and the bed height was measured. This process was repeated by adding incremental amounts of solid until a fairly deep bed about 40 cm in height was obtained. The incremental changes in bed heights following incremental additions of particles to the bed represent a direct quantitative measure of the solids volume fraction at the bottom of the bed. In this manner, ν_{max} was estimated to be 0.55. Although the bed could have been packed more densely by subjecting it to mechanical vibrations, the packing state achieved spontaneously in defluidization is the most relevant one for our problem. Having made a priori estimates of *n* and ν_{max}, the adjustable parameters remaining in the 1-D model described in Section 2 are *F*, v_t, ν_{min} and μ. The values of these parameters (see Table 2) were estimated by fitting the model to the data. The model predictions obtained with these parameter values are shown in Figs. 2–4 as solid curves. It is clear that the model is able to capture the hysteresis, the overshoots in the pressure and the bed heights upon defluidization reasonably well. All the parameter values used in the model are reasonable, with the exception of the wall friction coefficient, μ, which is smaller than what we would have expected (~ 0.2).

It is instructive to compare the actual height of the fluidized bed in the fluidization cycle in the region $\bar{u} > \bar{u}_c$ with the height, H_{ideal}, of an ideal fluidized bed where the particle volume fraction is independent of height and the

Table 2
Values of model parameters

v_t	Terminal velocity (cm/s)	6.8
n	Richardson–Zaki coefficient	5.0
μ	Coefficient of wall friction	0.07
j_{df}	Jannsen's coefficient for defluidization $=(1-\sin\phi)/(1+\sin\phi)$	0.63
j_f	Jannsen's coefficient for fluidization $=(1-\sin\phi)/(1+\sin\phi)$	1.58
F	Coefficient for σ_s (dynes/cm^2)	1570
ν_{min}	Solids volume fraction below which there is no frictional stress	0.45
ν_{max}	Upper limiting value of solids volume fraction for σ_s (see Eq. (5))	0.55

pressure drop balances the weight of bed per unit area of cross-section. The upward supporting force due to the gas drag, per unit cross-sectional area of such an ideal fluidized bed, is

$$H_{\text{ideal}} \frac{\rho_s \nu g}{\nu_t (1-\nu)^n} \bar{u}.$$

Equating this to the weight of the bed per unit cross-sectional area, mg,

$$H_{\text{ideal}} \frac{\rho_s \nu g}{\nu_t (1-\nu)^n} \bar{u} = mg.$$

However, $\rho_s \nu H_{\text{ideal}} = m$, so that $\nu = m/\rho_s H_{\text{ideal}}$. Inserting this into the force balance above

$$\frac{\bar{u}}{(1 - m/\rho_s H_{\text{ideal}})^n} = \nu_t$$

or

$$H_{\text{ideal}} = \frac{m/\rho_s}{1 - (\bar{u}/\nu_t)^{1/n}}.$$

This is also shown in Figs. 2b, 3b and 4b.

The percentage overshoot in the pressure drop during fluidization, predicted by the model for the combination of parameters in Table 2, is plotted in Fig. 5 as a function of D^{-1} (solid curve in this figure). According to the model, the wall friction effect becomes weaker and weaker as $D \to \infty$, and the overshoot goes to zero. The model is able to capture the experimental data quite nicely. Interestingly, the theoretical curve seems to flatten out as the tube diameter is decreased. As the diameter is decreased, friction at the wall supports a larger and larger fraction of the weight of the bed as a result of which the bed is more loosely packed. This leads to a decrease in σ_s and a corresponding decrease in the normal stress exerted at the wall. The effect of decrease in the tube diameter is thus countered by the decrease in the normal stress at the wall. (The model predicts that at even smaller values of D, the overshoot will decrease with decreasing tube diameter. At such small tube diameters, however, issues such as static arch formation enters the picture and the model becomes inadequate.)

5. Analysis of standpipe data

Experiments on flow behavior of XL glass beads (same as the ones used in the present study) in circulating fluid beds (CFBs) performed by Srivastava et al. [6] revealed that the shear stress experienced by the particles at the walls of the standpipe played an important role in ensuring stable particle circulation in the CFB loop. We refer the reader to Srivastava et al. [6] for details of the CFB experiments. In these experiments, the aeration gas was injected at equal rates through eight ports in the standpipe. Thus, for practical purposes, one can treat the aeration as being spatially uniform for most of the length of the standpipe (with the exception of a small segment of the standpipe near the slide valve). Fig. 6a–c [6,18] show the cross-sectional average solids volume fraction between ports 4 and 5 (which flanked the Electrical Capacitance Tomography unit) of the standpipe as a function of the external aeration rate for three different slide valve openings. The triangles denote results obtained from ECT measurements, with the filled triangles and open triangles representing steady and unsteady flow conditions, respectively. The pressure drop across ports 4 and 5 can be converted into an equivalent solids volume fraction by dividing by $\rho_p g h$ with h being the distance between the two ports. This quantity, measured only during stable operating conditions, is shown as filled diamonds and is a quantitative measure of the support provided by the gas to suspend the weight of the bed. The difference between the solids volume fraction estimated from ECT and pressure drop data, henceforth referred to as $\Delta\nu$, is a quantitative measure of support provided by shear stress at the wall and axial gradient in the vertical normal stress in the granular phase. It is clear from our fluidized bed experiments and modeling described in the previous sections that the axial gradient in the vertical normal stress in the granular phase is not likely to be the main source of the support, as this would have resulted in a rapid increase in particle volume fraction (within a depth of a few tens of cm) to a value very close to $\nu_{\max}$ and this was not the case in most of the operating conditions reported in Fig. 6a–c. Thus wall friction is the most likely explanation for the observed $\Delta\nu$. All the data reported in Fig. 6a–c in the stable operating region are summarized in Fig. 7, which shows a plot of $\Delta\nu$ against $\bar{\nu}$ estimated from the ECT measurements. In spite of the scatter, a trend can be observed, suggesting that a simple relation does indeed exist between these two quantities. A simple analysis of the wall friction in the standpipe, where one uses the frictional yield stress in XL glass beads (i.e. Eq. (5) and the parameter values) estimated through fluidization–defluidization measurements, is described below.

Consider a simple one-dimensional model of granular flow in a tall cylindrical standpipe of radius R under steady flow conditions. In particular, let us focus on a region away from the entrance or the exit, such as the region where the ECT measurements were made by Srivastava et al. [6]. Even though under such conditions ECT measurements revealed random low-amplitude high-frequency fluctuations in the solids volume fraction arising due to non-uniformities, one may assume to a good approximation that the bed at this location was essentially at a uniform solids volume fraction of $\bar{\nu}$, which was determined by time-averaging the ECT data. Assuming that the granular material is in compressive yield, the vertical stress σ_s can thus be determined from Eq. (4) and the model parameters estimated from defluidization–fluidization experiments. The normal stress σ_h exerted

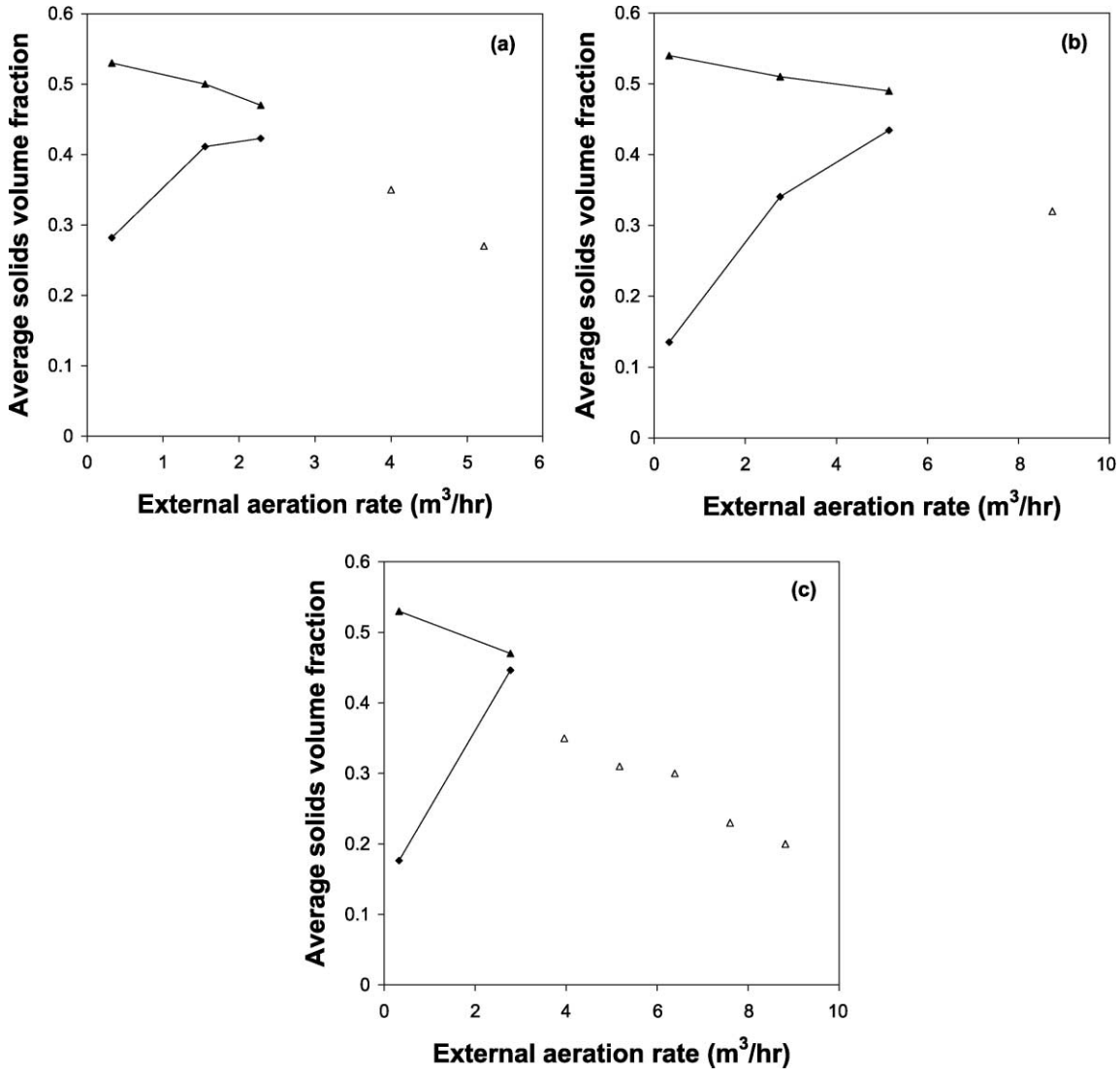

Fig. 6. Variation of time-averaged solids volume fraction of XL glass beads with external aeration rate for constant slide valve openings: (a) 10% slide valve opening, (b) 17.5% slide valve opening, (c) 35% slide valve opening; ▲: from ECT data (steady flow regime), △: from ECT data (unstable flow regime), ◆: pressure drop readings expressed as equivalent solids volume fractions. Source: Srivastava et al. [6], Srivastava [18].

on the wall would then be $j\sigma_s$ where j is the Janssen's coefficient. The shear stress at the wall would then be $\mu j\sigma_s$. A simple force balance under conditions where $\bar{\nu}$ is independent of axial position yields

$$\Delta\nu = \frac{2\mu j\sigma_s(\bar{\nu})}{\rho_p g R}.$$

From the slope of a plot of $\Delta\nu$ against $\sigma_s(\bar{\nu})$, the value of μj was estimated to be 0.225. The right hand side of the above equation is shown in Fig. 7 as a solid curve. It is clear that the 1-D model is able to capture the general trend in the standpipe data quite nicely, in spite of the presence of fluctuations recorded by the ECT unit.

In the presence of such fluctuations, it seems reasonable to expect that on an average j would have a value close to 1, so that the value of μ is indeed close to 0.225. It is remarkable to note that this is equal to $\sin\varphi$. Wall friction coefficient will be equal to $\sin\varphi$ when a layer of particles remains stuck to the wall, which was indeed the case in the standpipe experiments. Electrostatic effects are known to be important in transport of glass beads in Plexiglas pipes [19,20]. Adhesion of a layer of particles to the wall as a result of electrostatic effects in the standpipe is quite conceivable. This may also explain why a much smaller value of μ was required to fit our fluidization–defluidization data, where tribo-electric charging would have occurred to a much smaller extent. Indeed, upon emptying the fluidized bed at the end of our fluidization–defluidization experiments, we observed only a few spots where the particles remained adhered to the wall. In any case, the above argument is at best a speculation and we must conclude

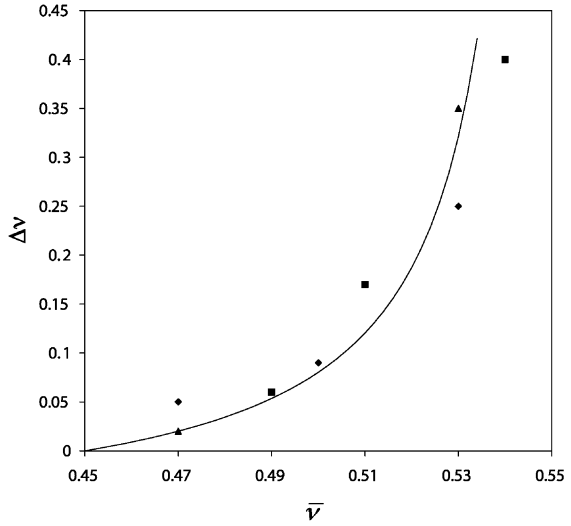

Fig. 7. Support provided by wall shear stresses to suspend the weight of the bed, quantified by $\Delta\nu$, as a function of ν, the average solids volume fraction in the standpipe (obtained from ECT measurements). Source of CFB data: Srivastava et al. [6], Srivastava [18]. The solid curve represents the 1-D model predictions. ◆: 10% slide valve opening, ■: 17.5% slide valve opening, ▲: 35% slide valve opening.

by noting that this difference in the value of μ between the standpipe and fluidization experiments remains unresolved.

6. Summary

Fluidization and defluidization experiments were conducted in tubes of different diameters in order to understand the role of friction in modifying fluidization–defluidization characteristics. Careful measurements of the gas flow rate, bed height and pressure drop across the bed were made during the process of both fluidization as well as defluidization. A marked hysteresis between the fluidization and defluidization curves in all the beds is observed. The process of fluidization is characterized by the presence of an overshoot in the pressure drop beyond that required to suspend the weight of particles in the bed. The hysteresis and pressure overshoot are more pronounced in the beds of smaller diameter. These features are very similar to those observed by Tsinontides and Jackson [9] with their experiments on cracking catalyst particles. In our study, these features appear to be a consequence of wall friction. Another noteworthy feature is the persistent offset in the pressure drop at high gas flow rates from the theoretical value, which was more pronounced in larger diameter tubes. We believe that this is due to the presence of lateral nonuniformities in the bed density.

An estimate of the magnitude of contact stresses was made by fitting the model of Jackson [10] to the fluidization–defluidization data. The model is able to capture the hysteresis, the pressure drop overshoot and the bed height upon defluidization quite well. The frictional yield stress obtained in this manner was used to analyze the standpipe data reported by Srivastava et al. [6]. A 1-D model based on a simple analysis of wall friction in the standpipe is able to capture the general trends in the standpipe data reasonable well. However, the values of the wall friction coefficient, μ, obtained from the standpipe and fluidization experiments are quite different. It is hypothesized that this could be due to electrostatic effects.

Acknowledgements

We are grateful to Roy Jackson for his helpful comments. This work was supported by ExxonMobil Research and Engineering Company and the US Department of Energy CDE-FC26-00NT40971.

References

[1] J.R. Grace, H. Bi, in: J.R. Grace, A.A. Avidan, T.M. Knowlton (Eds.), Circulating Fluidized Beds, Blackie Academic and Professional, New York, 1997, p. 1.
[2] R. Bader, J. Findlay, T.M. Knowlton, in: P. Basu, J. Large (Eds.), Proceedings of Second International Conference on Circulating Fluidized Beds, Pergamon, Oxford, 1988, p. 123.
[3] J.M. Matsen, Powder Technol. 7 (1973) 93.
[4] L.S. Leung, Powder Technol. 7 (1973) 343.
[5] J. Zhang, P. Jiang, L.-S. Fan, in: L.-S. Fan, T.M. Knowlton (Eds.), Fluidization IX, Engineering Foundation Publication, 1998, p. 245.
[6] A. Srivastava, K. Agrawal, S. Sundaresan, S.B. Reddy Karri, T.M. Knowlton, Powder Technol. 100 (1998) 173.
[7] S.M.P. Mutsers, K. Rietema, Powder Technol. 18 (1977) 239.
[8] K. Rietema, H.W. Piepers, Chem. Eng. Sci. 45 (1990) 1627.
[9] S.C. Tsinontides, R. Jackson, J. Fluid Mech. 255 (1993) 237.
[10] R. Jackson, in: L.-S. Fan, T.M. Knowlton (Eds.), Fluidization IX, Engineering Foundation Publication, 1998, p. 1.
[11] R. Jackson, The Dynamics of Fluidized Particles, Cambridge Univ. Press, Cambridge, 2000.
[12] J.F. Richardson, W.N. Zaki, Trans. Inst. Chem. Eng. 32 (1954) 35.
[13] J.H. Atkinson, P.L. Bransby, The Mechanics of Soils: An Introduction to Critical State Soil Mechanics, McGraw-Hill, England, 1978.
[14] D.G. Schaeffer, J. Differential Equations 66 (1987) 19.
[15] J.R. Prakash, K.K. Rao, Chem. Eng. Sci. 43 (1988) 479.
[16] P.C. Johnson, P. Nott, R. Jackson, J. Fluid Mech. 210 (1990) 501.
[17] S.C. Tsinontides, PhD dissertation, Princeton University, 1992.
[18] A. Srivastava, PhD dissertation, Princeton University, 2001.
[19] E.E. Smetltzer, M.L. Weaver, G.E. Klinzing, Ind. Eng. Chem. Process Des. Dev. 21 (1982) 390.
[20] A. Zaltash, C. Myler, G.E. Klinzing, J. Pipelines 7 (1988) 85.

Coarse-grid simulation of reacting and non-reacting gas-particle flows

Final Technical Report

Award # DE-FC26-00NT409071

DOE Vision 21 Virtual Demonstration Initiative

Appendix G

PERGAMON

Chemical Engineering Science 57 (2002) 5123–5141

Chemical Engineering Science

www.elsevier.com/locate/ces

The role of contact stresses and wall friction on fluidization

Peter N. Loezos, Paola Costamagna[1], Sankaran Sundaresan*

Department of Chemical Engineering, Princeton University, Princeton, NJ 08544, USA

Received 17 September 2001; received in revised form 8 July 2002; accepted 24 July 2002

Abstract

Fluidization and defluidization experiments, where we increased the gas superficial velocity in small increments and then decreased it, were performed in tubes of different diameters to probe the role of wall friction on pressure drop and bed height. Such experiments, covering the regimes of packed bed, stable bed expansion and bubbling bed, were carried out for several different particles. The compressive yield strength of the particle assemblies at various volume fractions was determined by measuring the height of fully defluidized beds at various mass loading levels. The systematic effect of the tube diameter on pressure drop and bed height hysteresis could be rationalized in terms of a one-dimensional model that accounted for the effect of wall friction and path-dependent contact stresses in the particle phase. Bubbling seemed to set in when the yield stress in the particle assembly could be overcome by the inherent fluctuations. Our experiments, which focused primarily on gas velocities below the minimum bubbling conditions, did not reveal any dramatic change across the Geldart A–B boundary. This is consistent with the original observation by Geldart (Powder Technol. 7 (1973) 285). The distinct difference between beds of group A and B particles in the gently bubbling regime reported by Cody et al. (Powder Technol. 87 (1996) 211) is thus likely to be due to changes in the dynamics of the bubbles, as we observed no striking difference between these beds at gas velocities below minimum bubbling conditions.

Keywords: Fluidization; Powders; Granular materials; Hydrodynamics; Wall friction; Contact stress

1. Introduction

The behavior of solids fluidized by gases is a subject of great practical relevance. Geldart (1973) classified the gas–solid systems into four categories on the basis of the nature of fluidization. Very fine particles, belonging to group C, are cohesive and are difficult to fluidize. Beds of somewhat larger particles, belonging to group A, manifest smooth expansion over a range of fluidizing gas velocities before bubbling begins. Even larger particles, belonging to group B, bubble almost immediately after fluidization. The rise velocity of bubbles in beds made up of particles belonging to group A or B is generally larger than the gas velocity through the dense phase. In contrast, in beds of very large particles belonging to Group D, the bubble rise velocity is smaller than the interstitial velocity of the gas in the dense phase, so that the mixing pattern in this case differs significantly from that observed in beds of group A or B particles.

Geldart (1973) noted that the superficial gas velocity at minimum bubbling conditions (u_{mb}) increased in a nearly linear manner with particle diameter (in the range 25–220 μm, covering group A and B particles), while the minimum fluidization velocity, u_{mf}, for particles of given density in a gas with specified density and viscosity increases quadratically with particle size. (Here, u_{mf} denotes gas superficial velocity where the pressure gradient exactly balances the weight of a unit volume of bed.) This led Geldart (1973) to observe that the range of gas velocities for which stable bed expansion could be achieved would decrease as the particle size increased. He estimated the particle diameter where this window would become *unobservably small* by equating u_{mf} and u_{mb}, and labeled it as representing a point on the A–B boundary.

The mechanism responsible for the window of stable bed expansion manifested by group A particles has been explored extensively. Jackson (1963) noted that in the absence of particle phase stress the uniformly fluidized state is always unstable, while Anderson and Jackson (1968) concluded that viscous stresses in the particle phase are not sufficient to impart stability. Garg and Pritchett (1975) pointed out that the uniform state could be stabilized by

* Corresponding author. Tel.: +1-609-258-4583; fax: +1-609-258-0211.
E-mail address: sundar@princeton.edu (S. Sundaresans).
[1] Present address: DICHEP-University of Genoa, Via Opera Pia 15, 16415 Genoa, Italy.

0009-2509/02/$ - see front matter © 2002 Elsevier Science Ltd. All rights reserved.
PII: S0009-2509(02)00421-9

adding to the particle phase momentum balance equation a force term of the form $-G\nabla\phi$ where ϕ is the particle volume fraction and G is a sufficiently large positive number. The origin of such a term has been debated extensively in the literature. Rietema (1973), Mutsers and Rietema (1977a) and Rietema and Piepers (1990) attributed it to cohesive forces at particle–particle contact. Mutsers and Rietema (1977b) argued that their data on fluidization of particles with different gases are consistent with a stabilizing force whose origin is enduring contact between particles.

Foscolo and Gibilaro (1984) rejected the idea that inter-particle forces stabilize the uniformly fluidized state and suggested that the gas–particle drag should include a term of the form $-G\nabla\phi$. Batchelor (1988) discounted the arguments by Foscolo and Gibilaro, and attributed this force to random fluctuations in particle velocity, which leads to hydrodynamic diffusion of the particles in the fluidized bed.

Tsinontides and Jackson (1993) performed fluidization–defluidization experiments using FCC particles fluidized by dry and humid air, and concluded that the particle assemblies exhibited yield stresses throughout the range of stable fluidization.

More recently, Cody, Goldfarb, Storch, and Norris (1996) concluded that their data on acoustic shot noise in fluidized beds containing glass beads of various mean diameters (63–595 μm) and narrow size distributions (henceforth referred to as Cataphote particles) supported "the concept that the distinction between Geldart A and B fluidization regimes lies in a fundamental difference in gas particle dynamics rather than an ad-hoc inhibition of bubbling". These authors used the acoustic shot noise to determine the granular temperature, $T = \langle C^2 \rangle$, of the particles in the bed, where $\langle\ \rangle$ denotes an ensemble-average and C is fluctuation velocity of the particles. They found that T was essentially zero until the gas superficial velocity was increased past some threshold value (u^*), and this is consistent with the observations by Menon and Durian (1997). The manner in which T changed as the superficial gas velocity, u, was increased further was found to be noticeably different for Geldart type A and B particles. In the case of type A particles, $\sqrt{T/u^2}$ increased nearly linearly with $u - u^*$ at first, and then decreased exponentially towards a non-zero plateau, with the intermediate maximum being rather pronounced. In contrast, $\sqrt{T/u^2}$ vs. u data for the type B particles manifested either a weak maximum or simply rose monotonically to the plateau.

Cody et al. (1996) found u^* to be close to u_{mf} for the Cataphote particles, although their plots suggest that u^* could easily have been 10–20% larger than u_{mf}. These authors performed similar experiments with FCC particles as well and found the behavior to be similar to that of the Cataphote particles falling in the Type A category, with the exception that u^* was roughly three times u_{mf}. They speculated that this large difference could have been a consequence of the wide size distribution of the FCC particles.

The observation by Menon and Durian (1997) that T was essentially zero until the bed began to bubble suggests that u^* recorded by Cody et al. (1996) is likely to be u_{mb}. If so, the differences in the manner in which $\sqrt{T/u^2}$ varied with gas velocity for type A and type B particles observed by Cody et al. (1996) may be more indicative of the effect of particle diameter and particle size distribution on the dynamics of a gently bubbling bed than the observability of a window of uniform bed expansion (which was the basis of Geldart's original classification).

Koch (1990) and Koch and Sangani (1999) concluded from a linear stability analysis of a uniformly fluidized bed of infinite extent that the fluctuating motion of particles resulting from the relative motion between the fluid and the particles in a uniformly fluidized suspension is not vigorous enough to impart stability to the uniform state. This result then suggests that the origin of stabilization in the gas-fluidized systems is likely to be non-hydrodynamic. The observations by Rietema and Piepers (1990), Tsinontides and Jackson (1993) and Menon and Durian (1997) suggest that yield stresses resulting from sustained contact between particles is the most probable mechanism for stable expansion of gas-fluidized beds. Questions that immediately follow are:

(Q1) How do the yield stress characteristics of a given material change as one increases the particle size from group A to group B? Is there any evidence of a significant qualitative change across the A–B boundary?

(Q2) What is the origin of the intermediate maximum in the $\sqrt{T/u^2}$ vs. u locus observed by Cody et al. (1996) in the bubbling regime with group A material?

We have probed the first of these two questions in the present study, and the second one will be addressed in a future publication. We will demonstrate that the yield stress characteristics change gradually as one increases the particle size and that no abrupt changes occur across the Geldart group A–B boundary.

We have also examined in the present study the role of wall friction on fluidization characteristics. Tsinontides and Jackson (1993) measured bed height and pressure drop at various gas flow rates through beds of FCC particles in 1″ and 2″ ID columns, probing carefully the path dependence of the results. They observed a hysteretic behavior for gas velocities below u_{mb}, which is indicative of path-dependent stresses. These authors found that as they increased the air flow rate through a bed of FCC particles (which was initially fully defluidized), the bed height remained invariant while the pressure drop increased. Such a state persisted even when the pressure drop exceeded significantly the weight of the bed per unit cross-sectional area. At some critical gas velocity, the bed expanded abruptly and the pressure drop decreased to a value below that required to fully support the weight of the bed. Such pressure drop overshoots have been observed by many researchers (e.g., see Valverde, Ramos, Castellanos, & Watson, 1998). Tsinontides and Jackson (1993) found the overshoot to

depend on the tube diameter, which suggested the possible influence of wall friction. In contrast, Valverde et al. (1998), who worked with much finer powders (belonging to Geldart group C) and tubes of much larger cross-sectional area, did not observe an appreciable effect of tube diameter on the overshoot. Tsinontides and Jackson (1993) and Valverde et al. (1998) used the pressure drop overshoot to estimate cohesive strength of the materials.

Through simple one-dimensional (1-D) models for fluidization and defluidization (described in Section 2), Jackson (1998, 2000) showed that wall friction can lead to pressure drop overshoot even for a non-cohesive material. We have studied the fluidization and defluidization characteristics of a number of particles (including those used by Cody et al., 1996) in tubes of different diameters, in order to expose the role of wall friction. We will show that the fluidization–defluidization characteristics (including the pressure drop overshoot) of all the particles reported here, can be rationalized on the basis of wall friction and compressive yield stress characteristics of the particle assemblies, without requiring an additional influence of cohesion between particles or particles and the distributor.

It will also become clear that, in every single system for which measurements have been made in the present study, bubbling commenced only after the yield stress in the particle assembly became very small. Furthermore, no interval of stable bed expansion was observed after the bed has expanded sufficiently to drive the yield stress to zero. This implies that hydrodynamic stabilization of the state of uniform fluidization is not observed in these beds (involving particles larger than $\sim$ 60 μm). (Recent experiments by Valverde, Castellanos, and Quintanilla (2001) suggest that hydrodynamic stabilization may be possible for finer particles ($\sim$ 9 μm), but we have not probed the behavior of such small particles.)

We will also see that, for gas velocities below u_{mb}, changes in the system characteristics with particle size are only gradual and that Geldart group A–B boundary separates *approximately* the systems where an interval of stable bed expansion is readily observed from those where it is too small to be observed (as originally intended by Geldart, 1973).

This paper is organized as follows. Section 2 summarizes the 1-D model for fluidization and defluidization branches. The experimental system and procedure are described in Section 3. Section 4 contains a detailed description of the experimental results along with a discussion on the basis of the 1-D model. We also discuss here the conditions at which bubbling commences in our systems. The main findings of the study are summarized in Section 5.

2. Theory

An analysis of the role of contact stresses on the mechanical behavior of fluidized beds of non-cohesive particles has been discussed recently by Jackson (1998), where a 1-D model has been proposed to describe the fluidization/defluidization behavior of these systems. The present treatment is a minor modification of his analysis, as suggested by Srivastava and Sundaresan (2002). In the regime of stable bed expansion, inter-particle forces are transmitted largely through sustained contact between particles, and the force balance for the particle assembly is written as

$$\frac{\mathrm{d}\sigma_s}{\mathrm{d}x} \pm \frac{4}{D}\mu j\sigma_s = \rho_p\phi g - \beta(\phi)\frac{\bar{u}}{(1-\phi)}. \tag{1}$$

The corresponding force balance on the gas is given by

$$\frac{\mathrm{d}p}{\mathrm{d}x} = \beta(\phi)\frac{\bar{u}}{(1-\phi)}. \tag{2}$$

In Eq. (1), x is the vertical coordinate measured from the upper surface of the bed (with the x axis pointing downward), and σ_s is the cross-sectional average of the xx-component of the compressive stress transmitted through enduring contact between particles. The second term on the left-hand side of Eq. (1) represents the force associated with friction between the particle assembly and the tube wall, where μ is the coefficient of friction, D is the diameter of the tube, and j is Janssen's coefficient (usually assumed to be a constant) which is the ratio between the normal stress exerted by the particles on the wall and σ_s (Janssen, 1895). The positive sign applies upon defluidization branch where the gas flow rate is being progressively decreased and bed is compacting (and the wall friction is pointing vertically upwards), while the negative sign applies in the fluidization branch where the gas flow rate is steadily increased. The first term on the right-hand side of Eq. (1) represents gravitational force, where ρ_p is the particle density, ϕ is the volume fraction of the particles, and g is the specific gravity force. The last term is the drag force exerted by the gas on the particles where β is the drag coefficient and $\bar{u}$ is the superficial gas velocity. Eq. (2) simply balances the pressure gradient in the gas phase with the drag force exerted on the fluid by the particles.

The drag coefficient β is taken to be of Richardson and Zaki (1954) form:

$$\beta(\phi) = \frac{\rho_p\phi g}{v_t}\frac{1}{(1-\phi)^{n-1}}, \tag{3}$$

where v_t is the terminal velocity of a single particle and n is the Richardson–Zaki exponent.

Non-cohesive granular materials can support only compressive stresses, and the compressive yield stress σ_s^x can be expected to be a monotonically increasing function of ϕ. Various expressions for σ_s^x have been proposed in the literature (Prakash & Rao, 1988; Johnson, Nott, & Jackson, 1990). As discussed below in a greater detail, we have employed the functional form for σ_s^x suggested by

Johnson et al. (1990):

$$\sigma_s^x(\phi) = \begin{cases} c\dfrac{(\phi-\phi_{\min})^a}{(\phi_{\max}-\phi)^b}, & \phi_{\min} < \phi < \phi_{\max}, \\ 0, & \phi < \phi_{\min}, \end{cases} \tag{4}$$

where $\phi_{\min}, \phi_{\max}, a, b$ and c are positive constants. This functional form postulates that sustained contact between particles occur only when the particle volume fraction exceeds $\phi_{\min}$. Furthermore, the compressive yield stress is assumed to diverge as $\phi \to \phi_{\max}$. Although volume fractions in excess of $\phi_{\max}$ may be achieved by mechanical means such as tapping, the model considers $\phi_{\max}$ as the upper bound for ϕ which is achieved in simple fluidization/defluidization experiments (involving deep beds). Srivastava and Sundaresan (2002) found that their fluidization/defluidization data for glass beads ($d_{p,50} = 50$ μm) could be captured by such a model with a further restriction that $a = b = 1$, which was the form used by Jackson (1998) in his illustrative examples. In the present study, where we report results for a number of different particles, the form given by Eq. (4), where the parameters for each particle sample were determined empirically, was found to be adequate.

2.1. Defluidization branch

Consider the case where the bed is in an expanded state, and the gas flow rate is reduced in small increments, allowing the bed to compact and equilibrate at each gas flow rate. A key assumption in the model is that the local volume fraction of the particles is such that the bed is in compressive yield everywhere, and $\sigma_s = \sigma_s^x$. For a given value of $\bar{u}$, Eqs. (1) and (3) can be combined and integrated numerically to yield ϕ as a function of bed height, starting with $\phi = \phi_{\min}$ at $x = 0$, and terminating at $x = H$, the total height of the bed, such that

$$\rho_p \int_0^H \phi(x)\,\mathrm{d}x = m. \tag{5}$$

Here, m denotes the specified mass loading of particles in the bed per unit cross-sectional area. Once the particle volume fraction profile is determined, the fluid pressure as a function of height is readily calculated from Eq. (2). In this manner, the theoretical defluidization curves describing variation of pressure drop and bed height with $\bar{u}$ can be determined.

2.2. Fluidization branch

Now let us consider the process of fluidizing a defluidized bed. When the gas velocity is increased gradually from zero, the height of the bed and the solids volume fraction profile $\phi(x)$ remain unaltered until a critical velocity $\bar{u}_c$ is reached. In the regime, where $\bar{u} < \bar{u}_c$, the upward drag force exerted by the gas on the particles supports an increasing fraction of the weight of the particles and this is accompanied by a steady increase in the pressure drop across the bed and a change in the stress profile, $\sigma_s(x)$. As argued by Jackson (1998), value of σ_s at the bottom of a bed will decrease monotonically with increasing $\bar{u}$ and vanish at some critical velocity $\bar{u} = \bar{u}_c$, while the stress σ_s at all other elevations in the bed ($x > 0$) will be greater than zero. At this critical gas velocity, the bed will lose contact with the distributor, provided the particle assembly does not interact with the bottom distributor cohesively, and the entire bed will be lifted as a block. As the bed rises, the particles will rain down from the lower surface and re-compact to form a new bed. The velocity $\bar{u}_c$ where this event occurs can be found as follows. Combining Eqs. (1) and (3):

$$\frac{\mathrm{d}\sigma_s}{\mathrm{d}x} - \frac{4}{D}\mu j \sigma_s = \rho_p \phi g - \frac{\rho_p \phi g}{v_t}\frac{\bar{u}}{(1-\phi)^n}, \tag{6}$$

where it has been recognized that the frictional force will act downward to oppose bed expansion and that the $\phi(x)$ profile is the same as that obtained from defluidization calculations with $\bar{u} = 0$. Integrating,

$$\sigma_s(x=H)\mathrm{e}^{-JH} - \sigma_s(x=0) = \rho_p g \int_0^H \phi \mathrm{e}^{-Jx}\,\mathrm{d}x - \frac{\rho_p g \bar{u}}{v_t}\int_0^H \frac{\phi}{(1-\phi)^n}\,\mathrm{e}^{-Jx}\,\mathrm{d}x, \tag{7}$$

where $J = (4/D)\mu j$. At the point where the bed rises, $\bar{u} = \bar{u}_c$ and $\sigma_s(x = H) = \sigma_s(x = 0) = 0$. Therefore,

$$\frac{\bar{u}_c}{v_t} = \frac{\int_0^H \phi \mathrm{e}^{-Jx}\,\mathrm{d}x}{\int_0^H (\phi/(1-\phi)^n)\mathrm{e}^{-Jx}\,\mathrm{d}x}. \tag{8}$$

The corresponding pressure drop can readily be found by integrating Eq. (2), once $\bar{u}_c$ is known.

Jackson (1998) assumed in his illustrative examples that the same value for the Janssen's coefficient j applied for both fluidization and defluidization branches. Srivastava and Sundaresan (2002) found that different values of μj were needed for the fluidization and defluidization branches to capture their fluidization/defluidization data for the 50 μm glass beads. (As discussed later, we found this to be the case in our analysis as well.) This is equivalent to using different values of j in the two branches, as there is no physical basis for using different values of μ in the two branches. The rationale for different j values in the two branches, suggested by Srivastava and Sundaresan (2002), is briefly outlined below.

Along the centerline of the cylindrical bed, the vertical and horizontal normal stresses (σ_s and ρ_h, respectively) will be the principal stresses, provided cylindrical symmetry holds. During defluidization, where the bed is gradually being compacted as we progressively lower the gas flow rate, the vertical stress σ_s will be the major principal stress, at least along

the centerline, and

$$\frac{\sigma_h}{\sigma_s} = j_{df} = \frac{1-\sin\varphi}{1+\sin\varphi}, \tag{9}$$

where φ is the angle of internal friction for the particles. Thus, it is reasonable to expect j to be less than unity in the defluidization branch, with a value close to j_{df}.

Srivastava and Sundaresan (2002) found that their data in the fluidization branch could be captured reasonably well only if the value of j in this branch was chosen to be greater than unity. They speculated that j in the fluidization branch will be close to $j_{df}^{-1}(=j_f$, say). This is equivalent to saying that the bed is close to a state of incipient yield where σ_s and σ_h are the minor and major principal stresses, respectively.

In the present study, we simply report the two values of μj used to fit the experimental data in the fluidization and defluidization branches (henceforth referred to as $(\mu j)_f$ and $(\mu j)_{df}$, respectively). If the speculation by Srivastava and Sundaresan (2002) that $j \approx j_f$ in the fluidization branch and $j \approx j_{df}$ in the defluidization branch holds,

$$\frac{(\mu j)_{df}}{(\mu j)_f} \approx \left(\frac{1-\sin\varphi}{1+\sin\varphi}\right)^2. \tag{10}$$

3. Experimental

Two different types of glass beads, henceforth referred to as Jaygo and Cataphote particles, having wide and narrow size distributions, respectively, were used in this study. Experiments were performed with two different Jaygo particles, referred to as fine Jaygo (sieved between 58 and 75 μm) and coarse Jaygo (sieved between 93 and 210 μm), and five different Cataphote particles having nominal particle diameters of 63, 88, 105, 150 and 210 μm.

Fluidization and defluidization experiments were performed in three different Plexiglas tubes (nominal ID 0.5″, 1.0″ and 2.0″). Following Tsinontides (1992), gas distributors were made by sandwiching two layers of fibrous material between two micronic mesh screens. De-humidified air, from compressed air cylinders, was used as the fluidization medium. The superficial velocity at each operating condition was determined using a bubble meter, which was attached to the exit of the fluidized beds. The total pressure drop across the distributor and the bed was measured at each air superficial velocity via a U-tube manometer. The distributor pressure drops at various air superficial velocities were separately measured in empty tubes. By subtracting the distributor pressure drop from the total pressure drop, one can readily determine the pressure drop across the bed.

Fluidization and defluidization experiments were performed as follows: A bed, approximately 30 cm in height, was formed by depositing a known mass of particles in the tubes. Air flow was initiated, and the bed was allowed to gently bubble for a period of time. The air flow rate was then decreased all the way down to zero in small increments, the system was allowed to equilibrate at each condition, and the bed height, the air superficial velocity and pressure drop were recorded. After completion of such a defluidization branch, the air flow was incrementally increased, and pressure drop, bed height and superficial velocity were once again recorded. Such measurements in the fluidization branch were made all the way into the bubbling regime.

4. Results and discussion

Figs. 1a–c show normalized pressure drop ($=\Delta P/mg$) as a function of scaled superficial velocity, ($=\bar{u}/u_m$ where u_m is a reference velocity given in Table 1 for each particle), for the fine Jaygo particles in the 0.5″, 1.0″ and 2.0″ tubes. The mass loading in every case was 39.8 g/cm^2. A normalized pressure drop of unity implies that the pressure drop across the bed exactly balances the weight of the bed. The corresponding scaled bed height ($=H/H_o$ where H_o refers to height of a fully defluidized bed) data are given in Figs. 2a–c. In these figures, the points refer to the experimental data, while solid lines represent model predictions (discussed later).

The fluidization–defluidization data for the 63 and 105 μm Cataphote particles are similar to those shown in Figs. 1 and 2, and are presented in Figs. 3 and 4, and 5 and 6, respectively. The results for the 88 μm Cataphote particles are similar to those shown in Figs. 3 and 4, and can be found elsewhere (Loezos, 2002). The trends observed in Figs. 1–6 are same as those obtained by Srivastava and Sundaresan (2002) for 50 μm glass beads, using the same experimental apparatus.

For every type of particles used in the present study, an essentially linear relation between pressure drop and $\bar{u}$ was obtained in the region $0 < \bar{u} < \bar{u}_c$ of the fluidization branch, where the bed height remained invariant. The critical gas superficial velocity, $\bar{u}_c$, was found to be dependent on the tube diameter (see Table 1). The scaled pressure drop at $\bar{u}_c$ exceeded unity in every case reported here. Such an overshoot has been noted by several authors (Tsinontides & Jackson, 1993; Valverde et al., 1998). We found that the extent of overshoot, defined as $(\Delta p/mg - 1)$, decreased as the tube diameter was increased (see Figs. 7 and 8 for the fine Jaygo particles and the Cataphote particles, respectively). It seems reasonable to extrapolate that the overshoot will decrease steadily towards zero as $D \to \infty$ for all the particles. This suggests that the pressure drop overshoots observed in all our experiments were primarily due to wall friction. With this in mind, we have assumed in our analysis of the data that none of the particle samples used in our experiments interacted with the distributor material cohesively. Srivastava and Sundaresan (2002) found a similar dependence of $\bar{u}_c$ and overshoot on the tube diameter for 50 μm glass beads.

When $\bar{u}$ was increased past $\bar{u}_c$, the bed expanded suddenly and the pressure drop registered a marked decrease. For both the 63 and 88 μm Cataphote particles, the bed

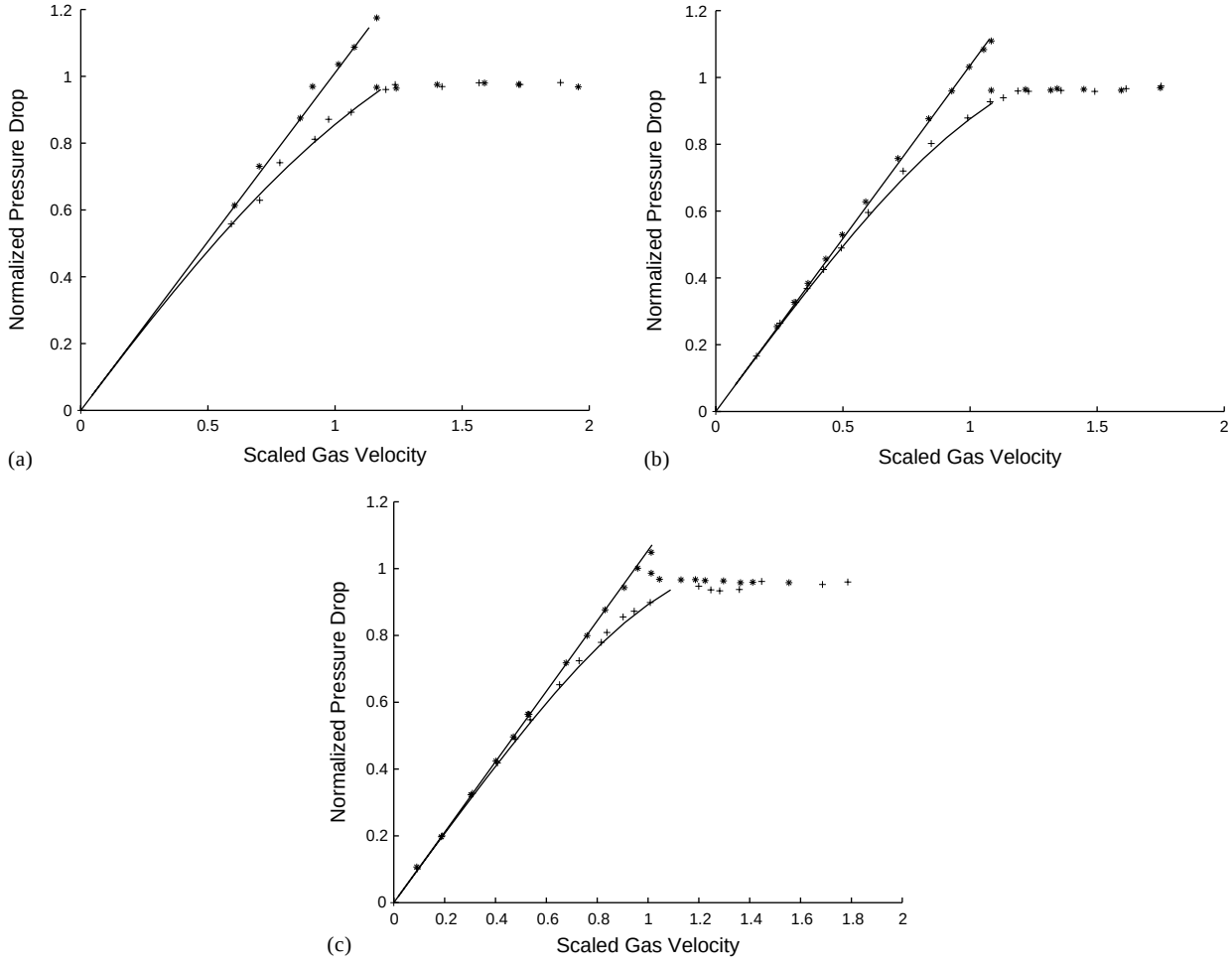

Fig. 1. Normalized pressure drop ($\Delta p/mg$) vs. scaled gas velocity ($\bar{u}/u_m$). Fine Jaygo particles. Tube diameter: (a) 0.5″; (b) 1.0″; (c) 2.0″. (+) Defluidization branch; (∗) Fluidization branch. Solid lines: model predictions.

Table 1
Summary of material properties and experimental data

Particle	Density (kg/m^3)	u_m (cm/s)	$\bar{u}_c$ (cm/s)			u_{mb} (cm/s)			$\langle\phi\rangle$ at minimum bubbling			
			0.5″ tube	1.0″ tube	2.0″ tube	0.5″ tube	1.0″ tube	2.0″ tube	0.5″ tube	1.0″ tube	2.0″ tube	ϕ_{mb}
Fine Jaygo 63 μm	2550	0.52	0.64	0.60	0.57	0.61/0.64	0.62	0.63	0.528	0.528	0.531	0.529
Cataphote 88 μm	2460	0.44	0.51	0.49	0.47	0.56	0.56	0.57	0.553	0.551	0.557	0.554
Cataphote 105 μm	2460	0.92	0.95	0.94	0.94	1.00	0.96	0.97	0.562	0.565	0.563	0.563
Cataphote	2460	1.59	2.01	1.94	1.83	1.94/2.01	1.95	1.92	0.575	0.576	0.579	0.577

Note: $u_m = v_{t,\exp}(1-\phi_{\max})^n$, where $\phi_{\max}$ is given in Table 3; $v_{t,\exp}$ and n are given in Table 4.

assumed a smooth appearance after this expansion. With further increase in air superficial velocity ($\bar{u}_c < \bar{u} < \bar{u}_{mb}$), the bed maintained a smooth appearance while its height increased steadily. It was difficult to identify a single value for u_{mb} for these particles. An occasional bubble could be observed in the bed even when the gas superficial velocity was only slightly larger than $\bar{u}_c$, where the bubbles were first visible at a depth slightly below the top surface of the bed. (For example in the case of the 63 μm Cataphote particles, an occasional bubble could be seen at $\bar{u} = 0.51$ cm/s in all three tubes. Thus, the bed was truly smooth for 0.47 cm/s $< \bar{u} <$ 0.51 cm/s in the 2″ tube and

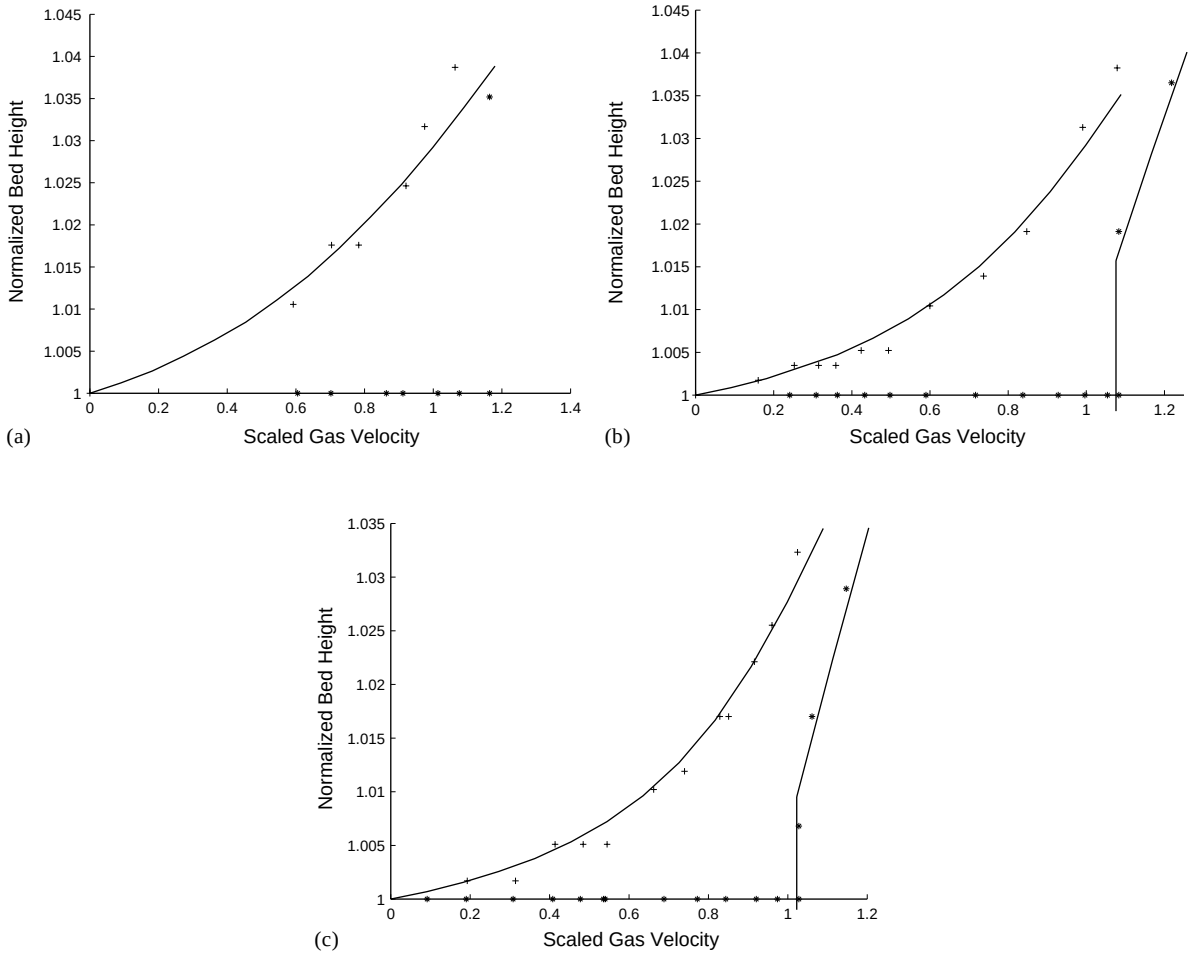

Fig. 2. Normalized bed height (h/h_o) vs. scaled gas velocity ($\bar{u}/u_m$). Fine Jaygo particles. Tube diameter: (a) 0.5″; (b) 1.0″; (c) 2.0″. (+) Defluidization branch; (∗) Fluidization branch. Solid lines: model predictions. h_o: height of a fully defluidized bed.

for 0.49 cm/s $< \bar{u} <$ 0.51 cm/s in the 1″ tube, while in the case of the 0.5″ tube, an occasional bubble could be seen immediately after bed expansion at 0.51 cm/s.) As we increased the gas velocity, the frequency of bubbling increased and the bubbles could be observed at a greater depth. We have labeled as u_{mb} the gas velocity at which bubbles were observed at a rate of about one bubble per minute. At this gas velocity, bubbling could be seen almost at the distributor level. When the gas superficial velocity was increased beyond u_{mb}, the frequency of bubbling increased rapidly. The existence of an observable window of stable fluidization ($\bar{u}_c < \bar{u} < u_{mb}$) for these particles is consistent with their classification as Geldart A type particles (Geldart, 1973).

The fluidization characteristics observed for the fine Jaygo particles differed from those of the 63 μm Cataphote particles in two ways:

(1) The transition from the state of an occasional bubble to sustained bubbling at a frequency of one bubble per minute occurred over a much narrower window of gas velocities in the case of the Jaygo particles.

(2) In the case of the Jaygo particles, $\bar{u}_c$ increased more rapidly as the tube diameter was decreased. This increase was so pronounced that $\bar{u}_c$ in the 0.5″ tube was larger than the value of u_{mb} observed in the wider tubes (see Table 1). Indeed, the bed of Jaygo particles in the 0.5″ tube bubbled quite vigorously immediately after bed expansion at $\bar{u}$. Thus, in the fluidization branch of our experiments using the fine Jaygo particles, there was an observable window of stable bed expansion in the 1″ and 2″ tubes, but not in the 0.5″ tube. Interestingly, in the 0.5″ tube in the defluidization branch of our experiments using the Jaygo particles, the state of bubbling could be maintained at gas velocities below $\bar{u}_c$! This is noted in Table 1 by presenting two values for the minimum bubbling velocity (in the 0.5″ tube), one of which is $\bar{u}_c$ to denote our observation in the fluidization branch while the other is the value recorded in the defluidization experiment.

In any case, there is no doubt that the peculiar behavior noted here for the fine Jaygo particles in the 0.5″ tube is limited to narrow tubes and that a well defined window of

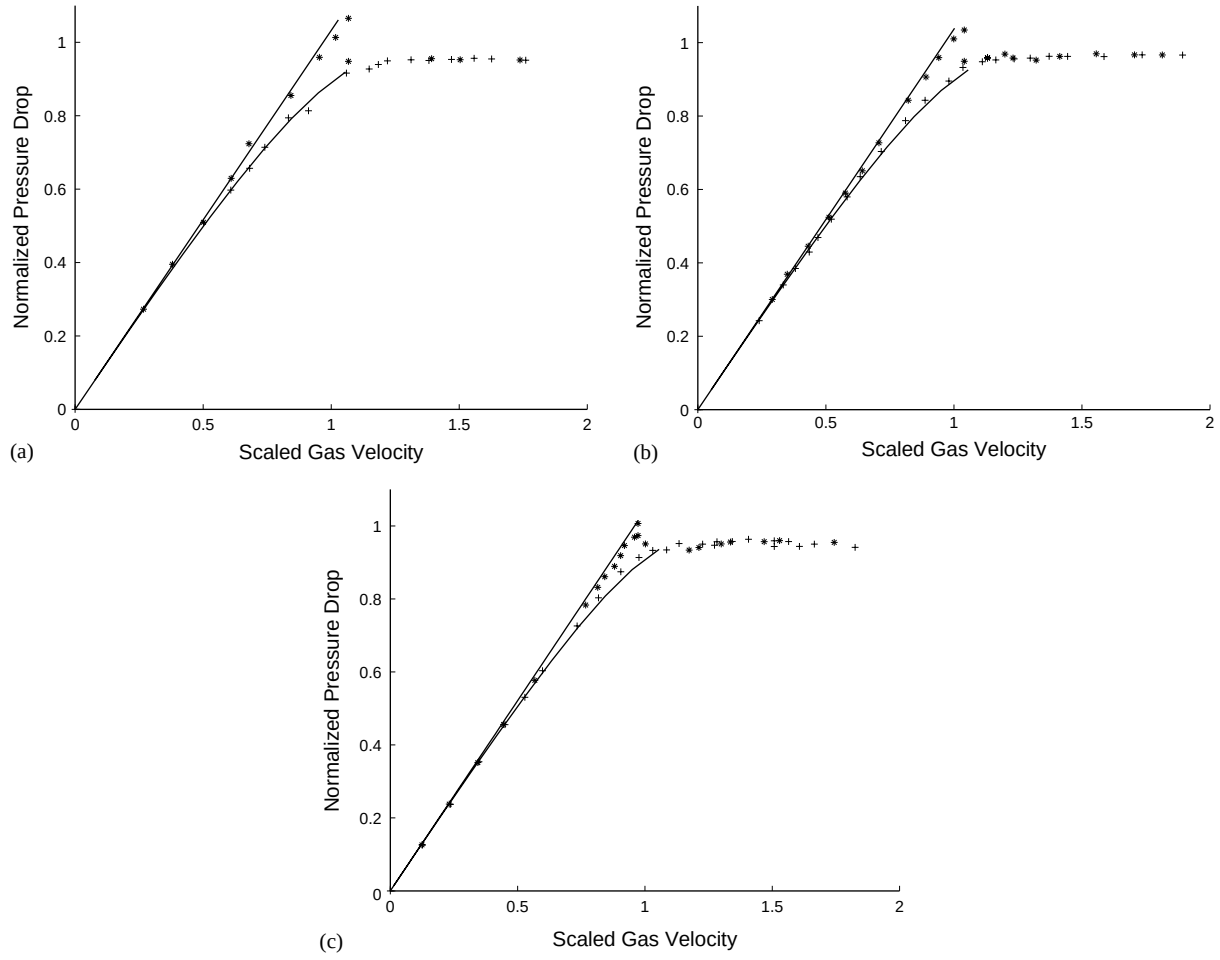

Fig. 3. Normalized pressure drop ($\Delta p/mg$) vs. scaled gas velocity ($\bar{u}/u_m$). 63 μm Cataphote particles. Tube diameter: (a) 0.5″; (b) 1.0″; (c) 2.0″. (+) Defluidization branch; (∗) Fluidization branch. Solid lines: model predictions.

stable bed expansion exists for this particle in wide tubes, which is consistent with its label as a group A particle.

The 105 μm Cataphote particles lies slightly to the right of the A–B transition (in the group B side) as per Geldart's original classification (Geldart, 1973). We could indeed observe a window of stable expansion for this particle in the 2″ tube (see Table 1). There was a very small (almost negligible) window of stable expansion in the 1″ tube. However, the behavior observed in the 0.5″ tube was similar to that seen in the case of the fine Jaygo particles.

In the bubbling regime ($\bar{u} > \bar{u}_c$ or u_{mb}, whichever is larger), nearly same average pressure drop and bed height were obtained in both fluidization and defluidization branches, suggesting that the results obtained in this regime were path-independent. The normalized pressure drop in this regime was found to be slightly less than one in every tube. This has been noted previously by Tsinontides and Jackson (1993) who performed similar experiments with FCC catalyst and sand. The presence of such an offset clearly implies that the bed of particles was not completely fluidized by the gas and that a portion of its weight was being supported by the distributor and the tube wall. (The height of a bubbling bed fluctuates in time, as the inventory of bubbles in the bed changes with time. The bubbles lift up the particles near the distributor, and after the bubbles pass the particles fall down and bounce on the distributor. In this manner, the distributor may bear a part of the bed weight.) Srivastava and Sundaresan (2002) found in their study of fluidization characteristics of 50 μm glass beads that this offset from unity increased with tube diameter. We found in our study with several different particles that in all but one case (63 μm Cataphote particles) the offset indeed increased with tube diameter (see Table 2).

The value of u_{mb} determined in the defluidization branch was, within the confidence limits of our measurements, the same as that observed in the fluidization cycle in all our experiments with the exception of the fine Jaygo and the 105 μm Cataphote particles in the 0.5″ tube (as noted already).

The average solids volume fraction in the bed, $\langle\phi\rangle_{mb}$, at u_{mb} (determined in defluidization branch) for each of the particles in each of the tubes is also shown in Table 1. It

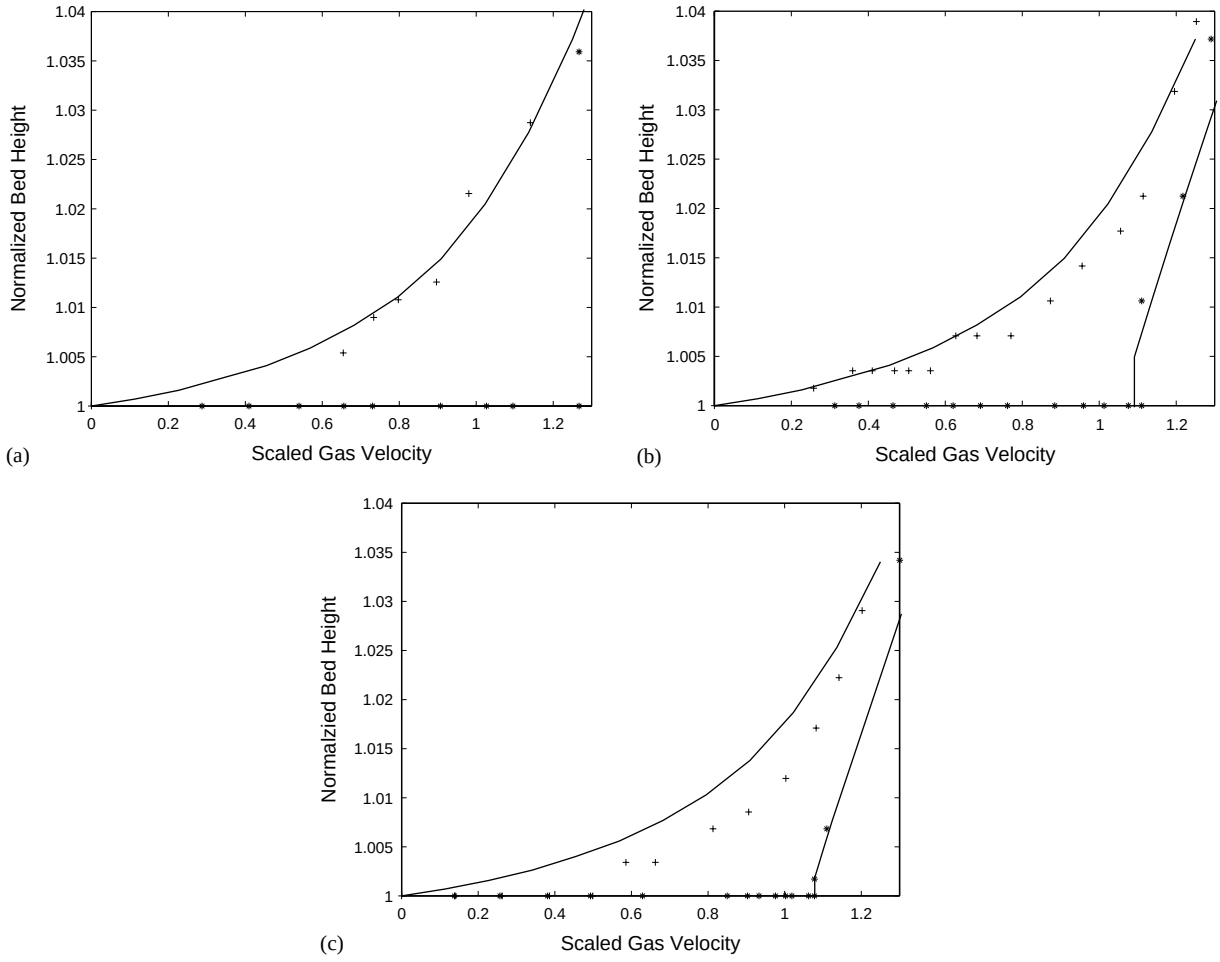

Fig. 4. Normalized bed height (h/h_o) vs. scaled gas velocity ($\bar{u}/u_m$). 63 μm Cataphote particles. Tube diameter: (a) 0.5″; (b) 1.0″; (c) 2.0″. (+) Defluidization branch; (∗) Fluidization branch. Solid lines: model predictions. h_o: height of a fully defluidized bed.

appears that $\langle\phi\rangle_{mb}$ is only weakly dependent on the tube diameter. The average of the three values of $\langle\phi\rangle_{mb}$ shown in this table for each particle was treated in our analysis as an estimate of ϕ_{mb} for that particle.

In the defluidization branch, as $\bar{u}$ was decreased below u_{mb}, the system entered a regime of stable bed expansion (but for occasional bubbles, as mentioned earlier), where the bed appeared to be mostly uniform. At still smaller values of $\bar{u}$, the bubbling ceased completely. It is clear from Figs. 1 and 2 that both the bed height and pressure drop across the bed decreased steadily as $\bar{u}$ was decreased. It is also clear that, as $\bar{u}$ was decreased, more and more of the weight of the bed was being supported by the tube wall and the distributor.

In the cases of the coarse Jaygo particles and the two large Cataphote particles (150 and 210 μm), a window of stable expansion could still be detected; however, this window was very small, which is indeed consistent with the classification of these particles as Geldart type B particles. We found ϕ_{mb} to be 0.571, 0.580 and 0.590 for the coarse Jaygo, 150 μm Cataphote and 210 μm Cataphote particles, respectively.

A close inspection of the experimental data on various particles revealed that the results obtained with the 1″ and 2″ tubes were quite close to each other over most of the defluidization branch. This suggested that the wall friction played only a minor role in the manner in which the particles packed in the defluidization branch in these tubes. Assuming that the wall friction played a negligible role in the defluidization experiments performed in the 2″ tubes, we were led to employ the following methodology to determine the compressive yield stress, $\sigma_s^y(\phi)$, of the particles used in our study. A known mass of particles was placed in the 2″ ID tube, the bed was allowed to bubble gently for a period of time and then slowly defluidized to the rest state (i.e. zero gas velocity) and the bed height was recorded. A measured amount of particles was then added to the bed, the bed was again allowed to bubble gently, then defluidized, and the rest height was recorded. By repeating this procedure, the rest height of bed (h) was determined as a function of the particle mass loading (M). The average solids volume fraction, $\langle\phi\rangle$, is simply equal to $M/A\rho_p gh$, where A is the cross-sectional area of the tube. Fig. 9 shows the variation

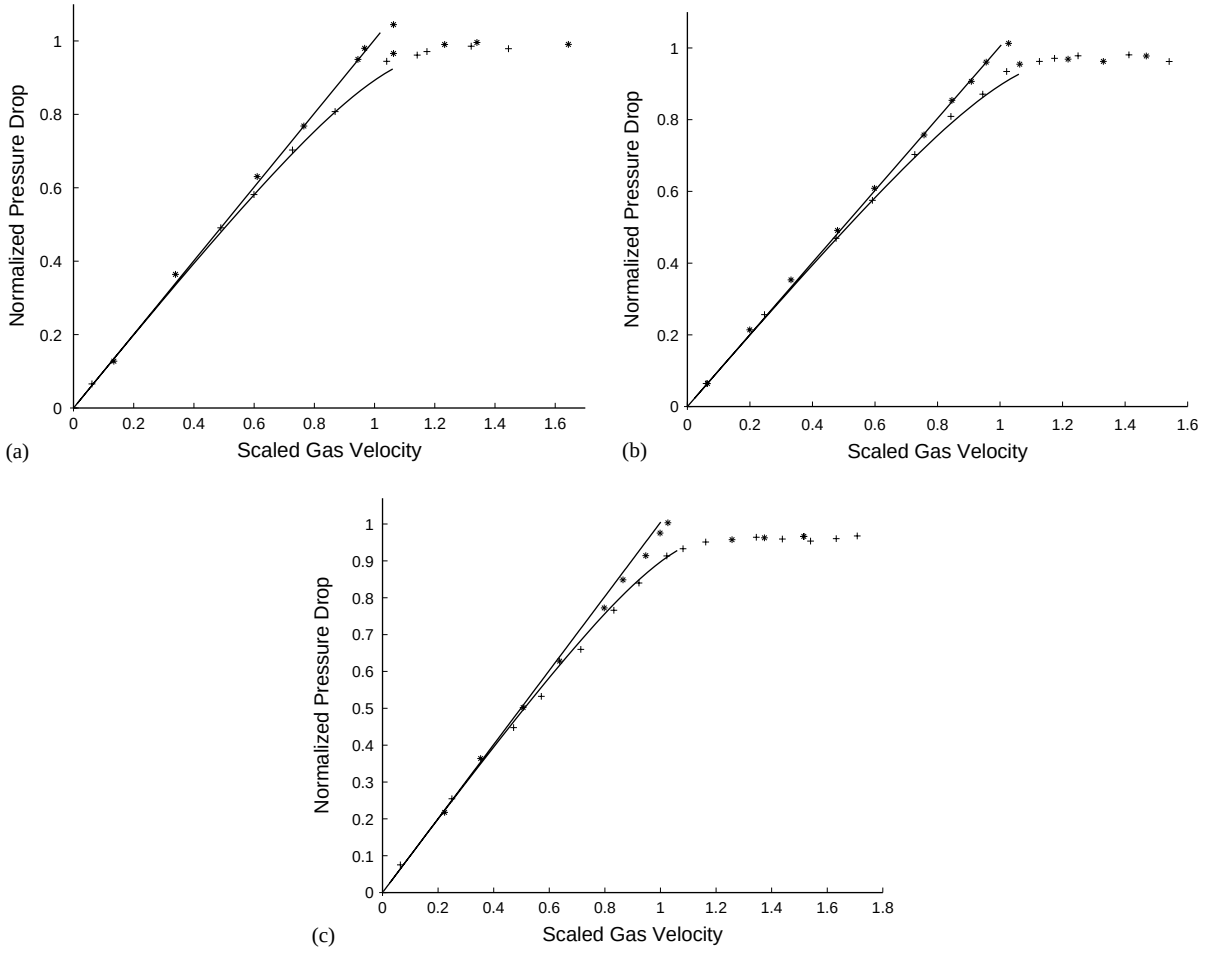

Fig. 5. Normalized pressure drop ($\Delta p/mg$) vs. scaled gas velocity ($\bar{u}/u_m$). 105 μm Cataphote particles. Tube diameter: (a) 0.5″; (b) 1.0″; (c) 2.0″. (+) Defluidization branch; (∗) Fluidization branch. Solid lines: model predictions.

of $\langle\phi\rangle$ with h for the two Jaygo particles. Also shown in this figure are smooth curves representing empirical curve-fits of the data. It can be shown that the volume fraction of the solids at the bottom of the bed, ϕ_b, is given by

$$\phi_b = \langle\phi\rangle + h\,\frac{\mathrm{d}\langle\phi\rangle}{\mathrm{d}h} \tag{11}$$

and the vertical normal stress there (in the absence of wall friction), $\sigma_s^x(\phi_b)$, is equal to $\rho_p g h\langle\phi\rangle$. Thus, one can readily determine $\sigma_s^x(\phi_b)$ from the curve-fit function $\langle\phi\rangle(h)$. Such an approach has already been used by Valverde et al. (1998) to estimate compressive yield strength of particles. Fig. 10 shows the variation of compressive yield strength with particle volume fraction for the two Jaygo particles, determined in such a manner. The general *elbow* shape of the two curves is readily apparent, and the primary difference appears to be that the curve for the coarser particles is displaced towards higher packing densities. Also shown in this figure as vertical dashed lines are the ϕ_{mb} values for these two particles. Bubbling seems to begin when the average particle volume fraction in the bed has decreased enough so that the compressive yield strength of the particles in the bed is to the left of the elbow.

Fig. 11 summarizes the experimental data on $\langle\phi\rangle$ as a function of bed height (in the 2″ tube) for various Cataphote particles. (The experimental data for the 150 μm particles are not shown in order to preserve the clarity of this figure, but can be found elsewhere (Loezos, 2002).) The compressive yield strengths of these particles are presented in Fig. 12, where the experimentally determined value ϕ_{mb} are also shown. The *elbow* shape of these curves is similar to what was obtained for the Jaygo particles. As in the case of the Jaygo particles, bubbling occurs with each of the Cataphote particles when the average particle volume fraction in the bed has decreased past the elbow in the compressive yield strength curve. It is thus reasonable to conclude that a modest compressive yield strength is sufficient to stabilize a fluidized bed.

It is also interesting to note that the compressive yield strength curves for the Cataphote particles shift to the right in an orderly manner as the particle size increases, just as in the case of the Jaygo particles. This could be due to a

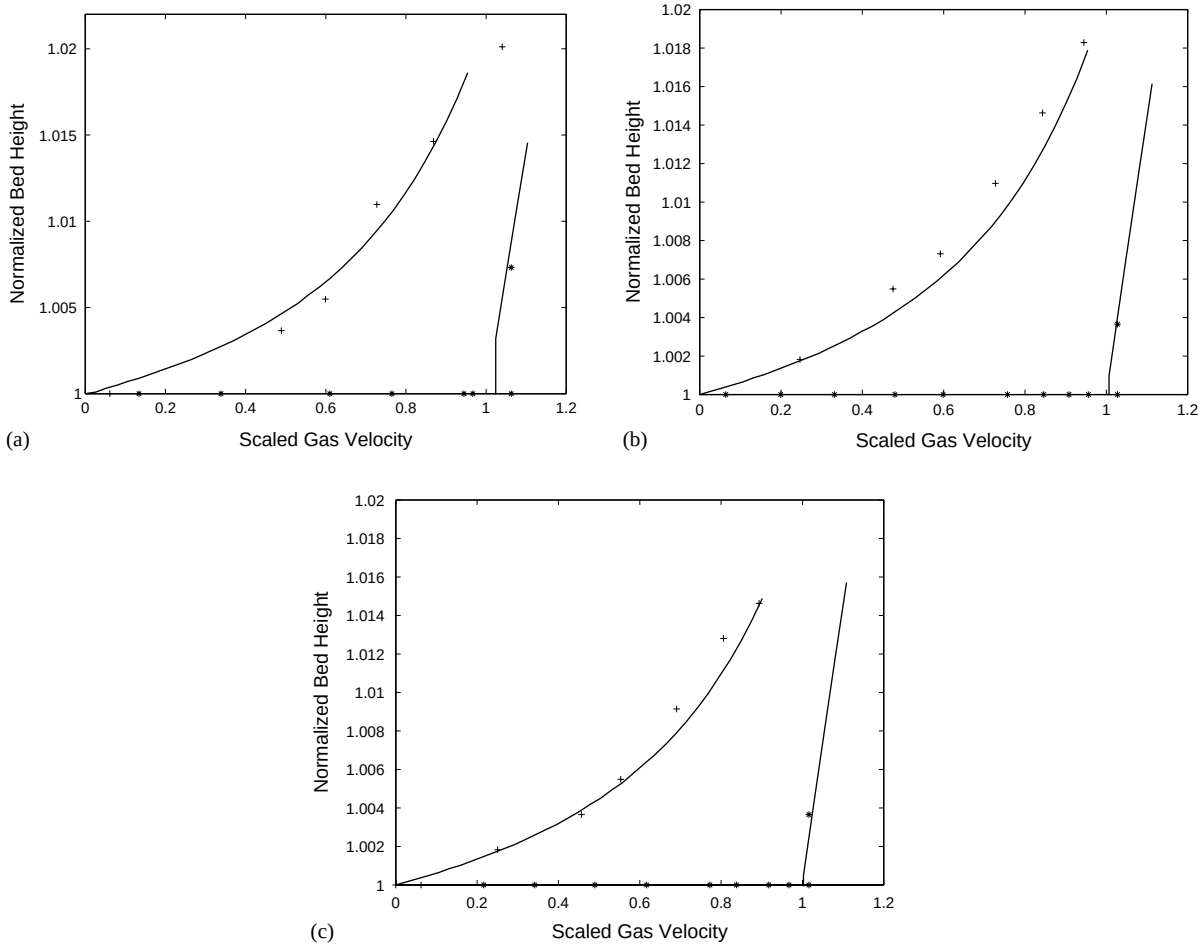

Fig. 6. Normalized bed height (h/h_o) vs. scaled gas velocity ($\bar{u}/u_m$). 105 μm Cataphote particles. Tube diameter: (a) 0.5″; (b) 1.0″; (c) 2.0″. (+) Defluidization branch; (∗) Fluidization branch. Solid lines: model predictions. h_o: height of a fully defluidized bed.

combination of frictional and cohesive interactions between the particles. Intuitively, one can anticipate that as the apparent coefficient of friction at particle–particle contact increases, the particles will pack less tightly under a given stress. Thus, the orderly shift seen in Figs. 10 and 12 may be due to a gradual shift in the apparent coefficient of friction. Although it is possible that the actual coefficient of friction in these samples decreased with increasing particle size, this seems unlikely. It is more likely that as the particle size increases the importance of cohesion relative to gravity decreases, which translates to a decrease in the apparent coefficient of friction.

Some general comments about Figs. 9–12 are in order. Note that $\langle\phi\rangle$ values below 0.5 are reported in Figs. 9 and 11, while the lowest value of ϕ_b to which the curves in Figs. 10 and 12 are shown is much larger. This because of the fact that at low values of $\langle\phi\rangle$, the second term on the right-hand side of (11) is quite large. Although one can, in principle, extend the curves in Figs. 10 and 12 to lower ϕ_b values, there is little confidence in such an extrapolation. In the limit $h \to 0$, we expect $\phi_b \to \langle\phi\rangle$ from above (see Eq. (11)), and so one can demand that the curves in Fig. 10 should be extended to particle volume fractions as small as 0.45 (and similarly for Fig. 12). While we recognized this, we did not insist on this requirement when we attempted to examine if the curves shown in Figs. 10 and 12 could be fitted to simple functional forms of the type shown in Eq. (4) (so that these expressions could be used in the analysis described below). For the purpose of the analysis described in the present study, accurate fits of the yield strength data were needed primarily for ϕ larger than ϕ_{mb} and hence we were content to accept $\phi_{\min}$ values which are larger than the lowest $\langle\phi\rangle$ values recorded in Figs. 9 and 11, but are well below the corresponding ϕ_{mb} values.

The curves shown in Figs. 10 and 12 could be captured nicely with Eq. (4) (except at very low particle volume fractions, as discussed in the previous paragraph), and the values of parameters appearing in this equation for all the Jaygo and Cataphote particles are summarized in Table 3. The fact that we could fit the yield strength results nicely using the same value of c for all the particles merely implies that five independent parameters are not required to

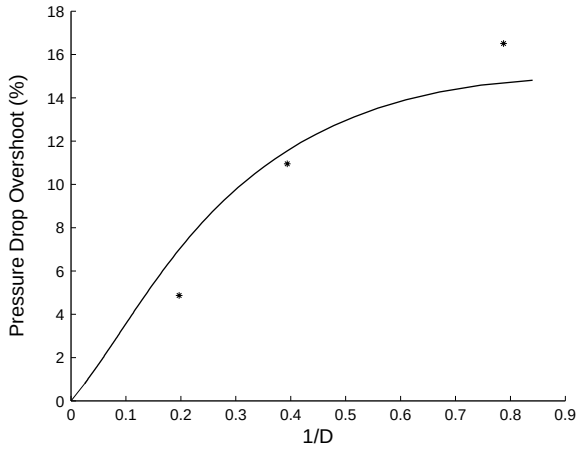

Fig. 7. Pressure drop overshoot (%) vs. $(1/D)$, where D is the tube diameter in cm. Fine Jaygo particles. (∗) Experimental data. Solid line: model prediction.

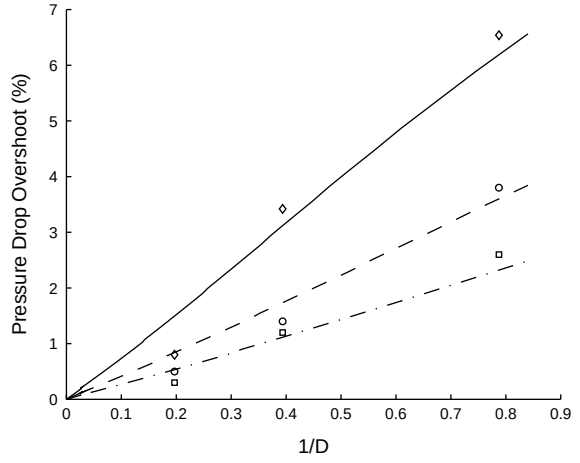

Fig. 8. Pressure drop overshoot (%) vs. $(1/D)$, where D is the tube diameter in cm. Cataphote particles. (◇) 63 μm data; (○) 88 μm data; (□) 105 μm data. Model predictions: (—) 63 μm; (—) 88 μm; (- - -) 105 μm.

Table 2
Percent offset, $100(1-\Delta p/mg)$, for various particles

Particle	0.5″ ID tube	1.0″ ID tube	2.0″ ID tube
Fine Jaygo	2.5	3.5	4.5
63 μm Cataphote	4.5	3.0	5.0
88 μm Cataphote	2.0	3.5	4.5
105 μm Cataphote	2.0	3.5	4.0

fit the data. It should also be noted that several other functional forms could also be used equally satisfactorily to fit the data. Thus, there is no basis for assigning any significance to the numerical values shown in Table 3, with the possible exception of $\phi_{\max}$ which could be estimated fairly accurately. The sole purpose of this curve-fit was to obtain

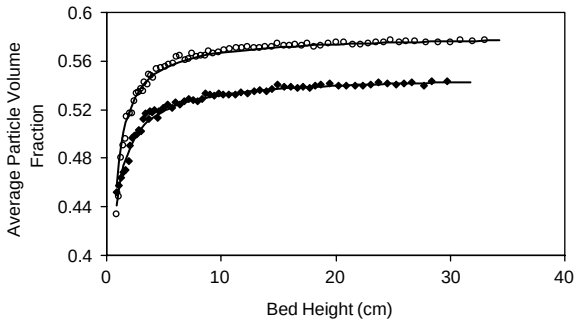

Fig. 9. Average particle volume fraction, $\langle\phi\rangle$, vs. bed height, h. Jaygo particles. (♦) fine; (○) coarse. Solid lines: Curve fits. Data were obtained in the 2″ tube.

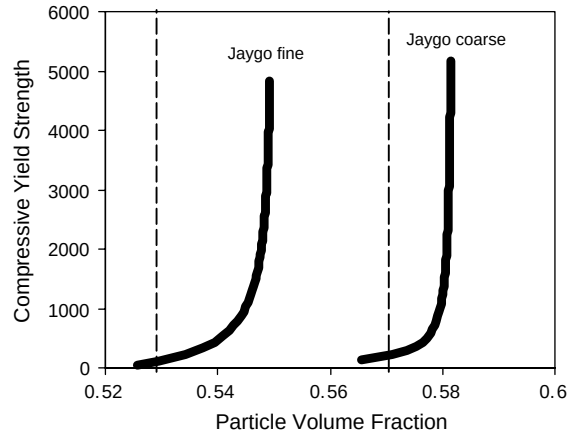

Fig. 10. Compressive yield strength, σ_s^x (in N/m^2) vs. particle volume fraction, ϕ. Jaygo particles. Vertical dashed lines: ϕ_{mb}.

convenient expression for $\sigma_s^x(\phi_b)$ which could be used in the fluidization–defluidization calculations described below. We simply note that our conclusions remain unaffected by the choice of expression used to fit $\sigma_s^x(\phi_b)$.

An initial estimate of the Richardson–Zaki exponent for each particle sample was obtained as follows. Rearranging Eq. (2)

$$\ln\left(\frac{1}{\bar{u}\phi}\frac{\mathrm{d}p}{\mathrm{d}x}\right) = n\ln(1-\phi) + \ln\left(\frac{\rho_p g}{v_t}\right). \tag{12}$$

Using the pressure drop and bed height data gathered in the defluidization branches for each material, $\ln((1/\bar{u}\langle\phi\rangle)\Delta p/h)$ and $\ln(1-\langle\phi\rangle)$ were determined and were plotted against each other for each particle sample, see Figs. 13a and b for two illustrations. The results obtained for the same sample in different tubes did not always fall on the same line, and this could be attributed to the fact that we replaced, in Eq. (12), ϕ by $\langle\phi\rangle$, and $\mathrm{d}p/\mathrm{d}x$ by $\Delta p/h$. Nevertheless, we observed that roughly the same slope was obtained for a given particle sample on all three tubes (for example, see Fig. 13b). Therefore, we adopted this procedure to estimate the Richardson–Zaki exponent

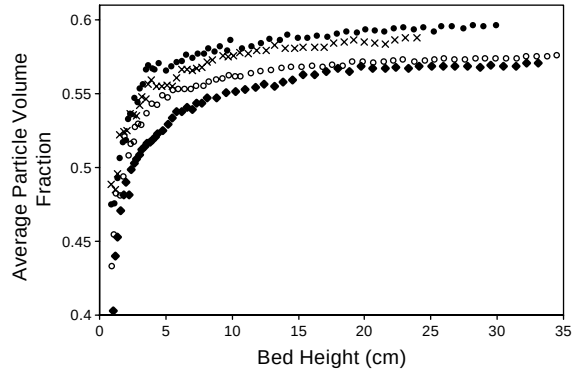

Fig. 11. Average particle volume fraction, $\langle\phi\rangle$, vs. bed height, h (in cm). Cataphote particles. (♦) 63 μm; (○) 88 μm; (×) 105 μm; (●) 210 μm. Curve fits are not shown. Data were obtained in the 2″ tube.

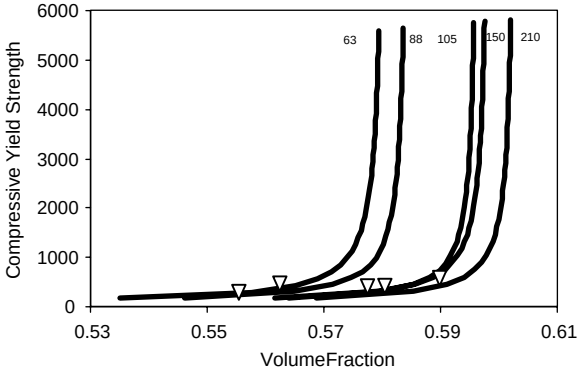

Fig. 12. Compressive yield strength, σ_s^x (in N/m^2) vs. particle volume fraction, ϕ. Cataphote particles. (△) ϕ_{mb}.

(see Table 4). As expected, the value of n decreases with increasing particle size (see the entries for the Cataphote particles in Table 4).

We determined the angle of internal friction of the Jaygo particles to be 19.5° through Jenike shear cell measurements. The Cataphote particles employed in our study were loaned to us by Dr. George Cody and are very expensive. We did not wish to contaminate these particle samples by placing them in the direct shear cell box, and therefore the angles of internal friction for these particles were not measured. We note, however, that these particles heaped in a manner similar to the Jaygo particles, so the angle of internal friction of the Cataphote particles is probably close to that of the Jaygo particles.

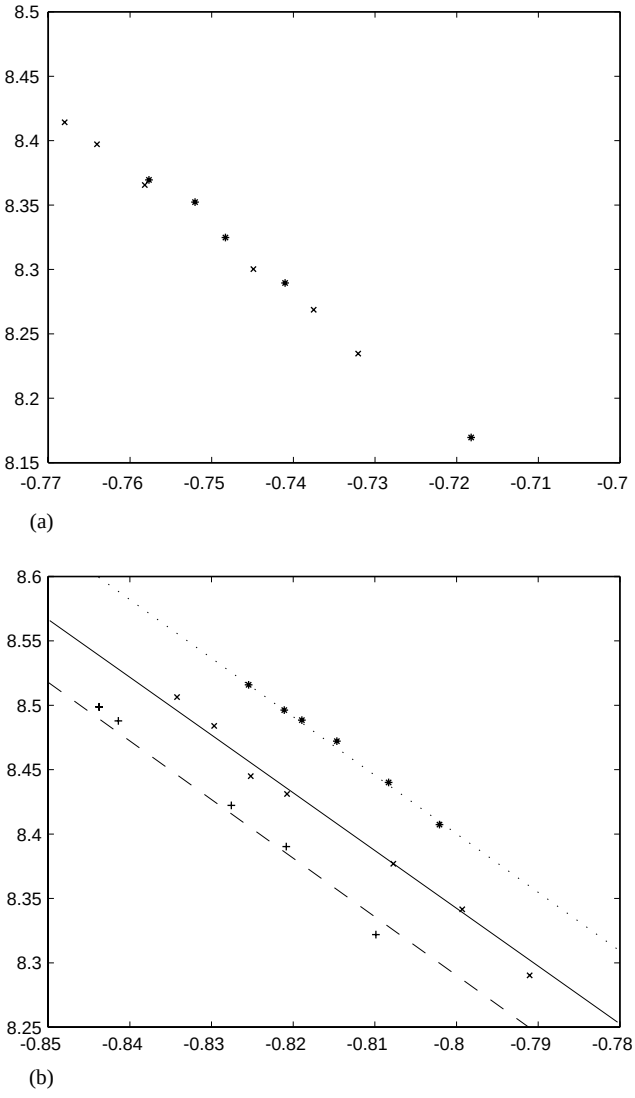

Fig. 13. Estimation of Richardson–Zaki exponent, n, as the slope of from a plot of $\ln((1/\bar{u}\langle\phi\rangle)\Delta p/h)$ vs. $\ln(1-\langle\phi\rangle)$. (a) Fine Jaygo particles. (∗) 2″ tube data; (×) 1″ tube data. Solid lines: fits of data. (b) 63 μm Cataphote particles. (∗) 2″ tube data; (×) 1″ tube data; (+) 0.5″ tube data. Solid lines: fits of data.

Table 3
Summary of compressive yield strength model parameters (see Eq. (4))

Particle	a	b	c (N/m^2)	$\phi_{\min}$	$\phi_{\max}$
Fine Jaygo	1.25	0.70	2500	0.520	0.550
Coarse Jaygo	1.74	0.93	2500	0.555	0.582
63 μm Cataphote	1.53	0.80	2500	0.540	0.580
88 μm Cataphote	1.59	0.81	2500	0.540	0.584
105 μm Cataphote	1.77	0.83	2500	0.540	0.596
150 μm Cataphote	1.80	0.85	2500	0.540	0.598
210 μm Cataphote	1.95	0.91	2500	0.540	0.602

Table 4
Summary of model parameters

Particle	$v_{t,\exp}$ (cm/s)	$v_{t,\mathrm{th}}$ (cm/s)	n	$(\mu j)_f$	$(\mu j)_{df}$
Fine Jaygo	26	30	4.94	0.220	0.055
63 μm Cataphote	24	25	4.61	0.050	0.013
88 μm Cataphote	40	44	4.30	0.033	0.0083
105 μm Cataphote	60	58	4.05	0.023	0.0058

For all the particles, $(\mu j)_f$, $(\mu j)_{df}$, and v_t were treated as adjustable parameters, and were estimated by matching the experimental fluidization/defluidization data with the 1-D model outlined earlier. The solid lines in Figs. 1–6 show the 1-D model predictions with the $v_{t,\exp}$, $(\mu j)_f$ and $(\mu j)_{df}$ values presented in Table 4. This table also shows the theoretical terminal velocity ($v_{t,\mathrm{th}}$) estimated on the basis of the nominal sizes of the Cataphote particles. The $v_{t,\exp}$ values are quite close to the theoretical values. We could have fixed the terminal velocity at the theoretical value or some other value close to the numbers shown in Table 4 and adjusted the Richardson–Zaki exponent slightly to get equally good fits (Loezos, 2002). This simply implies that Eq. (3), along with several combinations of n and $v_{t,\exp}$ values which are close to the nominal values shown in Table 4, captured the drag coefficient adequately in the narrow range of solids volume fractions encountered in our experiments.

The sequence of dynamic events that follow bed expansion when the gas superficial velocity is increased past $\bar{u}_c$ is rather complex and hence it is not simple to construct a model for the bed expansion characteristics in the region $\bar{u} > \bar{u}_c$. Nevertheless, one can easily compare the actual height of the fluidized bed in this region with the height, H_{ideal}, of an ideal fluidized bed where the particle volume fraction is independent of height and the drag force balances the weight of bed. Equating the upward supporting force per unit volume of the bed due to the gas drag with the weight of the bed per unit volume,

$$\frac{\rho_p \phi g}{v_t (1-\phi)^n}\,\bar{u} = \rho_p \phi g.$$

Therefore,

$$\phi = 1 - \left(\frac{\bar{u}}{v_t}\right)^{1/n}.$$

As $\rho_p \phi H_{\mathrm{ideal}} = m$, we can rewrite this to obtain

$$H_{\mathrm{ideal}} = \frac{m/\rho_p}{1-(\bar{u}/v_t)^{1/n}}.$$

H_{ideal} is also shown in Figs. 2, 4 and 6. It is not shown in Figs. 2a and 6a, as the bed bubbled immediately upon expansion in these cases. The quality of fit is reasonable, suggesting that the expansion characteristic of the bed in this region is not too different from that of an ideal bed.

The lines in Figs. 7 and 8 indicate the predicted pressure drop overshoots, and they compare well with the data. The model predicts that the overshoot is roughly proportional to $1/D$ for small $1/D$, and it can be attributed to the fact that the perimeter per unit cross-sectional area of the tube is proportional to $1/D$. As seen in Fig. 7, this dependence becomes weaker as $1/D$ becomes sufficiently large, and at even larger $1/D$ values, the overshoot is predicted to decrease with increasing $1/D$. This can be traced to the fact that as the tube diameter decreases, the particles packed less and less tightly in the fully defluidized state. We observed in our experiments in the 0.5″ tube using the fine Jaygo particle that the particles tended to bridge across the gap, particularly during the lift-off in the fluidization branch (which occurs when $\bar{u}$ was increased past $\bar{u}_c$). As the 1-D model does not consider the occurrence of such bridges, its predictions for large $1/D$ values should not be over-interpreted.

As we measured the angle of internal friction for the Jaygo particles, we specifically tried to check if the data for the fine Jaygo particles could be fitted by restricting the values of $(\mu j)_f$ and $(\mu j)_{df}$ to satisfy Eq. (10). It turned out that we could indeed achieve a reasonable fit of the data with the 1-D model and the parameter values shown in Table 4 for the fine Jaygo do satisfy Eq. (10) with $\varphi = 19.5°$. (In contrast, the best fit we could obtain if we insisted that $(\mu j)_f/(\mu j)_{df} = 1$, as assumed by Jackson (1998), was rather poor and was deemed unsatisfactory.) If one further supposes that Eq. (9) holds, then the value of the wall friction coefficient for the fine Jaygo particles (on Plexiglas walls) needed to fit the data turns out to be 0.11. Relaxing the restriction that Eq. (10) holds and allowing $(\mu j)_f$ and $(\mu j)_{df}$ to be completely independent parameters did not lead to any noticeable improvement of the fit of the results obtained with the fine Jaygo particles.

It can be seen from Table 4 that the values of $(\mu j)_f$ and $(\mu j)_{df}$ required to fit the experimental data on Cataphote particles decreases monotonically as the particle size increases. An explanation for this trend is elusive (and may be related to the relative importance of cohesion and gravity). For all the particles shown in Table 4, we have kept the same $(\mu j)_f/(\mu j)_{df}$ ratio, i.e. Eq. (10) holds with $\varphi = 19.5°$. This, by no means, validates Eq. (10), as we could have obtained a similar quality of fit with a slightly different value for this ratio. It simply means that a definitive statement about the values assumed by the Janssen's coefficient in the

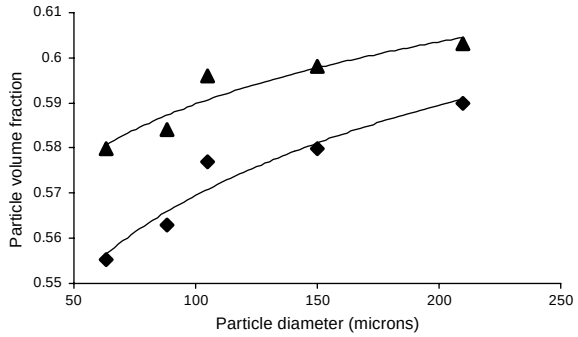

Fig. 14. ϕ_{mb} (♦) and $\phi_{\max}$ (▲) for various Cataphote particles. Particle diameter is in μm.

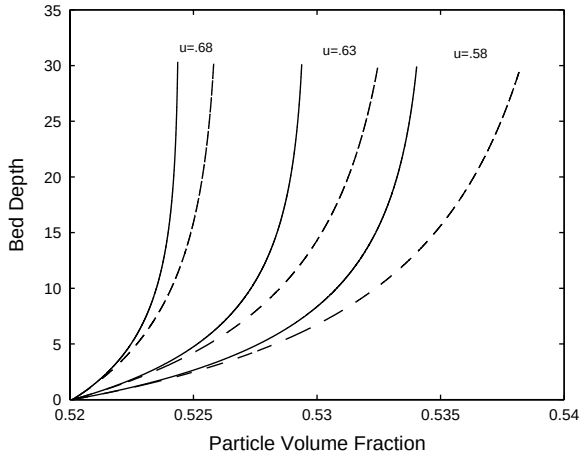

Fig. 15. Particle volume fraction as a function of depth below bed surface (in cm). Fine Jaygo particles. Model predictions for various gas superficial velocities in the defluidization branch. Solid lines: 2″ tube with wall friction. Broken lines: no wall friction.

fluidization and defluidization branches cannot be made on the basis of our measurements.

4.1. Stability of a uniformly fluidized bed

When $\bar{u}$ was appreciably larger than u_{mb}, the beds bubbled vigorously, and as $\bar{u}$ was decreased slowly towards u_{mb}, the frequency of bubbling decreased gradually. As mentioned earlier, we labeled $\bar{u}$ at which bubbles were observed at a rate less than one bubble per minute as u_{mb}. As seen in Table 1, ϕ_{mb} was found to be nearly independent of tube diameter for all the particles. Furthermore, it was observed that the compressive yield strength of the granular assembly was rather small at $\phi = \phi_{mb}$ (see Figs. 10 and 12). Quite remarkably, the shapes of the compressive yield strength loci for the various particles are very similar and there is no abrupt change in the behavior as ones crosses the Geldart A–B boundary. In the case of the Cataphote particles, both ϕ_{mb} and $\phi_{\max}$ increase monotonically with particle size (see Fig. 14), with no apparent discontinuities.

The solid lines in Fig. 15 show the particle volume fraction profiles in the *defluidization branch* in the 2″ ID tube at various gas velocities for the case of the fine Jaygo particles. These profiles were obtained from the 1-D model using the experimentally determined parameter values. Also shown as broken lines are the model predictions for the case of zero wall friction coefficient (or equivalently, infinite tube diameter with finite wall friction coefficient). As one would expect, the difference between the solid and broken lines becomes smaller and smaller as the average solids volume fraction in the bed decreases, and at the experimentally observed u_{mb}, this difference is rather small. (When $\bar{u} = v_t(1-\phi_{\min})^n$, which is larger than the experimentally observed u_{mb}, the solid and broken lines will overlap exactly and $\phi = \phi_{\min}$ at all elevations.) This was indeed the case with all the other particles as well.

Strictly speaking, one should include the effect of tube diameter on the bed dynamics, while seeking a quantitative explanation for the observed onset of bubbling, as the tube diameter had an influence on value of u_{mb} (see Table 1). However, it seems reasonable to expect that friction at the wall, per se, would only suppress fluctuations and thus exert a stabilizing influence. In other words, we should be able to identify the physical processes driving the onset of bubbling by simply considering frictionless walls.

As described in Section 1, a large body of literature exists on the analysis of linear stability of fluidized beds. These studies either neglect particle phase stresses or consider only reversible stresses in the particle phase. If the stresses were truly reversible, fluidization and defluidization branches in our experiments would overlap exactly. Clearly, this is not the case. Thus, there is no basis for expecting that a stability analysis based on reversible stresses can be used to explain the onset of bubbling in our experiments. Nevertheless, it is instructive to examine the outcome of such a stability analysis where one treats the particle phase stresses as reversible and neglects wall friction. This analysis becomes simpler if one considers a bed of infinite extent and neglects the compressibility of the gas so that the voidage in the base state is uniform everywhere. The details of such a linear stability analysis for an infinite bed can be found in many places in the literature (e.g., see Jackson, 2000). When the fluid density is much smaller than that of the particles, a uniformly fluidized state is linearly stable if (Jackson, 2000)

$$\left.\frac{\mathrm{d}p_s}{\mathrm{d}\phi}\right|_{\phi_o} > \rho_p v_t^2 n^2 \phi_o^2 (1-\phi_o)^{2(n-1)},$$

where ϕ_o is the particle volume fraction in the uniform state and p_s is the reversible pressure (associated with the elastic deformation) of the particle phase. For elasto-plastic materials, we expect that

$$\frac{\mathrm{d}p_s}{\mathrm{d}\phi} > \frac{\mathrm{d}\sigma_s^x}{\mathrm{d}\phi}.$$

Therefore, one can find an upper bound (ϕ^*) for the critical particle volume fraction (ϕ_{crit}) above which the uniform

state is linearly stable, by setting

$$\left.\frac{\mathrm{d}\sigma_s^x}{\mathrm{d}\phi}\right|_{\phi^*} = \rho_p v_t^2 n^2 (\phi^*)^2 (1-\phi^*)^{2(n-1)}.$$

We found that for every particle examined in our study, ϕ^* is only slightly larger than $\phi_{\min}$ (typically by 0.0001). The values of ϕ_{mb} observed in our experiments are considerably larger than $\phi_{\min}$ in Table 3, which further confirms that the onset of bubbling in our system cannot be captured by such a linear stability analysis.

As noted earlier in the context of Figs. 11 and 12, our confidence in the compressive yield strength measurements is low in the vicinity of $\phi_{\min}$. In particular, there is a modest level of uncertainty in the value of $\phi_{\min}$ estimated from these measurements. However, near $\phi = \phi_{mb}$ we do have a fairly large number of data points in our compressive yield strength measurements and it is highly unlikely that the experimentally observed ϕ_{mb} is the true $\phi_{\min}$. Thus, one needs to explain how bubbling can come about at $\phi = \phi_{mb} > \phi_{\min}$, where the bed still retains some yield stress. We propose that the onset of bubbling is associated with conditions where the yield stress in the particle assembly can be overcome *by fluctuations*.

In order to understand the minimum bubbling conditions, let us examine partial defluidization branches, which have been discussed previously by Tsinontides and Jackson (1993). Starting from a bubbling bed, let us gradually decrease the gas velocity to $\overline{u_L}$ and then begin increasing the gas velocity. In such an experiment, the bed would compact progressively as we decreased the gas velocity, and when the gas velocity is increased the bed height would remain invariant until a critical velocity, $\overline{u_u}$, which is a function of $\overline{u_L}$, was reached. At this critical velocity, the bed height would jump abruptly and the bed would continue to expand beyond that point till u_{mb}. Fluidization branches shown in Figs. 1–6 correspond to the specific case where $\overline{u_L} = 0$. Fig. 16a shows the plots of $\Delta\bar{u} \equiv (\overline{u_u} - \overline{u_L})$ against $\overline{u_L}$ in a 2″ ID bed for the fine Jaygo and the 63 μm Cataphote particles. These were computed using the model parameters estimated from our experiments. As expected, for both particles, $\Delta\bar{u}$ decreases monotonically as $\overline{u_L}$ increases. According to the model, $\Delta\bar{u} = 0$ when $\overline{u_L} = v_t(1-\phi_{\min})^n$ which is independent of tube diameter.

Let us now consider the effect of temporal fluctuations in the gas superficial velocity, which are inevitable in any experimental system. Let us suppose that the time-average gas superficial velocity is $\langle\bar{u}\rangle$ and that the amplitude of the fluctuation is a. Let us first consider the case where the characteristic time for these fluctuations, t_f, is much larger than that for bed response, so that we can assume that the bed is in a quasi-steady state at each instant of time. As the gas superficial velocity decreases during the course of the normal fluctuations (to $\overline{u_L} \approx \langle\bar{u}\rangle - a$), the bed will compact (as in the defluidization branch) and when the superficial velocity increases the bed height will remain constant until

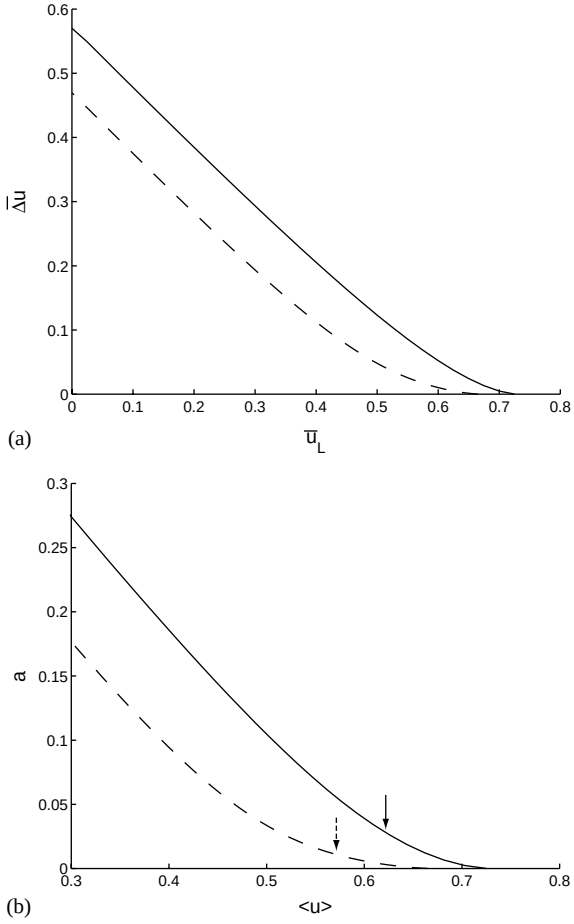

Fig. 16. Increase in gas velocity, $\Delta\bar{u}$ (in cm/s), needed for bed expansion following partial defluidization down to various gas velocities, $\overline{u_L}$ (in cm/s). Solid line: Fine Jaygo particles. Broken line: 63 μm Cataphote particles. 2″ tube. (b) Amplitude of velocity fluctuation (cm/s) at various average gas velocities (cm/s) which can give rise to one bubble per fluctuation branch. Solid line: Fine Jaygo particles. Broken line: 63 μm Cataphote particles. 2″ tube. Arrows indicate gas velocity at minimum bubbling conditions.

the stress at the bottom of the bed becomes zero and the bed can lift off at the bottom. When lift-off occurs, the particles will detach themselves from the bottom of the plug of solids being lifted and then will descend to form a new bed. Thus this event takes the form of a voidage wave which may evolve in a bubble or a slug. Such a lift-off will occur if $\Delta\bar{u}$ $(\overline{u_L})$ is smaller than $\sim 2a$. Persistent fluctuations in the gas superficial velocity can give rise to a sustained sequence of such lift-offs, and hence bubbles or slugs. In this physical picture, the value of u_{mb} depends on the magnitude of the inherent velocity fluctuations.

As we did not measure the velocity fluctuations in our systems, we can only speculate about their magnitude. The curves in Fig. 16a can readily be replotted in the form of an amplitude $a = \Delta\bar{u}/2$ which will be needed to produce one bed lift-off event per fluctuation cycle at various average gas velocities, $\langle u\rangle = \overline{u_L} + a$, see Fig. 16b. Also shown

in this figure (by arrows) are the u_{mb} values for these two particles. This figure suggests that slow fluctuations in gas velocities, with $a \approx 0.05\langle u\rangle$, can explain our u_{mb} data for the fine Jaygo particles (while the 63 μm Cataphote particles required $a \approx 0.02\langle u\rangle$). Such a large (±5%) and slow fluctuation is unlikely in our experimental system. However, it seems reasonable to expect that the required amplitude will be smaller at smaller t_f values where the bed does not have enough time to defluidize to the fullest possible extent (during the phase of the fluctuation where the gas velocity is decreasing). A dynamic analysis of the behavior of the bed will be needed to probe this point further.

Lateral non-uniformity in either gas flow rate through the distributor or particle volume fraction in the bed, can also lead to onset of bubbling at a gas superficial velocity well below $v_t(1-\phi_{\min})^n$. In reality, both temporal fluctuations and spatial non-uniformity are likely to be present in every experimental system and we suspect that their combined influence is the reason why u_{mb} is smaller than $v_t(1-\phi_{\min})^n$.

4.2. Geldart A–B transition

One of the motivations for the present study was to investigate whether there is any evidence of a dramatic shift in the fluidization characteristics between Geldart group A and group B particles, as Cody et al. (1996) had suggested. It is clear from Fig. 12 that the compressive yield strength characteristics of particles vary gradually with particle size, with no evidence of a dramatic change at the A–B transition. The window of stable bed expansion does become smaller and smaller as particle size increases, as originally suggested by Geldart (1973), who also said that the A–B transition represents only a gradual change. Our results are consistent with those of Geldart (1973). We can assert that, for gas velocities *below* u_{mb}, there is no evidence of any qualitative change in the bed behavior as we move from Geldart group A to group B.

We do add, however, that Cody et al. (1996) based their suggestion of qualitative changes in bed dynamics (as one goes from group A to group B) on observations made for gas velocities *above* u_{mb}. Additional work is needed to fully explain their results.

4.3. Role of wall friction

The effect of tube diameter on pressure drop overshoot observed in this study (and in the earlier studies by Tsinontides and Jackson (1993) and Srivastava and Sundaresan (2002)) is very remarkable. As we are able to capture this effect on the basis of a model based on wall friction for several different particles, it is reasonable to conclude that wall friction is the primary reason for the overshoot in beds of particles in the size range studied here. Therefore, one should not simply attribute the overshoot to cohesive forces. It will be interesting to perform analysis and experiments of the type described in the present study with smaller and smaller particles to see if one can decouple the contributions resulting from cohesive forces and wall friction.

5. Summary

We have performed fluidization–defluidization experiments using several different particles in beds of three different diameters. These have been supplemented by static bed height vs. mass loading experiments, which were used to estimate the compressive yield strength of the particle assemblies. The major results of this study are as follows:

- A simple 1-D steady state model allowing for wall friction and path-dependent contact stresses was able to capture all the key trends and most of the results almost quantitatively.
- In all the cases examined, the pressure drop overshoot observed in the fluidization branch could be attributed to wall friction, without a need to invoke the presence any cohesive interactions between the assembly and the distributor. It then follows that for sufficiently wide tubes, the pressure drop overshoot will be negligibly small for all the particles used in the present study.
- The compressive yield strength characteristics of the Cataphote particles did not show any dramatic change as one crossed the Geldart A–B boundary. Neither did wall friction or drag force characteristics. Collectively, these imply that changes in the fluidization–defluidization characteristics across the Geldart A–B boundary are only gradual, which was indeed the case in our experiments.
- It was difficult to define precisely the minimum bubbling velocity, u_{mb}. We labeled as u_{mb} the gas velocity at which bubbles appeared at a rate of approximately one bubble per minute. The average solids volume fraction in the bed at this condition, ϕ_{mb}, was found to be larger than $\phi_{\min}$ where the compressive yield strength was estimated to become vanishingly small. Conventional linear stability analysis based on reversible particle phase pressure cannot explain why the bed would bubble at the observed ϕ_{mb}. We propose that bubbling occurs when the yield stress can be overcome by spatial and/or temporal fluctuations in velocities.
- For all the particles studied, no interval of stable bed expansion was observed when the average particle volume fraction in the bed was below $\phi_{\min}$.

The observation by Cody et al. (1996) that there is a distinct difference between beds of group A and B particles in the gently bubbling regime is intriguing. This difference is most likely to be due to changes in the dynamics of the bubbles,

as we observed no striking difference between these beds at gas velocities below minimum bubbling.

Notation

a	amplitude of fluctuation or model parameter appearing in Eq. (4)
b, c	model parameters (see Eq. (4))
C	fluctuating velocity
D	diameter of the tube
g	specific gravity force
h, H	bed height
H_{ideal}	height of an ideal fluidized bed
H_o	height of a fully defluidized bed
j, j_f, j_{df}	Janssen's coefficient
J	see definition immediately after Eq. (7)
m	mass loading of particles in the bed per unit cross-sectional area
n	Richardson–Zaki exponent
p	gas pressure
Δp	pressure drop across the bed
p_s	reversible pressure in the particle phase
T	granular temperature
$u, \bar{u}$	gas superficial velocity
$\langle u \rangle$	average gas superficial velocity in the presence of fluctuations
$\Delta\bar{u}$	$(\overline{u_u} - \overline{u_L})$
$\overline{u_c}$	gas superficial velocity at which a fully defluidized bed expands
$\overline{u_L}$	lowest gas superficial velocity reached in a defluidization experiment
$\overline{u_u}$	gas superficial velocity at bed expansion
u_{mf}	gas superficial velocity at minimum fluidization
u_{mb}	gas superficial velocity at minimum bubbling
v_t	terminal velocity of particles
x	vertical coordinate measured from the upper surface of the bed

Greek letters

β	drag coefficient
μ	coefficient of friction
ρ_p	particle density
σ_h	horizontal normal stress
σ_s	vertical normal stress
σ_s^x	compressive yield stress
ϕ	volume fraction of the particles
ϕ_b	volume fraction of the particles at the bottom of the bed
ϕ_{mb}	average volume fraction of the particles in the bed at minimum bubbling conditions
$\phi_{\min}, \phi_{\max}$	parameters in Eq. (4)
ϕ_o	particle volume fraction in the uniform state
φ	angle of internal friction

Acknowledgements

We are grateful to Roy Jackson and Anuj Srivastava for their helpful comments. We are grateful to Dr. George Cody for supplying the Cataphote particles. This work was funded by the US Department of Energy CDE-FC26-00NT40971, the Millenium Inorganic Chemicals and the ExxonMobil Research & Engineering Company.

References

Anderson, T., & Jackson, R. (1968). Fluid mechanical description of fluidized beds. Stability of the state of uniform fluidization. *Industrial and Engineering Chemistry Fundamentals*, *7*, 12–21.

Batchelor, G. K. (1988). A new theory of the instability of a uniformly fluidized bed. *Journal of Fluid Mechanics*, *193*, 75–110.

Cody, G. D., Goldfarb, D. J., Storch Jr., G. V., & Norris, A. N. (1996). Particle granular temperature in gas fluidized beds. *Powder Technology*, *87*, 211–232.

Foscolo, P. U., & Gibilaro, L. G. (1984). A fully predictive criterion for the transition between particulate and aggregative fluidization. *Chemical Engineering Science*, *39*, 1667–1675.

Garg, S. K., & Pritchett, J. W. (1975). Dynamics of gas fluidized beds. *Journal of Applied Physics*, *46*, 4493–4500.

Geldart, D. (1973). Types of gas fluidization. *Powder Technology*, *7*, 285–292.

Jackson, R. (1963). The mechanics of fluidized beds. *Transactions of the Institution of Chemical Engineers*, *41*, 13–28.

Jackson, R. (1998). The nature and role of effective stress in fluidized systems. In L.-S. Fan, & T.M. Knowlton (Eds.), *Fluidization IX* (pp. 1–13). Engineering Foundation Publication, New York.

Jackson, R. (2000). *The dynamics of fluidized particles*. Cambridge: Cambridge University Press.

Janssen, H. A. (1895). Versuche uber getreidedruck in silozellen. *Z. Ver. Deutsch. Ing.*, *39*, 1045–1049.

Johnson, P. C., Nott, P. R., & Jackson, R. (1990). Frictional–collisional equations of motion for particulate flows and their application to chutes. *Journal of Fluid Mechanics*, *210*, 501–536.

Koch, D. L. (1990). Kinetic theory for a monodisperse gas–solid suspension. *Physics of Fluids A*, *2*, 1711–1723.

Koch, D. L., & Sangani, A. S. (1999). Particle pressure and marginal stability limits for a homogeneous monodisperse gas fluidized bed: Kinetic theory and numerical simulations. *Journal of Fluid Mechanics*, *400*, 229–263.

Loezos, P. N. (2002). Ph.D. dissertation, Department of Chemical Engineering, Princeton University.

Menon, N., & Durian, D. J. (1997). Particle motions in a gas-fluidized bed of sand. *Physical Review Letters*, *79*, 3407–3410.

Mutsers, S. M. P., & Rietema, K. (1977a). The effect of inter-particle forces on the expansion of a homogeneous gas-fluidized bed. *Powder Technology*, *18*, 239–248.

Mutsers, S. M. P., & Rietema, K. (1977b). Gas–solid fluids fluidization in a centrifugal field. The effect of gravity upon bed expansion. *Powder Technology*, *18*, 249–256.

Prakash, J. R., & Rao, K. K. (1988). Steady compressible flow of cohesionless granular materials through a wedge-shaped hopper: The smooth wall, radial gravity problem. *Chemical Engineering Science*, *43*, 479–494.

Richardson, J. F., & Zaki, W. N. (1954). Sedimentation and fluidization: Part I. *Transactions of the Institution of Chemical Engineers*, *32*, 35–53.

Rietema, K. (1973). The effect of interparticle forces on the expansion of a homogeneous gas-fluidized bed. *Chemical Engineering Science*, *28*, 1493–1497.

Rietema, K., & Piepers, H. W. (1990). The effect of interparticle forces on the stability of gas-fluidized beds—I. Experimental evidence. *Chemical Engineering Science*, *45*, 1627–1639.

Srivastava, A., & Sundaresan, S. (2002). Role of wall friction in fluidization and standpipe flow. *Powder Technology*, *124*, 45–54.

Tsinontides, S. C. (1992). *A theoretical and experimental investigation of the mechanics of fluidized gas–particle systems*. Ph. D. dissertation, Princeton University.

Tsinontides, S. C., & Jackson, R. (1993). The mechanics of gas fluidized beds with an interval of stable fluidization. *Journal of Fluid Mechanics*, *255*, 237–274.

Valverde, J. M., Castellanos, A., & Quintanilla, M. A. S. (2001). Self-diffusion in a gas-fluidized bed of fine powder. *Physical Review Letters*, *86*, 3020–3023.

Valverde, J. M., Ramos, A., Castellanos, A., & Watson, P. K. (1998). The tensile strength of cohesive powders and its relationship to consolidation, free volume and cohesivity. *Powder Technology*, *97*, 237–245.

Coarse-grid simulation of reacting and non-reacting gas-particle flows

Final Technical Report

Award # DE-FC26-00NT409071
DOE Vision 21 Virtual Demonstration Initiative

Appendix H

ELSEVIER

Powder Technology 129 (2003) 72–85

POWDER TECHNOLOGY

www.elsevier.com/locate/powtec

Analysis of a frictional–kinetic model for gas–particle flow

Anuj Srivastava, Sankaran Sundaresan*

Department of Chemical Engineering, The Engineering Quadrangle, Princeton University, Princeton, NJ 08544-5263, USA

Received 24 January 2002; received in revised form 12 June 2002; accepted 12 June 2002

Abstract

A frictional–kinetic rheological model for dense assemblies of solids in a gas–particle mixture is described. This model treats the kinetic and frictional stresses additively. The former is modeled using the kinetic theory of granular materials. For the latter, we begin with the model described by Schaeffer [J. Differ. Equ. 66 (1987) 19] and modify it to account for strain rate fluctuations and slow relaxation of the assembly to the yield surface. Results of simulations of two model problems, namely, the gravity discharge of particles from a bin and the rise of a bubble in a fluidized bed, are presented. The simulations capture the height-independent rate of discharge of particles from the bin, the dilation of particle assembly near the exit orifice, the significant effect of the interstitial air on the discharge behavior of fine particles and the occurrence of pressure deficit above the orifice. However, the stagnant shoulder at the bottom corners of the bin is not captured; instead, one obtains a region of slow flow at the corners. The bubble rise example shows the significant effect of frictional stresses on the bubble shape. In both examples, a simplified version of the rheological model obtained by invoking a critical state hypothesis is found to be adequate.

Keywords: Bin discharge; Fluidized bed; Simulation; Frictional stress; Critical state

1. Introduction

Flows of dense assemblies of granular materials are encountered in a variety of industrial devices, such as bins, hoppers, rotary blenders, fluidized beds, circulating fluidized beds (CFBs), spouted beds, etc. [1]. In many of these applications, the interstitial fluid (say, gas) is essential for the operation of the device, while in others dealing with fine powders, the interstitial gas interferes with the flow sufficiently that, even when there is no forced gas flow, the system must be analyzed as a two-phase flow problem. Thus, there is a significant scientific and technological interest in understanding and modeling gas–particle flows involving dense assemblies of particles. In these systems, the particles interact with each other largely through enduring frictional contact between multiple neighbors and, to a lesser extent, through collisions. In many instances, the gravitational compaction of granular materials under their own weight is sufficient to ensure that frictional interaction is a significant, if not dominant, contributor to the particulate stress. As the particle volume fraction decreases, the collisional stress becomes more dominant. The development of a rheological model of the granular assembly in such flows (to be used with continuum models for such flows), its implementation in numerical codes for solving the continuum flow models, analysis of model flow problems to understand the consequences of the proposed closures and experimental validation are all practically important [2–7].

The volume fraction of solids in dense fluidized beds, hoppers and bin is high enough that particles make enduring contact with multiple neighbors. Particulate stresses in such dense phase flows are generated by frictional interactions between particles at points of sustained contact. Indeed, it is well known that frictional interactions play a very important role in many dense phase gas–solid flows. For example, it has been shown that frictional stresses play a critical role in maintaining stable operation of CFBs [8,9]. Constitutive models for frictional stresses under slow, quasi-static flow conditions are largely based on ideas which were originally developed in soil mechanics [10–13].

In fast-fluidized beds and risers, particle concentration is typically in the range of 1–30% by volume and particle–particle interactions occur largely through binary collisions. Constitutive models for the stresses in this system have been deduced in the literature by adapting the kinetic theory of dense gases [14,15]. This approach is often referred to in the literature as the kinetic theory of granular materials.

* Corresponding author. Tel.: +1-609-258-4583; fax: +1-609-258-0211.
E-mail address: sundar@princeton.edu (S. Sundaresan).

0032-5910/03/$ - see front matter
PII: S0032-5910(02)00132-8

In many gas–particle flows of industrial significance, one can find regions in the flow domain where kinetic stresses dominate, other regions where frictional stresses dominate and finally, regions where contributions of both are comparable. Thus, it is of practical interest to synthesize rheological models that combine the frictional and kinetic contributions. However, given the disparate nature of theories of both contributions, it is still unclear as to how they should be combined.

In this article, we describe a frictional–kinetic closure for the particle phase stress, which treats the frictional and kinetic stresses in an additive manner [16,17]. The kinetic stresses are based on the kinetic theory of granular materials, which also takes into account the effect of the interstitial gas [18]. For frictional stress, we begin with a model for quasi-static flow proposed by Schaeffer [12] and modify it to account for strain rate fluctuations [19] and slow relaxation of the assembly to the yield surface. We then use the closure to analyze two model flow problems. The first example considers gravity discharge of particles from a 2-D bin, where we have simulated the dilation of particles in the vicinity of the exit orifice and also examined the effect of interstitial gas on the discharge characteristics. It will be seen that these simulations do capture the height-independent rate of discharge of the particles from the bin, the dilation of the granular assembly in the vicinity of the exit orifice and the pressure deficit above the orifice. These simulations, however, fail to capture the formation of stationary shoulders in the bottom corners of the bin. The second example is a detailed simulation of a rising gas bubble in a fluidized bed of Geldart B particles, where we see a significant effect of the frictional stress on the shape and size of the bubble. A simplified closure, which invokes a critical state hypothesis to evaluate the frictional stresses, is shown to be adequate in both examples.

2. Model equations

We treat the gas and solid phases as interpenetrating continua and model them through the volume-averaged equations of Anderson and Jackson [20].

$$\frac{\partial v}{\partial t} + \nabla \cdot (v\underline{v}) = 0 \tag{1}$$

$$\frac{\partial (1-v)}{\partial t} + \nabla \cdot [(1-v)\underline{u}] = 0 \tag{2}$$

$$\rho_s v \left[\frac{\partial \underline{v}}{\partial t} + \underline{v} \cdot \nabla \underline{v}\right] = -\nabla \cdot \boldsymbol{\sigma}_s - v \nabla \cdot \boldsymbol{\sigma}_g + \underline{f} + v\rho_s \underline{g} \tag{3}$$

$$\rho_g (1-v)\left[\frac{\partial \underline{u}}{\partial t} + \underline{u} \cdot \nabla \underline{u}\right] = -(1-v)\nabla \cdot \boldsymbol{\sigma}_g - \underline{f} + (1-v)\rho_g \underline{g} \tag{4}$$

Here, v is the volume fraction of particles; $\underline{v}$ and $\underline{u}$ are the local average velocities of the particle and gas phases, respectively; ρ_s and ρ_g are the densities of the solids and the gas, respectively. $\boldsymbol{\sigma}_s$ and $\boldsymbol{\sigma}_g$ are the stress tensors associated with the two phases and are defined in a compressive sense; $\underline{f}$ is the interaction force between the two phases per unit volume; $\underline{g}$ is the specific gravity force.

A simple Newtonian closure is used for the effective gas phase stress $\boldsymbol{\sigma}_g$ [21].

$$\boldsymbol{\sigma}_g = p_g \boldsymbol{I} - \mu_{g,\mathrm{eff}} \left[\nabla \underline{u} + (\nabla \underline{u})^T - \frac{2}{3}(\nabla \cdot \underline{u})\boldsymbol{I}\right] \tag{5}$$

Here, p_g is the gas pressure, $\mu_{g,\mathrm{eff}}$ is the effective gas phase viscosity and $\boldsymbol{I}$ is the unit tensor. More elaborate models, which account for the effect of gas turbulence, have been developed [22]. However, in the case of dense gas–particle flows under investigation where $\rho_s v \geq \rho_g(1-v)$, the deviatoric part of the gas phase stress plays a negligible role and hence, $\boldsymbol{\sigma}_g = p_g \boldsymbol{I}$ is adequate [18].

In dense gas–solid systems, the dominant contributor to the interaction term $\underline{f}$ is the drag force. In the simulations presented here, the drag correlation of Wen and Yu [23] is used.

$$\underline{f} = \beta(\underline{u} - \underline{v}); \quad \beta = \frac{3}{4} C_D \frac{\rho_g (1-v) v\, |\underline{u} - \underline{v}|}{d} (1-v)^{-2.65} \tag{6}$$

$$C_D \begin{cases} \frac{24}{Re_g}(1 + 0.15 Re_g^{0.687}) & Re_g < 1000; \quad Re_g = \frac{\rho_g (1-v) d\, |\underline{u} - \underline{v}|}{\mu_g} \\ 0.44 & Re_g \geq 1000 \end{cases} \tag{7}$$

Here, β is the interphase drag coefficient, Re_g is the Reynolds number and d is the particle diameter.

Following Savage [16,19], it is assumed that the particulate stress tensor $\boldsymbol{\sigma}_s$ is simply the sum of the kinetic stress tensor $\boldsymbol{\sigma}_s^k$ and the frictional stress tensor $\boldsymbol{\sigma}_s^f$, each contribution evaluated as if it acted alone:

$$\boldsymbol{\sigma}_s = \boldsymbol{\sigma}_s^k + \boldsymbol{\sigma}_s^f \tag{8}$$

The physical basis for such an assumption remains unproven, but it captures the two extreme limits of granular flow; the rapid shear flow regime where kinetic contributions dominate and the quasi-static flow regime where friction dominates. Frictional–kinetic theories based on this simple additive treatment have been used to examine a wide variety of flows such as flow down inclined chutes and vertical channels [19,24], plane shear between parallel plates [17,25] and flow through hoppers [26,27]. The additive theory has been shown to capture the qualitative features of such flows.

The kinetic stress tensor is now commonly modeled by the kinetic theory of granular materials [14,28]. Accord-

ingly, the averaged equations of motion are supplemented by an equation representing the balance of pseudo-thermal energy (PTE) of particle velocity fluctuations,

$$\frac{3}{2}\rho_s v\left[\frac{\partial T}{\partial t}+\underline{v}\cdot\nabla T\right]=-\nabla\cdot\underline{q}-\boldsymbol{\sigma}_s^{\mathrm{k}}:\nabla\underline{v}-J_{\mathrm{coll}}-J_{\mathrm{vis}} \tag{9}$$

where T denotes the granular temperature. The first term on the right-hand side of this equation represents the diffusive transport of PTE, where $\underline{q}$ is the diffusive flux of PTE. The second term represents the rate of production of PTE by shear, with the implicit assumption that work done by the frictional component of stress is translated directly into thermal internal energy and does not contribute to the PTE of the particles [17]. The third term in the equation represents dissipation of PTE through inelastic collisions, whereas the fourth term denotes the net dissipation of PTE through fluid–particle interactions.

Closure relations for $\boldsymbol{\sigma}_s^{\mathrm{k}}$ and $\underline{q}$ used in our study are presented in Table 1 (see Eqs. (1.1) and (1.3)). These expressions represent slight modifications of those proposed by Lun et al. [14] to account for the effects of interstitial gas on particle phase viscosity and thermal diffusivity [18,22,29] (see Eq. (1.5)). Setting μ^* and λ^* to μ and λ, respectively, will recover the model proposed by Lun et al. [14]. The rate of dissipation of PTE due to inelastic collisions J_{coll} is modeled following Lun et al. [14] (see Eq. (1.4)).

The net rate of dissipation of PTE by gas–particle interactions, J_{vis}, consists of two terms as shown in Eq. (1.8). The first term, $3\beta T$, denotes the dissipation of PTE due to gas–particle slip and is modeled following Gidaspow [28]. The second term is the production of PTE by gas–particle slip. The expression shown in Eq. (1.8) for this term, without the g_o term appearing there, was derived by Koch [30] for dilute systems. Koch and Sangani [31] have developed a more elaborate closure for this term; the g_o term in Eq. (1.8) accounts for bulk of the refinement in concentrated suspensions.

2.1. Frictional stress model

At high particle volume fractions, individual particles interact with multiple neighbors through sustained contact. Under such conditions, the normal reaction forces and the associated tangential frictional forces at these sliding contacts are dominant. The frictional model used here is largely based on the critical state theory of soil mechanics [10,11]. It is assumed that the granular material is noncohesive and follows a rigid–plastic rheological model of the type proposed by Schaeffer [12] and Tardos [13] which is given by

$$\boldsymbol{\sigma}_s^{\mathrm{f}}=p_{\mathrm{f}}\boldsymbol{I}+A(p_{\mathrm{f}},v)\frac{\boldsymbol{S}}{\sqrt{\boldsymbol{S}:\boldsymbol{S}}} \tag{10}$$

Table 1
Kinetic theory closures

Stress

$$\boldsymbol{\sigma}_s^{\mathrm{k}}=[\rho_s v(1+4\eta v g_o)T-\eta\mu_b\nabla\cdot\underline{v}]\boldsymbol{I}-\left(\frac{2+\alpha}{3}\right)\times\left\{\frac{2\mu^*}{g_o\eta(2-\eta)}\left(1+\frac{8}{5}v\eta g_o\right)\left[1+\frac{8}{5}\eta(3\eta-2)g_o\right]+\frac{6}{5}\eta\mu_b\right\}\boldsymbol{S} \tag{1.1}$$

$$\boldsymbol{S}=\frac{1}{2}\left\{\nabla\underline{v}+(\nabla\underline{v})^T\right\}-\frac{1}{3}(\nabla\cdot\underline{v})\boldsymbol{I};\quad \alpha=1.6 \tag{1.2}$$

Pseudo-thermal energy flux

$$\underline{q}=-\frac{\lambda^*}{g_o}\left\{\left(1+\frac{12}{5}v\eta g\right)\left[1+\frac{12}{5}\eta^2(4\eta-3)vg_o\right]+\frac{64}{25\pi}(41\eta-33)(\eta v g_o)^2\right\}\nabla T \tag{1.3}$$

Rate of dissipation of pseudo-thermal energy

$$J_{\mathrm{coll}}=\frac{48}{\sqrt{\pi}}\eta(1-\eta)\frac{\rho_s v^2}{d}g_o T^{3/2} \tag{1.4}$$

$$\mu^*=\frac{\mu}{1+\frac{2\beta\mu}{(v\rho_s)^2 g_o T}};\quad \lambda^*=\frac{\lambda}{1+\frac{6\beta\lambda}{5(v\rho_s)^2 g_o T}} \tag{1.5}$$

$$\mu=\frac{5\rho_s d(\pi T)^{1/2}}{96};\quad \mu_b=\frac{256\mu v^2 g_o}{5\pi};$$

$$\lambda=\frac{75\rho_s d(\pi T)^{1/2}}{48\eta(41-33\eta)};\quad \eta=\frac{(1+e_p)}{2} \tag{1.6}$$

$$g_o(v)=\frac{1}{1-(v/v_{\max})^{1/3}} \tag{1.7}$$

$$J_{\mathrm{vis}}=3\beta T-\frac{81 v\mu_g^2(\underline{v}-\underline{u})^2}{g_o d^3\rho_s(\pi T)^{1/2}} \tag{1.8}$$

where

$$p_{\mathrm{f}}=\frac{\sigma_{\mathrm{s},xx}^{\mathrm{f}}+\sigma_{\mathrm{s},yy}^{\mathrm{f}}+\sigma_{\mathrm{s},zz}^{\mathrm{f}}}{3}$$

$$\boldsymbol{S}=\frac{1}{2}\left\{\nabla\underline{v}+(\nabla\underline{v})^T\right\}-\frac{1}{3}(\nabla\cdot\underline{v})\boldsymbol{I}$$

and A is a function to be specified. According to Eq. (10), the frictional stresses manifest an order-zero dependence on the rate of strain. Such a behavior is well known in the quasi-static regime of flow [10,11]. The following properties of Eq. (10) can be proven readily:

(i) the principal axes of stress and rate of deformation are coaxial, and

(ii) the granular material is isotropic and its deformation satisfies an extended von Mises yield condition

$$F(\sigma_1,\sigma_2,\sigma_3,\nu) = (\sigma_1-\sigma_2)^2+(\sigma_2-\sigma_3)^2 + (\sigma_3-\sigma_1)^2 - 3A^2 = 0 \quad (11)$$

Here σ_i, $i=1, 3$ denote the principal stresses. The yield function F can equivalently be expressed in terms of the stress components σ_{ij} referred to an (x, y, z) coordinate system by

$$F = \sigma_{xx}^2+\sigma_{yy}^2+\sigma_{zz}^2+2\sigma_{xy}^2+2\sigma_{yz}^2+2\sigma_{xz}^2-3p_f^2-A^2=0 \quad (12)$$

Additionally, if the postulate is made that the material obeys an associated flow rule, the following compatibility condition can be deduced [13,32]

$$\nabla\cdot\underline{v} = -\sqrt{\boldsymbol{S}:\boldsymbol{S}}\frac{\partial A}{\partial p_f} \quad (13)$$

A variety of models for $A(p_f, \nu)$ have been described in the soil and granular mechanics literature [13,26]. In our illustrative examples, we have considered a form discussed by Prakash and Rao [26]

$$A = -\sqrt{2}p_f\sin\phi\left\{n-(n-1)\left(\frac{p_f}{p_c}\right)^{\frac{1}{n-1}}\right\} \quad (14)$$

where ϕ is the angle of internal friction, $p_c=p_c(\nu)$ is the critical state pressure and n is an exponent that determines the shape of the yield surface. Combining Eqs. (10), (13) and (14), we get

$$\frac{\boldsymbol{\sigma}_s^f}{p_c(\nu)} = \frac{p_f}{p_c}\boldsymbol{I} - \sqrt{2}\frac{p_f}{p_c}\sin\phi\left\{n-(n-1)\left(\frac{p_f}{p_c}\right)^{\frac{1}{n-1}}\right\} \times\frac{\boldsymbol{S}}{\sqrt{\boldsymbol{S}:\boldsymbol{S}}} \quad (15)$$

and

$$\frac{p_f}{p_c(\nu)} = \left\{1-\frac{\nabla\cdot\underline{v}}{n\sqrt{2}\sin\phi\sqrt{\boldsymbol{S}:\boldsymbol{S}}}\right\}^{\frac{1}{n-1}} \quad (16)$$

If the assembly dilates as it deforms, $\nabla\cdot\underline{v}>0$ and $p_f<p_c(\nu)$. Similarly, if the assembly compacts as it deforms, $\nabla\cdot\underline{v}<0$ and $p_f>p_c(\nu)$. At the critical state, where the granular assembly deforms without any volume change, $\nabla\cdot\underline{v}=0$, Eq. (16) reduces to $p_f=p_c(\nu)$, and Eq. (15) becomes

$$\frac{\boldsymbol{\sigma}_s^f}{p_c(\nu)} = \boldsymbol{I} - \sqrt{2}\sin\phi\frac{\boldsymbol{S}}{\sqrt{\boldsymbol{S}:\boldsymbol{S}}} \quad (17)$$

This expression, which is valid only at the critical state, is sometimes used as a simpler representation of the stresses in the granular assembly even when $\nabla\cdot\underline{v}\neq 0$.

Returning to Eqs. (15) and (16), the dilation and compaction branches of the yield surface are usually modeled separately (see, for example, Prakash and Rao [26]). In our work, we retain the same functional form for $A(p_f, \nu)$ in both branches, but choose different values of n for dilation and compaction as discussed below (Fig. 1).

Setting $n=\sqrt{3}/2\sin\phi$ in the dilation branch ensures that the granular assembly is not required to sustain tensile stress anywhere on the yield surface. On the compaction side, n can assume any value greater than unity; however, it appears from literature data that n is only marginally larger than unity [27,33]. The value of n is thus set to 1.03, which is the value determined by Jyotsna [33] for Leighton–Buzzard sand. Fig. 2 shows the master curve for the family of yield loci represented by Eqs. (15) and (16) in 2-D principal stress space for $\phi=28.5°$ and $n=1.03$.

It only remains to discuss the critical state pressure $p_c(\nu)$, which is used to collapse the nest of yield surfaces to a single surface. p_c (ν) is the mean stress at the critical state corresponding to that value of ν. In general, p_c increases monotonically with ν and is expected to become very large ($\sim$ diverge) as ν approaches random close packing ν_{max}. Various expressions have been proposed for the functional dependence of p_c on ν in the literature [9,10,12,13,17,19,26]. In our test simulations, we have used the form considered by Johnson and Jackson [17],

$$p_c(\nu) = \begin{cases} F\frac{(\nu-\nu_{min})^r}{(\nu_{max}-\nu)^s} & \nu>\nu_{min} \\ 0 & \nu\le\nu_{min} \end{cases} \quad (18)$$

where F, r and s are constants. This model asserts that frictional interactions do not occur at values of $\nu<\nu_{min}$.

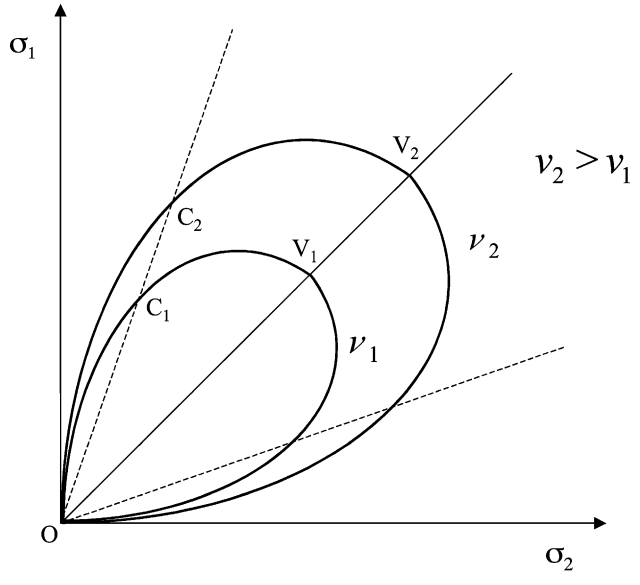

Fig. 1. Yield loci in 2-D principal stress (σ_1, σ_2) space for different values of the solids volume fraction ν. C_1 and C_2 denote critical states at volume fractions ν_1 and ν_2, respectively. The segments OC_1 and OC_1 represent dilation branches; C_1V_1 and C_2V_2 represent compaction branches. The dotted lines represent the critical state loci.

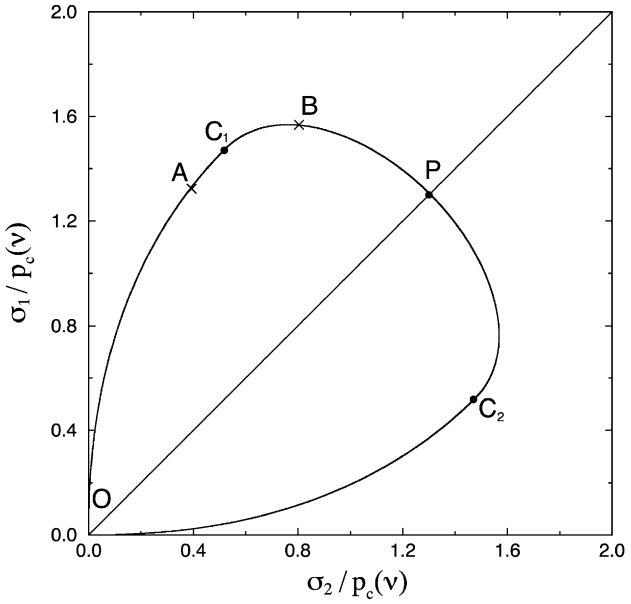

Fig. 2. Scaled yield locus in principal stress (σ_1, σ_2) space. C_1 and C_2 denote critical states. The segments OAC_1 and C_1BP represent dilation and compaction branches, respectively.

2.2. Modification of frictional–kinetic model

Savage [19] argued that even in purely quasi-static flow there exist fluctuations in the strain rate associated with the formation of shear layers and that these fluctuations will lower the shear stress in the assembly. These shear layers are typically tens of particle diameters in thickness. The length scales, therefore, associated with the microscale, i.e. particle diameter d, and the macroscale, i.e. thickness of a shear layer, are not very different. Using this reasoning, Savage suggested a simple estimate for the root mean square strain rate fluctuation, ε, as

$$\varepsilon = \frac{\psi T^{1/2}}{d} \tag{19}$$

where ψ is a constant of order unity. In the present manuscript, we consider an ad hoc modification of Eqs. (15) and (16), which recognizes the effect of strain rate fluctuations in an approximate manner, and write

$$\frac{\boldsymbol{\sigma}_s^f}{p_c(\nu)} = \frac{p_f}{p_c}\boldsymbol{I} - \sqrt{2}\frac{p_f}{p_c}\sin\phi\left\{n-(n-1)\left(\frac{p_f}{p_c}\right)^{\frac{1}{n-1}}\right\} \times \frac{\boldsymbol{S}}{\sqrt{\boldsymbol{S}:\boldsymbol{S}+T/d^2}} \tag{20}$$

with

$$\frac{p_f}{p_c(\nu)} = \left\{1-\frac{\nabla\cdot\underline{v}}{n\sqrt{2}\sin\phi\sqrt{\boldsymbol{S}:\boldsymbol{S}+T/d^2}}\right\}^{\frac{1}{n-1}} \tag{21}$$

With such a formulation, numerical singularity is avoided in regions where $\boldsymbol{S}:\boldsymbol{S}$ is zero as long as the granular temperature T is nonzero. If, however, the physical system does contain regions where both $\boldsymbol{S}:\boldsymbol{S}$ and T are zero, the present model will fail. Thus, in a bin discharge problem, the stagnant shoulders at the bottom corners of the bin, which are indeed physically real features, cannot be captured by this rheological model unless we bring in additional considerations. This, however, is beyond the scope of this paper and we will simply investigate the consequence of the above closure—one can anticipate that in the bin discharge problem the stagnant shoulder will be replaced by a region of slow flow when we simplify the above rheological model everywhere. Eq. (17), which invokes the critical state hypothesis, is also modified in an analogous manner.

$$\frac{\boldsymbol{\sigma}_s^f}{p_c(\nu)} = \boldsymbol{I} - \sqrt{2}\sin\phi\frac{\boldsymbol{S}}{\sqrt{\boldsymbol{S}:\boldsymbol{S}+T/d^2}} \tag{22}$$

2.3. Test simulations—grid-scale flutter

The frictional–kinetic model described in the preceding sections was implemented within the framework of the finite-volume based MFIX code [34]. This code uses a staggered grid arrangement and the SIMPLER algorithm of Patankar [35] to solve the volume-averaged equations of motion.

A number of test simulations involving discharge of granular material from a two-dimensional rectangular bin were run to examine the robustness of the code. In all the test cases, persistent grid-scale flutter in the solids volume fraction profile and velocity field was observed after some time steps [32]. This flutter did not arise if the critical state hypothesis was invoked (i.e. $p_f = p_c$). The origin of this flutter was traced to Eq. (21), which requires the frictional pressure to respond to the rate of deformation instantaneously. As discussed in a greater detail elsewhere [32], a simple and physically reasonable approach to remedy this problem, without compromising on the essential features of the frictional model, is to let the granular material relax to the state dictated by the compatibility condition. This can be represented as

$$\frac{\partial(p_f/p_c)}{\partial t} + \underline{v}\cdot\nabla(p_f/p_c) = \frac{(p_f/p_c)^* - (p_f/p_c)}{\tau} \tag{23}$$

where

$$\left(\frac{p_f}{p_c}\right)^* = \left\{1-\frac{\nabla\cdot\underline{v}}{n\sqrt{2}\sin\phi\sqrt{\boldsymbol{S}:\boldsymbol{S}+T/d^2}}\right\}^{\frac{1}{n-1}} \tag{24}$$

and τ being the relaxation time. This relaxation time can be viewed as a physically meaningful quantity if one argues that particles do not respond instantaneously to deformation. On

the other hand, it can simply be viewed as a small numerical damping introduced to eliminate grid-scale flutter from simulations as well. With this relaxation model implemented in MFIX, all test simulations ran robustly and did not manifest any grid-scale flutter.

3. Simulations

3.1. Discharge from a two-dimensional bin

Simulations of particle discharge from a 2-D rectangular bin, 8 cm wide, 100 cm high and open at the top, were performed. The width of the central orifice at the bottom varied between 1.4 cm and 2 cm. A schematic of the simulation domain is shown in Fig. 3a. A 5-cm high region below the bin was included in the domain so that a boundary condition was not required right at the exit of the bin. Symmetry of the solution about the vertical centerline of the bin was assumed.

The grid resolutions are 1 and 2 mm in the horizontal and vertical directions, respectively. Such a fine mesh was required to effectively resolve variations in the velocities and solids volume fractions near the orifice region. Initially, the bin was filled with particles at a solids volume fraction of 0.60. The initial granular temperature was taken to be non-zero everywhere (1 cm^2/s^2). As noted earlier, our simulations require that $\boldsymbol{S}:\boldsymbol{S}+T/d^2$ is not zero at any location. Table 2 lists the values of the model parameters used in the simulations, most of which were taken from Johnson and Jackson [17]. The flow behavior of particles of two different sizes were investigated—100 μm (Geldart A) and 1 mm (Geldart B) particles.

Table 2
Values of model parameters used in simulations

ρ_g	gas density	1.3×10^{-3} g/cm^3
μ_g	gas viscosity	1.8×10^{-4} g/cm.s
ρ_s	solids density	2.9 g/cm^3
d	particle diameter	1 mm, 100 μm (bin discharge), 400 μm (rising bubble)
τ	relaxation time for solids	10^{-3}, 10^{-2}, 10^{-1} s
ϕ	angle of internal friction	28.5°
δ	angle of wall friction	12.3°
ϕ'	specularity coefficient	0.25
e_p	particle–particle coefficient of restitution	0.91
e_w	coefficient of restitution at wall	0.91
n	parameter for shape of yield surface	$\sqrt{3}/2\sin\phi$ (dilation branch), 1.03 (compression branch)
F	Constant in equation for $p_c(v)$	0.5 dynes/cm^2
r	exponent in equation for $p_c(v)$	2
s	exponent in equation for $p_c(v)$	5
v_{min}	threshold volume fraction for friction	0.5
v_{max}	maximum solids packing	0.65

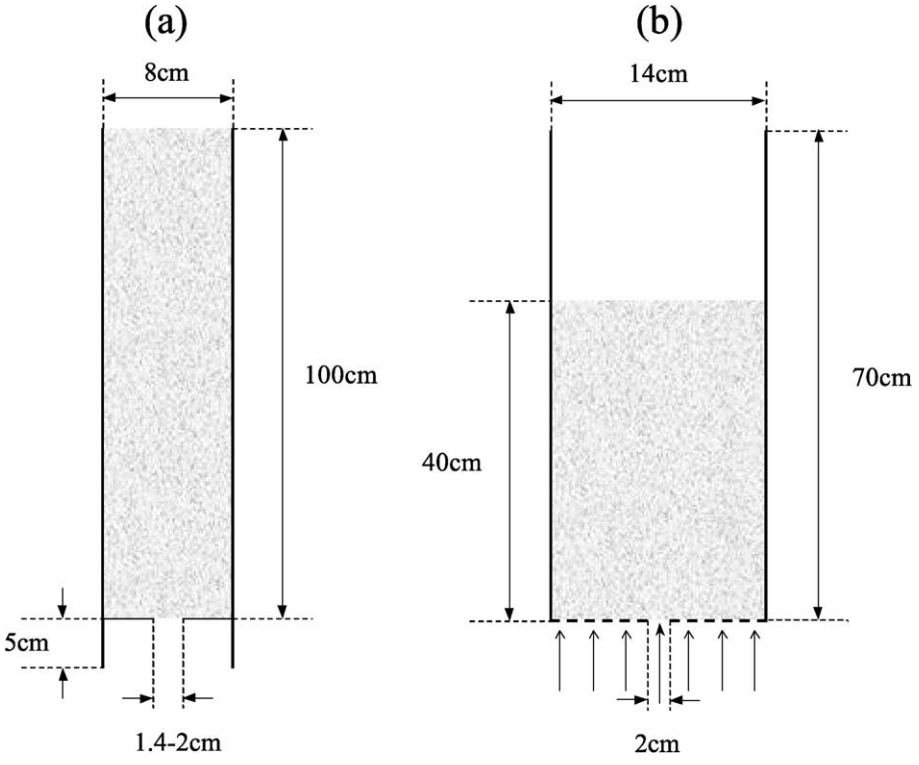

Fig. 3. Schematic diagrams showing the geometries used in the test simulations. (a) Bin discharge; (b) Bubble rise in a fluidized bed.

The momentum and PTE boundary conditions for the particulate phase at the walls of the bin were taken from Johnson and Jackson [17]. These can be written as

$$\underline{n}\cdot(\boldsymbol{\sigma}_s^k+\boldsymbol{\sigma}_s^f)\cdot\frac{\underline{v}_{sl}}{|\underline{v}_{sl}|}+(\underline{n}\cdot\boldsymbol{\sigma}_s^f\cdot\underline{n})\tan\delta + \frac{\pi\sqrt{3}}{6v_{max}}\phi'\rho_s\nu g_o T^{1/2}\underline{v}_{sl}=0 \quad (25)$$

$$\underline{n}\cdot\underline{q}=\frac{\pi\sqrt{3}}{6v_{max}}\phi'\rho_s\nu g_o T^{1/2}|\underline{v}_{sl}|^2-\frac{\pi\sqrt{3}}{4v_{max}}(1-e_w^2)\rho_s\nu g_o T^{3/2} \quad (26)$$

where $\underline{n}$ is the unit normal from the boundary into the particle assembly, δ is the angle of wall friction for the material, ϕ' is the specularity coefficient, e_w is the coefficient of restitution at the wall and $\underline{v}_{sl}$ is $\underline{v}-\underline{v}_{wall}$, the slip velocity of the particle assembly at the wall. The gas was allowed to slip freely at the wall.

At the open boundaries of the integration domain, the gas pressure was set to be atmospheric. For all other dependent variables, the usual continuation condition (i.e. zero gradient in the direction normal to the boundary) was applied.

3.2. Rising bubble in fluidized bed

Simulations involving the rise of a single bubble in a fluidized bed were done for two reasons: (a) to contrast the flow patterns obtained with and without the frictional stresses, and (b) to examine the consequences of assuming that the granular material is in a critical state everywhere (for the purpose of computing the stresses), i.e. $\nabla\cdot\underline{v}=0$ and $p_f=p_c$. This assumption leads to considerable simplification of the frictional model.

The simulation domain was a two-dimensional fluidized bed, 14 cm in width and 70 cm in height. The grid resolution was 3 mm in both the horizontal and vertical directions. Symmetry of the solution about the vertical centerline was assumed. Initially, the fluidized bed was filled with particles at a solids volume fraction of 0.58 up to a height of 40 cm. A schematic of the simulation domain is shown in Fig. 3b. The values of the parameters used in these simulations are the same as in the bin discharge problem and are listed in Table 2. However, the particle diameter here was 400 μm.

At the walls, free-slip boundary conditions were imposed so that one can remove the effect of a partial slip boundary from the comparisons. A pressure at the top boundary was set to be atmospheric. The bed was fluidized by a steady airflow at a vertical velocity 22 cm/s (entering through the bottom surface of the fluidized bed). In addition, in the first 0.2 s of simulation time, a jet of air at a velocity of 100 cm/s was introduced into the bed through a centrally located 2 cm slit at the bottom. After 0.2 s, the velocity of the fluidizing air through this slit was restored to 22 cm/s. The purpose of the jet was to create a bubble which then rose through the fluidized bed.

4. Results

4.1. Bin discharge—1 mm particles

The temporal variation of the discharge rate of 1 mm particles from the bin with an orifice width of 1.4 cm is shown in Fig. 4. In these simulations, the gas phase was turned off and only the particle phase equations were solved. The three different curves in this figure correspond to three different values of the relaxation time constant τ. At early times, there was a rapid increase in the discharge rate, which was then followed by a plateau region where the discharge rate did not vary appreciably with time. We will loosely refer to this plateau as the steady discharge region. It is worth noting that the discharge rate in this plateau did not change much even when τ was varied over two orders of magnitude. In all the results presented below, τ was set to 10^{-3} s.

During the period of steady discharge, the depth of material in the bin varied considerably. For example, at time $t=1.5$ s, the depth was 85 cm while at time $t=4.5$ s it was 53.9 cm. The discharge rate was, therefore, roughly independent of the height of the material in the bin. Experimentally, it has long been known that the flow rate of Geldart type B granular material from bins and hoppers is independent of the surcharge level [36].

Simulations including the gas phase equations yielded essentially the same discharge rate, showing that the gas had a negligible effect on the discharge behavior of the 1-mm particles, which is entirely reasonable [36,37].

The particle phase velocity (at an instant of time in the plateau region) in the bottom region of the bin is shown in

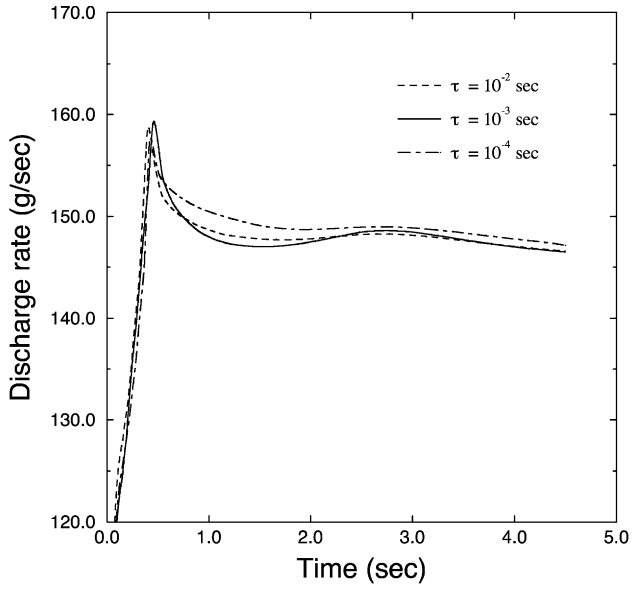

Fig. 4. The rate of discharge of 1-mm particles as a function of time. See Fig. 3a for a schematic of the geometry of the bin. The results corresponding to three different relaxation times are shown. The gas phase equations were not considered in these simulations. In calculating the discharge rate, the thickness of the bin was taken to be 1 cm.

Fig. 5. The corresponding solids volume fraction distribution is superimposed. The width of the orifice in this case was 1.4 cm. The region far above the orifice was characterized by a nearly uniform particle concentration where the material was effectively in (nearly) plug flow. As particles approached the orifice region, the flow converged towards the orifice, as one would expect. At the orifice, there was a substantial decrease in the particle concentration accompanied by a simultaneous increase in the velocities as the particles were discharged. There was further dilation and increase in the downward velocity as particles accelerated down after discharge.

It is clear from Fig. 5 that there was some flow even in the corners of the bin, regions which should truly be stagnant. The frictional model was thus unable to predict the formation of the experimentally observed stagnant zones on either side of the orifice. This was due to the addition of the term T/d^2 in the denominator; the conduction of PTE from regions of high shear near the orifice to the corners ensured that granular temperatures in the latter regions were nonzero.

Fig. 6 shows solids volume fraction profiles at three elevations below the plane of the orifice for the preceding simulation. The vertical lines indicate the positions of the edges of the orifice. Just below the orifice, the profile displayed a marked convexity. At lower depths the profiles manifested greater lateral spreading as the material dilated after being discharged, with the particle concentration being maximum on the centerline. Very similar experimental profiles were observed by Fickie et al. [38] for discharge of 1-mm particles from a wedge-shaped hopper.

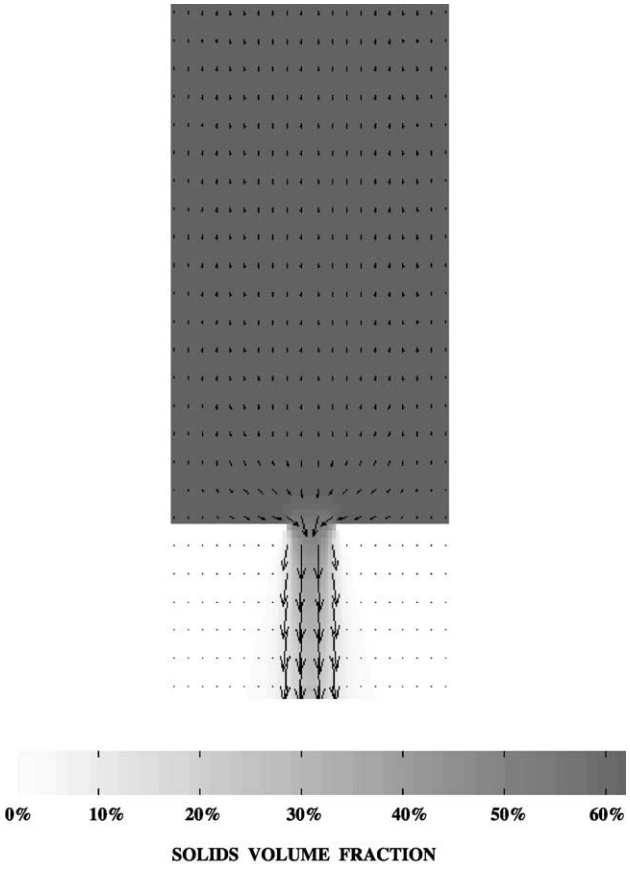

Fig. 5. A vector plot of particle phase velocity. See Fig. 3a for a schematic of the geometry of the bin. This is a magnified view of the bottom region of the bin. A grayscale plot of the particle phase volume fraction field is superimposed. Discharge of 1-mm particles from the bin. The results represent an instantaneous snapshot in the steady discharge rate plateau.

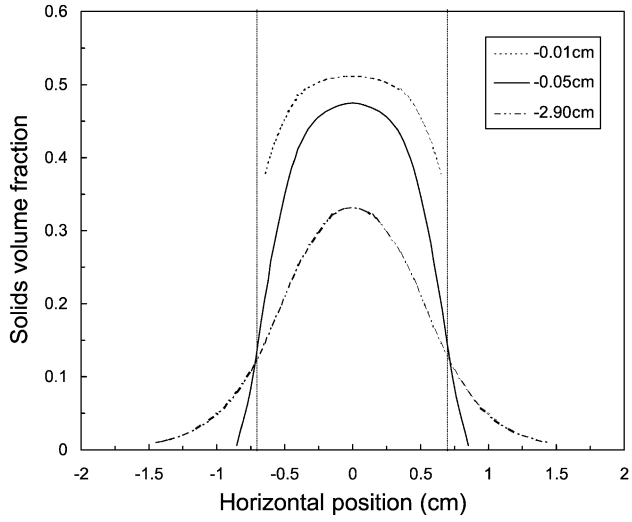

Fig. 6. The lateral variation of solids volume fraction at various distances below the exit orifice. Discharge of 1-mm particles from the bin. See Fig. 3a for a schematic of the geometry of the bin. The results represent a time-average of data in the steady discharge rate plateau.

The variation in the solids volume fraction along the vertical centerline (during the steady discharge rate period) as a function of height above the plane of the orifice is shown in Fig. 7 (as solid line). From a value of 0.60 high in the bin, v fell rapidly on approaching the orifice, reaching a value of 0.52 at the plane of exit. Below the orifice, particle concentration decreased rapidly as the stream of particles accelerated under gravity. Experimental investigations such as those of Bransby et al. [39] and Fickie et al. [38] do reveal considerable changes in the particle concentration from point to point within the hopper. Discrete element simulations of discharge from a hopper also show the same trend [40].

The bin discharge simulation described in Figs. 4–7 was repeated invoking the critical state hypothesis for the frictional stresses (i.e. postulate that $p_f = p_c$). It was found that the results were virtually indistinguishable. This is illustrated in Fig. 7, where the broken line corresponding to the critical state hypothesis overlaps very nearly the solid line obtained with the more detailed stress model. The variation of the ratio p_f/p_c along the centerline, obtained with the detailed stress model, is shown in Fig. 8. Only a small region near the orifice is shown in this figure. It is clear that this ratio was very close to unity well above the orifice; as the granular assembly approached the orifice, it dilated and the ratio decreased. Note that this ratio dropped by only ~ 10%,

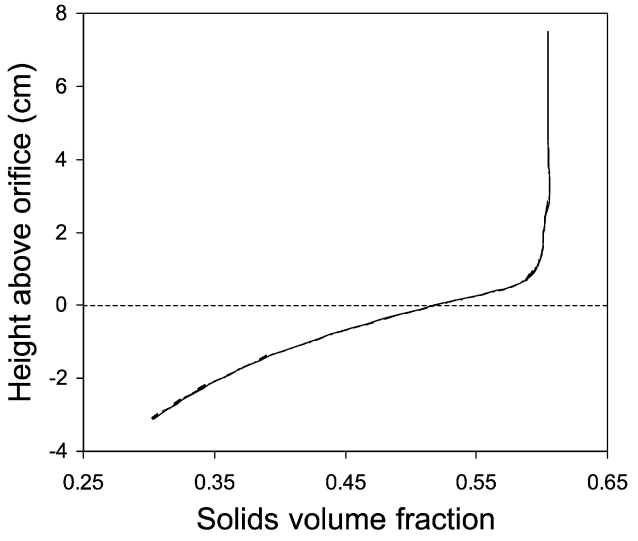

Fig. 7. The variation of solids volume fraction with height along the centerline. The horizontal (dashed) line indicates the location of the exit orifice. Discharge of 1-mm particles from the bin. See Fig. 3a for a schematic of the geometry of the bin. The results represent a time-average of data in the steady discharge rate plateau. The solid curve was obtained from a simulation which ignored the interstitial air. The broken line, which overlaps almost exactly with the solid curve, was obtained in a simulation which included the effect of the interstitial air.

even though there was appreciable dilation. This was because of the large rate of strain (and hence $\boldsymbol{S}:\boldsymbol{S}$) near the orifice. Thus, even in the presence of appreciable dilation near the orifice, critical state hypothesis is reasonable for the purpose of estimating the stresses in the present problem. This is in line with the finding of Tardos [13] who analytically showed that flow in a wedge plane hopper takes place under conditions very close to the critical state.

Many of the early attempts to predict the mass flow rate of Geldart type B particles discharging from a bin under the action of gravity were based on dimensional analysis or semi-empirical correlations. All these studies have tended to rely heavily on the concept of a "free-fall surface" in the neighborhood of the orifice. Above the free-fall arch, particles are in contact with one another and the granular material is usually treated as a noncohesive incompressible Coulomb powder. Below the arch, particles are no longer in contact with one another and accelerate freely under gravity.

Since the discharge rate of granular materials from bin is dependent on conditions near the orifice, it has been argued that the free-fall surface scales with the orifice diameter or width (D_o). Ignoring the possible effects of particle diameter d, dimensional analysis suggests that particle velocity $\underline{v}$ at the orifice then scales as $(gD_o)^{1/2}$. Scaling for the discharge rate W of material from a hopper or bin should therefore be

$$W = \begin{cases} \rho g^{1/2} D_o^{5/2} & 3-\text{D bin or hopper flow} \\ \rho g^{1/2} D_o^{3/2} H & 2-\text{D channel} \end{cases} \quad (27)$$

where ρ is a density characteristic of the flowing material and H is the thickness of the hopper/bin. Indeed, semi-empirical correlations found in the literature are of the form shown above. The well-known Beverloo correlation [41] for discharge from two-dimensional hoppers and bins can be written (when the orifice diameter is much larger than that of the particles) in simplified form as

$$W = C\rho_i g^{1/2} D_o^{3/2} H \quad (28)$$

where ρ_i is the initial density achieved during the filling process and C is an empirical constant in the range $0.55 < C < 0.65$. The variation of the discharge rate with orifice width for our system is shown Fig. 9 where the discharge rate is seen to scale as $D_o^{1.4}$. This compares well with the expected value of 1.5 for the exponent. However, the steady discharge rates obtained in our simulations yield $C \approx 1.6$, which is significantly larger than the typical experimental value. It is possible that this discrepancy is due to the fact that simulation failed to capture the stagnant shoulder; however, it should be noted that theoretical analyses tend to overestimate the discharge rate of particles from a small-angled hopper as well.

Tardos [13] studied the discharge of compressible powder from a wedge-shaped hopper, using an equation of the form $p_c v^{1/n} = \text{constant}$ for the critical state pressure. He found that as n was varied from 0 to 0.25, corresponding to the granular flow becoming increasingly compressible, the coefficient C reduced from 2.0 to 0.90.

As mentioned above, most theoretical analyses of bin or hopper discharge postulate the existence of a free-fall arch at the exit orifice, where the normal stress is assumed to vanish. Kaza and Jackson [42] have argued that this sce-

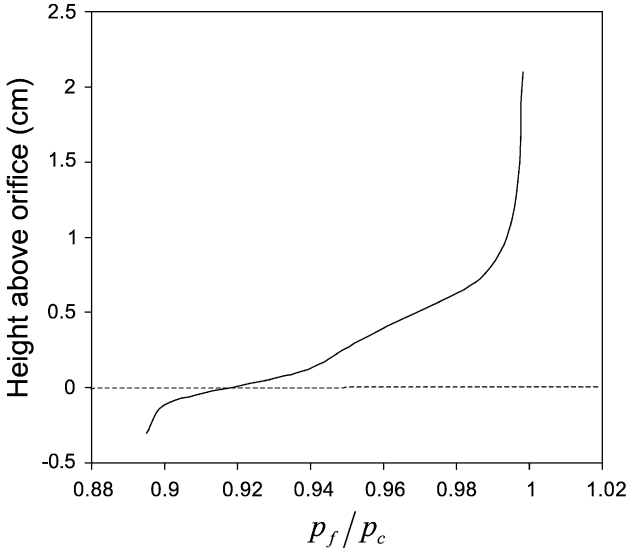

Fig. 8. The variation of p_f/p_c with height along the centerline. Discharge of 1-mm particles from the bin. See Fig. 3a for a schematic of the geometry of the bin. The results represent a time-average of data in the steady discharge rate plateau. Simulations ignored the interstitial air.

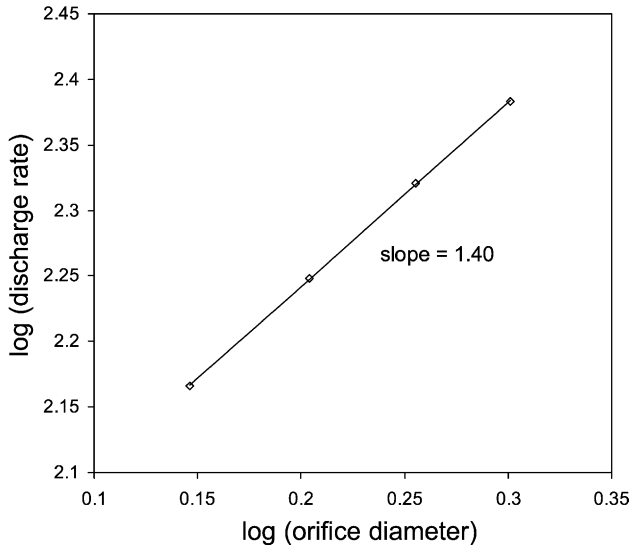

Fig. 9. The rate of discharge of particles with orifice diameter. Discharge of 1-mm particles from the bin. See Fig. 3a for a schematic of the geometry of the bin. The results represent a time-average of data in the steady discharge rate plateaus. Simulations ignored the interstitial air.

nario with the density of the material remaining constant up to the free-fall surface, below which it accelerates, is inconsistent with the laws of motion. The results of our simulations support this argument. For example, there is no evidence of a discontinuous change in the slope of v in Fig. 7, as one would expect at a free-fall surface of the type described previously. Furthermore, the decrease in the bulk density of the granular material starts well within the regime where frictional interactions are dominant and makes the zero normal stress boundary condition questionable.

The decrease in the particle concentration v also has implications for semi-empirical correlations. Such correlations require a density ρ for dimensional consistency as shown in Eq. (28), but there is significant controversy as to the appropriate value to use. Beverloo et al. [41] used the initial density achieved during the filling process, ρ_i, in their correlation. Kotchanova [43] argued that the bulk density in the vicinity of the orifice region should be used although how this value is to be evaluated is unclear according to Nedderman [44].

4.2. Bin discharge—100 μm particles

The temporal variation in the discharge rates of 100 μm particles in the presence and absence of air is shown in Fig. 10. In the absence of air, the discharge rate manifests the plateau region as is expected. It is noteworthy that the steady state discharge rate is almost the same as that for the 1-mm particles. Indeed, the frictional model is independent of the diameter of the particle in the regions where the $\boldsymbol{S}:\boldsymbol{S}$ term dominates over the T/d^2 term, as is the case for the orifice region in bin discharge.

The discharge rate is significantly lower in the presence of air than that in the absence of air. It is well known that the discharge rate decreases as the particle size decreases [45] primarily because the motion of the particles is significantly impeded by drag exerted by the air and that the Beverloo correlation cannot be used to predict discharge rates of particles less than 400 μm in size [44].

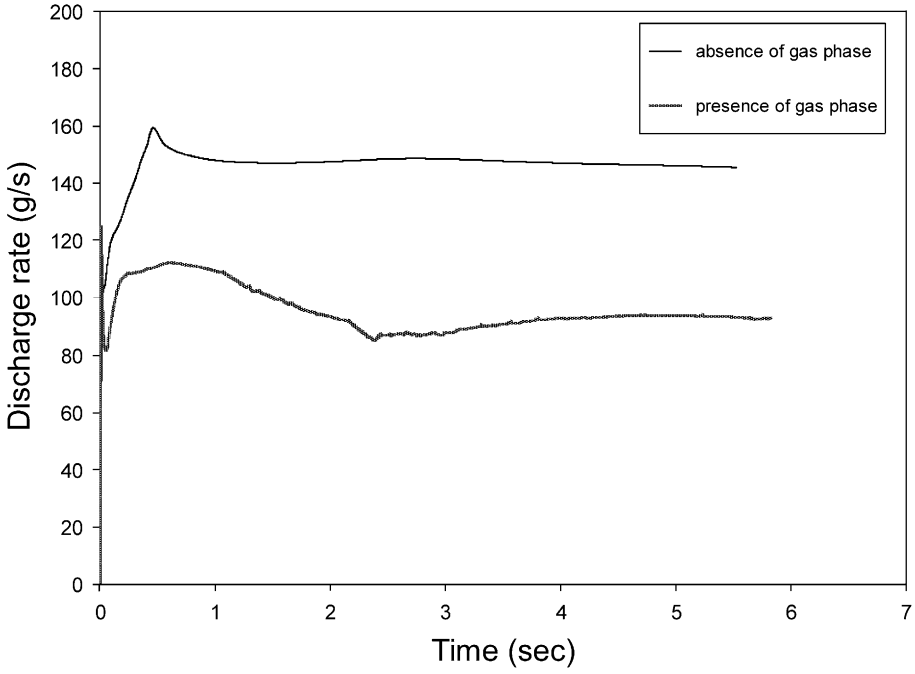

Fig. 10. The rate of discharge of 100 μm particles as a function of time. See Fig. 3a for a schematic of the geometry of the bin. In calculating the discharge rate, the thickness of the bin was taken to be 1 cm.

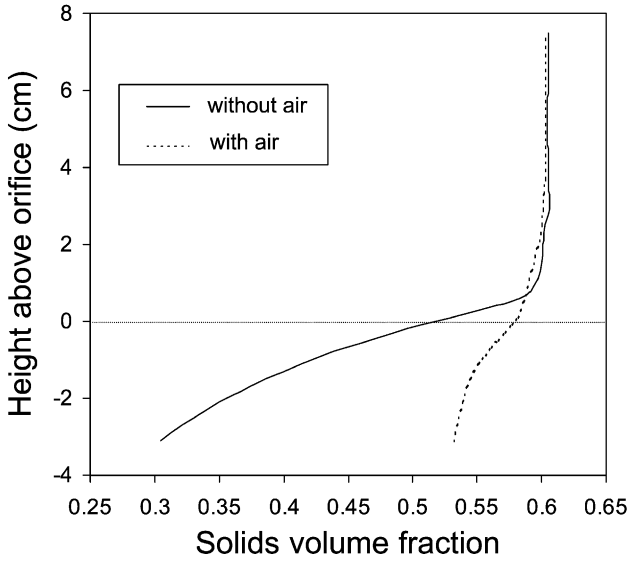

Fig. 11. The variation of solids volume fraction with height along the centerline. See Fig. 3a for a schematic of the geometry of the bin. The horizontal line indicates the location of the exit orifice. Discharge of 100-μm particles from the bin. The results represent a time-average of data in the steady discharge rate plateau. The solid curve was obtained from a simulation which ignored the interstitial air. The broken line was obtained in a simulation which included the effect of the interstitial air.

Nedderman [44] has shown that for a hopper, in the absence of voidage changes, the gas and solids flow through with the same velocities and there is no drag on the particles. Thus, the influence of drag on the discharge of fine particles must be due to relative velocities between the two phases induced by changes in the particle concentration. The variation of the time-averaged solids volume fraction along the centerline (in the plateau region where the discharge rate is nearly constant) is shown in Fig. 11. Indeed, the presence of air changes the v-profile near the orifice region appreciably. It is noteworthy that the magnitude of the change in v in the presence of air is much smaller than that in the absence of air. There is some experimental evidence to support this observation. The experiments of Fickie et al. [38] for 1-mm particles, which are insensitive to fluid drag, reveal considerable changes in particle concentration along the centerline of the hopper. The experiments of Spink and Nedderman [45] for the discharge of 110-μm sand particles from a hopper, show a relatively small but rapid change in the particle concentration immediately above the orifice.

During discharge of a fine material through a hopper or a bin, a subatmospheric pressure is known to develop just above the orifice [45], when both the top and the bottom of the bin are exposed to atmospheric pressure. This was indeed observed in our simulations. The time-averaged pressure profile along the centerline is shown in Fig. 12. Just above the orifice region the air pressure was lower than the ambient pressure just below the orifice. The magnitude of this pressure deficit is comparable to the values recorded experimentally [45,46].

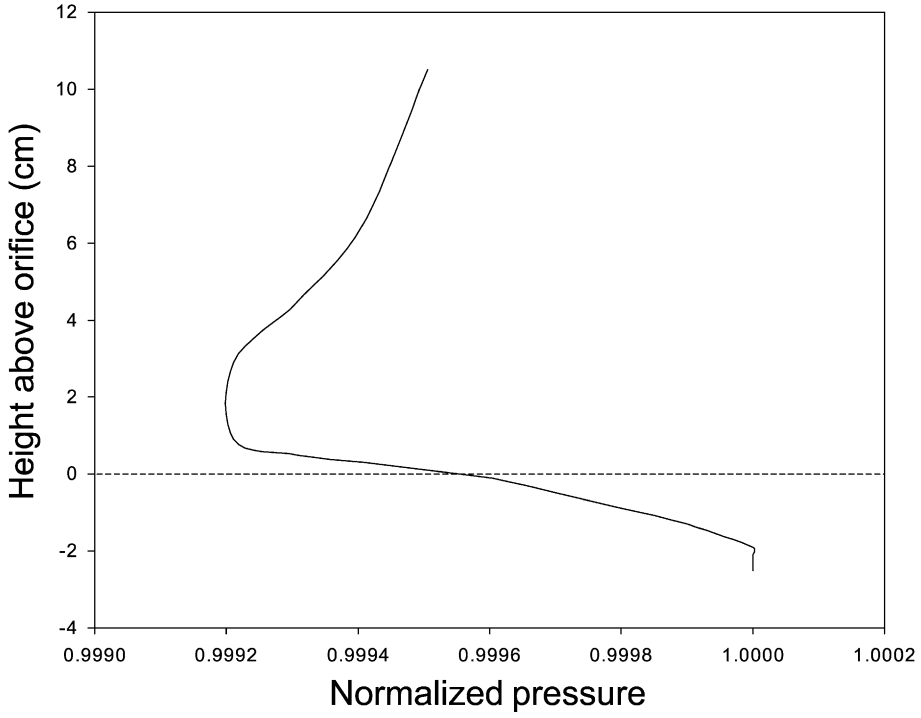

Fig. 12. The variation of gas pressure (scaled with atmospheric pressure) with height along the centerline. See Fig. 3a for a schematic of the geometry of the bin. The horizontal line indicates the location of the exit orifice. Discharge of 100-μm particles from the bin. The results represent a time-average of data in the steady discharge rate plateau.

4.3. Rising bubble in fluidized bed

Instantaneous snapshots of the solids volume fraction profile of a bubble (circular cap) in a fluidized bed at time $t = 0.5$ s are shown in Fig. 13a–c. Panel (a) was obtained with the full frictional model. The relaxation time constant τ was 10^{-3} s for this case. Panel (b) was obtained from a simulation where the critical state hypothesis was used to determine the frictional stresses. Finally, panel (c) represents the situation where frictional stresses were turned off and only the kinetic stresses were considered.

It is clear that neglecting the frictional stresses altogether changed the dynamics of the bed considerably. When only collisional stresses were present, as depicted in Fig. 13c, the spherical cap was more elongated along the vertical axis and rose faster than when frictional stresses were present. As the cap rose, it produced nonuniformities in its wake. These nonuniformities then grew as can be seen in the bottom portion of Fig. 13c.

Comparing Fig. 13a and b, it can be seen that the shapes of the circular caps in both panels are very similar. Thus, the assumption that the granular material is at a critical state everywhere appears to be quite adequate for dense fluidized beds as well as gravity discharge from bins. This has important implications in the modeling of frictional stresses. The critical state assumption leads to considerable simplification of the frictional stress model described here. In addition to the equations becoming much simpler, the critical state assumption obviates the need of solving Eqs. (23) and (24) for the relaxation of p_f/p_c. This speeds up the computations and also makes it more robust.

5. Summary

A frictional–kinetic constitutive model for particle phase stresses is described. This model assumes that the frictional and kinetic stresses are additive [16,17]. For the frictional stresses, we began with a model based on an extended von Mises yield criterion and an associated flow rule [12,13], modified it in a simple, but ad hoc, manner to account for strain rate fluctuations [19] and also allowed the granular material to relax slowly to the yield surface. A simplified version of the model was obtained by invoking the critical state hypothesis [10]. The kinetic stresses have been modeled using the kinetic theory of granular materials with some modifications to account for the presence of the gas phase [18,28,31]. These models have been implemented within the framework of the finite-volume based MFIX code [34].

Simulations of discharge of granular material from a 2-D rectangular bin were performed for two different particle sizes. The discharge rate for 1-mm particles was found to plateau out with time and become approximately independent of the height of the material in the bin [36,41]. As expected, the gas phase did not affect the rate of discharge of these large particles. These simulations also revealed a significant variation in particle concentration near the orifice region, which is in line with experimental observations [38].

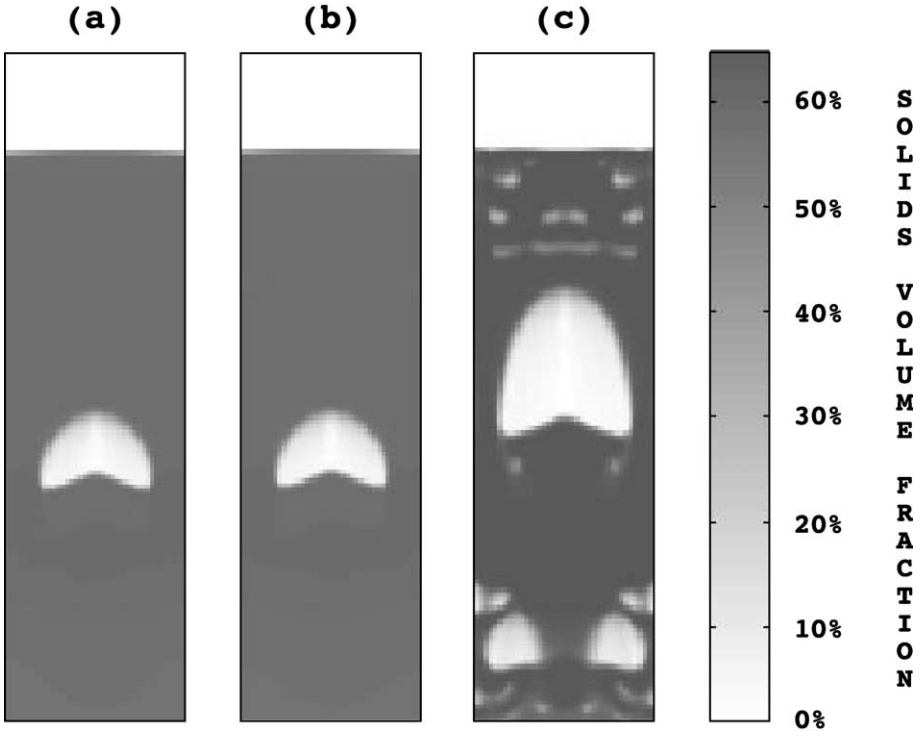

Fig. 13. Instantaneous grayscale plots of solid volume fraction field in a bubble rise simulation. (a) Full frictional–kinetic model; (b) Critical state hypothesis; (c) Kinetic stresses only. 400 μm particles in air. See Fig. 3b for a schematic of the geometry.

The discharge behavior of 100 μm particles was affected by the interstitial gas appreciably. The discharge rate in the presence of air was substantially lower than that in the absence of air. This well-known effect [45] is correctly captured by the simulations.

Although the frictional stress model described here is able to qualitatively predict many of the features of gravity discharge from a bin, it suffers from two main defects. First, it cannot predict the formation of stagnant shoulders at the corners of the bin. Second, it overestimates the discharge rate.

Simulations of a rising bubble in a fluidized bed revealed that the shape of the bubble changed appreciably when the frictional stresses were dropped, demonstrating the significant effect of the frictional stress on the bubble shape.

The critical state hypothesis was found to be fairly accurate for both problems. It simplifies the frictional stress model, renders the code more robust and increases the computational speed.

Nomenclature

A	function defined by Eq. (14)
C_D	drag coefficient (see Eq. (7))
d	particle diameter
D_o	orifice diameter or width
e_p	coefficient of restitution for particle–particle collisions
e_w	coefficient of restitution for particle–wall collisions
$\underline{f}$	interaction force between the two phases per unit volume
F	yield function (see Eqs. (11) and (12))
$\underline{g}$	specific gravity force
g_o	see Eq. (1.7)
$\boldsymbol{I}$	unit tensor
J_{coll}	rate of dissipation pseudo-thermal energy by inelastic collisions per unit bed volume (see Eq. (1.4))
J_{vis}	net rate of dissipation pseudo-thermal energy by gas–particle interactions per unit bed volume (see Eq. (1.8))
n	see Eq. (14)
$\underline{n}$	unit normal from the boundary into the particle assembly
p_c	critical state pressure
p_f	frictional pressure in the particle phase
p_g	gas pressure
$\underline{q}$	diffusive flux of pseudo-thermal energy (see Eq. (1.3))
Re_g	Reynolds number (see Eq. (7))
T	granular temperature
$\underline{u}$	local average velocity of the gas phase
$\underline{v}$	local average velocity of the particle phase
$\underline{v}_{sl}$	slip velocity of the particle assembly at the wall

Greek symbols

β	interphase drag coefficient
v	volume fraction of particles
v_{min}, v_{max}	see Eq. (18)
ρ_s, ρ_g	densities of the solids and the gas, respectively
$\boldsymbol{\sigma}_s$, $\boldsymbol{\sigma}_g$	stress tensors associated with the solid and gas phases, respectively
$\boldsymbol{\sigma}_s^k$, $\boldsymbol{\sigma}_s^f$	kinetic and frictional stress tensors, respectively
σ_i, $i=1, 3$	principal stresses
$\mu_{g,eff}$	effective gas phase viscosity
ϕ	angle of internal friction
ε	magnitude of strain rate fluctuation
τ	relaxation time
δ	angle of wall friction for the material
ϕ'	specularity coefficient

Acknowledgements

This work was supported by the US Department of Energy CDE-FC26-00NT40971. We are grateful to Dr. Madhav Syamlal (Fluent, Morgantown, WV, USA) and Dr. Thomas O'Brien (National Energy Technology Laboratory, Morgantown, WV, USA) for their numerous helpful suggestions.

References

[1] J. Yerushalmi, A.A. Avidan, in: J. Davidson, R. Clift, D. Harrison (Eds.), Fluidization, Academic Press, London, 1985, p. 226.
[2] A. Boemer, H. Qi, U. Renz, Chem. Eng. Sci. 53 (1998) 1835.
[3] B.G.M. van Wachem, J.C. Schouten, R. Krishna, C.M. van den Bleek, Comput. Chem. Eng. 22 (1998) S299.
[4] H. Enwald, A.E. Almstedt, Chem. Eng. Sci. 54 (1999) 329.
[5] H. Enwald, E. Peirano, A.E. Almstedt, B. Leckner, Chem. Eng. Sci. 54 (1999) 311.
[6] B.G.M. van Wachem, J.C. Schouten, C.M. van den Bleek, R. Krishna, J.L. Sinclair, AIChE J. 47 (2001) 1035–1051.
[7] B.G.M. van Wachem, J.C. Schouten, R. Krishna, C.M. van den Bleek, Chem. Eng. Sci. 54 (1999) 2141–2149.
[8] A. Srivastava, K. Agrawal, S. Sundaresan, S.B. Reddy Karri, T.M. Knowlton, Powder Technol. 100 (1998) 173.
[9] A. Srivastava, S. Sundaresan, Powder Technol. 124 (2002) 45–54.
[10] J.H. Atkinson, P.L. Bransby, The Mechanics of Soils: An Introduction to Critical State Soil Mechanics, McGraw-Hill, England, 1978.
[11] R. Jackson, in: R. Meyer (Ed.), Theory of Dispersed Multiphase Flow, Academic Press, New York, 1982, p. 291.
[12] D.G. Schaeffer, J. Differ. Equ. 66 (1987) 19.
[13] G.I. Tardos, Powder Technol. 92 (1997) 61.
[14] C.K.K. Lun, S.B. Savage, D.J. Jeffrey, N. Chepurniy, J. Fluid Mech. 140 (1984) 223.
[15] P.K. Haff, J. Fluid Mech. 134 (1983) 401.
[16] S.B. Savage, Proc. US–Japan Seminar on New Models and Constitutive Relations in the Mechanics of Granular Materials, in: J.T. Jenike, M. Satake (Eds.), Elsevier, 1983, p. 261.
[17] P.C. Johnson, R. Jackson, J. Fluid Mech. 176 (1987) 67.
[18] K. Agrawal, P.N. Loezos, M. Syamlal, S. Sundaresan, J. Fluid Mech. 445 (2001) 151.
[19] S.B. Savage, J. Fluid Mech. 377 (1998) 1.

[20] T.B. Anderson, R. Jackson, Ind. Eng. Chem. Fundam. 6 (1967) 527.
[21] J.L. Sinclair, R. Jackson, AIChE J. 35 (1989) 1473.
[22] G. Balzer, A. Boelle, O. Simonin, Fluidization VIII, Engineering Foundation, 1995, p. 1125.
[23] C.Y. Wen, Y.H. Yu, Chem. Eng. Prog. Symp. Ser. 62 (1966) 100.
[24] L.S. Rao, P.R. Nott, K.K. Rao, Chem. Eng. Sci. 52 (1997) 913.
[25] M. Alam, P.R. Nott, J. Fluid Mech. 343 (1997) 267.
[26] J.R. Prakash, K.K. Rao, Chem. Eng. Sci. 43 (1988) 479.
[27] R. Jyotsna, K.K. Rao, Chem. Eng. Sci. 46 (1991) 1951.
[28] D. Gidaspow, Multiphase Flow and Fluidization: Continuum and Kinetic Theory Descriptions, Academic Press, California, 1994.
[29] D. Ma, G. Ahmadi, Powder Technol. 56 (1988) 191.
[30] D.L. Koch, Phys. Fluids A 2 (1990) 1711.
[31] D.L. Koch, A.S. Sangani, J. Fluid Mech. 400 (1999) 229.
[32] A. Srivastava, PhD Dissertation, Princeton University, 2002.
[33] R. Jyotsna, PhD Dissertation, Indian Institute of Science, Bangalore, 1993.
[34] M. Syamlal, W. Rogers, and T.J. O'Brien, MFIX Documentation, U.S. Department of Energy, Federal Energy Technology Center, Morgantown, 1993.
[35] S.V. Patankar, Numerical Heat Transfer and Fluid Flow, Hemisphere Publishing, USA, 1980.
[36] R.M. Nedderman, U. Tüzün, S.B. Savage, G.T. Houlsby, Chem. Eng. Sci. 37 (1982) 1597.
[37] A. Castellanos, J.M. Valverde, A.T. Pérez, A. Ramos, P.K. Watson, Phys. Rev. Lett. 82 (1999) 1156.
[38] K.E. Fickie, R. Mehrabi, R. Jackson, AIChE J. 35 (1989) 353.
[39] P.L. Bransby, P.M. Blair-Fish, R.G. James, Powder Technol. 8 (1973) 197.
[40] P.A. Langston, U. Tüzün, D.M. Heyes, Chem. Eng. Sci. 51 (1996) 873.
[41] W.A. Beverloo, H.A. Leniger, J. Van de Velde, Chem. Eng. Sci. 15 (1961) 260.
[42] K.R. Kaza, R. Jackson, Chem. Eng. Sci. 39 (1984) 915.
[43] I.I. Kotchanova, Powder Technol. 4 (1970) 32.
[44] R.M. Nedderman, Statics and Kinematics of Granular Materials, Cambridge University Press, Great Britain, 1992.
[45] C.D. Spink, R.M. Nedderman, Powder Technol. 21 (1978) 245.
[46] B.J. Crewdson, A.L. Ormond, R.M. Nedderman, Powder Technol. 16 (1977) 197.

Coarse-grid simulation of reacting and non-reacting gas-particle flows

Final Technical Report

Award # DE-FC26-00NT409071

DOE Vision 21 Virtual Demonstration Initiative

Appendix I

Available online at www.sciencedirect.com

SCIENCE DIRECT®

Powder Technology 145 (2004) 190–202

POWDER TECHNOLOGY

www.elsevier.com/locate/powtec

Silo music and silo quake: granular flow-induced vibration

Benson K. Muite[a], Shandon F. Quinn[a], Sankaran Sundaresan[a,*], K. Kesava Rao[b]

[a]School of Engineering and Applied Science, Princeton University, Princeton, NJ 08544, United States
[b]Department of Chemical Engineering, Indian Institute of Science, Bangalore, India

Received 7 October 2003; received in revised form 5 May 2004; accepted 21 July 2004

Abstract

Acceleration and sound measurements during granular discharge from silos are used to show that silo music is a sound resonance produced by silo quake. In tall and narrow silos, the latter is produced by stick–slip friction between the wall and the granular material. For the discharge rates studied, the occurrence of flow pulsations is determined primarily by the surface properties of the granular material and the silo wall. The measurements show that the pulsating motion of the granular material drives the oscillatory motion of the silo.

Keywords: Silo quake; Silo music; Stick–slip flow; Resonance; Creep; Granular discharge

1. Introduction

The discharge of granular materials from silos is often characterized by vibrations or pulsations of the silo, termed ‘silo quake’, and a loud noise, termed ‘silo music’ [1–9]. Both of these are undesirable as silo quake may cause structural failure, and silo music is a source of noise pollution. Unfortunately, the numerous conflicting studies published in the literature [1–9] do not give the silo designer a simple model to understand the physical processes that cause the pulsations and to guide the silo design or modification that would prevent the pulsations or at least minimize their effect. The purpose of this study is to investigate the cause of the noise and the pulsations, and the interaction between the motion of the granular material and the motion of the structure.

Several studies of the discharge of granular material from silos have noted fluctuations in discharge rate and the production of noise and vibration [1–9]. The top of the granular material has been observed to move in discrete steps, although the discharge from the bottom of the silo was continuous [1,6]. For smooth-walled, tall, narrow silos, pulsations occurred during both mass and mixed flow. The pulsations were observed to stop at a critical height of granular material in the silo [2,10]. Methods suggested for preventing pulsations include roughening the walls in the transition zone between the bunker and the orifice [2,4,10] and the placement of inserts along the silo walls [1].

In an early study, Phillips [6] observed the motion of sand in a tube which had a glass face and was closed at the lower end by a flat bottom having a central orifice. When the orifice was opened, the sand in the upper part of the tube moved downward intermittently in jerks. Phillips noted, “when the flow begins, a curious rattling sound is heard which changes to a distinct musical note”. He also did experiments in which the tube was first partly filled with mercury and then filled with sand. Once again, the free surface of the sand descended intermittently when the mercury was allowed to flow through the orifice. He observed that the length of the column of sand increased by about 2% during the ‘stick’ phase. Furthermore , the motion of the granular material caused the wall of the tube to vibrate. Thus, both silo music and silo quake occurred in his experiments, and he suggested that the stick–slip motion of the sand may be responsible for these phenomena.

* Corresponding author. Tel.: +1 609 258 4583; fax: +1 609 258 0211.
E-mail address: sundar@princeton.edu (S. Sundaresan).

0032-5910/$ - see front matter © 2004 Elsevier B.V. All rights reserved.
doi:10.1016/j.powtec.2004.07.003

Some recent studies have suggested that the pulsations are intensified by a resonant interaction between the granular material and the silo structure [3,5,10,11]. However, in one of these studies, Tejchman [10] also noted that the magnitude and presence of the flow pulsations were influenced by environmental factors, such as temperature and electrostatic effects, which suggests that while resonant interaction can intensify the pulsations it is not the only requirement for pulsations to occur. Olvarez and Clément [12] have also observed that the humidity, an environmental factor, can have a strong influence on the sliding motion of a slowly pushed granular column. They found that particle and wall frictional properties are important in determining stick–slip motion in granular systems.

Hardow et al. [1] conducted experiments in a silo whose natural frequencies were significantly greater than the pulsation frequency. In these experiments, pulsations clearly occurred even in the absence of resonance. These authors proposed that the motion of the silo was driven by the rapid acceleration and deceleration of the granular material in the bin section, which were caused by the stress fluctuations in the granular material in the hopper section. As the granular material in the hopper region deforms, there are periods where the mass of granular material in the bin is not supported and the bed collapses in a downward step creating a large impulse which shakes the silo structure. These authors observed pulsations during core flow in a silo that was 6 m high, 0.6 m deep, and 1.2 m wide, and hence the flow kinematics were considerably different from those in tall narrow silos.

Wensrich [8,9] proposed that these pulsations are due to compression and dilation waves in the granular material, which are created by stick–slip motion between the granular material and the silo walls. However, pulsations have also been observed in funnel flow bunkers, where the granular material at the walls does not slip during discharge [1]. Wensrich [8,9] has suggested that the pulsation creation mechanism is entirely different in funnel flow, but does not give evidence to support his conjecture.

Finally, Moriyama and Jimbo's [4] findings suggest that the magnitude of the pulsations is determined by how the granular material changes from a compressed state in the bunker to a dilated state in the hopper. They also found that the likelihood of a silo discharging with pulsations was dependent on the method used to fill the silo. They did not propose a physical mechanism to explain their observations.

The aim of this study, which is largely experimental, is to obtain a mechanistic understanding of silo music and flow pulsations. Through a combination of sound, bed height, and acceleration measurements, it is shown that silo music is driven by the stick–slip pulsating motion of the granular material during discharge and is associated with a sound resonance in the air column above the bed. Different wall and granular materials have been used to probe their role on flow pulsations and silo music during silo discharge.

2. Related studies on stick–slip friction in granular materials

To explain the rationale in the choice of experimental measurements, it is worth reviewing the generally understood kinematics of the discharge of granular material from a bin or hopper and relating these to stick–slip friction in granular materials. Experiments show that in a tall, flat-bottomed cylindrical bin, with walls having a lower friction coefficient than the internal friction angle of the granular material, there is a region of plug flow at the top of the full silo. As the silo empties, the size of the plug flow region decreases, and eventually all of the flowing material is in converging flow. The discharge rate from the bin is independent of the height of material in the bin, provided the height is greater than a few multiples of the diameter of the orifice [13] and scales as $g^{1/2}D^{5/2}$, where D is the orifice diameter and g is the acceleration due to gravity.

Radiographic studies of slow dense granular flow in model bunkers show that velocity discontinuities exist at the transition from the bin to the hopper [14]. Measurements in a discharging bunker indicate that there is a dynamic arch at the transition where the nature of the material flow changes from one without deformation (above the arch) to one where the material deforms (below the arch) as it approaches the orifice [15]. Pressure measurements [1,3,4] near the transition from the bin to the hopper indicate that there is also a stress discontinuity [15] and that there can be large pulsating stresses, which correspond to the cyclical formation and breakage of the dynamic arch. This pulsating behavior only occurs for dense assemblies [15] and is very similar to silo quake.

The experiments that identified the dynamic arch [15] were conducted in a bunker where the bin to hopper transition determined the location of the dynamic arch. In a flat-bottomed silo (such as the one used in our study), the stagnant material adjacent to the orifice creates a hopperlike region. Thus, the discharge from a flat-bottomed silo can be expected to show many of the features observed in bunkers. If the density of the material in the plug flow region above the dynamic arch is high, it must dilate as it crosses the arch in order to deform in the hopperlike region.

Nasuno et al. [16] have studied stick–slip motion in granular materials using a simple shear device with 70–110 μm glass beads and 100–600 μm sand. They observed stick–slip motion at low average slip rates, which became continuous at very large average slip rates. They also observed that at very small driving velocities, the period of stick–slip fluctuations was inversely proportional to the driving velocity. For glass beads, the system fluctuated with a nearly constant period, while for sand, the period varied stochastically. As the sliding velocity was increased, the period became independent of velocity, and finally at large sliding velocities, the motion became continuous. In these simple shear experiments, the spring constant connecting the driving piston to the sliding mass was varied, and it was

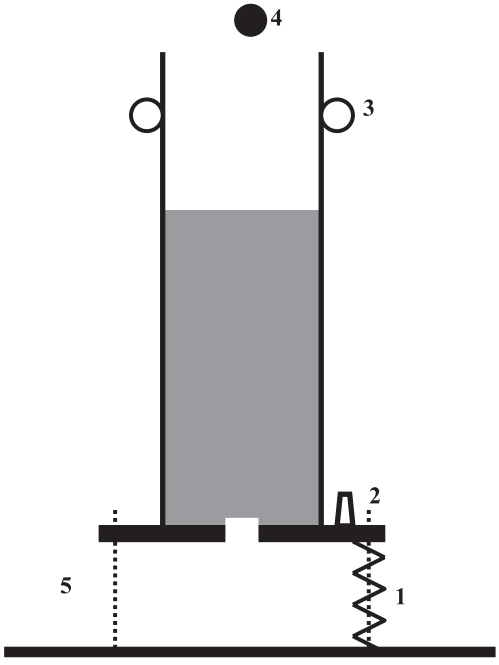

Fig. 1. Experimental setup for vertical acceleration and sound measurements. The numbers indicate (1) spring on positioning slider, (2) accelerometer, (3) positioning roller, (4) microphone, and (5) positioning slider.

found that the spring constant influenced both the pulsation frequency and the critical driving velocity at which the pulsation frequency became independent of the driving velocity.

Nasuno et al. [16] also observed that a lengthy period of slow vertical dilation preceded rapid slip events in the horizontal direction. This dilation was measured by Geminard et al. [17], who found that in the shear zone, particles climb slowly over each other. Once the particle is ~5% of a particle diameter over the particle below it, slip occurs and the top layer jumps forward before slowing down again and settling into another zone of particles [17]. In the experiments of Geminard et al. [17], the particle volume fraction was indistinguishable from the random close-packed volume fraction of 63%.

These studies show that granular materials can undergo stick–slip motion, and that this can couple with the mechanical system (for example, a mass–spring system) in a complicated fashion, which depends on the system parameters. Together, these studies suggest that stick–slip motion can occur in tall flat-bottomed silos during the discharge of granular materials. Excellent reviews on stick–slip friction can be found in Bowden and Tabor [18], Krim [19], and Berman et al. [20] who discuss the various postulated stick–slip friction mechanisms. The mechanism of most relevance to this study is adhesive stick–slip friction, which occurs when slowly weakening, time-dependent forces exist between sliding surfaces. The hypothesis in this study is that adhesive stick–slip friction is the determining factor in cyclical dynamic arch formation and breakage, which creates impulses that drive the silo structure.

3. Experimental method

Aluminum, plain steel, and acrylic tubes, open at the top and covered at the bottom with a flat acrylic plate having a concentric orifice (see below for details of this plate), were used as silos. A number of experiments were conducted using silos resting on supporting springs (see Fig. 1), which in turn were attached to a steel frame that was rigidly connected to the laboratory walls. The silo was also equipped with rollers and sliders, which were attached to the steel frame. These allowed vertical oscillation of the silos and restricted lateral motion. The supporting springs had spring constants ranging from 4 to 2265 N/mm. Experiments were also done using an aluminum block in place of the spring or simply bolting the silo directly to the supporting steel frame—these configurations afforded the two largest natural frequencies for vertical silo oscillation reported in this study. Properties of the tubes and granular materials are listed in Tables 1–3. Photographs of the granular materials, obtained using a microscope, are shown in Fig. 2a–c. The granular materials did not exhibit squeaking or booming when sheared. The temperature and humidity were recorded in each experiment. The temperature varied between 20 and 25 °C (from one day to another), and the relative humidity between 18% and 40%. During experiments with each tube and granular material combination (which lasted a few hours), the humidity variation was within 5%, and the temperature variation was within 2 °C.

The angle of internal friction of each granular material was estimated by measuring the angle of repose of the granular material between two plane walls 1.9 cm apart. These values are presented in Table 2. The angle of wall friction for each granular material and tube combination

Table 1
Tube properties

Tube material	Length (m)	ID (cm)	Wall thickness (cm)	Surface finish	Calculated lowest natural frequency (Hz)
6061-T6 aluminum alloy	1.8	6.37±0.01	0.51±0.1	Smooth	26
Plain steel	1.8	6.38±0.01	0.57±0.01	Rough	25
Cast acrylic	1.5	6.35±0.01	0.64±0.01	Smooth	12

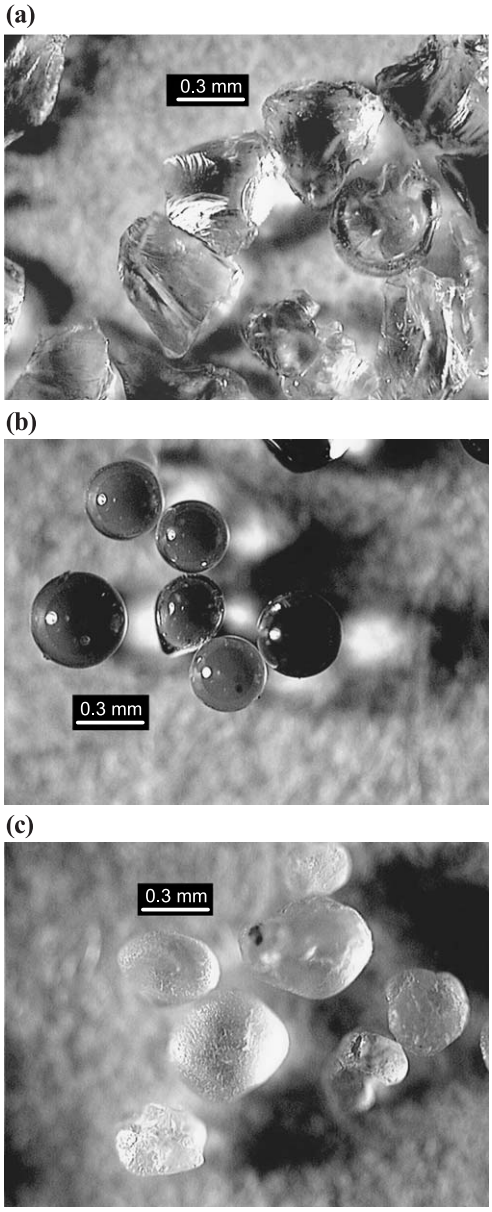

Fig. 2. Photographs of the granular materials: (a) crushed glass, (b) glass beads, and (c) sand.

was estimated by measuring the angle of inclination of the tube above the horizontal at which the granular material began to slide; these values are listed in Table 3. We could not estimate the angle of wall friction for the plain steel tube through such experiments, as the granular material began to slide over itself before it slid at the wall.

To determine if resonance (i.e., when the pulsation frequency f_p is equal to a natural frequency of the silo) was important, the dominant natural frequency of vertical silo oscillations, f_v, was changed by using different springs between the silo and the steel frame. To estimate the lowest natural frequencies of the empty silo tube, we used the method of Naeem and Sharma [21] with clamped-free boundary conditions. The lowest natural frequency estimates for each tube are given in Table 1.

Table 2
Granular material properties

Material	Supplier	Particle size (μm)	Particle density (g/cm^3)	Angle of repose (°)
Crushed glass	Potters Industries	450±50	2.5±0.1	34±1
Ballotini impact beads	Potters Industries	480±60	2.5±0.1	26±1
Washed and ignited Standard Ottawa sand	EMD Science	400±100	2.7±0.1	33±1

Acrylic plates with centrally located orifices (with diameters between 1.3 and 2.5 cm) were bolted to a 1.21-kg aluminum flange, which was screwed on the bottom of the tubes. To fill the silo, the orifice at the bottom of the tube was first sealed with a piece of duct tape. The granular material was poured into the silo through a funnel placed at the top of the tube. Stripping away the duct tape seal over the orifice initiated discharge. The mean discharge rate was measured using a stopwatch. For the acrylic tube, the height of material in the silo could also be measured during discharge to confirm that the discharge rate was constant with time. To ensure that the tubes had reached a steady state of wear, the granular material was discharged several times through the same tube before final measurements were taken. Steady state wear was reached when repeatable granular material acceleration measurements could be taken.

Accelerations were measured both in the granular material and on the silo structure. Vertical accelerations inside the granular material were measured using a unidirectional Kistler 8774A50 low-impedance ceramic shear accelerometer with an output sensitivity that deviated less than 1.5% for frequencies between 10 Hz and 10 kHz. The accelerometer was embedded approximately 5 cm below the top surface of the granular material. This depth ensured that during discharge, the accelerometer was held upright by the granular material and was still shallow enough that the acceleration could be measured for the bulk of the discharge. As the granular material discharged, the accelerometer cable was carefully fed into the silo to ensure that the cable did not affect the motion of the accelerometer. This accelerometer had a range +/−500 m/s^2 and was accurate to within +/−5 m/s^2. It had a diameter of 0.8 cm, a length of 2.6 cm, and a

Table 3
Angle of wall friction for various silo wall and granular material combinations

Silo wall material → granular material	Acrylic[a] (°)	Aluminum[a] (°)	Plain steel
Crushed glass	28	33	Fully rough
Glass beads	17	17	Fully rough
Sand	25	30	Fully rough

[a] The angles are accurate to within ±2°.

mass of 4 g, and hence was considerably larger than a sand grain. However, the wide frequency response allowed better time resolution of the bulk granular material acceleration than would be possible with smaller accelerometers of comparable cost.

Silo structural vibrations were measured using a Kistler 8784A5 low-impedance ceramic shear accelerometer, which had a greater sensitivity but a smaller range than the accelerometer used to measure granular material accelerations. To measure vertical accelerations, this accelerometer was wax-mounted on the flange at the bottom of the silo. This accelerometer had a sensitivity that varied by less than 0.5% for frequencies between 10 Hz and 6 kHz. It had a range of +/−50 m/s^2, an accuracy of +/−0.5 m/s^2, and a mass of 21 g.

The accelerometer output was sent through a Kistler 5118B2 signal conditioner to a Measurement Computing PCI-DAS1002 data-acquisition card on a 400-MHz Pentium II computer. The sampling rate on the data acquisition card was 20 kHz. For both accelerometers, the manufacturer-supplied calibration was used to convert the accelerometer voltage output to acceleration. The accelerometers could not be used simultaneously because only one data acquisition system was available.

The bulk of the sound measurements was taken in an apparatus made from an acrylic tube, for which the resonant frequency for vertical silo oscillations was not well controlled [22]. However, several measurements were then repeated in the experimental setup used for the acceleration measurements to check that the same results were obtained. In these experiments, an omnidirectional Optimus 33-3026 lapel microphone with a constant amplitude response for a frequency range between 30 Hz and 15 kHz was used to collect the sound data through a sound card on a personal computer. During discharge, the sound was recorded, and a discrete Fourier transform of 1 s of sound data was used to determine the dominant frequency as a function of time during discharge. In the acrylic tube, the time at which the top of the granular material crossed a marked height in the tube during discharge was also recorded using a stopwatch. From these measurements, the height of the granular material as a function of time since discharge started was found.

4. Results

In what follows, sound measurements are shown for sand discharging from the acrylic tube, and acceleration measurements are shown for crushed glass and glass beads discharging from the aluminum tube. Additional sound and acceleration measurements are reported in Quinn [22] and Muite [23], respectively.

The variation of the pulsation frequency (f_p) with the dominant natural frequency for vertical oscillations (f_v) was examined for all tube and granular material combinations, except for the plain steel tube, as pulsations did not occur in this tube. Silo pulsations also did not occur when sand was discharged from the aluminum tube, but did occur when sand was discharged from the acrylic tube. A few experiments with a smooth-walled galvanized steel tube [23] showed that silo pulsations occurred when sand was discharge from this tube. This suggests that in tall and narrow silos, pulsations occur for specific combinations of granular material and wall material. This is in agreement with studies which show that stick–slip friction depends on the composition of the sliding surface [18–20].

4.1. Sound measurements

Fig. 3 shows the sound amplitude level as a function of time for the discharge of sand from the acrylic tube (no units are given, because although the amplitude is a direct voltage reading from the microphone that is linearly related to the sound decibel level, by moving the microphone, different absolute decibel levels can be recorded for the same sound signal). The discharge lasted for 51 s, and as shown in the figure, silo music occurred for approximately half of this time. Fig. 4 shows a typical power spectrum for the sound measurements during discharge, determined by analyzing data obtained over a 1-s time interval. There are three types of prominent peaks. The first peak is at a frequency of approximately 40 Hz, and it will be shown later that this is the pulsation frequency for this particular granular material and silo combination. The second peak corresponds to the resonant frequency of the air column above the tube. This resonance is well documented, and a good account can be found in Rayleigh [24]. At the time the data shown in the figure was collected, this frequency was 200 Hz. The fact that this peak represents a resonance frequency is demonstrated in Fig. 5, which shows the quarter wavelength corresponding to this frequency as a function of time since

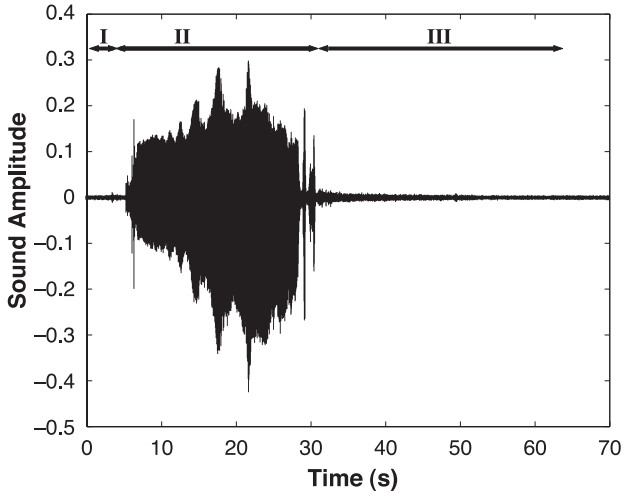

Fig. 3. Variation of sound amplitude with time during discharge of sand from an acrylic tube of 7.6 cm outer diameter, wall thickness 0.3 cm, and having an orifice of diameter 1.9 cm: region I—no flow, region II—flow with pulsations, and region III—flow after pulsations have ended.

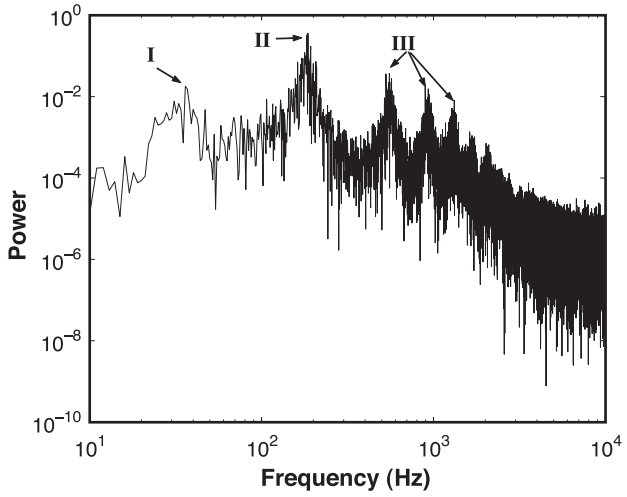

Fig. 4. Typical power spectrum for 1 s of sound measurements during silo music when sand is discharged from an acrylic tube of 7.6 cm outer diameter, wall thickness 0.3 cm, and having an orifice of diameter 1.9 cm: (I) the pulsation frequency, (II) the dominant sound frequency, and (III) the higher harmonics of the dominant sound frequency.

the beginning of discharge. The wavelength, λ_a, is found from the relationship $\lambda_a=c/f_a$, where c is the speed of sound in air, and f_a is the frequency of the air column. Also shown is the height of the air column above the sand in the tube. This figure shows that the dominant quarter wavelength and the height of the air column are the same confirming the resonant behavior. It is clear from the *quarter* wavelength that this resonance corresponds to a standing wave mode with a node at the granular material surface and an antinode at the open end of the tube (as the open end of the tube cannot be a node). Fig. 4 also shows a number of other peaks at higher frequencies, which are simply the odd harmonics of the fundamental (lowest) resonance frequency of the air column.

4.2. Determination of the natural frequency for vertical oscillations of the silo

To determine the dominant natural frequency for vertical oscillations, f_v, the silo was filled with granular material and the orifice closed. The base of the filled silo was then struck with a soft mallet, and the resulting vertical acceleration during free oscillations recorded. The value of f_v was found either by using the largest peak in the power spectrum of the acceleration or by counting the number of free oscillations during a specified time directly from the acceleration measurements. The two measurements gave essentially the same results; however, when $f_v<30$ Hz, counting the number of oscillations in a specified time gave a more accurate measurement of the natural frequency than locating the center of the broad peak obtained from the power spectrum. Similarly, when the $f_v>30$ Hz, the power spectrum was a better indicator of the natural frequency, because an unambiguous sharp peak could be located, while the acceleration vs. time trace showed rapidly decaying oscillations which were not easy to count. For spring constants, $k<1000$ N/mm, $f_v \approx f_n=(1/2\pi)(k/m)^{1/2}$, where m is the oscillating mass, and f_n is the theoretical natural frequency for a spring mass system. For $k>1000$ N/mm, f_v was significantly less than f_n, possibly because of flange and tube deformations, which reduced the effective stiffness of the system. This effect was important for $f_v>25$ Hz.

4.3. Acceleration measurements during discharge

Fig. 6 shows measurements of the vertical acceleration of the silo when crushed glass was discharged through a 1.9-cm orifice. The accelerometer was mounted on the base of the silo. Once the flow started, there was a period of

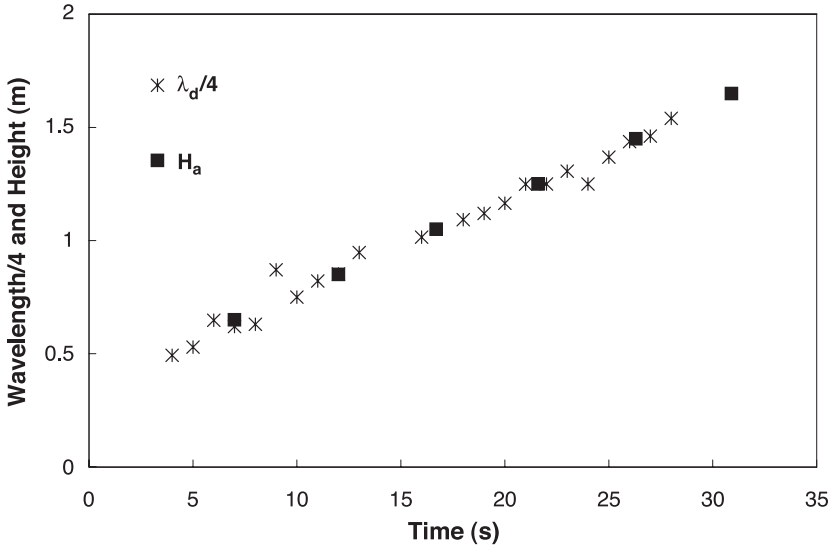

Fig. 5. Variation of the dominant quarter wavelength ($\lambda_d/4$) and the height of the air column (H_a) with time during discharge of sand from an acrylic tube of 7.6 cm outer diameter, wall thickness 0.3 cm, and with an orifice of diameter 1.9 cm.

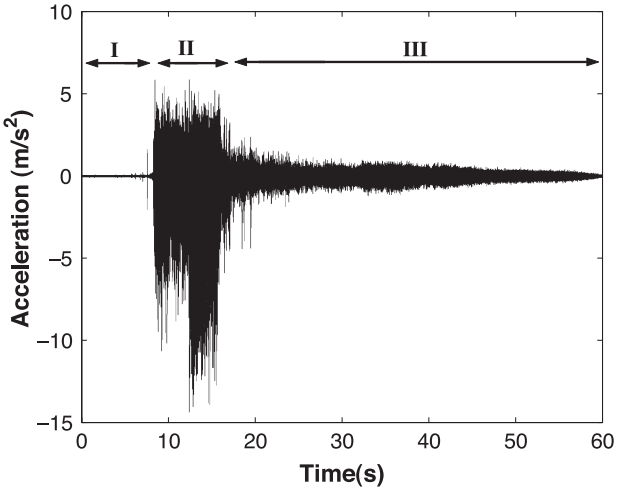

Fig. 6. Vertical acceleration measurements on the base of the aluminum silo during discharge of crushed glass through a 1.9-cm orifice. The silo had a dominant natural frequency of vertical oscillations of 8 Hz: region I—no flow, region II—flow with pulsations, and region III—flow after pulsations have ended.

pulsations during which the silo experienced large negative accelerations towards the earth. Halfway during the pulsations, the magnitude of the negative pulsations suddenly doubled. After the height of the granular material in the silo fell below a critical level, the pulsations stopped, and the silo structure experienced only small accelerations until the flow ended. While the pulsations occurred regularly, this doubling of the pulsation magnitude was not always repeatable. It is not clear what changes in the flow resulted in these changes in the magnitude of the pulsations, because the basic setup was unchanged from run to run.

The closeup of the acceleration measured during pulsations (Fig. 7) reveals that the periods of large negative accelerations were short compared to the gradual rebound after each pulsation. On this time scale, the pulsations had a very reproducible and steady frequency, but the absolute magnitude of the maximum acceleration varied from pulse to

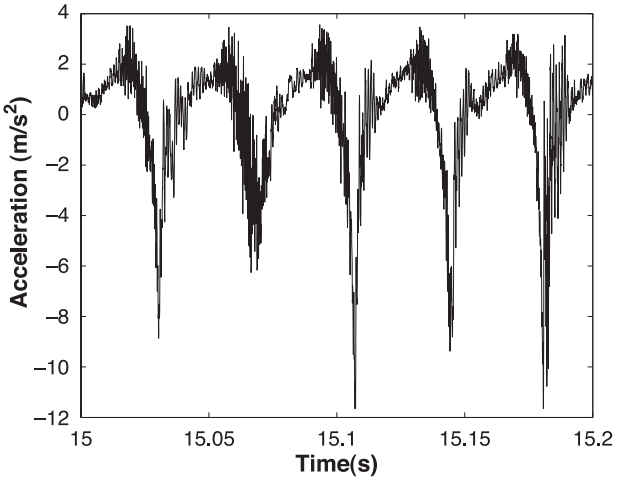

Fig. 7. Closeup showing individual pulsations measured by the accelerometer on the silo structure for the flow in Fig. 6.

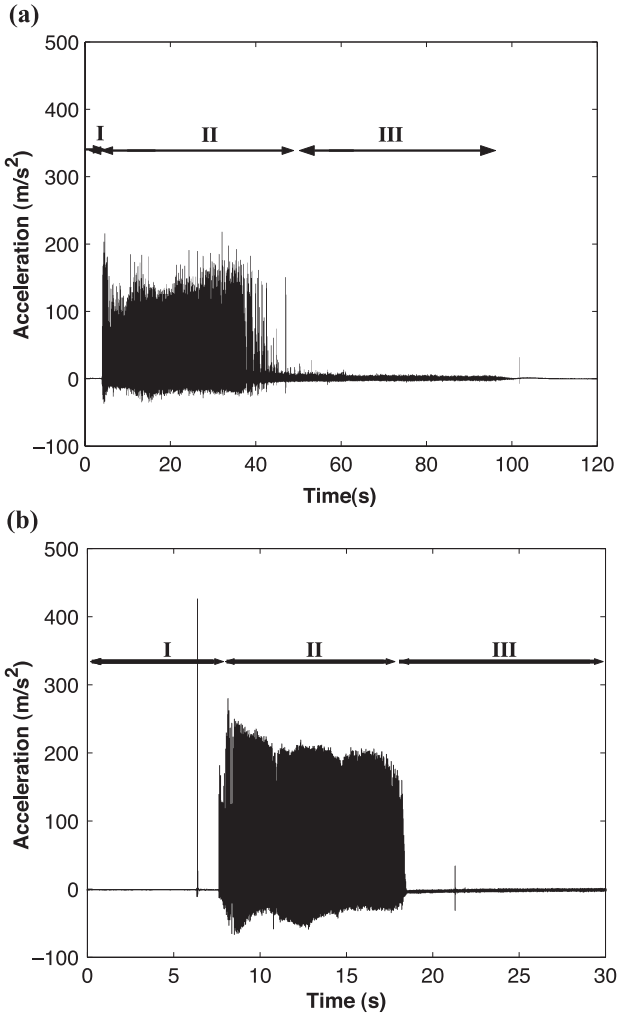

Fig. 8. Vertical acceleration measurements made when the accelerometer was embedded in the granular materials [(a) crushed glass, (b) glass beads] and allowed to translate with it during discharge from the aluminum silo: region I—no flow, region II—flow with pulsations, and region III—flow after pulsations have ended. In (a), orifice diameter is 1.3 cm; the dominant natural frequency of vertical oscillations of the filled silo is 8 Hz. In (b), orifice diameter is 1.9 cm; the dominant natural frequency of vertical oscillations of the filled silo is 6 Hz.

pulse. We found that f_p~30 Hz for discharge of granular material through a 1.3-cm orifice and through a 1.9-cm orifice, i.e., f_p was roughly independent of the discharge rate.

Fig. 8a shows measurements obtained with the accelerometer buried in the granular material. The flow conditions were the same as in Fig. 6, except that the orifice diameter was 1.3 cm instead of 1.9 cm. Also as in Fig. 6, negative accelerations are towards the earth. Fig. 8a shows that large positive accelerations occurred in the granular material during pulsations, while Fig. 6 shows that the silo experienced large negative accelerations. The two figures show that during each pulsation, the granular material fell a short distance and impacted the tube wall and flange bottom.

Fig. 9a shows a closeup view of the acceleration reported in Fig. 8a. A comparison of Figs. 7 and 9a reveals that the pulsation frequency in the granular material is the same as the

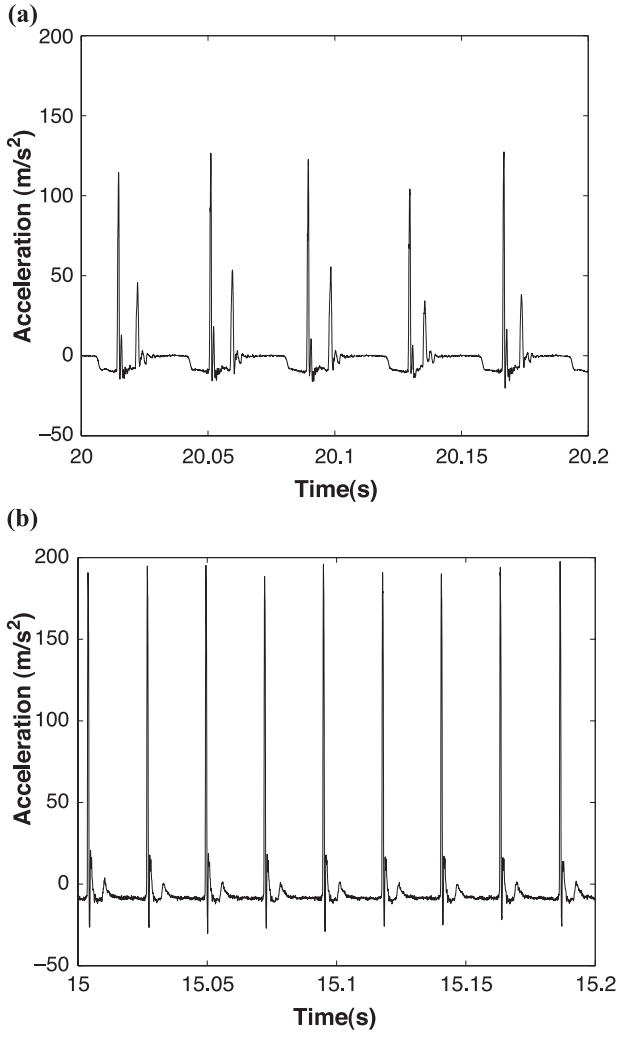

Fig. 9. Closeup showing individual pulsations measured by the accelerometer embedded in the granular material for the flow in Fig. 8: (a) closeup from Fig. 8a, and (b) closeup from Fig. 8b.

frequency with which the silo moves, suggesting that the motion of the granular material drives the motion of the silo. Fig. 9a also shows that each pulsation was followed by a negative acceleration within the material and then a second large positive acceleration, after which the acceleration of the granular material was close to zero until the next pulsation. Fig. 10a shows a power spectrum for the acceleration measured during 1 s of pulsations in the crushed glass. It has a peak at f_p~30 Hz followed by a flat-band region between 200 and 1000 Hz, after which the power spectrum decays.

Figs. 8b, 9b, and 10b are similar to Figs. 8a, 9a, and 10a but are for glass beads discharging through a 1.9-cm orifice (the acceleration spike seen in Fig. 8b before the discharge was initiated came about because of an accidental tap of the tube, and its effect decayed well before discharge was started). The pulsations again stopped at a critical height, and the individual pulsations can be seen in Fig. 9b. The nature of each pulsation for glass beads (Fig. 9b) is a little different than for the crushed glass (Fig. 9a), and this is reflected in their power spectra; compare Fig. 10a and b. Both spectra have the same high-frequency decay for frequencies above 1000 Hz; however, for frequencies below 1000 Hz, the glass beads have a larger number of distinct harmonics than the crushed glass. The crushed glass power spectrum is typical of white noise with a high-frequency cutoff, while the glass bead power spectrum is typical of a signal produced by a well-correlated periodic but non-sinusoidal function [25].

Surprisingly, all the power spectra for acceleration measurements inside the granular material for all tube and granular material combinations that pulsated decayed for frequencies above 1000 Hz. The high-frequency cutoff of 1000 Hz was neither due to any limitation of the accelerometer (which could measure frequencies up to 10 kHz) or the lowest natural frequency of the tube (which was varied in these experiments and did not affect the high-

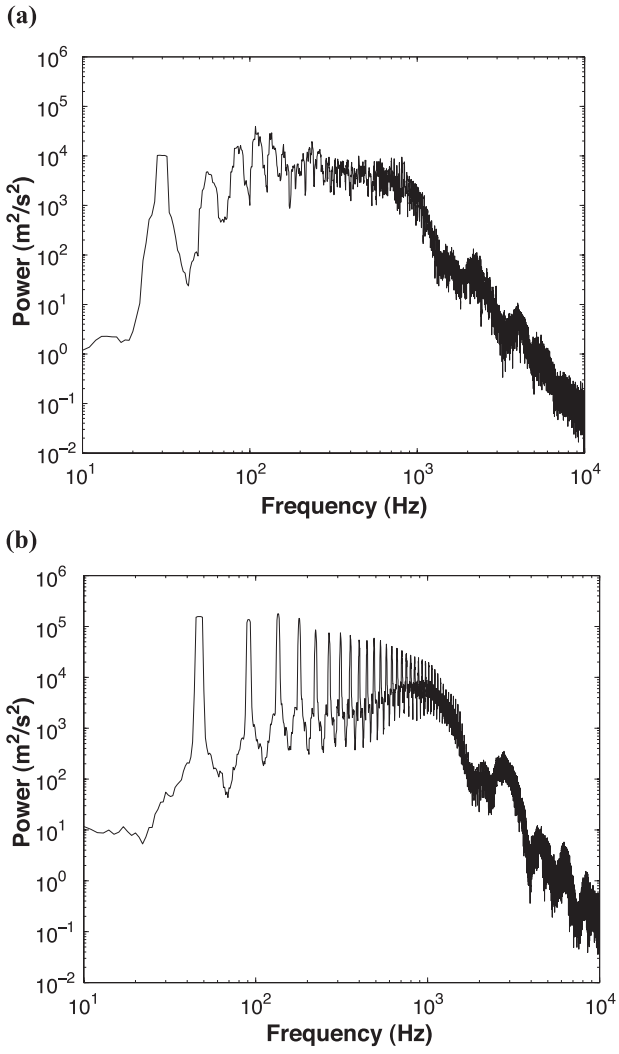

Fig. 10. Power spectra for 1 s of the measurements in Fig. 8. The power spectra have been averaged over 4 points in frequency to make average trends clearer: (a) 20th second of measurements of Fig. 8a, and (b) 15th second of measurements of Fig. 8b.

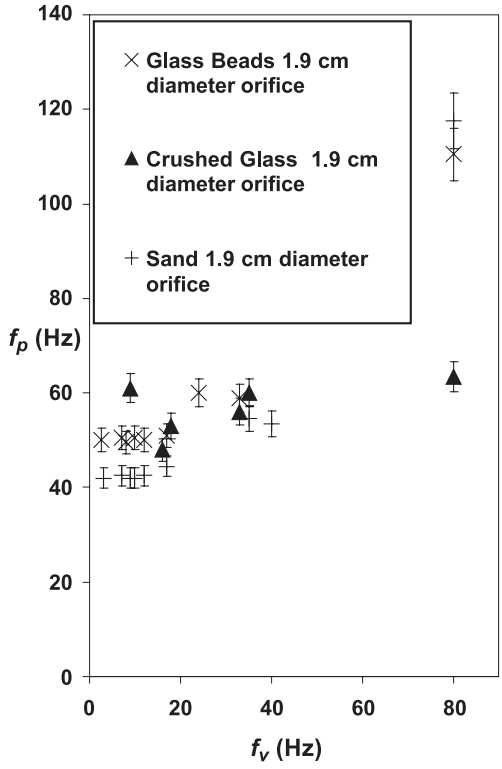

Fig. 11. Variation of the pulsation frequency (f_p) of the filled silo with the dominant natural frequency for vertical oscillations of the silo (f_v) for granular materials discharging from the acrylic tube.

frequency cutoff). It may be related to the tube diameter or to the particle size and particle density, which were not varied in the experiments.

In Figs. 7, 9a, and b, the maximum downward accelerations of the silo and particles are roughly comparable, whereas the maximum upward acceleration of the granular material is significantly greater than that of the silo. This suggests that during each pulsation, the granular material slips past the silo walls and is forced to rest over a very short time period. This impact creates a shock wave that travels through the granular material and is recorded as the large upward acceleration. The granular material and silo then move together so that the resulting accelerations are of similar magnitude.

4.4. Dependence of the pulsation frequency of the granular material on the natural frequency of vertical silo oscillations

Figs. 11 and 12 show the variation of the pulsation frequency (f_p) for different granular material and silo wall combinations as a function of f_v (recall that f_v was changed by changing the spring on which the silo was mounted). To determine f_p, the number of peaks per unit time above a certain threshold in the acceleration time data was counted. The threshold was determined by looking at the acceleration time trace and picking a value approximately equal to a half of the maximum acceleration. The threshold was adjusted depending on the type of acceleration time graph to ensure the correct periodicity was obtained. In particular, by comparing Fig. 9a and b, one observes that if the threshold is too low, a higher periodicity would be measured in some experiments, because the "aftershock" would also be included. Similarly, if the threshold is set too high, some quakes could be missed, because as shown in Fig. 8a and b, the peak amplitude could vary during quaking. The pulsation frequency was determined for each second of flow pulsations and an average pulsation frequency during pulsating discharge obtained. The standard deviation in the average frequency measured during a single discharge was typically less than 10%.

When f_v<25 Hz, f_p had no dependence on f_v as shown in Figs. 11 and 12. Fig. 12 also shows that doubling the orifice diameter and hence increasing the discharge rate by nearly a factor of 6 had a negligible effect on the pulsation frequency (doubling the orifice diameter gives a nearly sixfold increase in discharge rate in a silo of constant cross-sectional area, because the discharge rate is proportional to the orifice diameter to the power 2.5 [13]). When f_v>25 Hz, f_p had a positive correlation with f_v for all

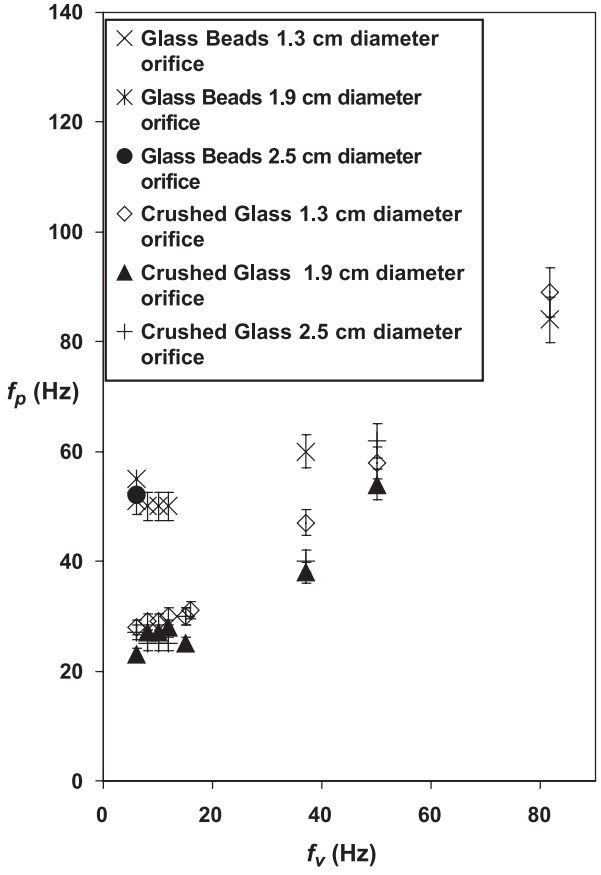

Fig. 12. Variation of the pulsation frequency (f_p) of the filled silo with the dominant natural frequency for vertical silo oscillations (f_v) for granular materials discharging from the aluminum tube.

granular material tube wall combinations that pulsated, except for the acrylic and crushed glass combination. The figures show that glass beads have similar frequency behavior in the acrylic and aluminum silos. Crushed glass has a lower pulsation frequency in the aluminum silo as compared to the acrylic silo. As sand did not pulsate during discharge from the aluminum silo, no data points are shown.

4.5. Critical height

The critical height (H_c) was taken as the height of the granular material above the base of the silo at which pulsations stop. The time at which this occurred was recorded from the acceleration measurements, and as the discharge rate was independent of time, the critical height could be calculated. This method gave critical heights that were in agreement with direct measurements made for the transparent acrylic silo. For f_v<25 Hz, H_c did not vary by more than 0.1 m when the orifice diameter and spring constant were changed. For f_v>25 Hz, the variation of H_c with silo and granular material properties was not closely examined.

For all the granular materials, the values of H_c for the acrylic silo were smaller than those for the aluminum silo (Table 4). In the aluminum silo, crushed glass had a significantly smaller value of H_c than glass beads. In the acrylic silo, all three granular materials had similar values of H_c.

As frictional properties can depend on stress level [16], an experiment was performed in the aluminum silo, where the top of the granular material was loaded with a known weight after the silo had been filled. As explained in Vanel et al. [26] and Ovarlez et al. [27], such a test may yield different stress transmission characteristics for different experimental procedures; nevertheless, it can also increase the stress level inside a granular material. The weights were placed on top of the granular material in the filled silo and away from the walls of the silo. The values of H_c and f_p were calculated using time and acceleration measurements during discharge. The experiments showed that f_p was independent of the overload. For glass beads, H_c did not vary with overload; however, for crushed glass, H_c decreased linearly with as the overload increased (Fig. 13). Experiments in the acrylic silo gave similar results.

Table 4
Variation of critical height with silo wall and granular material properties

Silo wall material	Granular material	Critical height[a] (m)
Aluminum	Crushed glass	0.9
Aluminum	Glass beads	1.3
Acrylic	Crushed glass	0.8
Acrylic	Glass beads	0.6
Acrylic	Sand	0.7

[a] The accuracy of the critical height data is ±0.1 m.

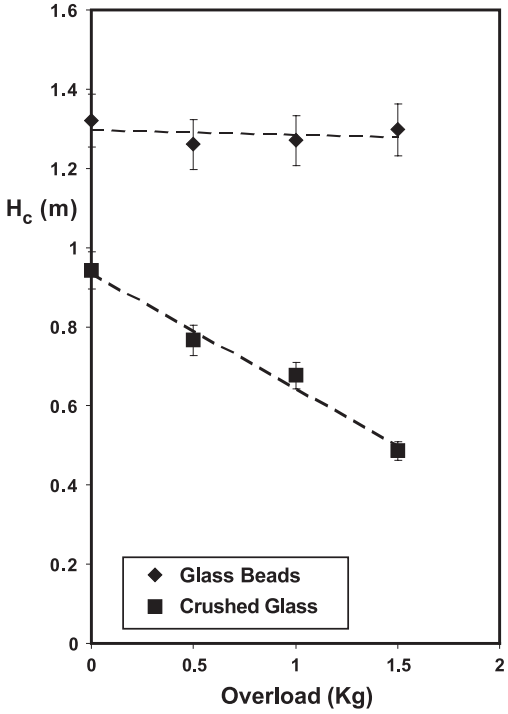

Fig. 13. Variation of critical height with overload for glass beads and crushed glass in the aluminum tube when the dominant natural frequency of vertical oscillations of the filled silo is 8 Hz and the silo has a 1.9-cm orifice.

5. Discussion

In this section, a mechanism for the production of pulsations is suggested. The results are then compared with those obtained in previous work on pulsating granular materials, and some suggestions for further work are made.

5.1. A mechanism for producing silo quake

Using the background on stick–slip friction in granular materials discussed earlier, one can compare the experimental observations in this study with those in previous studies to qualitatively explain the physical mechanism for stick–slip motion. The dynamic arch which forms in such flows is part of a force chain—that is, a particle contact network through which stresses are transmitted [28]. The arch is fragile, and consequently when the material below it has discharged enough so that the arch is unsupported from below, a slow creep typically observed in adhesive stick–slip flow begins. During this creep, the adhesive friction forces become progressively weaker and weaker, and eventually the arch will break. Once the arch collapses, complete slip occurs, a quake is observed, and a new arch is created. This quake can set up structural vibrations of decaying amplitude that then collapse the newly formed arch; in this manner, a series of self-sustained pulsations results. This is the pulsation process observed in this study, where the discharge rate is *fast* enough (between 1 and 8 cm/s) that it does not affect the f_p unlike in Wensrich's study [8,9].

In Wensrich's experiments [8,9], the entire bottom of a cylindrical model silo was slowly lowered. There is no region of converging flow in such an experiment, but there is a region near the bottom where the granular material dilates as the piston descends. Here, the arch may be regarded as the boundary between the dense and dilated material. For the *slow* discharge rates examined by Wensrich, creep and external perturbations did not determine f_p. Instead, the arch collapsed whenever the particles below the arch had dropped enough to lose contact with the arch. Consequently, it is entirely reasonable that f_p was inversely proportional to the discharge velocity. Wensrich estimated the distance that particles at the base of the silo moved between pulsations to be ~0.03 d_p (where d_p is the particle diameter), which is comparable to the dilation distance of ~0.05 d_p required for slip to occur in stick–slip flow in simple shear experiments with granular materials [17].

5.2. Comparison with previous work

Wensrich [8,9] observed that the acceleration produced by each quaking impulse grew with distance traveled by the wave carrying the information of the impulse from the dynamic arch to the top of the silo. In contrast, the granular material accelerations recorded in our experiments with the accelerometer at a fixed depth below the free surface did not change appreciably as the bed height decreased during discharge.

The granular material accelerations measured by Wensrich [8,9] were less than 15 m/s^2, while those measured in this study were typically more than 100 m/s^2. Tejchman [10] also observed silo wall acceleration levels greater than 100 m/s^2. Nonlinear effects may be responsible for the height independence of the acceleration at the large accelerations seen in this study.

It is interesting to contrast the acceleration power spectra obtained with crushed glass and glass beads to see the effect of particle shape on granular dynamics. The power spectra for acceleration measurements in the glass beads (Fig. 10b) showed many harmonics of f_p before the high-frequency decay region was approached. The power spectra for crushed glass (Fig. 10a) showed only a few harmonics, followed by a band-limited white noise region, and then a high-frequency decay. This suggests that the glass beads showed a highly correlated distributed response to slip which originated at the arch. Crushed glass had a significantly less correlated response, quite possibly because of the heterogeneity in particle shape and particle contacts between them. This is consistent with the suggestions by Mair et al. [29] that smooth round particles have force chains that are stable over a narrow range of orientations, whereas rough particles such as the crushed glass have force chains that are stable over a wider range of orientations. Consequently, the force chains in the glass beads break in a highly correlated manner during a pulsation, whereas those in the crushed glass break in a less-correlated manner.

Acrylic surfaces are prone to stick–slip motion [30]. As acrylic is softer than all the particles used in this study, the acrylic surface can be expected to be the dominant factor in determining the adhesive relaxation time for the stick–slip motion, and indeed it was found that the pulsation frequencies for all granular materials are similar in the acrylic silo.

The hypothesized difference in stress chain behavior between smooth and rough particles suggested by Mair et al. [29] can also explain the difference in the value of the critical height when an overload is imposed on the granular material. For rough particles, the critical height decreased linearly with imposed overload, whereas for smooth particles, the critical height was independent of the imposed overload. As the force chains in a granular material composed of smooth spheres will have narrow directionality, the effects of the imposed overload will be transmitted to the side walls of the silo rapidly and will not affect stress levels between the silo wall and the granular material a significant distance away from the overload. These force chains form a bridge so that the bulk of the overload is transmitted to the silo walls. For rough particles, the force chains will have a much broader directionality, as friction and asperity interlocking allows rough particles to transmit forces in a variety of directions without failure. Because bridging in the granular material is less effective, the imposed overload is not screened, and its effects on the stress field can be transmitted further in to the granular material. Consequently, the critical height decreases, because stresses at the arch are large and allow pulsations to occur for a longer time during discharge, in agreement with studies that slip–stick friction is dependent on the local stress level [16].

The Janssen solution for the effect of an overload on the stress field in a granular medium in a silo [13] predicts that the effect of the overload on the stress field inside the granular material decays faster as the angle of wall friction is increased. Crushed glass has a larger angle of wall friction than the glass beads, and so the finding that an overload has more effect on the crushed glass than the glass beads does not agree with the predictions from the Janssen solution. Nedderman [13] has suggested that the Janssen solution is not a good method for predicting stress levels inside a granular material when an overload is imposed. Further work examining the shear and wall normal stresses in silos for different shapes and distributions of particle sizes with varying overloads would help in obtaining appropriate constitutive relations to describe granular material stress fields macroscopically, an area which is the subject of current debate [26,27].

Mair et al. [29] found that particle shape influences granular material sliding characteristics. This study confirms this finding, because granular materials made of the same glass with similar sizes but different shapes had different pulsation frequencies in the aluminum tube. In particular, surfaces that are rough are less likely to have stick–slip

friction, because the asperities can lock and prevent slip occurring at all contact points. This argument is consistent with our finding that no pulsations occurred in the fully rough plain steel tube. These results are also in accord with findings by Tejchman [10], Moriyama and Jimbo [4], and Jahagirdar [2] that to prevent silo quake, mass flow silos should have rough walls.

Hardow et al. [1], whose study did not examine a variety of granular materials, suggested that wall friction was not the cause of silo quake, a finding that this study has shown is not always correct. As their study was for a core flow silo, they did not consider the possibility that stick–slip friction can occur at sliding surfaces inside the granular material, as shown in the study by Nasuno et al. [16], and not just between the granular material and the silo wall.

Finally, Hardow et al. [1] suggested that resonance is not always required for silo quake, while other studies have suggested that it is an important factor in amplifying the amplitude of the pulsations [3,5,10,11]. Our study does not give a conclusive answer to this question, as we have measured only the dominant natural frequency of vertical oscillations of the silo; careful measurements of the natural frequencies associated with radial vibration of the filled silo tube are required to make a more definitive statement, but these were not measured.

6. Conclusion

This study has shown that stick–slip motion generates silo music and silo quake. Silo music is driven by the stick–slip pulsating motion of the granular material during discharge and is associated with a resonance in the air column above the bed. When the pulsating motion disappears, so does the silo music. Over the range of discharge rates studied here (equivalent to average velocities of descent through the tube of 1–8 cm/s), the pulsation frequency was independent of discharge velocity. Both silo music and flow pulsations stopped abruptly when the bed height fell below a critical value. The critical height could be changed by placing an overload in the case of crushed glass, but not in the case of the smooth glass beads. This may be rationalized, although only speculatively at this point, by differences in stress chain behavior.

Acknowledgements

We are grateful to Professors J. Tejchman and A. Smits for many helpful discussions. The authors also wish to thank C. Wensrich for providing a copy of his thesis in advance of publication. KKR is very grateful to Mr. P.T. Raghuram for directing his attention to this problem by demonstrating the silo music experiment in 1996. BKM was supported by a Princeton University Francis Upton graduate fellowship and by the African Institute for Mathematical Sciences. SFQ acknowledges financial support provided by the Derek Lidow senior thesis fund. This work was supported by the U.S. Department of Energy CDE-FC26-00NT40971.

References

[1] B. Hardow, D. Schulze, J. Schwedes, An experimental analysis of the 'silo quaking' phenomenon, Proc. Of the 3rd World Congress on Particle Technology, Brighton, England, 1998.
[2] S. Jahagirdar, An experimental study of sound emission during granular flow, Department of Chemical Engineering, Indian Institute of Science, Bangalore, India, 1999.
[3] J. Kmita, Silo as a system of self-induced vibration, ASCE J. Struct. Eng. 111 (1985) 190.
[4] R. Moriyama, G. Jimbo, Reduction of pulsating wall pressure near the transition point in a bin, Bulk Solids Handl. 8 (1988) 421.
[5] M. Niedostatkiewicz, J. Tejchman, Experimental and theoretical studies on resonance dynamic effects during silo flow, Powder Handl. Proc. 15 (1) (2003) 36.
[6] C.E.S. Phillips, Electrical and other properties of sand, Proc. R. Inst. G. B. 19 (1910) 742.
[7] J. Tejchman, G. Gudehus, Silo-music and silo-quake, experiments and a numerical cosserat approach, Powder Technol. 76 (1993) 201.
[8] C.M. Wensrich, Experimental behaviour of quaking in tall silos, Powder Technol. 127 (2002) 87.
[9] C.M. Wensrich, Analytical and Numerical Modeling of Quaking in Tall Silos, PhD thesis, University of Newcastle, Australia (2002).
[10] J. Tejchman, Technical concept to prevent the silo honking, Powder Technol. 106 (1999) 7.
[11] J. Tejchman, M. Niedostatkiewicz, Resonance effects during granular flows in silos, Proc. International Congress for Particle Technology, Nuremburg, Germany, 2001.
[12] G. Ovarlez, E. Clément, Slow dynamics and aging in a confined granular flow, Phys. Rev., E 68 (2003) 031302.
[13] R.M. Nedderman, Statics and Kinematics of Granular Materials, Cambridge University Press, 1992.
[14] G.W. Baxter, R.P. Behringer, T. Fagert, G.A. Johnson, Pattern formation in flowing sand, Phys. Rev. Lett. 62 (24) (1989) 2825.
[15] M.G. Perry, M.F. Handley, The dynamic arch in free flowing granular material discharging from a model hopper, Trans. Inst. Chem. Eng. 45 (1967) T367.
[16] S. Nasuno, A. Kudrolli, A. Bak, J.P. Gollub, Time-resolved studies of stick–slip friction in sheared granular layers, Phys. Rev., E 58 (2) (1998) 2161.
[17] J.C. Géminard, W. Losert, J.P. Gollub, Frictional mechanics of wet granular material, Phys. Rev., E 59 (5) (1999) 5881.
[18] F.P. Bowden, D. Tabor, The Friction and Lubrication of Solids, Oxford University Press, 1950.
[19] J. Krim, Friction at macroscopic and microscopic length scales, Am. J. Phys. 70 (9) (2002) 890.
[20] A.D. Berman, W.A. Ducker, J.N. Israelachivili, Experimental and theoretical investigation of stick–slip friction mechanisms, in: B.N.J. Persson, E. Tosatti (Eds.), Physics of Sliding Friction, Kulwer Academic Publishers, 1996.
[21] M.N. Naeem, C.B. Sharma, Prediction of natural frequencies for thin circular cylindrical shells, Proc. Inst. Mech. Eng. C214 (2000) 1313.
[22] S.F. Quinn, Silo Music, BS thesis, Princeton University, Princeton, New Jersey, USA (2002).
[23] B.K. Muite, The effects of boundaries on granular and fluid mechanics, MSE thesis, Princeton University, Princeton, New Jersey, USA (2003).
[24] J.W.S. Rayleigh, The Theory of Sound, vol. II, Dover Publications, 1945.

[25] P. Bergé, Y. Pomeau, C. Vidal, Order Within Chaos, Wiley, 1984.
[26] L. Vanel, Ph. Claudin, J.-Ph. Bouchaud, M.E. Cates, E. Clément, J.P. Wittmer, Stresses in silos: comparison between theoretical models and new experiments, Phys. Rev. Lett. 84 (7) (2000) 1439.
[27] G. Ovarlez, C. Fond, E. Clément, A giant overshoot effect in the Janssen granular column, Phys. Rev., E 67 (2003) 60302.
[28] M.E. Cates, J.P. Wittmer, J.P. Bouchaud, P. Claudin, Jamming, force chains, and fragile matter, Phys. Rev. Lett. 81 (9) (1998) 1841.
[29] K. Mair, K.M. Frye, C. Marone, Influence of grain characteristics on the friction of granular shear zones, J. Geophys. Res. 107 (B10) (2002) 2219.
[30] S. Bouissou, J.P. Petit, M. Barquins, Normal load, slip rate and roughness influence on the polymethylmethacrylate dynamics of sliding: 1. Stable sliding to stick–slip transition, Wear 214 (1998) 156.